ÉCOLE POLYTECHNIQUE DE BRUXELLES
UNIVERSITÉ LIBRE DE BRUXELLES

Electrochemical Modeling, Supervision and Control of Lithium-Ion Batteries

Thesis submitted by Luis D. COUTO
in fulfilment of the requirements of the PhD Degree in Engineering Sciences and Technology ("Docteur en Sciences de l'Ingénieur et Technologie")
Academic year 2018-2019

Supervisor: Professor Michel KINNAERT

Department of Control Engineering and System Analysis

Wallonie

fnrs LA LIBERTÉ DE CHERCHER

Thesis jury:

Philippe BOGAERTS (Université libre de Bruxelles, Chair)
Johan GYSELINCK (Université libre de Bruxelles, Secretary)
Emanuele GARONE (Université libre de Bruxelles)
Alexandre LÉONARD (Université de Liège)
Scott MOURA (University of California, Berkeley)
Noshin OMAR (Vrije Universiteit Brussel)

"It is interesting to note that most of the early contributors to estimation theory were primarily astronomers rather than mathematicians. They used mathematics as a means to an end. Then, as now, the most outstanding and lasting contributions to theory were driven by practical engineering interests. "There is nothing so practical as a good theory". "

Dan Simon

UNIVERSITÉ LIBRE DE BRUXELLES

Abstract

École Polytechnique de Bruxelles
Department of Control Engineering and System Analysis

Submitted for the PhD Degree in Engineering Sciences and Technology

Electrochemical Modeling, Supervision and Control of Lithium-Ion Batteries

by Luis D. COUTO

This thesis develops an advanced battery monitoring and control system based on the electrochemical principles that govern lithium-ion battery dynamics. This work is motivated by the need of having safer and better energy storage systems for all kind of applications, from small scale portable electronics to large scale renewable energy storage. In this context, lithium-ion batteries have become the enabling technology for energy autonomy in appliances (e.g. mobile phone, electric vehicle) and energy self-consumption in households. However, batteries are oversized and pricey, might be unsafe, are slow to charge and may not equalize the lifetime of the application they are intended to power. This work tackles these different issues.

This document first introduces the general context of the battery management problem, as well as the particular issues that arise when modeling, supervising and controlling the battery short-term and long-term operation. Different solutions coming from the literature are reviewed, and several standard tools borrowed from control theory are exposed. Then, starting by well-known contributions in electrochemical modeling, we proceed to develop reduced-order models for the battery operation including degradation mechanisms, that are highly descriptive of the real phenomena taking place. This modeling framework is the cornerstone of all the monitoring and control development that follows.

Next, we derive a battery diagnosis system with a twofold objective. First, indicators for internal faults affecting the battery state-of-health are obtained. Secondly, detection and isolation of sensor faults is achieved. Both tasks rely on state observers designed from electrochemical models to perform state estimation and residual generation. Whereas the former solution resorts to system identification techniques for health monitoring, the latter solution exploits fault diagnosis for instrumentation assessment.

We then develop a feedback battery charge strategy able to push in performance while accounting for constraints associated to battery degradation. The fast and safe charging capabilities of the proposed approach are ultimately validated through long-term cycling experiments. This approach outperforms widely used commercial charging strategies in terms of both charging speed and degradation.

The main contribution of this thesis is the exploitation of first principles models to develop battery management strategies towards improving safety, charging time and lifetime of battery systems without jeopardizing performance. The obtained results show that system and control theory offer opportunities to improve battery operation, aside from the material sciences contributions to this field.

Acknowledgements

This dissertation is the result of four years of research at the Université Libre de Bruxelles, Department of Control Engineering and System Analysis. It is, however, the combined effort of several high-quality researchers and extraordinary people who have accompanied me during this journey. In this page, I will try to acknowledge all these people, and I apologize in advance if you, the reader, should have been mentioned.

First and foremost, I want to thank my advisor, Prof. M. Kinnaert, to whom I dedicate this thesis. I recall when he interviewed me four years ago, and how he trusted me and gave me the opportunity to get on this boat. He is one of the best researchers I have met (possibly I will ever meet), and he is a better person than a researcher. He taught me how to do research with an open mind and a critical spirit. Many thanks for your advice, patience and kindness, Michel. I will always be grateful.

I would also like to thank Prof. E. Garone. Although he was not directly my advisor, I felt like he was. He was always there every time I needed him. He is one of the smartest people I know, and we have been validating intuitions that he had four years ago. There are still some thoughts that we need to test, but he is probably right. He always is. Continuing with professors at the ULB, I want to thank the members of my thesis committee, namely Prof. P. Bogaerts and Prof. J. Gyselinck. Their curiosity and thorough feedback during the committee meetings will always be appreciated. Finally, I would also like to thank Prof. A. Léonard, with whom I collaborated for my first journal paper as a first author. He provided invaluable help in the achievement of the referred paper.

My gratitude also goes to the people at the Department that helped me during my first steps here. Without any priority order, I would like to thank Marco, who was one of my closest friends at the beginning of this adventure. Special thanks for Jingjing, who was always there to support me during the hardest initial moments of hesitation and uncertainty. Also thanks to Julien, my first office mate and dear friend. He had the patience to guide me and he believed in me from the start. He still does it. Also thanks to Laurent, Pascale, Serge and Prof. R. Hanus, who received me with open arms when I arrived. I want to give a shout-out to my other friends in the lab, namely Tam, Raffaele, Johnny, Sandra, Chris L., Robin, Chris M., Silvia, Nico, Sadja, Medhi, Silvane, Andres, Alejandro, Alberto, Satoshi, Kelly and Bryan. Most of them have tolerated me during the last months of the thesis, and that requires special abilities.

I also want to give a warm thanks to Prof. S. Moura from UC Berkeley. He received me in his department for seven months and without his collaboration, the results of this work would not have been possible. Besides letting us use his facilities, he was always open to have deep discussions and allowed me to contribute in different projects. Thank you very much Prof. Moura for giving me the opportunity to live such an intellectually stimulating experience. He leads an awesome team of people. Among them, I would like to thank Dong, Saehong, Zach and Hector, who made me feel as a part of the group from the beginning.

When I look back, I cannot help but remembering all the different steps that I have been taking in life, and there are many people that I am deeply grateful. They gave me my first opportunities to carry out research, what turned out to be my passion. Going backwards in time, thanks to Prof. M.A. Camblor from UAM and to Prof. F. Ribeiro and Prof. J. Madeira Lopes from IST, who notably taught me about zeolites. Also thanks to Prof. J. Guerra, who followed my last year project in college, and Prof.

S. Di Scipio who taught me separation processes and always was a close friend. They both are from the USB.

Last but not least, I want to thank my friends from my home country university and school, as well as my friends from life and family. I remember fondly Edu, Eli, Mou, Kathy, Dani, Fabi, Gian, Amaia, Kevin, Valen, Leo, Sergio and Dario, from the years back at the university. Special mention for Luis F., Santi, David, Pedro, Popi, Eu, Ori and Carito, my unforgettable and invaluable friends from school. They showed me what the true friendship is when you are a kid and you simply do not care about e.g. appearance or money. Thanks to my friends of life, who I met just because we happened to be in the right place at the right time, like Sylvie, Lau, Loui, Anita, Sirine, Emily, Ionel, Clau, Isa, Rebecca, Sophie, Alejandra and Ruta. Many thanks Loui, for holding me there the last 100 m of the race. And the most important thanks for the end, to my family. My mom, dad and sister, together with my aunts, cousins, grandparents and godfathers. I could not be here if it were not for you.

Finally, I would like to acknowledge the BATWAL project (Convention 1318146, PE Plan Marshall 2.vert) financed by the Walloon region (Belgium) and the Fonds pour la Formation à la Recherche dans l'Industrie et dans l'Agriculture (FRIA), since these were the funding sources that allowed me to perform this work.

Thanks to everyone who has participated to a greater or lesser extent in achieving this goal. I would not have reached the end without you all.

Contents

Abstract **v**

Acknowledgements **vii**

1 Introduction **1**
1.1 Motivation . . . 2
1.2 Open Challenges . . . 2
1.3 Contributions . . . 4
1.4 Thesis Structure . . . 5

2 State of the Art **7**
2.1 Battery Operation . . . 7
2.2 Battery Aging . . . 9
2.3 Battery Modeling . . . 11
2.4 State Estimation . . . 20
2.5 Parameter Estimation . . . 22
2.6 Fault Detection and Isolation . . . 24
2.7 Constrained Control . . . 26
2.8 Concluding Remarks . . . 27

3 Prerequisite Material **29**
3.1 State Estimation . . . 29
3.1.1 The Kalman Filter . . . 29
3.1.2 The Extended Kalman Filter . . . 31
3.1.3 The Unscented Kalman Filter . . . 33
3.2 Parameter Estimation . . . 37
3.2.1 Least Squares Estimation . . . 37
3.2.2 The Standard Instrumental Variable Estimation . . . 39
3.2.3 The Simplified Refined Instrumental Variable Estimation . . . 40
3.3 Fault Detection and Isolation . . . 44
3.4 Constrained Control . . . 47

4 Battery Modeling **51**
4.1 Battery Cell Simulator . . . 51
4.2 Modeling for State Estimation & Control . . . 52
4.2.1 Diffusion Equations & Material Balance . . . 53
Solid-Phase Diffusion Equation . . . 53
Electrolyte-Phase Diffusion Equation . . . 54
Model-Order Reduction . . . 55
Material Balance . . . 59
4.2.2 Thermal Equation . . . 60
4.2.3 State Space Model Summary . . . 61
4.2.4 Output Equation . . . 61

4.2.5 Analysis of Aging . . . 62
Aging Model . . . 63
Electrochemical Constraints . . . 66
4.2.6 Summary of Reduced-Order Model with Constraints . . . 67
4.2.7 Analysis of Equilibrium Points . . . 68
4.2.8 Discretization for Implementation . . . 70
4.3 Concluding Remarks . . . 71

5 System Identification & Fault Detection and Isolation 73
5.1 State/Parameter Estimation for SOH . . . 73
5.1.1 Constrained Extended Kalman Filter . . . 74
5.1.2 The SRIVC & LS Methods . . . 77
Estimation of the Diffusion Time Constant . . . 78
Estimation of the Film Resistance . . . 81
5.2 Validation of State/Parameter Estimation for SOH . . . 82
5.2.1 Validation Through Simulation . . . 82
5.2.2 Experimental Validation . . . 88
Setup and Testing Conditions . . . 89
Results and Discussion . . . 89
5.3 State/Parameter Estimation for Battery Monitoring & FDI . . . 93
5.3.1 From the EKF to the UKF . . . 93
5.3.2 The Dual Unscented Kalman Filter for NLDAE Systems . . . 95
5.3.3 Fault Detection and Isolation . . . 99
5.4 Validation of State/Parameter Estimation for Battery Monitoring & FDI 101
5.5 Concluding Remarks . . . 104

6 Fast Charging Constrained Control 107
6.1 State Feedback Constrained Control . . . 107
6.1.1 Pre-Stabilization . . . 108
6.1.2 Electrochemical Constraints Reformulation . . . 109
6.1.3 The Reference Governor with OR Constraints . . . 111
6.1.4 Digital Implementation . . . 114
6.2 Simulation Results . . . 114
6.3 Concluding Remarks . . . 118

7 Safe & Fast Charging Control 121
7.1 Output Feedback Constrained Control . . . 121
7.1.1 Model Identification . . . 121
7.1.2 The Reference Governor with OR Constraints . . . 124
7.1.3 The Extended Kalman Filter . . . 125
7.2 Experimental Results . . . 126
7.2.1 Setup and Testing Conditions . . . 126
7.2.2 Closed-loop Implementation . . . 129
7.2.3 Results and Discussion . . . 131
Commercial Charging Strategies: 1C vs 2C CCCV Comparison 131
The RG with OR constraints . . . 135
Commercial Charging Strategies vs RG Comparison . . . 138
7.3 Concluding Remarks . . . 147

8 Final Remarks **149**
8.1 Thesis Summary 149
8.2 Conclusions 151
8.3 Future Research Directions 152

A List of Publications **155**

B $\tilde{O}_\infty$ Computation in the Case of OR-Constraints **157**

C Battery Model Parameters for Simulation **159**

D Computation of Electrolyte-Phase Diffusion Model **163**

Bibliography **165**

List of Figures

1.1 Air/airport incidents involving batteries carried as cargo or baggage organized according to a) the number of incidents every five years and b) the battery state of use (adapted from [5]). 3

2.1 Schematic representation of a cross section of a lithium-ion battery cell subject to a charging process, highlighting the different battery components (adapted from [9]). Ions of lithium and hexafluorophosphate, and electrons are denoted by Li^+, PF_6^- and e^-, respectively, while negative electrode, separator, positive electrode and battery cell thicknesses are denoted by L^-, L^s, L^+ and L, respectively. L^{-s} represents the negative electrode and separator thickness combined. 8
2.2 Schematic representation of the charging process of a lithium-ion battery cell. At the top: the battery cell domains (negative electrode ($-$), separator (s) and positive electrode ($+$)), in the middle: the electrolyte phase (e), at the bottom: a particle solid phase (s). The indicated variables are: solid and electrolyte phase concentration (c_s and c_e, respectively), solid and electrolyte phase electric potential (ϕ_s and ϕ_e, respectively), pore-wall molar flux (j_n), electrolyte and solid-phase diffusion coefficients (D_e and D_s, respectively) and spherical particle radius (R_s). 14
2.3 Schematic representation of main and side reactions, namely solvent reduction reaction and lithium plating. Li^+, $Li(s)$ and e^- denote lithium-ions, solid lithium and electrons, respectively, S and P are electrolyte solvent and side reaction product, respectively, and R_s and δ_f are spherical particle radius and film thickness, respectively. 15

4.1 Equivalent-hydraulic model consisting of n tanks, where u, q_i, $g_{i,i+1}$ and β_i, $i = 1, \ldots, n$, are respectively the input current, tank level state, valve coefficient and tank cross-section area for a given number of tanks n. 56
4.2 Equivalent-hydraulic model representing the spherical particle with n sections, where u and $g_{i,i+1}$ represent the input current and valve coefficient, respectively. 57
4.3 Bode plots of the irrational transfer function Eq. (4.5) in black, and from the 2nd to the 3rd-order Padé approximations of Eq. (4.17) and Table 4.2 in red, green and blue respectively. 59
4.4 Present situation of a BMS (purple region) together with the ideal situation of an advanced BMS (green region) in terms of the operational envelope defined by the accounted constraints. The operating map is derived from a) measured variables and b) electrochemical variables. Safe operation region, region where lithium plating takes place and region where solvent reduction reaction occurs are represented by green, red and orange regions, respectively. 64

4.5 Galvanostatic charge of a graphite | LCO battery cell at 5C. The left y-axis portrays the different negative electrode potential contributions to the battery voltage, as well as the side reaction potentials. The right y-axis shows the battery voltage. 65
4.6 Dependence of side reaction current density due to SEI growth on surface overpotential. 70

5.1 Block diagram of the monitoring system for a battery cell. 73
5.2 Block diagram of the identification scheme. 74
5.3 a) Series of galvanostatic charge/discharge current profile of C/5, C/2 and 1C consecutive cycles; b) simulated voltage (noise free as solid black curve) and predicted voltage (dashed blue curve). 83
5.4 Stochastic stability simulation study considering three cases, namely: 1) small initial error and small measurement noise (solid red curve), 2) small initial error and large measurement noise (dashed green curve), and 3) large initial error and small measurement noise (dotted blue curve). The plotted signals are a) series of galvanostatic charge/discharge current profile of C/5, C/2 and 1C consecutive cycles, and associated voltage (noise free simulation); b) simulated (solid black curve) and estimated CSC; c) estimation error of CSC. 84
5.5 Hola10 85
5.6 State estimation study: a) simulated (solid black curve) and predicted CSC (dashed blue curve); b) CSC estimation error. 86
5.7 State estimation study: a) fixed (solid black curve) and predicted g_s (dashed blue curve); b) solid and dashed black lines respectively depict the lower and upper bound of the contact-resistance distribution R_r while dashed blue curve is the predicted R_f. 87
5.8 a) Series of galvanostatic charge/discharge current profile of C/5, C/2 and 1C consecutive cycles carried out at 25°C between 2.0 and 4.2 V; b) experimental (solid black curve) and predicted voltage (dashed blue curve). 90
5.9 State estimation study: a) Coulomb-counted (solid black curve) and estimated SOC (dashed blue curve); b) estimated CSC. 90
5.10 State estimation study: a) estimated g_s; b) experimentally determined contact resistance mean $\bar{R}_r$ (solid black curve) and estimated R_f (dashed blue curve). 91
5.11 Block diagram of the fault detection and isolation scheme. 93
5.12 Nonlinear (in red), linearized (in green) and unscented transformed (blue) mean (symbol) and covariance (curve) of normally distributed random variables for a) case 1, b) case 2 and c) case 3 in Table 5.8. The gray dots correspond to the sampled probability distribution of the random variable. 96
5.13 Primary reaction current state ($\hat{z}$) estimated with the dual UKF in the left y-axis, where solid black and dashed red, green and blue (overlapping) curves represent the scenarios of fault-free, internal faults, voltage sensor fault and surface temperature sensor fault, respectively. The right y-axis corresponds to the associated estimation error (dotted blue curve). 101

5.14 State estimation study: a) solid-phase diffusion states; b) electrolyte-phase diffusion states; c) thermal states. Solid black and dashed red, green and blue (overlapping) curves represent the scenarios of fault-free, internal faults, voltage sensor fault and surface temperature sensor fault, respectively. 103
5.15 State estimation study: a) capacity fade state; b) normalized aging parameters, namely rate capability and power fade on the left and right y-axis, respectively. Solid black and dashed red, green and blue curves represent the scenarios of fault-free, internal faults, voltage sensor fault and surface temperature sensor fault, respectively. 104
5.16 Fault detection study considering the voltage sensor: a) generated residuals and b) associated GLR decision function. Solid red, dashed green and dotted blue curves represent the scenarios of internal faults, voltage sensor fault and surface temperature sensor fault, respectively. 105
5.17 Fault detection study considering the surface temperature: a) generated residuals and b) associated GLR decision function. Solid red, dashed green and dotted blue curves represent the scenarios of internal faults, voltage sensor fault and surface temperature sensor fault, respectively. 105

6.1 Block diagram of the control system for a battery cell. 107
6.2 Block diagram of the optimal constrained control scheme. 108
6.3 Electrochemical constraints mapping, where a) nonlinear nonconvex operating region delimited by constraint boundaries; admissible area for b) lower and c) upper bounds of constraint Eqs. (4.49a),(4.49b); union of linear approximations of constraint Eqs. (2.32c)-(2.32e), i.e. d) lines 5,1 and 5,2 and e) lines 6,1 and 6,2; and f) resulting admissible (green) and unsafe (red) regions resulting from the intersection of all the approximated constraints. 110
6.4 DFN model critical conditions for η_{sr}^{+} at the positive electrode/separator interface (electrode dependent), $\eta_{sr}^{-} = 0.0$ V at the negative electrode/separator interface and $c_e = 1.0$ mol·m^{-3} at the current collector/negative electrode interface (common for both batteries). The green, orange and red regions represent the admissible, safety margin and unsafe operating regions, respectively. The solid red and cyan curves represent the DFN simulator states and the EKF state estimates, respectively. 116
6.5 Current and voltage profiles from the DFN simulator using CCCV (as dashed curves) and the proposed RG method (as solid curves) for LCO (in magenta) and LMO (in blue). 117
6.6 Profiles of the constrained variables from the DFN simulator using CCCV (as dashed curves) and the proposed RG method (as solid curves) for LCO (in magenta) and LMO (in blue). 119

7.1 a) 2C CC applied current at 25°C, and associated response of the battery in terms of b) voltage and c) surface temperature. Different system models are also shown in the voltage plots, namely V_{exp} is the experimental voltage; $V_{\text{mod},0}$ is the battery OCV; $V_{\text{mod},1}$ is the surface overpotential; $V_{\text{mod},2}$ is the electrolyte potential drop; and $V_{\text{mod},3}$ is an ohmic resistance potential drop. The temperature plots show the experimental surface temperature $T_{bs,\text{exp}}$ and the modeled core $T_{bc,\text{mod}}$ and surface temperatures $T_{bs,\text{mod}}$. 122
7.2 Flow chart of the cycling aging (CAT) and reference performance (RPT) tests. 126
7.3 a) Current and b) voltage response of a battery subject to C/2 CCCV charging profile at 25°C. 128
7.4 Schematic representation of the experimental layout needed to implement the charging strategy based on the proposed RG with OR constraints scheme. 130
7.5 Simulink diagram for the implementation of the proposed RG with OR constraints charging strategy. 132
7.6 Performance comparison between two commercial charging strategies, namely 1C CCCV (in green) and 2C CCCV (in blue), in terms of a) retained capacity, b) resistance increase and c) charge time. Both CATs (curves) and RPTs (symbols) are shown. Dashed and solid curves respectively represent variables for the CC and the CCCV stage of a CCCV charging strategy. Symbols ● and ○ represent charge (chg) and discharge (dchg) variables, respectively. 133
7.7 Measurements gathered from the PEC tester for the first cycle block of CAT, namely a) current, b) voltage (V_{exp}) and c) surface temperature ($T_{bs,\text{exp}}$). Superimposed to these signals are the voltage (V_{ekf}) and both surface ($T_{bs,\text{ekf}}$) and core temperature ($T_{bc,\text{ekf}}$) predicted by the EKF. . . 136
7.8 EKF estimated internal state of the battery cell during the first cycle block, namely a) solid (SOC and CSC) and b) electrolyte-phase (C_{eb} and C_{es}) diffusion states, and c) film resistance. The figure inset is a close-up of the solid-phase diffusion state at the last cycle. 137
7.9 Signals generated by the RG during the first cycle block, namely a) desired reference r and applied reference v, together with real SOC, and b) gain κ. 138
7.10 I-CSC plane portraying the trajectories followed by the battery system state under the charging protocol generated from the RG during the first cycle block. The red-yellow color gradient reflects the cycle number from 1 to 11. 139
7.11 Performance comparison between 1C CCCV commercial (in green) and proposed RG (in red) charging strategies in terms of a) retained capacity, b) resistance increase and c) charge time. Both CATs (curves) and RPTs (symbols) are shown. The dashed black lines represent the reference SOC used at each cycle block. Symbols ● and ○ represent charge (chg) and discharge (dchg) variables, respectively. The figure inset highlights the difference between the RPTs for each charging strategy. 140

7.12 Performance comparison between two commercial charging strategies, namely 1C CCCV (in green) and 2C CCCV (in blue), and the proposed RG (in red) charging strategy in terms of a) retained capacity, b) resistance increase and c) charge time. Both CATs (curves) and RPTs (symbols) are shown. Symbols ● and ○ represent charge (chg) and discharge (dchg) variables, respectively. 142
7.13 Performance comparison between two commercial charging strategies, namely 1C CCCV (in green) and 2C CCCV (in blue), and the proposed RG (in red) charging strategy in terms of a) charging speed and b) capacity evolution with charge/discharge throughput. Both CATs (curves) and RPTs (symbols) are shown. Symbols ● and ○ represent charge (chg) and discharge (dchg) variables, respectively. 143
7.14 a) Current, b) voltage and c) surface temperature profiles from the 1st cycle block of a battery cell subject to different charging strategies, namely 1C CCCV (dashed green curves), 2C CCCV (dotted blue curves) and proposed RG (solid red curves). The figure inset is a close-up of the three signals during the 2nd charge cycle. 143
7.15 a) Current, b) voltage and c) surface temperature profiles from the 5th cycle per cycle block of a battery cell subject to different charging strategies, namely 1C CCCV (dashed green-olive curves), 2C CCCV (dotted pink-blue curves) and proposed RG (solid red-yellow curves). The first-second color corresponds to first-last cycle block, the color gradient reflects the cycle blocks in-between and the arrows in plot c) highlight the evolution of the thermal profile with cycle blocks. The figure inset is a close-up of the charging currents for the last cycle blocks during 2C CCCV charge. 145
7.16 Common stress factors considered for lithium-ion batteries, namely a) maximum (solid curves) and average (dashed curves) applied current, b) maximum (dashed curves, denoted as "max") and end of charge voltage (solid curves, denoted as "EOC") and c) maximum surface temperature. Green, blue and red curves correspond to 1C CCCV, 2C CCCV and proposed RG, respectively. 146
7.17 Capacity fade correlation plot obtained by pairing the retained capacity of each charging strategy with each other, namely 1C vs 2C (green), RG vs 2C (red) and 1C vs RG (blue). 147

List of Tables

2.1 Main DFN model equations. The nomenclature for this table is provided in the List of Symbols. . . . 13
2.2 Two-states thermal model equations. The nomenclature for this table is provided in the List of Symbols. . . . 14
2.3 Aging model equations for a generic side reaction sr, where $sr = \{\text{SEI}, lp\}$ for SEI growth and lithium plating, respectively [11, 33, 34, 12] . The nomenclature for this table is provided in the List of Symbols. 16

3.1 The Kalman filter algorithm†. . . . 30
3.2 The extended Kalman filter algorithm†. . . . 32
3.3 The unscented Kalman filter algorithm†. . . . 35
3.4 The standard instrumental variable algorithm†. . . . 40
3.5 The simplified refined instrumental variable method for continuous-time systems algorithm, where s denotes the Laplace variable†. . . . 43

4.1 Electrolyte-phase diffusion partial differential equations. . . . 54
4.2 State A_j and input B_j matrices for the diffusion equation of different orders, where $j \in \{s, e\}$ for solid and electrolyte phases, respectively. . 58
4.3 Functions associated to the material balance and output equations. . . 60

5.1 Extended Kalman filter with state constraints†. . . . 77
5.2 The simplified refined instrumental variable method for continuous-time systems for the parameter identification of the transfer function Eq. (5.19) given the measurements Eq. (5.20)†. . . . 80
5.3 Initial estimates and measurement noise variance for the stochastic stability study. . . . 83
5.4 Results obtained using the SRIVC method for the estimation of D_s and R_s, and the LS method for the estimation of R_f on each cycle block of simulated data. . . . 87
5.5 Fit results obtained from comparing the EKF estimation with the Padé approximation model using the true (θ) and estimated ($\hat{\theta}_{\text{phys}}$) parameters. 88
5.6 Results obtained using the LS method for the estimation of D_s and R_s on each cycle block of simulated data. . . . 88
5.7 Results obtained using the SRIVC method for the estimation of D_s and R_s, and the LS method for the estimation of R_f on each cycle block of experimental data. . . . 92
5.8 Mean and standard deviation values of the random variables used to simulate model Eqs. (5.40),(5.41). . . . 95
5.9 The dual unscented Kalman filter algorithm for the considered NLDAE system [156, 126]†. . . . 100
5.10 Equations describing parameter drift, sensor fault magnitudes and fault injection time instants for each variable. . . . 102

6.1 Values for the DFN model constraints Eqs. (2.32) associated to degradation mechanisms. 115
6.2 Values for the constraints Eq. (6.9). 115

7.1 Instrumentation accuracy of the battery tester, namely current, voltage and temperature sensor, as well as data sampling time. 128
7.2 Fitting parameters of the linear function Eq. (7.20) describing the retained capacity for a battery subject to 1C and 2C CCCV charging strategies. The fitted data is the RPT points of Fig. 7.6(a), and a set of parameters is obtained for each C-rate and cycle stage. 134
7.3 Fitting parameters of the linear function Eq. (7.21) describing the resistance increase for a battery subject to 1C and 2C CCCV charging strategies. The fitted data is the RPT points of Fig. 7.6(b), and a set of parameters is obtained for each C-rate and charge/discharge mode. . . 135
7.4 Fitting parameters of the linear function Eqs. (7.20) and (7.21) describing the retained capacity and resistance increase for a battery subject to the proposed RG charging strategy. The fitted data is the RPT points of Fig. 7.11(a), and a set of parameters is obtained for each cycle stage and charge/discharge mode. 140

8.1 Summary of the different contributions proposed throughout this thesis. 151

C.1 List of parameters for the LFP half battery cell [148] used in Section 5.2 to set up the DFN-based simulator. 159
C.2 List of parameters used for setting up the DFN-based simulator used in Section 5.4 and Chapter 6 for a graphite | LCO [157] and a graphite | LMO [22, 157, 159] battery cell. 160
C.3 List of parameters used for setting up the DFN-based simulator used in Chapter 7 for a graphite | NCA battery cell [90]. 160

List of Abbreviations

BMS	**B**attery-**M**anagement **S**ystem
CC	**C**onstant **C**urrent
CV	**C**onstant **V**oltage
CAT	**C**ycling **A**ging **T**est
CSC	**C**ritical **S**urface **C**oncentration
DAE	**D**ifferential **A**lgebraic **E**quation
DFN	**D**oyle-**F**uller-**N**ewman
ECM	**E**quivalent-**C**ircuit **M**odel
EKF	**E**xtended **K**alman **F**ilter
EChM	**E**lectro**Ch**emical **M**odel
FDI	**F**ault **D**etection and **I**solation
GLR	**G**eneralized **L**ikelihood **R**atio
IV	**I**nstrumental **V**ariable
KF	**K**alman **F**ilter
LS	**L**east **S**quares
LCO	**L**ithium-**C**obalt-**O**xide
LFP	**L**ithium-**I**ron-**P**hosphate
LMO	**L**ithium-**M**anganese-**O**xide
LQR	**L**inear **Q**uadratic **R**egulator
LTO	**L**ithium-**T**itanium-**O**xide
LRPT	**L**ong **R**eference **P**erformance **T**est
MPC	**M**odel **P**redictive **C**ontrol
NCA	**N**ickel-**C**obalt-**A**luminum
NMC	**N**ickel-**M**anganese-**C**obalt
NLDAE	**N**on**L**inear **D**ifferential **A**lgebraic **E**quation
OCP	**O**pen **C**ircuit **P**otential
OCV	**O**pen **C**ircuit **V**oltage
ODE	**O**rdinary **D**ifferential **E**quation
PDE	**P**artial **D**ifferential **E**quation
RG	**R**eference **G**overnor
RPT	**R**eference **P**erformance **T**est
SEI	**S**olid-**E**lectrolyte **I**nterphase
SIV	**S**tandard **I**nstrumental **V**ariable
SOC	**S**tate-**O**f-**C**harge
SOH	**S**tate-**O**f-**H**ealth
SPM	**S**ingle **P**article **M**odel
SRG	**S**calar **R**eference **G**overnor
SVF	**S**tate **V**ariable **F**ilter
SRPT	**S**hort **R**eference **P**erformance **T**est
SRIVC	**S**implified **R**efined **IV** method for **C**ontinuous-time
UKF	**U**nscented **K**alman **F**ilter

Physical Constants

Universal gas	$R_g = 8.31\ \mathrm{J \cdot mol^{-1} \cdot K^{-1}}$
Faraday's	$F = 96487\ \mathrm{C \cdot mol^{-1}}$

List of Symbols

Electrochemical modeling		
A	cross-sectional area of the cell	m^2
a_s	specific interfacial area	m^{-1}
c	concentration of lithium	$\mathrm{mol} \cdot \mathrm{m}^{-3}$
C_p	specific heat capacity	$\mathrm{J} \cdot \mathrm{g}^{-1} \cdot \mathrm{K}^{-1}$
CSC	critical-surface-concentration	-
D	diffusion coefficient	$\mathrm{m}^2 \cdot \mathrm{s}^{-1}$
E	activation energy	$\mathrm{J} \cdot \mathrm{mol}^{-1}$
$f_{c/a}$	activity coefficient	-
g	inverse of the diffusion time constant	s^{-1}
h_c	heat transfer coefficient	$\mathrm{W} \cdot \mathrm{m}^{-2} \cdot \mathrm{K}^{-1}$
i_0	exchange current density	$\mathrm{A} \cdot \mathrm{m}^{-2}$
I	applied current	$\mathrm{A} \cdot \mathrm{m}^{-2}$
j	pore-wall molar flux	$\mathrm{mol} \cdot \mathrm{m}^{-2} \cdot \mathrm{s}^{-1}$
k	reaction rate constant	$\mathrm{A} \cdot \mathrm{m}^{2.5} \cdot \mathrm{mol}^{-1.5}$
k_c	thermal conductivity	$\mathrm{W} \cdot \mathrm{m}^{-1} \cdot \mathrm{K}^{-1}$
L	electrode/separator thickness	m
M	molecular weight	$\mathrm{g} \cdot \mathrm{mol}^{-1}$
n^{Li}	number of lithium moles	mol
Q_b	battery capacity	Ah
Q_e	electrode capacity	Ah
Q_{loss}	battery capacity loss	Ah
r	radial coordinate	m
R	particle radius	m
R_b	battery resistance	Ω
R_f	film resistance	$\Omega \cdot \mathrm{m}^2$
SOC	state-of-charge	-
t	time	s
t_c^0	transference number	-
T_{amb}	ambient temperature	K
T_b	battery temperature	K
U	open-circuit potential	V
V	voltage	V
x	coordinate across the cell thickness	m
y	stoichiometry of lithium	-
∇	cutoff frequency	Hz
System monitoring and control		
$\hat{a}$	estimated value of a	
$\tilde{a}$	error $a - \hat{a}$	
$\bar{a}$	mean of a	
$\mathring{a}$	noise-free variable	
a^-	predicted value of a	

a^+	projected value of a	
k	discrete-time variable	
t	continuous-time variable	
t_k	sampled data time variable	
t_0	initial time	
t_f	final time	
T_s	sampling period	
r	desired reference	
u	input vector	
v	applied reference	
v_n	measurement noise vector	
w_n	process noise vector	
x	dynamic state vector	
y	output vector	
z	algebraic state vector	
A	state matrix	
B	input matrix	
C	output matrix	
F	state function Jacobian	
H	output function Jacobian	
I_d	d by d identity matrix	
K	Kalman gain	
K_i	LQR gain for integrator state	
K_c	LQR gain $= [K_c, K_i]$	
K_x	LQR gain for dynamic state	
P	estimation error covariance matrix	
P_c	solution to the control algebraic Riccati equation	
Q	process noise variance matrix	
Q_c	tracking error weighting matrix	
R	measurement noise variance matrix	
R_c	control effort weighting matrix	
$f(\cdot)$	nonlinear function characterizing the state dynamics	
$h(\cdot)$	nonlinear function in the output equation or the algebraic state equation	
$G(s)$	transfer function	
c_c	total number of constraints	
n_c	number of OR constraints	
f	fault magnitude	
g_{GLR}	generalized likelihood ratio decision function	
$\bar{h}$	threshold	
$S(\cdot)$	cumulative sum	

Greek

α_0	apparent transfer coefficient	-
ε	active material volume fraction	-
δ	thickness	m
δ_t	time delay	s
ϵ	Bruggeman's exponent	-
ζ	instrumental vector	
η	overpotential	V

ϕ	electric potential	V
φ	regressor vector	
κ_e	ionic conductivity	$S \cdot m^{-1}$
κ	reference governor gain	
ν	residual	
ρ	density	$g \cdot m^{-3}$
σ	electronic conductivity	$S \cdot m^{-1}$
τ	diffusion time constant	s
$\tau_{f,0}$	time instant of fault injection	s
Y	measurement	

Subscript

b	bulk
c	core
cl	closed-loop
coef	polynomial coefficient
e	electrolyte phase
eff	effective variable
f	film
f	filtered signal
l	linearized
lp	lithium plating
max	theoretical maximum
n	main reaction
nl	nonlinear
p	side reaction product
phys	physical
ref	reference
$(\cdot)s$	surface
s	solid phase
sr	side reaction
st	solvent
SEI	solid-electrolyte interphase
t	total
T	thermal
UT	unscented transformed
θ	parameter

Superscript

ac	active constraint
d	discrete-time
s	separator domain
$-$	negative electrode domain
$+$	positive electrode domain

Math notation

$\|\| \cdot \|\|$	2-norm
$1_{n\times 1}$	column vector of ones with n components
$0_{n\times 1}$	column vector of zeros with n components
$\overline{a}$	mean or upper bound
$\underline{a}$	lower bound
$\delta_{(\cdot)}$	Kronecker delta function

δx	error on the measurement of x
$\Delta\chi^{\pm}$	difference between χ^{+} and χ^{-} variables
$\mathrm{diag}(\cdot)$	diagonal elements of the matrix entry
$\bigwedge(\cdot)$	AND operator
$\bigvee(\cdot)$	OR operator
$\mathbb{E}(\cdot)$	expectation operator
$\mathcal{H}(\cdot)$	hypothesis
$\mathcal{L}(\cdot), P_{\theta}$	probability law
$\mathcal{N}(\mu, \sigma^2)$	normal distribution with mean μ and variance σ^2
$\mathcal{X}$	sigma-points for x
O_{∞}	maximal output admissible set
$\tilde{O}_{\infty}$	inner approximation of O_{∞}
Y_{k-1}	data sequence up to and including k
$\mathbb{N}$	natural numbers
$\mathbb{R}$	real numbers
R^2	coefficient of determination
s	Laplace variable
σ	standard deviation
σ^2	variance
p_{θ}	probability density function of θ

Note: The symbol "-" in the list of units corresponds to no units, while the lack of this symbol corresponds to any unit.

For the best advisor that someone could ever have asked for.

Chapter 1

Introduction

This document shows the improved performance and increased lifetime that can be extracted from lithium-ion batteries through their advanced management. More precisely, electrochemical models and degradation constraints are exploited to develop a battery monitoring and control system that is health-conscious and does not cut down on performance. These two aspects are highly relevant specially for large scale applications, such as electric vehicles and renewable energy storage systems. An improved operation of the battery has the potential to greatly reduce both the price of the system and the time of recharge, and increase both the battery lifespan and safety. Having a product with all these assets is very appealing from the point of view of the investor or consumer.

The proposed battery management system relies on physical models and control theoretic tools. On the one hand, various electrochemical models differing in complexity are studied in detail, together with model constraints that trigger degradation processes if violated. On the other hand, electrochemistry-based state observers, fault diagnostic systems and constrained controllers are developed and tested notably for the fast and safe charging of the battery. These solutions are not limited to any particular lithium-ion battery chemistry, and pieces of them can be used for problems in other energy storage related research topics like fuel cells.

This work pinpoints the main sources of battery degradation from the electrochemical perspective, and proposes ways to handle them during battery regular operation. It turns out that some degradation mechanisms cannot be avoided for a reasonable battery use, and they reduce battery capacity but do not imply a safety hazard. Other mechanisms however are more detrimental to both battery life and safety, but they can be mitigated through health-conscious strategies. Novel methods for battery monitoring and control are presented in this dissertation, which are for the first time (to the best of the author's knowledge) validated with a battery-in-the-loop experimental setup. Indeed, the proposed approach is able to charge faster and safer lithium-ion batteries when compared to commercially available charging strategies as CCCV protocols.

This first chapter is structured as follows. Section 1.1 provides the motivation behind developing advanced battery management systems able to reduce battery design conservatism, improve its performance and extend its lifetime while ensuring safe operation. Section 1.2 pinpoints the main challenges related to the monitoring and control of battery systems based on electrochemical models. Finally, the different contributions that arise from this thesis are gathered in Section 1.3, followed by the outline of the document in Section 1.4.

1.1 Motivation

Among the main concerns regarding battery systems are their price, safety, reliability and performance, not necessarily in this order of priorities. In this context, the work proposed here aims at providing solutions to these issues through the development of advanced battery management systems (BMSs). A lithium-ion battery controlled by an advanced BMS might be designed with less conservatism for the same performance as one operated by a traditional BMS. This aspect has the potential to reduce both the battery size and price, which would have a huge impact in large scale applications like electric vehicles. In fact, automotive applications have become the driving force to impulse the outbreak of lithium-ion batteries in other sectors, such as the grid and renewable energy storage. With battery cell prices ranging from 200 $\$\cdot kWh^{-1}$ to 500 $\$\cdot kWh^{-1}$ [1], the price of the battery can amount from 15% to 50% of the cost of an electric car[1]. A few dollar difference per kWh can have big repercussions for the car cost. In a market that is expected to boom from 3 to 125 million electric vehicles on the road worldwide by 2030 (according to the International Energy Agency), battery price may enable a thriving technology or doom it to fail.

Even though battery price or size are important factors when considering this energy storage technology, other concerns are by far more important such as safety and lifetime expectancy. In terms of safety, battery failures like short circuits can have serious consequences, as exemplified by the lithium-ion battery failures in certain Samsung mobile phones [2] or the blaze due to a battery in a Boeing 787 Dreamliner in 2013 at Heathrow Airport [3], just to name a few. One of the main agencies that have kept track of different battery incidents is the Federal Aviation Administration of the United States. A total of 225 air/airport incidents involving batteries carried as cargo or baggage have been recorded from 1991 to 2018 [4]. Fig. 1.1(a) depicts the number of incidents registered every five years starting from 1991, whereas Fig. 1.1(b) shows a pie chart with the incidents organized according to the battery state of use, namely new, in use by consumers or in equipment batteries. As the figure shows, there has been an increase in the amount of incidents related to batteries since 1991. Most of these incidents are associated to new batteries.

In terms of battery life span, batteries are expected to last as long as the application in which they are used, for instance 10-15 years (i.e. 20,000-30,000 cycles) of service life in automotive applications [6], and 20 years as autonomous power supply systems for solar panels [7]. Safer batteries with prolonged lifetime but without trading performance is what we look for with this work. This can be achieved via advanced monitoring and control tools.

1.2 Open Challenges

Although a rich body of literature has been already built on the topic of lithium-ion batteries development, monitoring and control, there are still some challenges that need to be faced, namely:

- The term "lithium-ion" does not denote a battery but a family of batteries that share the lithium chemistry. This issue complicates the modeling, monitoring and control problem, which nowadays counts with a myriad of solutions in the

[1] This price share has been obtained by considering battery prices ranging from 200 $\$\cdot kWh^{-1}$ to 500 $\$\cdot kWh^{-1}$, and several electric vehicle types of different prices and with different battery capacities, namely BMW i3, Renault ZOE40, Jaguar I-pace, Tesla Model S and Audi e-tron

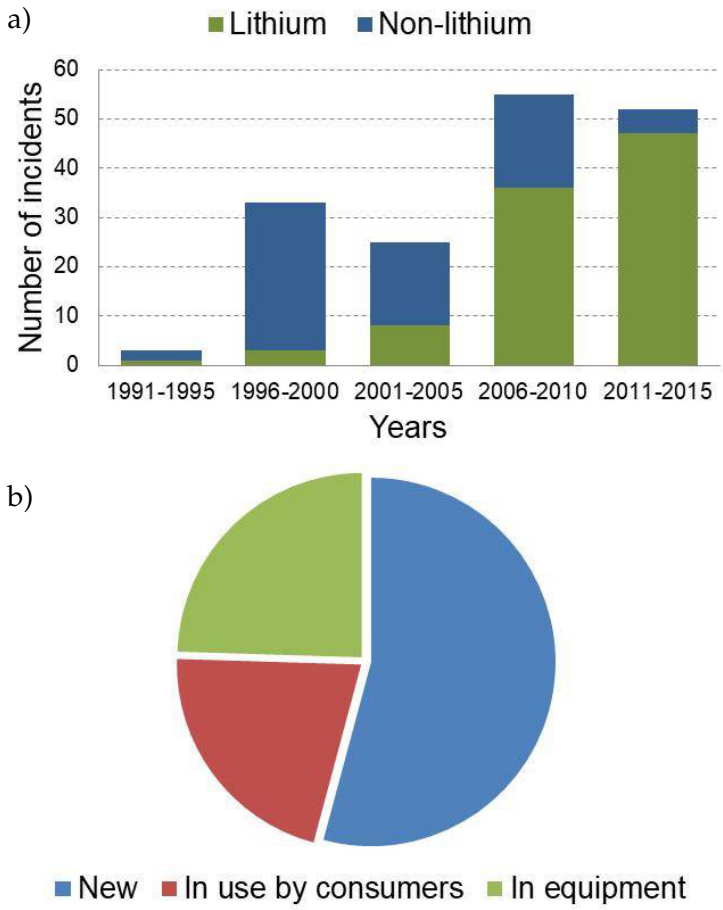

FIGURE 1.1: Air/airport incidents involving batteries carried as cargo or baggage organized according to a) the number of incidents every five years and b) the battery state of use (adapted from [5]).

literature. An unified framework to develop battery management systems built upon the most performant methods is still a pending task.

- Models that are highly descriptive of the processes taking place inside a battery are based on electrochemistry. These models are infinite-dimensional and nonlinear, and such sophistication prevents their exploitation for online battery monitoring and control. Reduced-order electrochemical models able to keep relevant battery dynamics exist, but they are typically limited to specific operating ranges.

- Online monitoring of internal states and degradation is difficult during battery regular operation given the limited number of measured quantities and the effect of measurement noise. Moreover, estimation schemes completely rely on the accuracy of the taken measurements and overlook possible instrumentation malfunctions. Diagnostic systems able to provide fault detection and robust and unbiased estimation are missing.

- Batteries are a very special application when it comes to its management. Since it is an energy storage system, the computational overload that is incurred should be ideally low and merit its use through improving battery performance.

This aspect still needs to be recognized, and solutions along these lines should be provided.

1.3 Contributions

In this thesis, we aim at designing and validating an advanced monitoring and control system for lithium-ion battery management that improves battery performance and lifetime. The derived control schemes are tested with different battery chemistries in order to highlight the generality of the proposed framework. To achieve this goal, three main categories of contributions can be distinguished, which are shown in the following and also gave rise to the list of publications reported in Appendix A.

- **Electrochemical modeling of lithium-ion batteries:** A full-order electrochemical model based on nonlinear partial differential algebraic equations is modified to account for degradation processes. This high-order model is then reduced by resorting to physically motivated approximations to come up with simpler models that are useful for monitoring tasks. Different aging mechanisms are considered and categorized according to their appearance during battery regular operation. Each mechanism is treated in a particular way. Electrochemically meaningful constraints associated to battery degradation are derived, so that their compliance improves the performance and extends the life of the battery. Even though different reduced-order electrochemical models have been proposed in the literature, the original one used here and later extended has never been associated to degradation mechanisms. Moreover, the clear distinction between battery aging tracking and degradation avoidance has been drawn and exploited here for the first time.

- **Battery diagnosis system:** State observers based on electrochemical models are designed, which account for parametric uncertainty, operating point changes, algebraic constraints arising from battery degradation and physical constraints. Although the state observers used are standard, their novelty with respect to the ones in the literature lies in i) the electrochemical models at their core, ii) the way of combining different design strategies to address the battery estimation problem at hand, like equality and inequality state constraints, and iii) the developed physics-based tuning procedure. Battery state-of-health indicators are deduced from the physics, and their estimation is tackled. Tools coming from the parameter identification community are exploited in order to properly handle the initialization and noise susceptibility (Refs. A.1-A.3) of more traditional parameter estimation approaches proposed by other authors. Sensor fault detection and isolation is also carried out in parallel to state-of-health estimation, which has been mostly overlooked by the battery research community so far (Ref. A.4).

- **Validation of feedback charge strategy:** A state feedback controller that is computationally cheaper than other more traditional control strategies (like model predictive control) is designed. This controller exploits the state information provided by the state observer to generate a control input signal for battery charging. This control scheme results from solving an unconstrained optimization problem for the control law design, while ensuring satisfaction of degradation-related constraints through an add-on control scheme (Ref. A.5, A.6). The proposed approach was intended to charge lithium-ion batteries in

a faster and safer way than commercial charging protocols based on CCCV protocols. This latter claim was verified via long-term battery cycling tests. This is the first time that reduced-order electrochemical models, state observers and constrained control schemes as the ones proposed in this dissertation have been proven successful experimentally for the advanced management of the charging process of lithium-ion batteries.

- Besides the work reported in this thesis, I also contributed to other research projects, see for instance Refs. A7-A11.

1.4 Thesis Structure

This thesis is organized as follows. The state of the art of the different topics covered by this dissertation is reviewed in Chapter 2. The main tools coming from control theory that are used in this work are presented in Chapter 3. In Chapter 4, simplified electrochemistry-based mathematical models are derived to describe the battery dynamic behaviour, along with equations that reflect the battery aging evolution with time and operating conditions. These models are exploited for monitoring and control purposes in the consecutive chapters. Two approaches for system fault diagnosis are introduced in Chapter 5, namely one focusing on battery state-of-health monitoring and the other one centered around sensor fault detection and isolation. In Chapter 6, the models and estimators of previous chapters are used to design a feedback strategy able to avoid degradation regimes while fast charging batteries. Finally, in Chapter 7, an experimental validation of the control scheme of the previous chapter is performed through prolonged cycling tests.

Chapter 2

State of the Art

The research concerning lithium-ion batteries is multidisciplinary, from battery development, passing by the ancillary electronics surrounding its operation (actuators, instrumentation), up to the software with suitable algorithms to monitor and control the working battery. At least three main bodies of literature can be distinguished in the field of batteries, each one of them associated to a major field in science. The first body comes from electrochemistry, and it focuses on the material science aspect of developing batteries. The resulting batteries are further tested to provide insight into the processes occurring inside them, i.e. how a given battery works and what limits its performance. The second body comes from electrical and electronic engineering, and it is related with the battery integration into a given power network, either a battery cell within a battery pack or a pack within an electrical network. The last body comes from automation and control engineering, and it is framed in the context of battery-management systems (BMSs). There is no consensus of the final definition and functions of a BMS, but a wide view adopted in [8] is also considered here, i.e. a BMS is any system that manages the battery. Among its tasks, a BMS has to protect the battery cells from being damaged, to guarantee their safety and prolong their service life as long as possible and to ensure that they fulfill the application requirements. The BMS involves then the development of software in charge of monitoring and controlling the battery during regular operation. This dissertation is centered around the first and third battery main topics, namely it exploits the knowledge from the electrochemical community to develop highly performant supervisory control systems.

In the following, the state of the art in the fundamental research of batteries and their supervisory control is covered. The former topic involves a description of the battery operation and of the source responsible of limiting its performance in the long run, i.e. battery aging. The latter topic includes battery modeling, state/parameter estimation, fault detection and isolation and optimal control, subtopics that are discussed subsequently.

2.1 Battery Operation

Lithium-ion batteries are electrochemical energy storage systems that stand out with respect to other accumulators of energy given their high efficiency and energy/power density. A battery cell is, roughly speaking, a sandwich made of different layers of porous materials, namely a negative electrode, a separator and a positive electrode, whereas a solution called electrolyte floods all the empty spaces (pores) of these materials. There is no single lithium-ion battery but a variety of chemistries. Negative electrodes can be made of graphite or lithium-titanium-oxide (LTO), although the former is the most widely used. Positive electrodes can be lithium-cobalt-oxide (LCO), lithium-iron-phosphate (LFP), lithium-manganese-oxide (LMO),

nickel-cobalt-aluminum (NCA) or nickel-manganese-cobalt (NMC), and blends of those. Besides these active materials, electrodes also incorporate a binder and a conductive filler to improve electrode particles cohesion and electric conductivity, respectively. The separator can be made of polyolefin materials such as polyethylene and polypropylene. It is placed in-between the two electrodes to isolate them electronically, although it is an ionic conductor. The electrolyte can be liquid or gel, and it is a solution of lithium salts (e.g. lithium hexafluorophosphate, $LiPF_6$) and organic solvents (e.g. carbonates such as ethylene and diethyl carbonate). Current collectors are placed at the negative and positive terminals of the battery cell. Copper and aluminum are the most commonly used materials for negative and positive electrodes, respectively. They both are electronic conductors.

During charging, a positive overpotential is applied to the battery cell, which promotes the deintercalation (oxidation) of lithium from the positive electrode. This process corresponds to the forward reaction in Eq. (2.1) for a generic graphite | LMeO battery, where Me stands for the metal of a given chemistry [9].

$$\begin{aligned} C_6 + xLi^+ + xe^- &\rightleftharpoons Li_xC_6 \\ LiMeO_z &\rightleftharpoons Li_{1-y}MeO_z + yLi^+ + ye^-. \end{aligned} \tag{2.1}$$

The resulting lithium-ions (Li^+) constitute an ionic current that travels throughout the electrolyte. It leaves the positive electrode, crosses the separator and reaches the negative electrode, where the intercalation (reduction) of lithium takes place. Simultaneously, an electric current leaves the system from the positive electrode, performs electrical work and comes back to the system through the negative electrode. This process is depicted Fig. 2.1. The opposite mechanism is the discharge process, which corresponds to the backward reaction in Eq. (2.1). The stored energy is a function of the potential difference between both electrodes. Both oxidation/reduction reactions constitute the desired intercalation reaction in a lithium-ion battery cell.

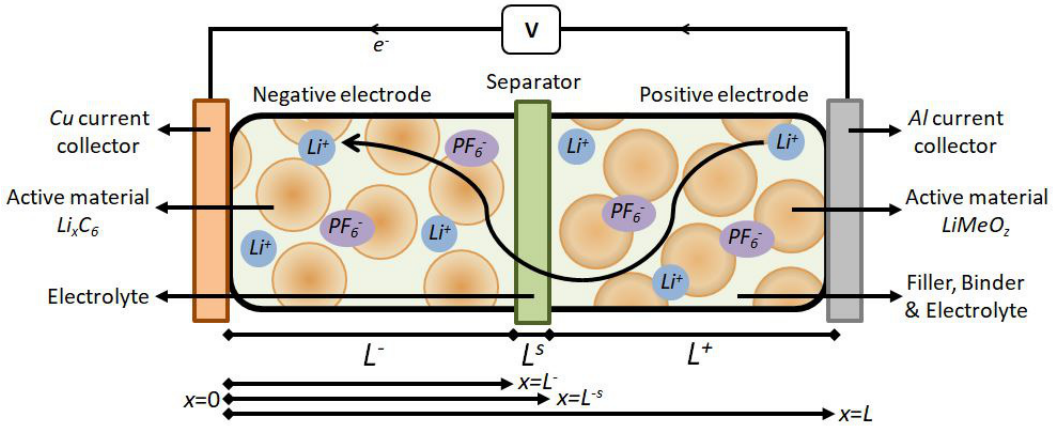

FIGURE 2.1: Schematic representation of a cross section of a lithium-ion battery cell subject to a charging process, highlighting the different battery components (adapted from [9]). Ions of lithium and hexafluorophosphate, and electrons are denoted by Li^+, PF_6^- and e^-, respectively, while negative electrode, separator, positive electrode and battery cell thicknesses are denoted by L^-, L^s, L^+ and L, respectively. L^{-s} represents the negative electrode and separator thickness combined.

2.2 Battery Aging

Besides the main intercalation reaction, lithium-ion batteries are prone to side reactions occurring simultaneously. The latter reactions consume available lithium, which leads to capacity/power fade and can even compromise the battery safe operation [9, 10]. Battery degradation might have different origins, which could be correlated and are dependent on the specific chemistry [9]. The most relevant sources of degradation that have been identified for a variety of electrode chemistries include solid-electrolyte interphase (SEI) formation and growth [11], and lithium plating [12].

The SEI is a passive film that is formed on the surface of the negative electrode during the first charging processes. Such a film is the product of reduction side reactions involving lithiated carbon, the electrolyte and the solvent. At the beginning, the SEI protects the electrode from further reacting with the electrolyte and slows down the battery degradation rate. However, in the long run the SEI limits battery performance through capacity and power fade. The reduction of solvent ethylene carbonate S occurring at the graphite electrode can be modeled as [11]

$$S + 2Li^{+} + 2e^{-} \rightarrow P \tag{2.2}$$

where P is the obtained product.

Another side reaction that consumes available lithium is the so-called lithium plating, and this one is by far more dangerous than SEI growth. Lithium plating occurs when the potential of the graphite negative electrode becomes negative, and it consists of lithium deposition onto the electrode surface instead of its intercalation. This deposition of metal lithium can lead to dendrites formation, which can pierce the separator and cause a short circuit. It turns out that lithium plating occurs at later stages of battery life, and it is responsible for the nonlinear aging behavior evidenced at such stages [12]. This reaction can be written as [13]

$$Li^{+} + e^{-} \rightarrow Li(s). \tag{2.3}$$

where $Li(s)$ is metal lithium.

Apart from side reactions resulting in SEI growth and lithium plating, some other relevant degradation mechanisms include electrolyte decomposition, SEI breakdown, gas generation, overcharge, overdischarge, self-discharge, loss of active material, migration of soluble species, particle fracture, mechanical stress and structural changes [9, 14, 15, 16, 17].

Battery degradation can occur either when batteries are in use or even when they are stored. The former operation condition is known as cycling aging while the latter is calendar aging. Empirical models for calendar aging assume that dominant degradations like impedance (denoted R_f) increase due to SEI growth and lithium capacity loss Q_{loss} have a power of time relationship such as

$$R_f \propto a_1 t^z, \;\; Q_{\text{loss}} \propto b_1 t^z \tag{2.4}$$

where a_1 and b_1 are constants, $z = 1/2$ for diffusion-controlled and $z = 1$ for a kinetic controlled aging processes, and it takes values of $z = [0.3, 1]$ for mixed mechanisms [18]. Empirical models for cycling aging assume that degradation rates are proportional to cycle number N such as

$$R_f \propto a_2 N^{1/(1+p)}, \;\; Q_{\text{loss}} \propto b_2 N^{1/(1+p)} \tag{2.5}$$

where a_2 and b_2 are constants, in general $p = 0$ for R_f whereas it takes values within the interval $[0, 3]$ for Q_{loss} according to the acceleration rate of the degradation process [18].

2.3 Battery Modeling

In order to perform battery monitoring and control, accurate models are required. The objectives of battery modeling are twofold. In one hand, battery simulators based on sophisticated models allow the numerical validation of control strategies, which on the other hand are built upon simpler models. Several lithium-ion battery cell models have been proposed in the literature, from data-driven [19] to equivalent-circuits [20] and electrochemical models. The first type of model has the drawback of requiring a large amount of data for training. Equivalent-circuit models (ECM) rely on the analogy between battery systems and electrical systems. However, the former systems involve lithium diffusion, migration, intercalation and reaction processes, besides the electrical ones, which cannot be modeled by the latter type of systems. Therefore, ECM variables suffer from lack of interpretability, preventing their link to e.g. the physics of battery degradation. Physically meaningless models cannot be exploited for developing high-fidelity battery simulators rooted in electrochemical principles. These inconveniences are not exhibited by the physics-based electrochemical models (EChMs). Furthermore, in contrast to other models, EChMs can be leveraged to perform battery fault diagnosis and constrained control that is less restrictive.

In the following, we only focus on electrochemical type of models in order to limit the scope of this work. Therefore, we deliberately leave aside a rich body of literature dealing with other modeling efforts such as ECMs. Interested readers are referred to [20] for a comprehensive review in ECMs. Regarding electrochemical models, they have been less exploited historically, although recent years have witnessed a boom in their development and use.

The Doyle-Fuller-Newman Model

Among the different EChMs, the Doyle-Fuller-Newman (DFN) model [21, 22, 23] is the most widely used one. The DFN model mathematically describes the electrochemical processes occurring inside a lithium-ion battery cell, which are detailed in Section 2.1. It considers the negative electrode $(-)$, the separator (s) and the positive electrode $(+)$ as three domains, with two phases, namely the porous solid phase (s) and the electrolyte solution phase (e) [1]. The solid phase of the system is assumed to be made of spherical particles. While the solid phase is only present in the electrode domains, the solution phase covers all three domains. Fig. 2.2 depicts a schematic representation of the charge process taking place within a lithium-ion battery cell. The whole cell with the three domains and two phases is shown at the top, the electrolyte phase is in the middle, and a spherical particle taken out from each electrode solid-phase is depicted at the bottom of the figure. The main partial differential and algebraic equations describing the electrochemical system dynamics are shown in Table 2.1[2]. Each of these five equations has an associated dependent variable, which is also represented in Fig. 2.2 using the same notation as the table. These variables are: the solid and electrolyte phase concentration (c_s and c_e, respectively), the solid and electrolyte phase electric potential (ϕ_s and ϕ_e, respectively) and the pore-wall molar flux (j_n). All these variables depend on the space (r- and x-axis along the radius of the electrodes spherical particles and the thickness of the battery cell, respectively) and the time (t). This model is a multi-particle model, in which a solid-phase spherical

[1] The symbols in parentheses are used as super-script and sub-script to denote the domain and phase of a model state variable, respectively.

[2] Continuous-time with time variable t and the time derivative as $\frac{d\chi}{dt}(\cdot, t)$ is adopted in this section for the DFN model, according to its traditional presentation in the literature.

particle can be located at each x position in the electrode domains. Within these spherical particles, diffusion takes place only in the r direction. This fact explains the other name with which the DFN model is known, i.e. pseudo-2D model.

Remark 2.3.1. *Even though the DFN model is the most widely used battery model based on electrochemistry, it has some limitations. Firstly, it is a pseudo-2D model where lithium-ions diffuse in 1D along the battery cell thickness, and it assumes homogeneous diffusion throughout the spherical particle radius. In large format batteries, a 1D description of the cell might not be sufficient to accurately capture its thermo-electrochemical behaviour. Thus, the DFN model has been extended to pseudo-3D [24] and 3D [25] models. Secondly, the original DFN model neglects some battery dynamics, such as thermal and aging dynamics, but it has been proven flexible to include them as additional phenomena, see for instance [26] for temperature evolution, [11] for solid-electrolyte interphase growth or [17] for intercalation-induced stress in active particles. More recently, the DFN model accuracy has been put in question for high currents and temperatures [27]. In spite of these restrictions, the DFN model still constitutes the virtual battery benchmark for excellence and therefore it is exploited in this dissertation for battery cell simulation. The considered DFN model is extended with thermal dynamics and some degradation mechanisms as explained below.*

The charge process in Fig. 2.2 shows, at the bottom plot, lithium diffusion from the bulk to the surface of the positive electrode spherical particle, where the main deintercalation reaction occurs and produces a pore-wall molar flux. The lithium then passes to the electrolyte phase (see middle plot), where it is in ionic form and travels from the positive electrode, through the separator up to the negative electrode. Once in the negative electrode, a pore-wall molar flux is produced while the main intercalation reaction takes place, followed by lithium diffusion from the surface to the bulk of the negative electrode spherical particle, as it can be seen again at the bottom plot. Meanwhile, the top plot portrays the electrons journey from the positive electrode to the negative electrode, generating electrical work outside the system.

While the original DFN model framework [21, 22] is the basis for battery cell modeling, other equations have been incorporated into this framework to capture more dynamics. For instance, thermal models derived from energy balance [28, 29, 30] have been coupled to the DFN model by replacing the constant temperature T_{amb} by a given dynamic battery temperature state T_b. Although these thermal balances consider a bulk temperature state with lumped thermal parameters, other works discriminate between the battery core (bc) and surface (bs) temperature [3] [31]. The main differential and algebraic equations describing the thermal system dynamics are shown in Table 2.2.

Other dynamics introduced in the DFN framework correspond to those of aging mechanisms, such as the ones described in Section 2.2. The equations behind side reactions (sr) have been formally derived from electrochemical principles. The main equations describing the aging induced by side reactions such as SEI growth (SEI) and lithium plating (lp)[3] are shown in Table 2.3. The cathodic Tafel approximation for the side reaction rate Eq. (2.22) is deduced by considering the Butler-Volmer kinetics (Eq. (2.14) considering $\alpha_0 = 0.5$) under the assumption of an irreversible solvent reduction reaction [23]. Moreover, although some models only consider side reactions during battery charge claiming that they are more relevant during this operation mode, here we opted for allowing battery degradation during discharge as well [32]. This approach avoids the degradation discontinuity depending on the operation mode and lets the side reaction to take place as a function of its given overpotential.

[3]The symbols in parentheses are used as sub-script of a model state variable.

TABLE 2.1: Main DFN model equations. The nomenclature for this table is provided in the List of Symbols.

Physical Process	Equation	Boundary Conditions	
Solid-phase:			
Conservation of Li^+	$\frac{\partial c_s^{\pm}}{\partial t}(x,r,t) = \frac{1}{r^2}\frac{\partial}{\partial r}\left(D_s^{\pm} r^2 \frac{\partial c_s^{\pm}}{\partial r}(x,r,t)\right)$	$\frac{\partial c_s^{\pm}}{\partial r}(x,r,t)\Big\|_{r=0} = 0$ $\frac{\partial c_s^{\pm}}{\partial r}(x,r,t)\Big\|_{r=R_s^{\pm}} = -\frac{1}{D_s^{\pm}} j_n^{\pm}(x,t)$	(2.6)
with	$\bar{c}_s^{\pm}(x,t) = \frac{3}{(R_s^{\pm})^3}\int_0^{R_s^{\pm}} r^2 c_s^{\pm}(x,r,t)dr$ and $c_{ss}^{\pm}(x,t) = c_s^{\pm}(x,r,t)\big\|_{r=R_s^{\pm}}$		(2.7)
Conservation of charge	$\frac{\partial}{\partial x}\left(\sigma_s^{\pm}\frac{\partial \phi_s^{\pm}}{\partial x}(x,t)\right) = a_s^{\pm} F j_n^{\pm}(x,t)$	$\frac{\partial \phi_s^{-}}{\partial x}(x,t)\Big\|_{x=L^-} = \frac{\partial \phi_s^{+}}{\partial x}(x,t)\Big\|_{x=L^s} = 0$ $-\sigma_s^{-}\frac{\partial \phi_s^{-}}{\partial x}(x,t)\Big\|_{x=0} = \sigma_s^{+}\frac{\partial \phi_s^{+}}{\partial x}(x,t)\Big\|_{x=L} = I(t)$	(2.8)
Electrolyte-phase:			
Conservation of Li^{+a}	$\frac{\partial c_e}{\partial t}(x,t) = \frac{\partial}{\partial x}\left(\frac{D_{e,\text{eff}}(c_e)}{\varepsilon_e}\frac{\partial c_e}{\partial x}(x,t)\right) + \frac{a_s(1-t_c^0)}{\varepsilon_e} j_n(x,t)$	$\frac{\partial c_e}{\partial x}(x,t)\Big\|_{x=0} = \frac{\partial c_e}{\partial x}(x,t)\Big\|_{x=L} = 0$	(2.9)
Conservation of charge[a]	$\frac{\partial}{\partial x}\left(\kappa_{e,\text{eff}}(c_e)\frac{\partial \phi_e}{\partial x}(x,t)\right) = -a_s F j_n(x,t) + \frac{\partial}{\partial x}\left(\kappa_{D,\text{eff}}(c_e)\frac{\partial \ln c_e}{\partial x}(x,t)\right)$	$\frac{\partial \phi_e}{\partial x}(x,t)\Big\|_{x=L^+} = \frac{\partial \phi_e}{\partial x}(x,t)\Big\|_{x=0} = 0$	(2.10)
where	$D_{e,\text{ref}}(c_e) = 5.34\cdot 10^{-10}\exp\left(\frac{-0.65 c_e(x,t)}{10^3}\right)$		(2.11)
	$\kappa_{e,\text{ref}}(c_e) = 0.0911 + 1.9101\frac{c_e(x,t)}{10^3} - 1.052(\frac{c_e(x,t)}{10^3})^2 + 0.1554(\frac{c_e(x,t)}{10^3})^3$		(2.12)
	$\kappa_{D,\text{eff}}(c_e) = \frac{2R_g T_{\text{amb}}}{F}(1-t_c^0)\kappa_{e,\text{eff}}(c_e)\left(1 + \frac{d\ln f_{c/a}}{d\ln c_e}(x,t)\right)$		(2.13)
Electrode kinetics:			
Intercalation reaction[b]	$j_n^{\pm}(x,t) = \frac{2}{F} i_0^{\pm}(c_{ss}^{\pm}, c_e)\sinh\left(\frac{\alpha_0 F}{R_g T_{\text{amb}}}\eta_s^{\pm}(\phi_s^{\pm}, \phi_e, c_{ss}^{\pm}, j_n^{\pm})\right)$		(2.14)
where	$\eta_s^{\pm}(\phi_s^{\pm}, \phi_e, c_{ss}^{\pm}, j_n^{\pm}) = \phi_s^{\pm}(x,t) - \phi_e(x,t) - U_s^{\pm}(c_{ss}^{\pm}(x,t)) - R_f^{\pm} F j_n^{\pm}(x,t)$		(2.15)
	$i_0^{\pm}(c_{ss}^{\pm}, c_e) = k_n^{\pm}\left(c_e(x,t)c_{ss}^{\pm}(x,t)\left(c_{s,\max}^{\pm} - c_{ss}^{\pm}(x,t)\right)\right)^{\alpha_0}$		(2.16)
Battery voltage:	$V(t) = \phi_s^{+}(x,t)\big\|_{x=L} - \phi_s^{-}(x,t)\big\|_{x=0}$		(2.17)

[a] $\Psi_{\text{eff}} = \Psi\varepsilon_e^{\epsilon}$, where Ψ could be D_e or κ_e [b] This is the Butler-Volmer equation assuming $\alpha_0 = 0.5$.

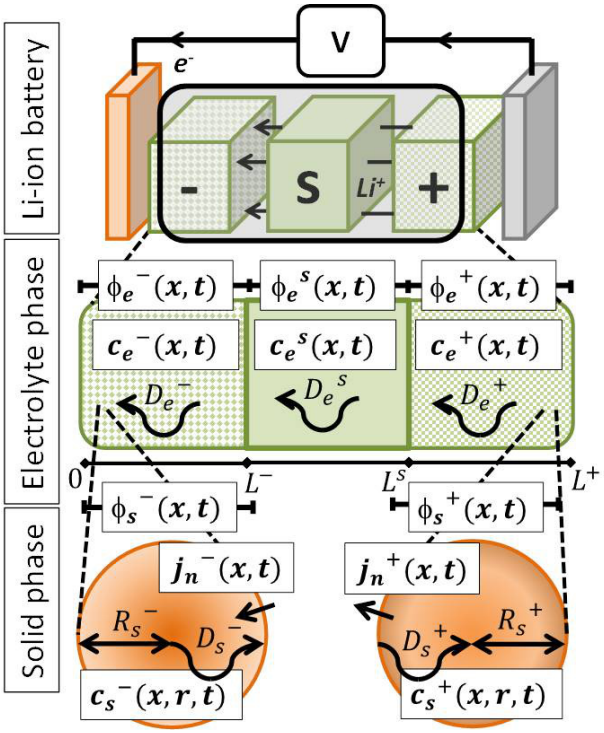

FIGURE 2.2: Schematic representation of the charging process of a lithium-ion battery cell. At the top: the battery cell domains (negative electrode ($-$), separator (s) and positive electrode ($+$)), in the middle: the electrolyte phase (e), at the bottom: a particle solid phase (s). The indicated variables are: solid and electrolyte phase concentration (c_s and c_e, respectively), solid and electrolyte phase electric potential (ϕ_s and ϕ_e, respectively), pore-wall molar flux (j_n), electrolyte and solid-phase diffusion coefficients (D_e and D_s, respectively) and spherical particle radius (R_s).

TABLE 2.2: Two-states thermal model equations. The nomenclature for this table is provided in the List of Symbols.

Physical Process	Equation	
Core Temperature	$\rho_c C_{pc} \frac{dT_{bc}}{dt}(t) = k_c\,(T_{bs}(t) - T_{bc}(t)) - I(t)V(t) - \int_0^L a_s^{\pm} F j_n^{\pm}(x,t)\Delta T(\bar{c}_s^{\pm}, T_{bc})dx$	(2.18)
	where $\Delta T(\bar{c}_s^{\pm}, T_{bc}) = \Delta U_b^{\pm}(\bar{c}_s^{\pm}(x,t)) - T_{bc}(t)\Delta\frac{\partial U_b^{\pm}}{\partial T_c}(\bar{c}_s^{\pm}(x,t))$	
Surface Temperature	$\rho_s C_{ps} \frac{dT_{bs}}{dt}(t) = k_c\,(T_{bc}(t) - T_{bs}(t)) + h_c\,(T_{\text{amb}} - T_{bs}(t))$	(2.19)
Arrhenius Equation[a]	$\Phi(T_{bc}) = \Phi_{\text{ref}} \exp\left(\frac{E_\Phi}{R_g}\left(\frac{1}{T_{\text{ref}}} - \frac{1}{T_{bc}(t)}\right)\right)$	(2.20)

[a] Φ could be D_s, D_e, k_n, κ_e or $i_{0,sr}$

Both capacity loss and impedance rise are proportional to the side reaction current density. Both the main intercalation reaction and the competing side reactions are

schematically represented in Fig. 2.3(a) and (b), (c), respectively. Two distinct side reactions are portrayed in the figure, namely solvent reduction reaction of Eq. (2.2) in Fig. 2.3(b) and lithium plating of Eq. (2.3) in Fig. 2.3(c). The former side reaction involves lithium-ions Li^+ and the electrolyte solvent S, and it creates an insoluble product P (in dark gray in Fig. 2.3(b)) whose accumulation gives rise to the SEI film. The latter side reaction generates solid lithium $Li(s)$ (in light gray in Fig. 2.3(c)). Both P and $Li(s)$ are deposited at the spherical particle surfaces (dark orange arc in Fig. 2.3). It is worth noticing that the conductive nature of the SEI film conditions the degradation response of the battery, as it is depicted in the close-up inset of Fig. 2.3(b). If the film conducts well electricity (e^- represents electrons) but poorly ions, lithium-ions and electrons likely undergo the main reaction at the surface of the film (upper reaction in Fig. 2.3(b) inset). Then, the film is said to be diffusion-controlled, and the lithium diffusion time is effectively increased from $\tau_s = \frac{R_s^2}{D_s}$ to $\tau_s = \frac{(R_s+\delta_f)^2}{D_s}$, where D_s, R_s and δ_f are respectively the solid-phase diffusion coefficient, spherical particle radius and film thickness. The arrow associated to δ_f pointing outwards indicates how the film gets thicker with the passage of time. Conversely, if ions get across easily and electrons have a harder time to go through the film, the main reaction occurs at the surface of the particle (lower reaction in Fig. 2.3(b) inset). The film is then said to be kinetic-controlled, and the battery voltage suffers an ohmic potential drop caused by the film resistance R_f. A mixed degradation mechanism happens in-between these two extremes. Empirical models representing the battery response to these limiting degradation conditions in terms of time and cycle number were shown above in Eqs. (2.4) and (2.5).

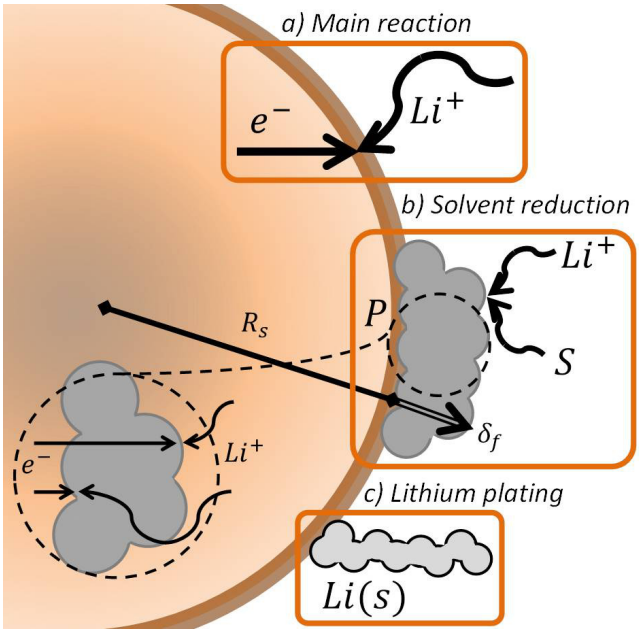

FIGURE 2.3: Schematic representation of main and side reactions, namely solvent reduction reaction and lithium plating. Li^+, $Li(s)$ and e^- denote lithium-ions, solid lithium and electrons, respectively, S and P are electrolyte solvent and side reaction product, respectively, and R_s and δ_f are spherical particle radius and film thickness, respectively.

Besides the side reaction equations derived from electrochemistry, aging mechanisms have also been associated to changes in model parameters. This parametric

TABLE 2.3: Aging model equations for a generic side reaction sr, where $sr = \{\text{SEI}, lp\}$ for SEI growth and lithium plating, respectively [11, 33, 34, 12] . The nomenclature for this table is provided in the List of Symbols.

Physical Process	Equation	
Current Balance	$j_t(x,t) = j_n(x,t) + \sum_{i \in sr} j_i(x,t)$	(2.21)
Side Reaction Rate	$j_{sr}(x,t) = -a_s L i_{0,sr} \exp\left(-\frac{\alpha_0 F}{R_g T_{bc}(t)} \eta_{sr}(\phi_s, \phi_e, j_t)\right)$	(2.22)
Side Reaction Overpotential	$\eta_{sr}(\phi_s, \phi_e, j_t) = \phi_s(x,t) - \phi_e(x,t) - U_{sr} - R_f(x,t) F j_t(x,t)$	(2.23)
Conservation of Solvent	$\frac{\partial c_{st}}{\partial t}(x,r,t) = D_{st} \frac{\partial^2 c_{st}}{\partial r^2}(x,r,t) - \frac{d\delta_f}{dt}(x,t) \frac{\partial c_{st}}{\partial r}(x,r,t)$	(2.24)
	with boundary conditions $-D_{st} \frac{\partial c_{st}}{\partial r}(x,r,t)\Big\|_{r=R_s} + \frac{d\delta_f}{dt}(x,t) c_{st}(x,r,t) = j_{sr}(x,t)$ $c_{st}(x,r,t)\|_{r=R_s+\delta_f} = \varepsilon_f c_{st}^b(x,r,t)$	
Capacity Loss	$\frac{dQ_{\text{loss}}}{dt}(t) = -\int_0^L \frac{F a_s A}{3600} j_{sr}(x,t) dx$	(2.25)
Film Growth	$\frac{d\delta_f}{dt}(x,t) = -\frac{M_p}{\rho_p} j_{sr}(x,t)$	(2.26)
Impedance Rise	$R_f(x,t) = R_f(0) + \frac{1}{\kappa_p} \delta_f(x,t)$	(2.27)

variations can be state dependent or take the form of empirical functions. Examples of the former variations are the side reaction-dependent electrolyte volume fraction [34] and solid-phase diffusion coefficient [35] given respectively by

$$\frac{d\varepsilon_e}{dt}(t) = \frac{1}{2} \frac{M_p}{\rho_p} \frac{3\varepsilon_s}{R_s} j_{sr}(t), \tag{2.28}$$

$$\frac{dD_s}{dt}(t) = -\frac{n_1 D_s(0)}{\varepsilon_s(0)} \left(\frac{\varepsilon_s(0) - \varepsilon_s(t)}{\varepsilon_s(0)}\right)^{n_1 - 1} \frac{M_p}{\rho_p} a_s j_{sr}(t) \tag{2.29}$$

where M_p and ρ_p are the side reaction product molar mass and density, respectively, ε_s and ε_e are active material volume fraction for the solid and electrolyte phases, respectively, D_s and R_s are the solid-phase diffusion coefficient and particle radius, respectively, a_s is the specific interfacial area and n_1 is an empirical factor representing the effect of the film formation on the lithium ion diffusion. Examples of empirical functions that represent loss of active material through a time-varying material volume fraction [36] and rate-capability fade through a time-varying diffusion coefficient

[37] are given respectively by

$$\frac{d\varepsilon_s}{dt}(t) = C_1(T_b)|Fj_n(t)| + C_2(T_b)\sqrt{|Fj_n(t)|}, \tag{2.30}$$

$$D_s(t) = k_1 \exp\left(\frac{k_2}{N}\right) \tag{2.31}$$

where $C_1(T_b)$ and $C_2(T_b)$ are fitting parameters that depend on temperature, k_1 and k_2 are constants and N is the cycle number. These equations are just examples of parametric variations linked to aging mechanisms.

Operating Constraints

Whether battery degradation comes from side reactions or parameter changes, the capacity/power fade to which the battery is subject to can compromise its safe operation [10, 9]. Interestingly enough, battery failure can be mitigated by avoiding certain operating regions where degradation is boosted. Such delimitation of the safe operating regions translates in constraints, which can be exploited by a controller to steer the battery state inwards the safe region. For the charging process, the constraints take the form

$$\begin{cases} \bar{c}_s^-(x,t)/c_{s,\max}^- \leq \bar{r}_{c_s}, \quad c_{ss}^-(x,t)/c_{s,\max}^- \leq \bar{r}_{c_s} & \text{(2.32a)} \\ \bar{c}_s^+(x,t)/c_{s,\max}^+ \geq \underline{r}_{c_s}, \quad c_{ss}^+(x,t)/c_{s,\max}^+ \geq \underline{r}_{c_s} & \text{(2.32b)} \\ \eta_{sr}^-(x,t) = \phi_s^-(x,t) - \phi_e(x,t) - U_{sr}^- > 0 & \text{(2.32c)} \\ \eta_{sr}^+(x,t) = \phi_s^+(x,t) - \phi_e(x,t) - U_{sr}^+ < 0 & \text{(2.32d)} \\ c_e(x,t) \geq \underline{r}_{c_e} & \text{(2.32e)} \end{cases}$$

where $\bar{c}_s$ and c_{ss} are the average and surface lithium concentration, respectively, whose normalization with respect to the maximum allowed lithium concentration $c_{s,\max}$ are lower and upper bounded by two constants $\underline{r}_{c_s}$ and $\bar{r}_{c_s}$, respectively, that depend on the electrode chemistry. The overpotential and the equilibrium potential of the side reactions are denoted by η_{sr} and U_{sr}, respectively. Eqs. (2.32a) and (2.32b) hinder the situation where Li is extracted/deposited beyond the maximum concentration allowed by the electrode, which can cause phase transformations, active material dissolution and oxygen loss in positive electrodes, and lithium dendrite formation in negative electrodes. Eqs. (2.32c) and (2.32d) prevent side reactions from taking place, which consume cyclable lithium and reduce the cell capacity (i.e. capacity fade) [38]. Such conditions occur first at the negative electrode/separator and the positive electrode/separator interfaces, respectively. Eq. (2.32e) precludes electrolyte depletion, which takes place first at the current collector/negative electrode.

Reduced-Order Models

Given the complexity of the nonlinear partial algebraic differential equations involved in the DFN model, authors have come up with reduced-order models for estimation and control purposes. The most widespread model simplification is to assume that the solid-phase diffusion processes within an electrode occur in a single spherical particle. The surface area of this particle is equivalent to the active material surface area of the porous electrode. Aside from the solid phase, the electrolyte phase is also simplified by considering a constant electrolyte concentration throughout the battery cell thickness [10]. This framework is known as the single-particle model

(SPM), which was first proposed in [39] for the metal hydride battery and later extended to lithium-ion batteries [40, 41, 42]. The SPM exhibits a reasonable accuracy at low C-rates (up to 1C), but at higher C-rates the electrolyte phase limitations are no longer negligible [43, 10].

Even though the SPM framework simplifies the modeling problem to one PDE per electrode, it is still infinite dimensional. The diffusion PDEs can be discretized in several ways, such as using finite-difference [44, 45] or finite-element methods [46]. However, these discretization schemes come with computational burden. To bypass this issue, some authors have proposed to approximate the solid-phase diffusion PDE with polynomials [47] and truncated transfer functions resulting from Padé's expansion [48] or residue grouping [49]. Besides the PDEs, the nonlinear model equations have also been approximated. For instance, the Butler-Volmer equation has been linearized about the origin, which is also known as low-field approximation or linear current-potential equation [50], while the open-circuit voltage function has been linearized about 50% SOC [46]. A quasi-linearization of the former equation, that amounts to linearize it at every integration step about the operating point, has been also proposed [48].

These reduced-order modeling efforts have yielded different generic EChMs. The electrode-average model [44] is a variation of the SPM that discretizes the single particle in M_r shells. The diffusion dynamics are then described by $(M_r - 1)$-order ordinary-differential equations (ODE). The state-variable model [46] is the state space representation of approximated impedance transfer functions. The solid-phase diffusion process is described by symbolic transfer functions, whereas the electrolyte-phase diffusion process is characterized by numerical transfer matrices. These diffusion transfer functions are truncated via residue grouping, whereas the Butler-Volmer kinetics and the open-circuit voltage (OCV) contributions to the voltage are linearized. The OCV linearization is also considered in Nernst-type models [51], in addition to the Nernst equation replacing the OCV function. This substitution characterizes electrochemical processes at equilibrium [23]. The equivalent-hydraulic model (EHM) [52], equivalent to the kinetic battery model [53], comprises a pure current integrator, a high-pass filter from the state-of-charge to the surface concentration, and the latter concentration is fed to a static nonlinearity consisting of the Butler-Volmer equation and the OCV. In spite of such model variety, some battery chemistries exhibit specific electrochemical features that can only be captured with chemistry-oriented models. That is the case of e.g. lithium iron phosphate ($LiFePO_4$ or LFP) batteries.

LFP electrodes exhibit high capacity, low price and environmental impact, and remarkable stability [54, 55], which makes them stick out among other chemistries. Despite the great interest aroused by this material since its discovery [56], it is still difficult to reconcile its outstanding high-power performance with the intercalation/deintercalation two-phase process [56]. The latter process has been properly described by a core-shell model [57], where the two phases are separated by a moving interface for each electrode particle. Lithium diffuses through a Li-rich growing shell surrounding a Li-poor shrinking core [57, 58]. This model has been extended to consider resistive-reactant effects [59], multiple two-phase boundaries [60, 61] and multiple scales [62]. However, these phase-change models are thermodynamically inconsistent since experiments show that each phase is simultaneously present in different particles forming a mosaic. This evidence has given rise to many-particle [63] and mesoscopic [64] models. Other results based on more complex phase-field models show that phase separation is suppressed in small particles subject to discharge currents [65, 66], which is aligned with the LFP carbon coating and particle size reduction to improve its intrinsic low conductivity and diffusivity.

Other LFP models neglect phase transformations completely, which are known as regular solid-solution models. Examples of these ones are a multi-particle resistive-reactant model with interparticle resistance distribution [55, 67], a variable solid-state diffusivity model with particle-size distribution [54, 55], and a model that enhances the last one with electrolyte dynamics [68]. Most of the efforts devoted to develop LFP models seek to provide insight into the limiting electrochemical processes that govern LFP electrode dynamics. Given the complexity introduced when modeling specific LFP features, these models might not be suitable for battery real-time monitoring in contrast to the other more generic reduced-order EChMs. Once a reduced-order EChM with good performance is obtained, it can be used with estimation techniques to look for the internal states and physical parameters of the battery cell.

2.4 State Estimation

Perhaps the most important battery internal state is the state-of-charge (SOC). It reflects the amount of energy available at a given time instant with respect to the total available energy, so this indicator is for the battery what the tank level indicator is for a car fuel tank. The SOC can be defined as

$$\frac{d\text{SOC}^{\pm}}{dt}(t) = \frac{3}{c_{s,\max}^{\pm} L^{\pm} (R_s^{\pm})^3} \int_0^{L^{\pm}} \int_0^{R_s^{\pm}} r^2 \frac{\partial c_s^{\pm}}{\partial t}(x, r, t) dr dx = \frac{I(t)}{Q_b} \tag{2.33}$$

where $I(t)$ is the input current applied to the battery and Q_b is the battery capacity (see the List of Symbols for a description of the other parameters). The first equality has a direct link with the battery electrochemistry and the solid-phase diffusion Eq. (2.6). The second equality can be obtained from the first one by integration, where the total battery capacity Q_b is given by the capacity limiting electrode $Q_e^{\pm}$ such as $Q_b = \min\{Q_e^{+}, Q_e^{-}\}$, with $Q_e^{\pm} = c_{s,\max}^{\pm} F \varepsilon_s^{\pm} L^{\pm}$. In this case, the SOC range is $[\underline{\theta}^{\pm}, \overline{\theta}^{\pm}]$, where $\underline{\theta}^{\pm}$ and $\overline{\theta}^{\pm}$ are the lower and upper reference stoichiometry points. This SOC range can be used to normalize the SOC variable such as $\text{SOC} \in [0, 1]$. Another notion of battery SOC that is more practical and widely used in applications is to define the battery capacity Q_b in the second equality of Eq. (2.33) as the total energy available when the battery is fully charged. In this case, the SOC range is automatically restricted to $[0, 1]$. The integration of current in order to obtain the battery SOC is known as Coulomb-counting.

The battery SOC estimation using Coulomb-counting as in Eq. (2.33) already reveals some flaws. For instance, a precise knowledge of the initial SOC as well as an unbiased input current measurement are both required to have an accurate SOC estimate. Such requirements are hardly met in practice. One way to tackle these issues is to resort to state observers based on reduced-order models. Similarly to the modeling Section 2.3, this section on state estimation focuses on electrochemical models. The interested reader is referred to [69] for a survey on observers designed from e.g. equivalent-circuits. Most of the generic reduced-order EChMs introduced in Section 2.3 have been used for state observer design. Two approaches can be distinguished in this field depending on the way they cope with the underlying PDEs of the system, namely early lumping and late lumping. While the former approach first discretizes the PDE and then develops an observer on the resulting system of ODEs, the latter approach derives a PDE observer that is then discretized for digital implementation.

The early lumping is by far the most common approach for state observer synthesis. An extended Kalman filter (EKF) based on the SPM [43] was one of the first state observers resorting to EChMs to tackle the battery estimation problem. The SPM was later dropped at the expense of the DFN model to cover a wider model validity range (higher C-rates). This time, an unscented Kalman filter (UKF) was implemented to avoid model linearization [70]. A linear KF was designed based on the state-variable model to estimate the internal battery potentials and concentration profiles besides the SOC [71]. The proposed filter had a low order of 4 to 7 states. SOC estimation was also achieved using the electrode-average model to derive an EKF [44]. The electrode-average model was also exploited in the design of a smooth variable structure filter [72]. This filter is a sliding mode-based observer and it involves the output equation linearization about the current state. However, computational issues arise when calculating the filter gain from the pseudoinverse of the linearized output matrix.

Nonlinear KFs other than EKF and UKF have also been explored, such as the iterative EKF (IEKF) based on a Nernst-type battery model [51, 73]. The IEKF exhibits less linearization errors when compared to e.g. an EKF. The Nernst model used in the IEKF was exploited in two ways. First, the state vector was augmented with unknown model parameters for joint state/parameter estimation [73]. In this work, even though parameter convergence was not reached, the SOC estimate was still considered reliable based on an observability analysis. Secondly, a multi-model estimation was pursued [51], which is motivated by its good performance when dealing with structural and parameter changes. In this work, the approach effectiveness was proven through an accurate SOC estimation and voltage prediction for simulated and experimental data. Away from KFs, a nonlinear geometric observer based on a Nernst model with linearized Butler-Volmer equation and voltage hysteresis was also designed [74]. This high gain observer provided convergent state and parameter estimates. However, input current discontinuities caused spikes in state and parameter estimates. This peaking phenomenon is notably associated to the derivative of the input, which is required when the system is transformed for high-gain observer design. Moreover, this adaptive observer is robust to process uncertainties but it is very sensitive to measurement noise.

Little work has been carried out by resorting to the late lumping. A PDE observer based on output error injection was designed using the SPM [75]. The observer gains were chosen in order to comply with the material balance. Although the observer robustness was proven against model mismatch and noise, thermal dynamics were missing and later added [76]. Another approach consisted in a backstepping PDE observer for adaptive SOC/SOH estimation [77]. The adaptation was achieved through parameter identification methods, such as filtering and a nonlinear least squares, in order to estimate SOH-related parameters. Despite the estimation convergence, some parameter estimates were biased given the model complexity. Anyhow, the estimation bias can be mitigated by carefully selecting the adaptation gains. The paper concludes highlighting the importance of either an accurate model knowledge or on-line adaptation for a successful state estimation.

2.5 Parameter Estimation

Besides the internal state of the system, one relevant concern in battery systems is their reliability and safety. Both issues get more compromised as the battery ages and the state of health of the battery diminishes. In contrast to the SOC definition of Eq. (2.33), the battery state-of-health (SOH) has not been formally defined by industry [8]. In general, any physical quantity that reflects the battery loss of performance with usage can be regarded as a SOH indicator [78]. Thus, the SOH can be defined as

$$\text{SOH} \triangleq \frac{\hat{\theta} - \theta(0)}{\theta(0)} \tag{2.34}$$

where $\hat{\theta}$ and $\theta(0)$ denote respectively the current and initial state of any chosen SOH variable.

The SOH estimation problem can be solved by resorting to two different approaches, namely experimental-based and model-based [79]. The former approach is simple from the computational standpoint, but it might require specific measurements only available in controlled environments. Besides, access to the entire cycling history of the battery might be needed. The second approach requires to develop an accurate parametric model to start with, to link degradation to specific model parameters and to devise a suitable procedure to estimate them from standard on-line measurements. The challenge with this approach lies in the limited available measurements (current, voltage, surface temperature). Roughly speaking, the experimental burden of the first approach is translated into model and estimator design efforts in the second. The payoff is a method that provides SOH estimation in real time during battery daily regular operation.

Here we are interested in model-based SOH monitoring. As stated above, the first step to achieve it is to build or select a parametric model that best describes the physical phenomena under study. Although equivalent-circuit models have been used as a basis for parameter identification of battery models, this modeling framework does not reflect the electrochemical processes of the battery. To this end, electrochemical models, such as the ones introduced in Section 2.3, are the most suitable ones, whose parameters are rooted in physical meaning. Once the parametric model is obtained, the next step is to identify the meaningful parameter set that captures SOH degradation.

Popular choices of SOH variables are parameters related to capacity and power fade. However, the isolation of any given degradation mechanism through a single parametric change is a tough task due to the intertwined nature of degradation sources. This means that different degradation mechanisms might contribute to the variation of a single parameter, and one degradation mechanism might be responsible for multiple parameters changing simultaneously. An example of the former situation is the effect that side reactions, electrode morphological changes, particles cracking and pores plugging have on the solid-phase diffusion coefficient. For its part, an example of the latter situation is the influence of side reactions over the diffusion coefficient, film resistance and moles of lithium. If that was not enough, the battery response to aging depends on the battery chemistry [9, 15, 80] and operating conditions, which further complicates the situation. Some efforts have been carried out to associate general sources of capacity and power loss to specific parameter variations. For instance, side reactions consume available lithium that contributes to capacity fade, which can affect the solid-phase diffusion coefficient parameter (D_s). For its part, film formation and growth yields power fade, which can be reflected in changes

of the film resistance parameter (R_f) [81, 37]. Magnitude changes of these parameters can be as large as 100% drop for D_s and 400% increase for R_f when a LCO battery is subject to 500 charge/discharge cycles of maximum 1C [37]. Similar degradation trends have been reported for other types of lithium-ion batteries [82, 83, 84].

SOH indicators deduced from models vary depending on the model choice. Similarly to the state estimation Section 2.4, this section on parameter estimation focuses on electrochemical models. The interested reader is referred to [78, 79] covering different SOH estimation methods. Model-based SOH indicators have been built resorting to two main tools, namely parameter estimation techniques and adaptive state observers. Within the first category lie optimization-based techniques, such as Levenberg-Marquardt method [85] and Gauss-Newton method [82, 86], as well as recursive parameter update laws such as gradient method [87][4]. These approaches may require specific battery tests, and the acquired data has to be processed off-line due to the computational complexity involved in the optimization problems. For its part, SOH assessment during real time operation may require access to the internal battery state, which leads to joint state/parameter estimation. Within this second category are state observers, such as the ones introduced in Section 2.5, with recursive parameter estimation update laws based on least squares [91, 77, 92], cascaded estimation resorting to sliding mode [93, 94], Lyapunov-based [95] and proportional-integral observers [96], as well as lumped parameter/state estimation via Kalman filters (KF) [51, 97, 73, 98, 99], particle filters [99, 100] and nonlinear geometric observers [74].

[4]This literature review focuses on parameter identification techniques that have been explicitly used to estimate SOH-related parameters. Therefore, we are leaving aside the body of literature dealing with a more general parameter identification problem of batteries, which notably encompasses methods such as genetic algorithm [88] and Levenberg-Marquardt method [89], and methodologies such as optimal experiment design [90].

2.6 Fault Detection and Isolation

Early detection of battery failure is a big concern nowadays. From applications with few battery cells such as mobile phones or laptops, to large scale battery packs of electric vehicles, battery malfunctions can potentially become a safety hazard for the user. This kind of threat coming from such an ubiquitous and autonomy-enabling technology cannot be tolerated. In recent years, fault detection and isolation (FDI) systems have been explored in order to make batteries safer and failure-proof.

The literature on FDI systems for batteries can be divided in two categories. In the first one, the design of state-of-health (SOH) indicators is considered. As battery degradation induces changes in the battery model, any parameter estimation approach for modeling a battery from experimental data can be seen as a method for SOH monitoring. Most of the work in this field resorts to equivalent circuit models (ECM) to describe battery behavior. However, among the possible battery internal faults, one can notably distinguish between capacity and power fade. Each one of these degradation sources is associated to different physico-chemical phenomena [37]. The only way to discern between such specific and relevant electrochemical faults is to use electrochemical models (ECheM) as opposed to ECMs. This approach corresponds to the line of research introduced in the previous Section 2.5 and references therein. In contrast to parameter estimation-oriented approaches, the diagnostics problem has also been framed in terms of observer-based FDI systems [101, 102] for residual generation. These approaches consider equivalent-circuit models together with additive faults [101] and experimentally characterized parametric changes [102] for observer design. All these contributions assume that the different sensors are fault free.

The second category of literature deals with the design of FDI systems for sensor and actuator faults in battery cells and packs. Notice that battery monitoring heavily relies on the information provided by the deployed sensors, while confining the battery state within a certain region of safe operation strongly depends on the effectiveness of the actuator. If the instrumentation delivers biased information, the output feedback control of the battery may result in a dangerous situation, specially when high currents are used as it is the case of fast charging. There is no simple table of sensor failure modes with their probability of occurrence, because the failure mode depends on the type of sensor, manufacturing practices, application and environmental conditions [103]. However, failure rates λ_s [failures$\cdot 10^{-6}$ h] for thermal sensors range from 1.50 to 20.00, while sensors based on the Hall effect (like current and voltage) can have 2.50 failure rate [103]. Large scale battery packs can have thousands of cells, whose voltages need to be properly monitored to guarantee safe operations, current sensors are used for each string of battery cells and a couple of temperature sensors are deployed for each battery module. On the one hand, more sensors involve a greater chance of one of them failing, even if they failure rate is low like for current and voltage. On the other hand, few sensors with a possibly higher failure rate as thermal sensors might compromise the use of the application. A proper study of sensor reliability in the context of battery packs does not exist yet to the best of our knowledge, despite its relevance.

Sensor faults have been considerably less explored than e.g. battery state and parameter estimation. The proposed solutions usually rely on simple, electric and thermal models of the cell or the pack. The diagnostic problem has been addressed notably through a nonlinear parity equation approach, possibly determined by structural analysis [104, 105] and state observers [106, 107]. The interplay between battery aging monitoring and sensor FDI has been very little studied so far. To the best of

the author's knowledge, sensor and battery internal resistance faults have been only explored using structural analysis [108] and state observers [109], respectively, both based on equivalent-circuit models.

2.7 Constrained Control

The most widely used battery charging strategy is the constant-current/constant-voltage (CCCV) protocol [110]. It consists of two stages. During the first stage, the battery is operated under a constant current (CC) or galvanostatic condition until the voltage reaches a pre-defined upper cut-off threshold. From this point onwards, the battery is operated under a constant voltage (CV) or potentiostatic condition until the current drops to a given pre-defined lower cut-off threshold. The CCCV protocol is an *ad hoc* solution where the parameters (e.g. current rate, and voltage and current thresholds) are specified *a priori* based on heuristic tuning [111]. Although they might be regarded as rather conservative at the battery beginning-of-life, these charging specifications could become a safety hazard in the long run [10]. To address this issue, a careful monitoring of the battery internal states is required, along with a control strategy that cashes in on such estimation to avoid unsafe operating conditions.

Recently, a few alternative strategies based on constrained optimal control have been proposed. In spite of the added complexity, these solutions are capable of fast charging lithium-ion batteries while ensuring a higher level of safety. There are two main routes for solving a constrained control problem, namely to solve the problem altogether as in model predictive control, or to separately solve the control and the constraint handling problems, and to put the pieces together as in the reference governor. The first route was followed in [112], where an optimal current profile for fast charging was obtained from a simple one-step predictive controller based on the DFN model. However, the use of the DFN model in this approach prohibits its on-line (closed-loop) implementation due to the high computing load. This makes the method unable to cope with modeling uncertainties and/or different initial conditions. To fight against computational burden, reduced-order models, such as the ones introduced in Section 2.3, have been exploited within model predictive control (MPC) schemes [113, 114]. Although the resulting schemes exhibit a much reduced computational complexity, it is still an open question if they can be easily implemented on-line on low-cost devices. An attractive alternative able to further reduce the computational demand is the reference governor (RG) [115, 116].

The second route, which concerns RG schemes, has produced a few preliminary results. An early use of a RG was based on a reduced-order linear EChM valid at 50% SOC and equipped with constraints only on the solid-phase lithium concentration [117]. Another approach involves a modified RG scheme that uses both the DFN model and a linearized version of it [118]. The authors showed that constraint satisfaction can be ensured for the DFN model but not for the linearized model. It is worth mentioning that both of the above approaches used modified versions of the classical RG to deal with marginally stable systems, which puts into question their robustness properties.

2.8 Concluding Remarks

This chapter focuses on the state of the art related to the different topics covered in this dissertation, namely description of the battery operation and aging, battery modeling, internal state and parameter estimation, sensor fault detection and isolation and optimal control subject to constraints.

The mathematical representation of the battery operation has been traditionally done through the so-called DFN model, which has been extended to include e.g. thermal and aging dynamics. Among the different degradation mechanisms that promote aging, parametric variations with time and side reactions leading to SEI growth and lithium plating are the most relevant ones. Some aging mechanisms can be mitigated by establishing suitable constraints, while others cannot be avoided in any way so what is left is to track them. An example of the former is lithium plating and of the latter are SEI growth and calendar aging.

Although the use of very detailed models such as the DFN model is highly advised for battery simulation, its complexity precludes its real time implementation for estimation and control. Then, reduced-order electrochemical models have been derived, which can be chemistry specific or chemistry agnostic. The former models are intended to provide physical insight into the electrochemical processes limiting the operation of a given battery chemistry. The latter models are generic and often simpler than the former ones. A generic model able to describe the dynamic behaviour of any battery chemistry is desirable. This model should be rooted in first principles so that the physical meaning of its states and parameters can be exploited for monitoring and control.

Some of the electrochemical models proposed in the literature have been already used to design state observers with a view to estimating the short-term battery dynamics, e.g. SOC. Late lumping of the system PDEs gives rise to PDE observers, which is a field where little work has been done. In contrast, observer design based on a system of ODEs resulting from early lumping is a more prolific research area. Kalman filters (KF) and its variants are by far the most used approach for state estimation. The wide use of KFs lie in its computational simplicity and proven success when implemented in real life applications. However, the KFs designed for batteries are usually based on restrictive models, consider specific operating conditions and often lack a systematic procedure to tune the filter.

Apart from the short-term battery operation, its SOH deteriorates in the long term affecting battery performance and price. To track the battery SOH, different parameter identification approaches have been proposed in the literature. However, most of them rely on least squares estimation, which requires some *a priori* knowledge of the unknown parameters to initialize the method and it produces biased estimates in presence of colored noise. While parameter estimation approaches are by far the most popular way to cope with the tracking of battery aging, other studies cast an observer-based fault diagnostics problem to generate residuals for parameter change detection.

Another way that fault detection and isolation systems for batteries have been exploited is to assess the reliability of the information provided by the sensors. This issue is relevant because both battery monitoring and closed-loop control strongly rely on the information available from the sensors. The fact that aging and sensor faults occur simultaneously is often overlooked in the literature.

So far, we have covered estimation methods able to infer the internal state and aging-related parametric changes of lithium-ion batteries from standard measurements, and diagnostic systems able to assess the reliability of such measurements.

The next step is to take advantage of this information to control the battery operation. More precisely, we focus here on feedback charge strategies for lithium-ion batteries. The standard approach to achieve this goal is through model predictive control (MPC). However, the computational burden associated to MPCs is not acceptable for an application whose main purpose is to store energy. The use of computationally lighter solutions such as reference governors (RG) has also been explored, but either modified RGs or RGs based on models that are too complex or limited in both their operating range and selected constraints were considered.

Chapter 3

Prerequisite Material

Before jumping into the development of techniques and strategies for battery monitoring and control, it is worth refreshing some notions of estimation, fault detection and control. All these notions have served as a basis to derive suitable solutions to the problem that concerns us. Model state estimation introduced in Section 3.1 has been performed by means of Kalman filters. Model parameter estimation of Section 3.2 resort to identification methods such as least squares and instrumental variables. The fault detection system shown in Section 3.3 relies on residual generation and statistical change detection algorithms. Finally the control scheme presented in Section 3.4 combines a standard linear quadratic regulator with a reference governor. The basics of all these topics are sequentially introduced and briefly described in the following.

3.1 State Estimation

More often than not, the available information that can be directly obtained from a given system through sensors is limited. It might be that only some linear or nonlinear combinations of the state of the system can be accessed via sensing. Furthermore, the gathered data is always corrupted by noise to a greater or lesser extent. In order to reconstruct the system state from such data one resorts to state observers or filters. One of the most widely used state observer that has been exploited across disciplines to estimate the state of stochastic systems is the Kalman filter. Originally proposed for linear discrete-time systems, Kalman filter-like algorithms have been developed for nonlinear systems, such as the extended and the unscented Kalman filters. These contributions are discussed next in terms of algorithm and properties.

3.1.1 The Kalman Filter

The Kalman filter was developed in discrete-time by Rudolph Kalman in 1960 [119], during the Apollo program. It provides the means to estimate the state $x(k)$ of a system from input-output measurements $u(k)$ and $y(k)$. Consider the following linear discrete-time stochastic system[1]

$$\begin{aligned} x(k) &= Ax(k-1) + Bu(k-1) + w_n(k-1) \\ y(k-1) &= Cx(k-1) + v_n(k-1) \end{aligned} \tag{3.1}$$

where $x(k) \in \mathbb{R}^n$ is the state vector, $u(k) \in \mathbb{R}^m$ is the input vector, $y(k) \in \mathbb{R}^p$ is the output vector, and $w_n(k) \in \mathbb{R}^n$ and $v_n(k) \in \mathbb{R}^p$ are process and measurement noise sequences, respectively, which are white, zero-mean and mutually uncorrelated with

[1] Discrete-time with time variable k is adopted in this section.

covariance matrices Q and R, respectively, i.e.

$$\begin{gathered} w_n(k) \sim \mathcal{N}(0, Q), \;\; v_n(k) \sim \mathcal{N}(0, R), \\ \mathbb{E}\left(\begin{bmatrix} w_n(k) \\ v_n(k) \end{bmatrix} \begin{bmatrix} w_n(l)^{\mathrm{T}} v_n(l)^{\mathrm{T}} \end{bmatrix} \right) = \begin{bmatrix} Q & 0 \\ 0 & R \end{bmatrix} \delta_{kl} \end{gathered} \tag{3.2}$$

where $\mathbb{E}$ is the expectation operator and δ_{kl} is the Kronecker delta function. Besides, the initial state $x(0)$ is supposed to be normally distributed and uncorrelated with the process and measurement noises. The Kalman filter provides the minimum variance estimate of the state. As the noise and the initial state are assumed to be normally distributed, this estimate, denoted $\hat{x}(k)$, is given as [120, 121]

$$\hat{x}(k) = \mathbb{E}[x(k)|Y(k-1)] \tag{3.3}$$

where $Y(k-1)$ is the data sequence up to and including time k, i.e. $Y(k-1) = \{y(k-1), y(k-2), \ldots, y(0), u(k-1), u(k-2), \ldots u(0)\}$.

Algorithm

The Kalman filter algorithm that provides the estimate described by Eq. (3.3) is given in Table 3.1.

TABLE 3.1: The Kalman filter algorithm[†].

Initialization: for $k = 0$ set
$\hat{x}_0 = \mathbb{E}[x_0], \; P_0 = \mathbb{E}[(x_0 - \hat{x}_0)(x_0 - \hat{x}_0)^{\mathrm{T}}]$
At each time instant compute:
Time-update:

$$\hat{x}_k^- = A\hat{x}_{k-1} + Bu_{k-1} \tag{3.4}$$

$$P_k^- = AP_{k-1}A^{\mathrm{T}} + Q \tag{3.5}$$

$$\hat{y}_k = C\hat{x}_k^- \tag{3.6}$$

Measurement-update:

$$\hat{x}_k = \hat{x}_k^- + K_k\left(y_k - \hat{y}_k\right) \tag{3.7}$$

$$K_k = P_k^- C^{\mathrm{T}} \left(CP_k^- C^{\mathrm{T}} + R \right)^{-1} \tag{3.8}$$

$$P_k = P_k^- - K_k \left(CP_k^- C^{\mathrm{T}} + R \right) K_k^{\mathrm{T}} \tag{3.9}$$

[†]For compactness, the time argument is set as an index.

Properties

As already indicated, the Kalman filter state estimate is the best (minimum variance) estimate that solves the following optimization problem [121]

$$\min. \;\; \mathbb{E}\left[\left(x(k) - \hat{x}(k)\right) \left(x(k) - \hat{x}(k)\right)^{\mathrm{T}} | Y(k-1) \right], \tag{3.10}$$

which implies that

$$\begin{gathered} \mathbb{E}[\left(x(k) - \hat{x}(k)\right) | Y(k-1)] = 0 \\ P(k) = \mathbb{E}\left[\left(x(k) - \hat{x}(k)\right) \left(x(k) - \hat{x}(k)\right)^{\mathrm{T}} | Y(k-1) \right] \leq P_f, \end{gathered} \tag{3.11}$$

where P_f is the error covariance of any other filter [120].

Remark 3.1.1. *By taking $A = I$, $B = 0$, $Q = 0$, $C = \varphi(k-1)^{\mathrm{T}}$, $R = I$ and $\theta(k) \triangleq x(k)$, the system becomes*

$$\begin{aligned} \theta(k+1) &= \theta(k) \\ y(k) &= \varphi(k-1)^{\mathrm{T}}\theta(k) + v_n(k), \end{aligned} \tag{3.12}$$

for which the Kalman filter reduces to the recursive least-squares algorithm [120]

$$\begin{aligned} \hat{\theta}(k+1) &= \hat{\theta}(k) + \tfrac{P(k-1)\varphi(k)}{\varphi(k)^{\mathrm{T}}P(k-1)\varphi(k)+1}(y(k+1) - \varphi(k)^{\mathrm{T}}\hat{\theta}(k)) \\ P(k) &= P(k-1) - \tfrac{P(k-1)\varphi(k)\varphi(k)^{\mathrm{T}}P(k-1)}{\varphi(k)^{\mathrm{T}}P(k-1)\varphi(k)+1}. \end{aligned} \tag{3.13}$$

3.1.2 The Extended Kalman Filter

The Kalman filter provides a simple and elegant solution to the state estimation problem of a linear stochastic dynamical system. However, all systems are ultimately nonlinear. One way to proceed is to extend this filtering method to nonlinear systems. This idea gives rise to the extended Kalman filter (EKF) firstly proposed by [122] , which is by far the most widely used nonlinear filtering technique [121]. It relies on the linearization of the nonlinear system about the current state estimate. Consider the following nonlinear discrete-time stochastic system

$$\begin{aligned} x(k) &= f\left(u(k-1), x(k-1), w_n(k-1)\right) \\ y(k-1) &= h\left(u(k-1), x(k-1), v_n(k-1)\right) \end{aligned} \tag{3.14}$$

with the same vector notation and noise assumptions as in Eqs. (3.1), (3.2). Let $\hat{x}(k)$ denote the estimate of the state at time k and linearize the system Eq. (3.14) about $x(k) = \hat{x}(k)$, $w_n(k) = 0$ and $v_n(k) = 0$, which results in

$$\begin{aligned} x(k) &\approx f(u(k-1), \hat{x}(k-1), 0) + F(k-1)\tilde{x}(k-1) + F_w(k-1)w_n(k-1) \\ y(k-1) &\approx h(u(k-1), \hat{x}(k-1), 0) + H(k-1)\tilde{x}(k-1) + H_v(k-1)v_n(k-1) \end{aligned} \tag{3.15}$$

where the estimation error is defined as $\tilde{x}(k) = x(k) - \hat{x}(k)$ and

$$F(k) = \frac{\partial f}{\partial x}(u(k), x(k), w_n(k))\bigg|_{\substack{x(k)=\hat{x}(k) \\ w_n(k)=0}}, F_w(k) = \frac{\partial f}{\partial w_n}(u(k), x(k), w_n(k))\bigg|_{\substack{x(k)=\hat{x}(k) \\ w_n(k)=0}} \tag{3.16}$$

$$H(k) = \frac{\partial h}{\partial x}(u(k), x(k), v_n(k))\bigg|_{\substack{x(k)=\hat{x}(k) \\ v_n(k)=0}}, H_v(k) = \frac{\partial h}{\partial v_n}(u(k), x(k), v_n(k))\bigg|_{\substack{x(k)=\hat{x}(k) \\ v_n(k)=0}} \tag{3.17}$$

Algorithm

The Kalman filter algorithm for the linearized system Eqs. (3.15)-(3.17), known as the extended Kalman filter (EKF), is given in Table 3.2.

Properties

Despite its wide use in real applications, there is no final and conclusive proof of the EKF convergence. Several authors have studied the deterministic EKF estimation

TABLE 3.2: The extended Kalman filter algorithm†.

Initialization: for $k = 0$ set

$\hat{x}_0 = \mathbb{E}[x_0],\ P_0 = \mathbb{E}[(x_0 - \hat{x}_0)(x_0 - \hat{x}_0)^{\mathrm{T}}]$

At each time instant compute:

Time-update:

$$\hat{x}_k^- = f(u_{k-1}, \hat{x}_{k-1}, 0) \tag{3.18}$$

$$P_k^- = F_{k-1} P_{k-1} F_{k-1}^{\mathrm{T}} + \bar{Q}_k \tag{3.19}$$

$$\hat{y}_k = h(u_k, \hat{x}_k^-, 0) \tag{3.20}$$

Measurement-update:

$$\hat{x}_k = \hat{x}_k^- + K_k (y_k - \hat{y}_k) \tag{3.21}$$

$$K_k = P_k^- H_k^{\mathrm{T}} \left(H_k P_k^- H_k^{\mathrm{T}} + \bar{R}_k \right)^{-1} \tag{3.22}$$

$$P_k = P_k^- - K_k \left(H_k P_k^- H_k^{\mathrm{T}} + \bar{R}_k \right) K_k^{\mathrm{T}} \tag{3.23}$$

where $\bar{Q}_k = F_{w,k} Q F_{w,k}^{\mathrm{T}}$, $\bar{R}_k = H_{v,k} R H_{v,k}^{\mathrm{T}}$, and

F_k, $F_{w,k}$, H_k and $H_{v,k}$ are given by Eqs. (3.16),(3.17).

†For compactness, the time argument is set as an index.

problem and provided some conditions under which the filter converges [123, 124]. Similar results in the stochastic framework are more limited, although the stochastic stability study proposed in [125] is particularly relevant for our purposes. It is summarized below.

Let us consider a particularization of the nonlinear system Eq. (3.14) where the noise terms enter linearly into the system, i.e.

$$\begin{aligned} x(k) &= f\left(u(k-1), x(k-1)\right) + w_n(k-1) \\ y(k-1) &= h\left(u(k-1), x(k-1)\right) + v_n(k-1). \end{aligned} \tag{3.24}$$

For the nonlinear system Eq. (3.24), the following definition holds.

Definition 3.1.1. Observability rank condition[2]. The nonlinear system Eq. (3.24) satisfies the nonlinear observability rank condition at x_k for the input sequence $U_{k,k+n-1} = \{u_k, \ldots, u_{k+n-1}\}$ if matrix $\mathcal{O}_c(U_{k,k+n-1}, x_k)$ defined below has full rank n.

$$\mathcal{O}_c(U_{k,k+n-1}, x_k) = \begin{bmatrix} \dfrac{\partial h}{\partial x}(u_k, x_k) \\ \dfrac{\partial h}{\partial x}(u_{k+1}, x_{k+1}) \dfrac{\partial f}{\partial x}(u_k, x_k) \\ \vdots \\ \dfrac{\partial h}{\partial x}(u_{k+n-1}, x_{k+n-1}) \dfrac{\partial f}{\partial x}(u_{k+n-2}, x_{k+n-2}) \cdots \dfrac{\partial f}{\partial x}(u_k, x_k) \end{bmatrix} \tag{3.25}$$

Let $U^*(x(k))$ denote the set of input sequences ensuring that the observability rank condition is fulfilled for a given $x(k)$. The main result of [125] is now recalled, which has been modified to accommodate the system input $u(k)$.

Theorem 3.1.2 (Stochastic stability of the EKF.)**.** *Consider system Eq.* (3.24) *and the associated EKF with state $\hat{x}(k)$ as in Table 3.2. Assume there exists a compact subset X in $\mathbb{R}^n$ such that the following conditions hold*

[2]For compactness of notation the time argument is set as an index in the definition.

1. *The nonlinear system Eq.* (3.24) *satisfies the observability rank condition for every* $x(k) \in X$ *and* $U(k, k+n-1) \in U^*(x(k))$.
2. *The nonlinear functions* f, h *are twice continuously differentiable with respect to* x, *for every* $u \in U^*$ *and* $\dfrac{\partial f}{\partial x}(u, x) \neq 0$ *holds for every* $x \in X$ *and* $u \in U^*$.
3. *The sample paths of* $x(k)$ *are bounded with probability one, and* X *contains these sample paths as well as points with distance smaller than* ϵ_X *from these sample paths, where* $\epsilon_X > 0$ *is a real number independent of* k.

Then the state estimation error $\tilde{x}(k) = x(k) - \hat{x}(k)$ *is exponentially bounded with probability one, provided that the initial estimation error satisfies* $\| \tilde{x}(0) \| \leq \epsilon$ *for some* $\epsilon > 0$, *and* $U(k, k+n-1) \in U^*(x(k))$ *for all* $k > 0$.

The EKF is, in general, not optimal [120]. Besides, the filter might provide unreliable estimates in the case of strong nonlinearities. In the EKF, the state distribution is approximated by a random variable, which is propagated analytically through the first-order linearization of the nonlinear system [126, 121]. Consider for instance a random vector x and an arbitrary nonlinear function

$$y = f(x) \tag{3.26}$$

whose true mean and covariance are respectively given by

$$\begin{aligned} \bar{y}_{nl} &= \mathbb{E}[f(x)] \\ P_{nl} &= \mathbb{E}[(y_{nl} - \bar{y}_{nl})(y_{nl} - \bar{y}_{nl})^{\mathrm{T}}]. \end{aligned} \tag{3.27}$$

The EKF approximates the mean and covariance of y as

$$\begin{aligned} \bar{y}_l &\approx f(\bar{x}) \\ P_l &\approx \left(\left. \frac{\partial f}{\partial x} \right|_{\bar{x}} \right) P_x \left(\left. \frac{\partial f}{\partial x} \right|_{\bar{x}} \right)^{\mathrm{T}} \end{aligned} \tag{3.28}$$

where $\bar{x} = \mathbb{E}[x]$ and the associated covariance is P_x. Another extension to the Kalman filter that reduces linearization errors is the unscented Kalman filter (UKF).

3.1.3 The Unscented Kalman Filter

Similarly to the EKF, the UKF also estimates the distribution of the random vector x for the dynamic model Eq. (3.14). In contrast to the EKF however, the UKF approximates the distribution through a minimal set of carefully chosen sample points. These sample points completely capture the true mean and covariance of the random variable, and provide second-order accuracy for the posterior mean and covariance after their propagation through the nonlinear system [126]. The process of deterministically sampling the distribution and the resulting sample points are respectively known as unscented transformation and sigma points.

The UKF heavily relies on the unscented transformation, which allows to calculate the statistics of a random variable that passes through a nonlinear function. Consider again the nonlinear transformation of Eq. (3.26), and the mean and covariance of the random variable $x \in \mathbb{R}^n$ are denoted as $\bar{x}$ and P_x, respectively. The statistics of y can be computed by forming a matrix of sigma points $\mathcal{X} \in \mathbb{R}^{n \times (2n+1)}$ given by

$$\begin{aligned} \mathcal{X}_0 &= \bar{x}, \\ \mathcal{X}_l &= \bar{x} + \left(\sqrt{(n+\lambda) P_x} \right)_l, \qquad l = 1, \ldots, n, \\ \mathcal{X}_l &= \bar{x} - \left(\sqrt{(n+\lambda) P_x} \right)_{l-n}, \quad l = n+1, \ldots, 2n, \end{aligned} \tag{3.29}$$

where $\lambda = \alpha^2(n+\kappa) - n$ is a scaling parameter involving the tuning parameters α and κ. According to [126], the tuning parameters can be selected as follows. The constant α is usually set to a small value between 10^{-4} and 1, and it reflects the spread of the sigma points around $\bar{x}$. The constant κ is usually set to $3-n$, and it is a secondary scaling parameter. The l-th column of the matrix square root is denoted by $\left(\sqrt{(n+\lambda)P_x}\right)_l$. These sigma points are propagated through the nonlinear function as

$$\mathcal{Y}_l = f(\mathcal{X}_l), \;\; l = 0, \ldots, 2n, \tag{3.30}$$

while the mean and covariance of y are approximated by the weighted sample mean and covariance of the posterior sigma points

$$\begin{aligned} \bar{y} &\approx \sum_{l=0}^{2n} W_l^{(m)} \mathcal{Y}_l \\ P_y &\approx \sum_{l=0}^{2n} W_l^{(c)} (\mathcal{Y}_l - \bar{y})(\mathcal{Y}_l - \bar{y})^{\mathrm{T}}, \end{aligned} \tag{3.31}$$

where W_l are weights given by

$$\begin{aligned} W_0^{(m)} &= \frac{\lambda}{n+\lambda} \\ W_0^{(c)} &= \frac{\lambda}{n+\lambda} + 1 - \alpha^2 + \beta \\ W_l^{(m)} &= W_l^{(c)} = \frac{1}{2(n+\lambda)}, \qquad l = 1, \ldots, 2n \end{aligned} \tag{3.32}$$

and β is a constant that can be set to 2 for Gaussian distributions, and it is in charge of incorporating prior knowledge of the distribution of x.

Algorithm

The UKF is a straightforward implementation of the unscented transform for recursive estimation [126]. Its algorithm is provided in Table 3.3 for a nonlinear system of the form of Eq. (3.14). As in the standard Kalman filter framework, the UKF consists of two steps: a time-update when the system state is predicted, and a measurement-update when the prediction is corrected once measurements arrive. We first focus on the time-update step, and denote $\hat{x}^-(k)$ and $\hat{x}(k)$ as the predicted and corrected state estimates, respectively. In order to obtain $\hat{x}^-(k)$, it is necessary to propagate $\hat{x}(k-1)$ through the nonlinear state function of Eq. (3.14). In contrast to the EKF where $\hat{x}(k-1)$ is directly passed through the nonlinear system, the UKF first generates a sampled probability distribution of the state random variable, and that is the one that is propagated through the system.

The system Eq. (3.14) at hand exhibits the noise entering the equations nonlinearly. In this case, the noise has to be augmented onto the state vector and error covariance matrix as [127, 126]

$$\begin{aligned} \hat{x}^a(k-1) &= [\hat{x}(k-1)^{\mathrm{T}} \;\; w(k-1)^{\mathrm{T}} \;\; v(k-1)^{\mathrm{T}}]^{\mathrm{T}} \\ P^a(k-1) &= \mathrm{diag}(P(k-1), Q, R), \end{aligned}$$

where $\hat{x}^a(k-1) \in \mathbb{R}^{n_a}$ and $P^a(k-1) \in \mathbb{R}^{n_a \times n_a}$ with $n_a = 2n + p$ denote the estimation of the mean and covariance of the augmented state random variable. Both the augmented state vector and covariance matrix can be initialized as in the initialization step in Table 3.3, and both are exploited in Eq. (3.33) to generate the matrix of sigma

TABLE 3.3: The unscented Kalman filter algorithm†.

Initialization: for $k = 0$, set

$\hat{x}_0 = \mathbb{E}[x_0], \quad P_0 = \mathbb{E}[(x_0 - \hat{x}_0)(x_0 - \hat{x}_0)^{\mathrm{T}}]$

$\hat{x}_0^a = \mathbb{E}[x_0^a] = [\hat{x}_0 \;\; 0 \;\; 0]^{\mathrm{T}},$

$P_0^a = \mathbb{E}[(x_0^a - \hat{x}_0^a)(x_0^a - \hat{x}_0^a)^{\mathrm{T}}] = \mathrm{diag}(P_0, Q, R)$

For $k = 1, 2, \ldots$ compute

Sigma points:

$$\mathcal{X}_{k-1}^a = \left[\hat{x}_{k-1}^a \;\; \hat{x}_{k-1}^a + \gamma\sqrt{P_{k-1}^a} \;\; \hat{x}_{k-1}^a - \gamma\sqrt{P_{k-1}^a}\right] \tag{3.33}$$

Time-update:

$$\mathcal{X}_{k|k-1}^x = f\left(u_{k-1}, \mathcal{X}_{k-1}^x, \mathcal{X}_{k-1}^w\right) \tag{3.34}$$

$$\hat{x}_k^- = \sum_{l=0}^{2n_a} W_l^{(m)} \mathcal{X}_{l,k|k-1}^x \tag{3.35}$$

$$P_k^- = \sum_{l=0}^{2n_a} W_l^{(c)} \left(\mathcal{X}_{l,k|k-1}^x - \hat{x}_k^-\right)\left(\mathcal{X}_{l,k|k-1}^x - \hat{x}_k^-\right)^{\mathrm{T}} \tag{3.36}$$

$$\mathcal{Y}_{k|k-1} = h\Big(u_k, \mathcal{X}_{k|k-1}^x, \mathcal{X}_{k-1}^v\Big) \tag{3.37}$$

$$\hat{y}_k = \sum_{l=0}^{2n_a} W_l^{(m)} \mathcal{Y}_{l,k|k-1} \tag{3.38}$$

Measurement-update

$$P_{y,k} = \sum_{l=0}^{2n_a} W_l^{(c)} \left(\mathcal{Y}_{l,k|k-1} - \hat{y}_k\right)\left(\mathcal{Y}_{l,k|k-1} - \hat{y}_k\right)^{\mathrm{T}} \tag{3.39}$$

$$P_{xy,k} = \sum_{l=0}^{2n_a} W_l^{(c)} \left(\mathcal{X}_{l,k|k-1}^x - \hat{x}_k^-\right)\left(\mathcal{Y}_{l,k|k-1} - \hat{y}_k\right)^{\mathrm{T}} \tag{3.40}$$

$$K_k = P_{xy,k} P_{y,k}^{-1} \tag{3.41}$$

$$\hat{x}_k = \hat{x}_k^- + K_k\left(y_k - \hat{y}_k^-\right) \tag{3.42}$$

$$P_k = P_k^- - K_k P_{y,k} K_k^{\mathrm{T}} \tag{3.43}$$

Parameters

$$\begin{aligned} &\gamma = \sqrt{n_a + \lambda}, \quad \lambda = \alpha^2(n_a + \kappa) - n_a \\ &W_0^{(m)} = \tfrac{\lambda}{n_a+\lambda}, \quad W_0^{(c)} = \tfrac{\lambda}{n_a+\lambda} + 1 - \alpha^2 + \beta \\ &W_l^{(m)} = W_l^{(c)} = \tfrac{1}{2(n_a+\lambda)}, \; l = 1, \ldots, 2n_a, n_a = 2n + p \end{aligned} \tag{3.44}$$

†For compactness, the time argument is set as an index.

points $\mathcal{X}^a \in \mathbb{R}^{n_a \times (2n_a+1)}$ as

$$\mathcal{X}^a(k-1) = \left[(\mathcal{X}^x(k-1))^{\mathrm{T}}, (\mathcal{X}^w(k-1))^{\mathrm{T}}, (\mathcal{X}^v(k-1))^{\mathrm{T}}\right]^{\mathrm{T}}.$$

The notation used for sigma point generation, namely $\hat{x}_{k-1}^a \pm \gamma\sqrt{P_{k-1}^a}$ stands for $\hat{x}_{k-1}^a \pm \gamma\left(\sqrt{P_{k-1}^a}\right)_l$, $l = 1, \ldots, n_a$, where $(\cdot)_l$ is the l-th column of the matrix. For the sake of compactness the above operation is rewritten as in Eqs. (3.33). These l sigma vectors are then passed through the nonlinear state function as in Eq. (3.34), and the mean and covariance of $\hat{x}^-(k)$ are approximated with a weighted sample mean and covariance of the posterior sigma points $\mathcal{X}_{k|k-1}^x$ such as in Eqs. (3.35) and (3.36),

respectively. The same procedure can be applied for the nonlinear output function Eq. (3.14) using Eqs. (3.37)-(3.39). The error cross-covariance matrix $P_{xy}(k)$ is computed using Eq. (3.40).

In the measurement-update step, the Kalman gain is obtained through Eq. (3.41) while the estimates for the state vector and error covariance matrix result from Eqs. (3.42) and (3.43), respectively. Notice the resemblance between the Kalman gain and the state vector and covariance matrix update of the UKF in Table 3.3 and the EKF in Table 3.2. By setting $P_{xy}(k) = P^{-}(k)H^{\mathrm{T}}(k)$ and $P_{y}(k) = H(k)P^{-}(k)H(k)^{\mathrm{T}} + R$ for the UKF in Eqs. (3.41)-(3.43), the EKF Eqs. (3.21)-(3.23) are recovered.

3.2 Parameter Estimation

Besides the model-based state estimation problem of the previous Section 3.1, the model that is exploited by the observer is built upon a given set of parameters. These model parameters can be identified a priory through feeding the system with appropriate input signals and post-processing the system measurements with parameter identification tools. However, a system that degrades with time suffers parametric changes that, if not accounted for, worsens the model performance. This issue can be mitigated by tracking parametric changes and adapting the model parameters as the system ages. One of the best known parameter identification techniques is the least squares method. Although this method is simple to implement and can be very accurate in specific situations, it provides biased estimates in the case of data corrupted by colored noise. To overcome this limitation, instrumental variable methods have been proposed, such as the standard instrumental variable and the simplified refined instrumental variable methods. These contributions are discussed next in terms of algorithm and properties.

Before entering into the mechanics of each parameter identification method, let us contrast the parameter estimation problem with the state estimation problem of the previous section. Consider a linear discrete-time stochastic dynamic system as the one introduced in Eq. (3.1), i.e.

$$\begin{aligned} x(k) &= Ax(k-1) + Bu(k-1) + w_n(k-1) \\ y(k) &= Cx(k) + v_n(k) \end{aligned} \tag{3.45}$$

with the same notation for vectors and assumptions for noise sequences as in Eq. (3.1). The parameter identification problem of the linear stochastic dynamic system Eq. (3.45) consists in inferring, in some statistical sense, the parameters of the matrices A, B and C based on measurements $u(k)$ and $y(k)$ over an observation interval $k = 1, 2, \ldots, N$ [128]. One way to do so is to estimate the parameters directly from the state space model using an EKF, just as the one introduced in Section 3.1.2. The state vector $x(k)$ can be augmented to include any unknown parameter in the system matrices. In contrast with this direct recursive estimation, this section explores the estimation of parameters in the observation-space transfer function model (as defined in [128] and explained below) obtained from model Eq. (3.45).

3.2.1 Least Squares Estimation

The least squares estimation was developed by Karl Friedrick Gauss in 1809 as a statistical tool, although it was Legendre who coined the term in an earlier publication of the theory in 1805 [128]. As Gauss stated, the least squares estimate has minimum mean square error among all linear error-consistent estimates [128].

The first step towards identifying the parameters in the state space model Eq. (3.45) is to transform it into the observation-space transfer function. This transformation can be achieved by first converting the model Eq. (3.45) into the innovations model in order not to have two but only one noise term, i.e. $w_n(k)$ and $v_n(k)$ are replaced by the innovation process $\nu(k)$[3]. Then, by introducing the z^{-1} operator and deriving the associated transfer function, the following observation equation is obtained

$$y(k) = \mathring{y}(k) + e(k) \tag{3.46}$$

[3]The innovation process follows from Kalman filter theory and it is defined as $\nu(k) = y(k) - C\hat{x}^-(k)$, where $\hat{x}^-(k)$ is the predicted state estimate.

where $e(k)$ is a white-noise sequence and $\mathring{y}(k)$ can be considered as a hypothetical and unmeasurable noise-free output of the system given by

$$\mathring{y}(k) = \frac{B(z^{-1})}{A(z^{-1})}u(k), \tag{3.47}$$

with the polynomials $A(z^{-1})$ and $B(z^{-1})$ defined as

$$\begin{aligned} A(z^{-1}) &= 1 + a_1 z^{-1} + \ldots + a_n z^{-n} \\ B(z^{-1}) &= b_0 + b_1 z^{-1} + \ldots + b_m z^{-m}. \end{aligned} \tag{3.48}$$

From Eqs. (3.47),(3.48), the deterministic output of the system is given by

$$\mathring{y}(k) = b_0 u(k) + b_1 u(k-1) + \ldots + u(k-m) - a_1 \mathring{y}(k-1) - \ldots - a_n \mathring{y}(k-n). \tag{3.49}$$

By substituting the observation Eq. (3.46) into Eq. (3.49), the resulting equation becomes explicit in the measured variables $u(k)$ and $y(k)$ as

$$\begin{aligned} y(k) = {} & b_0 u(k) + b_1 u(k-1) + \ldots + u(k-m) \\ & -a_1 y(k-1) - \ldots - a_n y(k-n) + \xi(k), \end{aligned} \tag{3.50}$$

where

$$\xi(k) = e(k) + a_1 e(k-1) + \ldots + a_n e(k-n). \tag{3.51}$$

The linear form of Eq. (3.50) is given by

$$y(k) = \varphi(k)\theta + \xi(k) \tag{3.52}$$

where

$$\begin{aligned} \varphi(k) &= [u(k), \ldots, u(k-m), -y(k-1), \ldots, -y(k-n)] \\ \theta &= [b_0, \ldots, b_m, a_1, a_2, \ldots, a_n]^{\mathrm{T}} \end{aligned} \tag{3.53}$$

and $\xi(k)$ is a colored noise.

Algorithm

The least squares estimate $\hat{\theta}_{\mathrm{LS}}$ of the parameter vector θ in the model Eq. (3.52) is given by

$$\hat{\theta}_{\mathrm{LS}} = \left(\sum_{k=0}^{N} \varphi(k)^{\mathrm{T}} \varphi(k) \right)^{-1} \left(\sum_{k=0}^{N} \varphi(k)^{\mathrm{T}} y(k) \right) \tag{3.54}$$

Properties

In the above framework, the least squares estimates are biased and inconsistent in the case of a noisy data set, which is commonly found in practice [128]. By using the true system Eq. (3.52) and subtracting the true θ parameter value from the parameter estimate $\hat{\theta}_{\mathrm{LS}}$, the following parameter difference $\tilde{\theta}_{\mathrm{LS}}$ is obtained [129]

$$\tilde{\theta}_{\mathrm{LS}} = \left(\frac{1}{N} \sum_{k=0}^{N} \varphi(k)^{\mathrm{T}} \varphi(k) \right)^{-1} \left(\frac{1}{N} \sum_{k=0}^{N} \varphi(k)^{\mathrm{T}} \xi(k) \right), \tag{3.55}$$

which, after making N tend to infinity, becomes

$$\tilde{\theta}_{\mathrm{LS}} = \left[\mathbb{E}\varphi(k)^{\mathrm{T}}\varphi(k)\right]^{-1}\left[\mathbb{E}\varphi(k)^{\mathrm{T}}\xi(k)\right]. \tag{3.56}$$

Thus, the least squares estimate is biased unless

$$\mathbb{E}\varphi(k)^{\mathrm{T}}\xi(k) = 0. \tag{3.57}$$

The condition in Eq. (3.57) is very restrictive since $\varphi(k)$ already depends on the output $y(k)$ and therefore on past values of $\xi(k)$. Eq. (3.57) holds true if and only if $\xi(k)$ is white noise [129]. To overcome the pitfalls of the least squares method in the parametric estimation of transfer functions from data corrupted by colored noise, instrumental variable (IV) methods have been developed [128].

3.2.2 The Standard Instrumental Variable Estimation

Instrumental variable methods are general and simple to implement in contrast to nonlinear estimation approaches such as the maximum likelihood method. IV methods retain the simplicity of linear least squares estimation while providing consistent, asymptotically unbiased and relatively efficient (low variance) parameter estimates of the system model [128].

Let us consider the linear Eq. (3.52) and bring it here for convenience, i.e.

$$y(k) = \varphi(k)\theta + \xi(k). \tag{3.58}$$

The instrumental variable estimate $\hat{\theta}_{\mathrm{IV}}$ of the parameter vector θ in the model Eq. (3.58) is given by

$$\hat{\theta}_{\mathrm{IV}} = \left(\sum_{k=0}^{N}\zeta(k)^{\mathrm{T}}\varphi(k)\right)^{-1}\left(\sum_{k=0}^{N}\zeta(k)^{\mathrm{T}}y(k)\right) \tag{3.59}$$

where $\zeta(k)$ is the instrumental variable.

The main difficulty in the application of IV algorithms is the selection of the instrumental variables. The IV vector must be chosen so that it should be as highly correlated as possible with the equivalent variables in the noise free vector of $\varphi(k)$, i.e. $\mathring{y}(k)$ and $u(k)$, and

$$\begin{cases} \mathbb{E}\left[\zeta(k)^{\mathrm{T}}\varphi(k)\right] \text{ is not singular} & \text{(3.60a)} \\ \mathbb{E}\left[\zeta(k)^{\mathrm{T}}\xi(k)\right] = 0. & \text{(3.60b)} \end{cases}$$

IVs could be a second output measurement corrupted by noise that is statistically independent of the output noise $\xi(k)$, or a deterministic input $u(k)$ that is obviously correlated with the noise-free part of the output $\mathring{y}(k)$ and uncorrelated with the noise $\xi(k)$ (in the absence of feedback control). However, the first option might occur in very specific cases whereas the second one requires to account for any time delay δ_t in the model.

Trying to find the appropriate time delay δ_t that maximizes the correlation between $\mathring{y}(k)$ and $u(k-\delta_t)$ can be very hard, particularly because $\mathring{y}(k)$ is unknown. Instead, an IV can be obtained by passing the input $u(k)$ through a transfer function so that the lag on the input caused by this filter is similar to that of the system. Such

transfer function is called auxiliary model, and it is iteratively updated based on the IV estimate at the previous iteration of the standard IV algorithm shown below.

Algorithm

The standard IV (SIV) algorithm that provides the estimate $\hat{\theta}_{\text{IV}}$ of the parameter vector θ in the model Eq. (3.58) is given in Table 3.4.

TABLE 3.4: The standard instrumental variable algorithm†.

Initialization: given the data sequence $Y_N=\{y_N, y_{N-1}, \ldots, y_0, u_N, u_{N-1}, \ldots u_0\}$
At iteration $j = 0$ compute

$$\text{LS estimate :} \quad \hat{\theta}_0 = \left(\sum_{k=0}^{N} \varphi_k^{\mathrm{T}} \varphi_k\right)^{-1} \left(\sum_{k=0}^{N} \varphi_k^{\mathrm{T}} \mathrm{Y}_k\right)$$

where $\varphi_k = [u_k,\ u_{k-1}, \ldots, u_{k-m},\ -y_{k-1}, \ldots, -y]$
and $\mathrm{Y}_k = y_k$

For iteration $j = 1, 2, \ldots$ compute

$$\text{Auxiliary output :} \quad \mathring{y}_k = \frac{B(z^{-1}, \hat{\theta}_j)}{A(z^{-1}, \hat{\theta}_j)} u_k$$

$$\text{Instrumental vector :} \ \zeta_k = [u_k,\ u_{k-1}, \ldots, u_{k-m},\ -\mathring{y}_{k-1}, \ldots, -\mathring{y}_{k-n}]$$

$$\text{Regressor vector :} \quad \varphi_k = [u_k,\ u_{k-1}, \ldots, u_{k-m}, -y_{k-1}, \ldots, -y_{k-n}]$$

$$\text{IV estimate :} \quad \hat{\theta}_{j+1} = \left(\sum_{k=0}^{N} \zeta_k^{\mathrm{T}} \varphi_k\right)^{-1} \left(\sum_{k=0}^{N} \zeta_k^{\mathrm{T}} \mathrm{Y}_k\right)$$

where $\mathrm{Y}_k = y_k$

If convergence occurs according to e.g. $\frac{||\theta_{j+1} - \theta_j||}{||\theta_j||} < \mu$ (for some user specified threshold μ), or the maximum number of iterations is reached, then stop, else set $j = j + 1$

†For compactness, the time argument is set as an index.

Properties

Once the SIV algorithm converges, the IV $\zeta(k)$ converges to the noise-free output $\mathring{y}(k)$ and the IV estimates have good statistical properties. Among these properties, the resulting parameter estimates are known to be asymptotically unbiased [128].

3.2.3 The Simplified Refined Instrumental Variable Estimation

Although the SIV of the previous section outperforms the least squares method by providing an unbiased identification of transfer function models associated to stochastic dynamical systems, it does so in a sub-optimal manner. In contrast, the simplified refined instrumental variable for continuous-time systems (SRIVC) method provides a statistically optimal solution, which is defined below. On the one hand, the term *refined* arises from the operation of pre-filtering the data with an estimation of the system model, which is iteratively updated with the IV parameter estimates. On the other hand, the term *simplified* involves the assumption of additive white-noise.

Notice that the SRIVC method has been cited instead of the SRIV, the discrete-time counterpart. Indeed, continuous-time identification is preferred since the world that

we inhabit is set up in this time domain, and so do the most scientific laws derived to describe it. Therefore, continuous-time identification inherently provides parameter estimates with physical relevance. Moreover, the continuous-time parameters are well defined and unique, in contrast to the discrete-time counterpart which depend on sampling time. However, conversion from continuous to discrete is straightforward if the latter parameter set is required [128]. The main challenge of continuous-time identification is the presence of time-derivatives that cannot be measured or easily obtained by differentiation due to data noise [128].

Consider the following linear continuous-time stochastic system

$$\begin{aligned} \dot{x}(t) &= Ax(t) + Bu(t) + w_n(t) \\ y(t) &= Cx(t) + v_n(t). \end{aligned} \tag{3.61}$$

The SRIVC algorithm aims at identifying the parameters in the TF model derived from the state-space model Eq. (3.61), which in turn implies the estimation of the parameters in the differential equation model given by

$$\mathring{y}^{(n)}(t) + a_1\mathring{y}^{(n-1)}(t) + \ldots + a_n\mathring{y}^{(0)}(t) = b_0u^{(m)}(t) + b_1u^{(m-1)}(t) + \ldots + b_mu^{(0)}(t) \tag{3.62}$$

where the superscripts in parentheses denote the differentiation order. The differential Eq. (3.62) can be written as the following transfer function

$$\mathring{y}(t) = \frac{B(s)}{A(s)}u(t) \tag{3.63}$$

where

$$A(s) = s^n + a_1s^{n-1} + \ldots + a_n, \;\; B(s) = b_0s^m + b_1s^{m-1} + \ldots + b_m$$

and s denotes the differential operator $s^px(t) = \frac{d^px(t)}{dt^p}$. The state matrices A, B in Eq. (3.61) should not be confused with the functions $A(s), B(s)$ in Eq. (3.62). Considering data uniformly sampled according to the sampling time T_s, the measured output $y(t_k)$, with $t_k = kT_s$, is assumed to be corrupted by an additive white-noise $e(t_k)$ as[4]

$$y(t_k) = \mathring{y}(t_k) + e(t_k). \tag{3.64}$$

Notice that the notion of a continuous-time white noise process involves both theoretical and practical problems, such as its associated infinite variance [128]. This shortcoming is overcome by considering hybrid models where the additive noise is taken in discrete-time, which is also coherent with sampled data. As stated in [128], the estimation problem posed by the hybrid continuous-discrete time model Eqs. (3.63),(3.64) is to estimate the parameters of the continuous-time TF Eq. (3.63) from N sampled measurements of the input and output. A suitable error function $\varepsilon(t_k)$ for estimating the parameters in the system model Eq. (3.64) is

$$\varepsilon(t_k) = y(t_k) - \frac{B(s,\hat{\theta}_j)}{A(s,\hat{\theta}_j)}u(t_k) \tag{3.65}$$

[4]For sampled signals, the adopted time variable notation is t_k, not to be confused with the discrete-time variable k.

By defining the pre-filter

$$f(s,\hat{\theta}_j) \triangleq \frac{1}{A(s,\hat{\theta}_j)} \tag{3.66}$$

and since the polynomial operators commute, Eq. (3.65) can be rewritten as

$$\varepsilon(t_k) = A(s,\hat{\theta}_j)y_{\mathrm{f}}(t_k) - B(s,\hat{\theta}_j)u_{\mathrm{f}}(t_k) \tag{3.67}$$

where the subscript f indicates that the associated variables have been pre-filtered by $f(s,\hat{\theta}_j)$. Optimal stochastic estimation can be achieved by minimizing a least squares criterion function in $\varepsilon(t_k)$. Expanding Eq. (3.67) results in

$$\begin{aligned}\varepsilon(t_k) \;=\; & y_{\mathrm{f}}^{(n)}(t_k) + a_1 y_{\mathrm{f}}^{(n-1)}(t_k) + \ldots + a_n y_{\mathrm{f}}^{(0)}(t_k) \\ & -b_0 u_{\mathrm{f}}^{(m)}(t_k) - b_1 u_{\mathrm{f}}^{(m-1)}(t_k) - \ldots - b_m u_{\mathrm{f}}^{(0)}(t_k)\end{aligned} \tag{3.68}$$

which can be expressed in the following pseudo-linear regression form

$$y_{\mathrm{f}}^{(n)}(t_k) = \varphi(t_k)\theta + \varepsilon(t_k) \tag{3.69}$$

where

$$\begin{gathered}\varphi(t_k) = \left[u_{\mathrm{f}}^{(m)}(t_k),\ldots,u_{\mathrm{f}}^{(0)}(t_k),-y_{\mathrm{f}}^{(n-1)}(t_k),\ldots,-y_{\mathrm{f}}^{(0)}(t_k)\right] \\ \theta = \left[b_0,\ldots,b_m,a_1,\ldots,a_n\right]^{\mathrm{T}}.\end{gathered} \tag{3.70}$$

The regression in Eq. (3.69) is equivalent to the one of Eq. (3.59) for the discrete-time SIV. Therefore, an iterative procedure similar to that of the SIV can be obtained for the SRIVC, which is shown next.

Algorithm

The SRIVC algorithm that provides the estimate $\hat{\theta}_{\mathrm{SRIVC}}$ of the parameter vector θ in the model Eq. (3.69) is given in Table 3.5.

Properties

The SRIVC parameter estimates $\hat{\theta}_{\mathrm{SRIVC}}$ are statistically optimal in the sense that they minimize the sum of the squares of the residuals associated with the IV normal equation

$$\left(\sum_{t_k=0}^{t_N}\zeta(t_k)^{\mathrm{T}}\varphi(t_k)\right)\theta - \left(\sum_{t_k=0}^{t_N}\zeta(t_k)^{\mathrm{T}}\mathrm{Y}(t_k)\right) = 0, \tag{3.71}$$

i.e. they are obtained from the solution of the following optimization problem [128]

$$\hat{\theta}_{\mathrm{SRIVC}} = \arg\min_{\theta}\left\|\left(\sum_{t_k=0}^{t_N}\zeta(t_k)^{\mathrm{T}}\varphi(t_k)\right)\theta - \left(\sum_{t_k=0}^{t_N}\zeta(t_k)^{\mathrm{T}}\mathrm{Y}(t_k)\right)\right\|^2. \tag{3.72}$$

The SRIVC method has been proven robust so that it can be applied in situations where the noise process is not white [128].

Remark 3.2.1. *Notice that parameter identification methods, such as the SRIVC method, solve the problem of measurement error models caused by noise on the output variables but not on the input variable. In the latter case, the transfer function parameter estimates are biased. One way to tackle this problem is by resorting to errors-in-variables method, or more complex estimation approaches such as maximum likelihood method.*

TABLE 3.5: The simplified refined instrumental variable method for continuous-time systems algorithm, where s denotes the Laplace variable†.

Initialization: given the data sequence $Y_{t_N}=\{y_{t_N}, y_{t_{N-1}}, \ldots, y_{t_0}, u_{t_N}, u_{t_{N-1}}, \ldots u_{t_0}\}$
At iteration $j = 0$ compute

$$\text{LS}-\text{SVF estimate}: \quad \hat{\theta}_0 = \left(\sum_{t_k=0}^{t_N} \varphi_{t_k}^{\mathrm{T}} \varphi_{t_k}\right)^{-1} \left(\sum_{t_k=0}^{t_N} \varphi_{t_k}^{\mathrm{T}} \mathrm{Y}_{t_k}\right)$$

$$\text{with } \varphi_{t_k} = \frac{1}{(s+\nabla)^n}\left[s^m u, \ s^{m-1}u, \ldots, u, \ -s^{n-1}y, \ldots, -y\right]_{t=t_k}$$

$$\text{and } \mathrm{Y}_{t_k} = \left.\frac{s^n}{(s+\nabla)^n} y\right|_{t=t_k}$$

For iteration $j = 1, 2, \ldots$ compute

$$\text{Auxiliary output}: \quad \mathring{y}(s) = \frac{B(s,\hat{\theta}_j)}{A(s,\hat{\theta}_j)} u(s)$$

$$\text{Instrumental vector}: \zeta_{t_k} = \frac{1}{A(s,\hat{\theta}_j)}\left[s^m u, \ s^{m-1}u, \ldots, u, \ -s^{n-1}\mathring{y}, \ldots, -\mathring{y}\right]_{t=t_k}$$

$$\text{Regressor vector}: \quad \varphi_{t_k} = \frac{1}{A(s,\hat{\theta}_j)}\left[s^m u, \ s^{m-1}u, \ldots, u, -s^{n-1}y, \ldots, -y\right]_{t=t_k}$$

$$\text{IV estimate}: \quad \hat{\theta}_{j+1} = \left(\sum_{t_k=0}^{t_N} \zeta_{t_k}^{\mathrm{T}} \varphi_{t_k}\right)^{-1} \left(\sum_{t_k=0}^{t_N} \zeta_{t_k}^{\mathrm{T}} \mathrm{Y}_{t_k}\right)$$

$$\text{with } \mathrm{Y}_{t_k} = \left.\frac{s^n}{A(s,\hat{\theta}_j)} y\right|_{t=t_k}$$

If convergence occurs according to e.g. $\frac{||\theta_{j+1}-\theta_j||}{||\theta_j||} < \mu$ (for some user specified threshold μ), or the maximum number of iterations is reached, then stop, else set $j = j + 1$

†For compactness, the time argument is set as an index.

3.3 Fault Detection and Isolation

The parameter identification methods introduced in the previous Section 3.2 are intended to estimate model parameter changes in stochastic dynamical systems, which can be seen as multiplicative faults. As opposed to these methods, the one presented in this section aims at identifying additive faults for the same model setting in the framework of fault diagnosis. A diagnosis system consists of two parts, namely a residual generator and a decision system [130]. A residual generator is a filter that exploits measured signals $u(k)$ and $y(k)$ as inputs to compute residuals $\nu(k)$. Consider the following linear discrete-time stochastic system

$$\begin{aligned} x(k) &= Ax(k-1) + Bu(k-1) + F_1 f(k-1) + w_n(k-1) \\ y(k-1) &= Cx(k-1) + F_2 f(k-1) + v_n(k-1), \end{aligned} \tag{3.73}$$

where $x(k) \in \mathbb{R}^n$ is the state vector, $u(k) \in \mathbb{R}^m$ is the input vector, $y(k) \in \mathbb{R}^p$ is the output vector, $f(k) \in \mathbb{R}^{n_f}$ is a vector of unknown input signals representing the faults to be detected and $w_n(k) \in \mathbb{R}^n$ and $v_n(k) \in \mathbb{R}^p$ are process and measurement noise sequences, respectively, with the classical noise assumptions as in Eqs. (3.1), (3.2). The considered faults are additive since they enter linearly in the system as additional input. Let $\nu(k)$ denote a residual given by

$$\nu(k) = y(k) - \hat{y}(k), \tag{3.74}$$

where $\hat{y}(k) \in \mathbb{R}^p$ is the output estimation given by a Kalman filter, and in this context the residual $\nu(k)$ is also called the innovation sequence. Resorting to the Kalman filter introduced in Table 3.1, and substituting Eqs. (3.6),(3.7) into (3.4), the following residual generator is obtained

$$\begin{aligned} \hat{x}(k) &= A(I - K(k-1)C)\hat{x}(k-1) + Bu(k-1) + AK(k-1)y(k-1) \\ \nu(k-1) &= y(k-1) - C\hat{x}(k-1) \end{aligned} \tag{3.75}$$

where the filter gain and the estimation error covariance matrix are given by Eqs. (3.19),(3.22) and (3.23) in Table 3.1. By defining the state estimation error as $\tilde{x}(k) = x(k) - \hat{x}(k)$, the error system takes the form

$$\begin{aligned} \tilde{x}(k) &= A(I - K(k-1)C)\tilde{x}(k-1) + (F_1 - AK(k-1)F_2)f(k-1) + w_n(k) - AK(k-1)v_n(k-1) \\ \nu(k-1) &= C\tilde{x}(k-1) + F_2 f(k-1) + v_n(k-1). \end{aligned} \tag{3.76}$$

By setting the noise sequences $w_n(k), v_n(k)$ equal to zero, the residual can be rewritten as

$$\nu(k) = \nu_0(k) + \rho(k) \tag{3.77}$$

where $\nu_0(k)$ and $\rho(k)$ are respectively generated by

$$\begin{aligned} \tilde{x}_0(k) &= A(I - K(k-1)C)\tilde{x}_0(k-1) \\ \nu_0(k-1) &= C\tilde{x}_0(k-1) \end{aligned} \tag{3.78}$$

and

$$\begin{aligned} \tilde{x}_\rho(k) &= A(I - K(k-1)C)\tilde{x}_\rho(k-1) + (F_1 - AK(k-1)F_2)f(k-1) \\ \rho(k-1) &= C\tilde{x}_\rho(k-1) + F_2 f(k-1), \end{aligned} \tag{3.79}$$

with $\tilde{x}_0(0) = x(0) - \hat{x}(0)$ and $\tilde{x}_\rho(0) = 0$. In steady state and without faults, $\nu(k) = \nu_0(k)$ and the associated probability law is given by the distribution of the innovation

sequence of the Kalman filter, i.e.

$$\mathcal{L}(\nu(k)) = \mathcal{N}(0, CP(k)C^{\mathrm{T}} + R). \tag{3.80}$$

For its part, in the presence of a fault of the form $\mathrm{f}(k) = \bar{\mathrm{f}}1_{k\geq k_0}$, $\nu(k) = \nu_0(k) + \rho(k, k_0)\bar{\mathrm{f}}$ where $\rho(k, k_0)$ is the step response of the system Eq. (3.79), and the associated probability law is given by

$$\mathcal{L}(\nu(k)) = \mathcal{N}(\rho(k, k_0)\bar{\mathrm{f}}, CP(k)C^{\mathrm{T}} + R). \tag{3.81}$$

As it can be seen from Eqs. (3.80) and (3.81), the residuals exhibit a change in the mean upon fault occurrence although the variance does not change. Therefore, residuals coming from e.g. a Kalman filter can be exploited to detect and isolate sensor faults.

In order to detect a change in the residual mean despite the effect of measurement noise on the residual, a generalized likelihood ratio (GLR) algorithm can be used [130]. This algorithm estimates *a posteriori* the most likely change in the residual mean and the most likely fault occurrence time. Given a sequence of n_ν-dimensional independent samples $\nu(1), \ldots, \nu(k)$, the GLR algorithm solves the following hypothesis testing problem:

$$\begin{aligned}
&\mathcal{H}_0: \quad \mathcal{L}(\nu(i)) = P_{\theta_0}\ i = 1, \ldots, k \\
&\mathcal{H}_1: \quad \textit{from time instant 1 up to an unknown time instant } k_0, \nu(i), i = 1, \ldots, j-1 \textit{ is} \\
&\qquad \textit{distributed as:} \\
&\qquad\qquad \mathcal{L}(\nu(i)) = P_{\theta_0} \\
&\qquad \textit{while for time instants } i \geq j \\
&\qquad\qquad \mathcal{L}(\nu(i)) = P_{\theta_1}
\end{aligned} \tag{3.82}$$

with $\mathcal{H}_0$ and $\mathcal{H}_1$ representing the fault-free and faulty scenarios, respectively, with probability law P_{θ_0} and P_{θ_1} (and associated probability density function $p_{\theta_0}(\nu(k))$ and $p_{\theta_1}(\nu(k))$), $\theta_1 = \theta_0 + \eta\mu$ where μ is a known change direction and η is an unknown scalar change magnitude and j is the time instant at which a given fault takes place.

In order to discern between both hypotheses in Eq. (3.82), a statistical test is carried out that consists of the following decisions:

$$\begin{aligned}
&\text{if } g_{\mathrm{GLR}}(k) \leq \bar{h} \text{ accept } \mathcal{H}_0 \\
&\text{if } g_{\mathrm{GLR}}(k) > \bar{h} \text{ accept } \mathcal{H}_1
\end{aligned} \tag{3.83}$$

where $\bar{h}$ is a user defined test threshold and $g_{\mathrm{GLR}}(k)$ is the GLR decision function taking the form

$$g_{\mathrm{GLR}}(k) = \max_{k\text{-}M+1 \leq j \leq k} \sup_{\eta} \mathcal{S}_j^k(\eta). \tag{3.84}$$

Let us break down the different pieces forming the decision function Eq. (3.84). First, the term $\mathcal{S}_j^k(\eta)$ is the cumulative sum of the log-likelihood ratio between faulty and fault-free mode given by

$$\mathcal{S}_j^k(\eta) = \sum_{i=j}^{k} \ln \frac{p_{\theta_1}(\nu(i))}{p_{\theta_0}(\nu(i))}. \tag{3.85}$$

Secondly, Eq. (3.84) is a double maximization problem over a moving window of fixed size M. By restricting the fault occurrence time to the last M time instants, the search duration for finding the optimum does not keep growing with time. Finally,

for a given time instant k, $\mathcal{S}_j^k(\eta)$ is a function of both the change time j and the change magnitude η, both unknown. To tackle this issue, the standard statistical approach of replacing j and η by their maximum likelihood estimates is used, which gives rise to the double maximization problem of Eq. (3.84).

3.4 Constrained Control

Besides battery supervision, our aim is also to achieve fast charging. This problem can be stated as a constrained control problem. A way to solve it is to resort to a reference governor (RG). A RG [115] is an *add-on* scheme that exploits state feedback, prediction, optimization and set-invariance arguments to suitably modify the reference of a pre-stabilized (closed-loop) system in order to cope with constraints. Continuous-time RGs were the first ones to appear in the literature [131]. Even though model predictive control (MPC) is the most widely used approach to optimally control systems with constraints, RGs turn out to be a very appealing alternative when a nominal controller exists and should not be modified. That is the case of a well-designed controller that provides the desired e.g. performance, stability, robustness and/or computational effort [115]. The latter aspect is the key concern when designing a BMS, since the energy required to carry out computations for estimation/control is energy drawn from the battery. Therefore, the higher the computational burden, the lower the battery energy efficiency.

The first step towards output tracking through RG techniques is to pre-stabilize the plant. To this end, we can design a feedback controller. Let us consider a discrete-time linear system of the form

$$\begin{aligned} x(k+1) &= A_d x(k) + B_d u(k) \\ y(k) &= C_d x(k) \end{aligned} \tag{3.86}$$

where $x(k) \in \mathbb{R}^n$ is the state vector, $u(k) \in \mathbb{R}^m$ is the input vector, $y(k) \in \mathbb{R}^p$ is the output vector, and $A_d \in \mathbb{R}^{n\times n}$, $B_d \in \mathbb{R}^{n\times 1}$ and $C_d \in \mathbb{R}^{1\times n}$ are the state, input and output matrices, respectively. A control law that makes system Eq. (3.86) asymptotically stable can be designed in different ways [132]. Let us consider a simple linear quadratic regulator (LQR), with trajectory tracking for the reference and integral action to eliminate the steady state error. To account for the integral feedback, the controller state $x(k)$ has to be augmented with an integral state $x_i(k)$ that integrates the error between the applied reference $v(k)$ and the output of the plant $y(k)$, i.e.

$$\begin{aligned} x_{cl}(k+1) &= A_e x_{cl}(k) + B_{u,e} u(k) + B_{v,e} v(k) \\ y_{cl}(k) &= C_e x_{cl}(k) \end{aligned} \tag{3.87}$$

where $x_{cl}(k) = [x(k), x_i(k)]^{\mathrm{T}}$ and $y_{cl}(k)$ are the closed-loop state and output vectors, respectively, and

$$A_e = \begin{bmatrix} A_d & 0 \\ -B_i C_d & A_i \end{bmatrix}, \; B_{u,e} = \begin{bmatrix} B_d \\ 0 \end{bmatrix}, \; B_{v,e} = \begin{bmatrix} 0 \\ B_i \end{bmatrix}, \; C_e = \begin{bmatrix} C_d \\ 0 \end{bmatrix}^{\mathrm{T}} \tag{3.88}$$

are the state, input, applied reference and output matrices, respectively, with $A_i = 1$ and $B_i = 1$.

The optimal state feedback law can be obtained by solving the following optimization problem [133]

$$\begin{aligned} \min_u \; & J = \frac{1}{2} \sum_{k=0}^{\infty} x_{cl}(k)^{\mathrm{T}} Q_c x_{cl}(k) + u(k)^{\mathrm{T}} R_c u(k) \\ \text{s.t. } & \text{Eqs. (3.87), (3.88)} \end{aligned} \tag{3.89}$$

where $Q_c \geq 0$ and $R_c > 0$, whose closed form solution is given by

$$u(k) = -K_c x_{cl}(k). \tag{3.90}$$

If the pair $(A_e, B_{u,e})$ is stabilizable and the pair (A_e, C_e) is detectable (with $Q_c = C_e^{\mathrm{T}} C_e$), then the steady-state feedback gain takes the form

$$K_c = (B_{u,e}^{\mathrm{T}} P_c B_{u,e} + R_c)^{-1} B_{u,e}^{\mathrm{T}} P_c A_e = [K_x \;\; K_i], \tag{3.91}$$

where P_c is the unique positive definite solution to the algebraic Riccati equation

$$P_c = A_e^{\mathrm{T}} P_c A_e - A_e^{\mathrm{T}} P_c B_{u,e} (B_{u,e}^{\mathrm{T}} P_c B_{u,e} + R_c)^{-1} B_{u,e}^{\mathrm{T}} P_c A_e + Q_c. \tag{3.92}$$

Substituting Eq. (3.90) into Eqs. (3.87),(3.88) results in the closed-loop system given by

$$x_{cl}(k+1) = A_{cl} x_{cl}(k) + B_{cl} v(k) \tag{3.93}$$

where

$$A_{cl} = \begin{bmatrix} A_d - B_d K_x & -B_d K_i \\ -B_i C_d & A_i \end{bmatrix}, \;\; B_{cl} = \begin{bmatrix} 0 \\ B_i \end{bmatrix}. \tag{3.94}$$

The closed-loop system Eqs. (3.93),(3.94) is asymptotically stable, i.e. the matrix A_{cl} is Schur. The weighting matrices Q_c and R_c are chosen in order to get an aggressive control regardless potential constraint violations. The capabilities to handle constraints are in turn provided by the RG scheme.

The most used RG for discrete-time linear systems of the form Eqs. (3.93),(3.94) was presented in [134]. The RG is able to manage n_c linear constraints associated to the closed-loop state of the system such as

$$S x_{cl}(k) \leq s \tag{3.95}$$

where $S \in \mathbb{R}^{n_c \times n}$ and $s \in \mathbb{R}^{n_c}$.

The goal of all RG schemes is to compute, at each time instant and on the basis of the current state $x_{cl}(k)$, an applied reference $v(k)$ approximating the desired reference $r(k)$ so that, if $v(k)$ is constantly applied from now to infinity, the constraints will always be satisfied [115]. In other words, on the basis of the currently available state $x_{cl}(k)$, the applied reference $v(k)$ ensures

$$S \hat{x}_{cl}(\ell | x_{cl}(k), v(k)) \leq s, \;\; \ell = 0, ..., \infty, \tag{3.96}$$

where the ℓ step ahead prediction $\hat{x}_{cl}(\ell | x_{cl}, v)$ starting from the initial state x_{cl} and with constant applied reference v is defined as

$$\hat{x}_{cl}(\ell | x_{cl}, v) = A_{cl}^{\ell} x_{cl} + (I - A_{cl})^{-1} (I - A_{cl}^{\ell}) B_{cl} v. \tag{3.97}$$

The set of all the initial states x_{cl} and applied references v for which Eq. (3.96) is satisfied is denoted as the maximal output admissible set O_∞ [135]. The computation of O_∞ is often avoided due to computational reasons. Instead, a slightly tightened version of O_∞, denoted as $\tilde{O}_\infty$, is usually used. To obtain $\tilde{O}_\infty$, the applied reference v is constrained in such a way that the steady state $\bar{x}_{cl,v} = (I - A_{cl})^{-1} B_{cl} v$ satisfies the constraints with an arbitrarily small margin $\epsilon > 0$ [115]. Moreover, if the constraints Eq. (3.95) define a compact set, then the set $\tilde{O}_\infty$ is finitely-computable, which means

that there exists a finite integer ℓ^* such that

$$\tilde{O}_\infty = \{(x_{cl}, v) \,|H_x x_{cl} + H_v v \leq h\} \tag{3.98}$$

where

$$H_x \triangleq \begin{bmatrix} SA^0 \\ SA^1 \\ SA^2 \\ \vdots \\ SA^{\ell^*} \\ 0 \end{bmatrix}, \; H_v \triangleq \begin{bmatrix} S(I-A_{cl})^{-1}(I-A_{cl}^0)B_{cl} \\ S(I-A_{cl})^{-1}(I-A_{cl}^1)B_{cl} \\ S(I-A_{cl})^{-1}(I-A_{cl}^2)B_{cl} \\ \vdots \\ S(I-A_{cl})^{-1}(I-A_{cl}^{\ell^*})B_{cl} \\ S(I-A_{cl})^{-1}B_{cl} \end{bmatrix}, \; h \triangleq \begin{bmatrix} s \\ s \\ s \\ \vdots \\ s \\ s(1-\epsilon) \end{bmatrix}. \tag{3.99}$$

All the matrices and the vectors defined above have the same number of rows $N_c \triangleq n_c \cdot (\ell^* + 2)$. Note that $\tilde{O}_\infty$ can be made arbitrarily close to O_∞ by reducing ϵ.

Remark 3.4.1. *Notice that the form of $\tilde{O}_\infty$ in Eq.* (3.98) *defines a set of linear inequalities. There are several ways to compute a minimal set $\tilde{O}_\infty$ [134, 115]. One way to do it is to draw the constraints Eqs.* (3.98),(3.99) *for a given time horizon ℓ and check if there are redundant constraints. If not, $\ell = \ell + 1$ and the verification is carried out again. This process continues until constraint redundancy is found, instant in which $\ell = \ell^*$.*

In the Scalar Reference Governor [136], a scalar $\kappa(k) \in [0, 1]$ indicates how much a previously applied reference $v(k-1)$ can move towards $r(k)$ while ensuring that $(x_{cl}(k), v(k)) \in \tilde{O}_\infty$. The scalar $\kappa(k)$ is an adjustable bandwidth parameter that can be computed through the following optimization problem

$$\kappa(k) = \max_{\kappa \in [0,1]} \; \kappa \tag{3.100}$$

$$\text{s.t. } H_x x_{cl}(k) + H_v(v(k-1) + \kappa(r(k) - v(k-1))) \leq h \tag{3.101}$$

and the command to be applied to the system is given by

$$v(k) = v(k-1) + \kappa(k)(r(k) - v(k-1)). \tag{3.102}$$

This scheme ensures recursive feasibility under the assumption that at time zero $(x_{cl}(0), v(0)) \in \tilde{O}_\infty$, and for a constant reference $r(k) = r$, it also guarantees finite time convergence of $v(k)$ to the best steady-state feasible approximation of r along the line segment connecting $v(0)$ and r [134].

The optimization problem Eqs. (3.100)-(3.101) can be computed very efficiently by inspecting one by one the lines of Eq. (3.101) [115]. By denoting as $H_{x,i}^{\mathrm{T}}, H_{v,i}^{\mathrm{T}}, h_i$ the i-th line of H_x, H_v, and h, respectively, the i-th constraint can be written as

$$\kappa \left(H_{v,i}^{\mathrm{T}}(r(k) - v(k-1)) \right) \leq h_i - H_{x,i}^{\mathrm{T}} x_{cl}(k) - H_{v,i}^{\mathrm{T}} v(k-1), \tag{3.103}$$

where κ is the only unknown. Thanks to recursive feasibility, $v(k-1)$ is always admissible and therefore the right-hand side of Eq. (3.103) is always positive. Only two cases are then possible:

- If $\left(H_{v,i}^{\mathrm{T}}(r(k) - v(k-1)) \right) > 0$, any positive κ such that

$$\kappa \leq \kappa_i^* \triangleq \frac{h_i - H_{x,i}^{\mathrm{T}} x_{cl}(k) - H_{v,i}^{\mathrm{T}} v(k-1)}{H_{v,i}^{\mathrm{T}}(r(k) - v(k-1))}$$

is a feasible solution.

- If $\left(H_{v,i}^{\mathrm{T}}(r(k)-v(k-1))\right) \leq 0$, any positive $\kappa \in [0,1]$ is a feasible solution. Accordingly, for this i-th constraint we can define $\kappa_i^* \triangleq 1$.

The optimal solution of Eqs. (3.100)-(3.101) is thus given by

$$\kappa(k) = \min\left\{\min_{i=1,\ldots,N_c}(\kappa_i^*, 1)\right\}. \tag{3.104}$$

Chapter 4

Battery Modeling

As stated in Section 2.3, battery models are developed with a double objective in mind, namely to become a battery simulator or to get a supervisory control system out of it. Dynamic models for both battery regular operation and battery degradation are derived. The degradation modeling is exemplified with a limited number of aging phenomena and it is exploited later for SOH monitoring and sensor diagnosis in Chapter 5. Only unavoidable aging mechanisms are represented in simulation, whereas others will be avoided by proper control in Chapters 6 and 7. Global validation through experiments is also provided. The electrochemical models used for the aforementioned different tasks are subsequently described in this chapter, which is structured as follows. Section 4.1 introduces the battery cell simulator based on the DFN model, whereas Section 4.2 derives a reduced-order electrochemical model for battery monitoring and control.

4.1 Battery Cell Simulator

Unless otherwise stated, the DFN model of Table 2.1 is the benchmark used as a virtual battery cell to test the different state estimation and control strategies developed in this work. The DFN model has been extended to include the thermal dynamics of Table 2.2 and aging dynamics of Table 2.3. However, some functions of the aging model have been neglected in order to avoid long simulations and some others have been modified to exhibit accelerated aging.

The only side reaction that has been considered here is the SEI growth, which translates in $j_{sr} = j_{\text{SEI}}$ in Eq. (2.21). Although the lithium plating mechanism is not explicitly modeled here, its associated electrochemical constraints are accounted for in the control law developed in Section 6.1 below. In this way, the degrading effect of this mechanism in battery life is alleviated. Diffusion limitations of the solvent are assumed to be negligible, and therefore Eq. (2.24) is not considered. The impedance increase Eq. (2.27) is modified so that the time instant $\tau_{R,0}$ triggers its degrading influence. This strategy allows to consider accelerated aging starting from a given time instant, which reduces simulation time without compromising the validity of the developed estimator/controller. Thus, power fade is given by[1]

$$\frac{dR_f}{dt}(t) = \begin{cases} 0 & \text{if } t < \tau_{R,0} \\ -\frac{M_p}{\kappa_p \rho_p} j_{sr}(t) & \text{if } t \geq \tau_{R,0} \end{cases} \tag{4.1}$$

[1]Continuous-time with time variable t and the time derivative as $\frac{d\chi}{dt}(\cdot, t)$ is adopted in this section for the DFN model modifications.

where $R_f(0) = R_{f,0}$ is a standard film resistance from a brand new battery electrode ($R_{f,0} \approx 0\ \Omega.\text{m}^2$) and $\tau_{R,0}$ is the time instant at which resistance degradation starts to occur.

Finally, the diffusion coefficient D_s is also considered to be time-varying due to aging caused by electrode phase changes. The functional form Eq. (2.30) has been adapted here, resulting in the following expression:

$$D_{s,\text{ref}}(t) = \begin{cases} D_{s,0} & \text{if } t < \tau_{D,0} \\ D_{s,0}\, k_1 \exp\left(\frac{k_2}{k_3(t-\tau_{D,0})+1}\right) & \text{if } t \geq \tau_{D,0} \end{cases} \tag{4.2}$$

where $D_{s,0}$ is a standard diffusion coefficient from a brand new battery electrode, $k_i, i = 1, 2, 3$ are constants, and $\tau_{D,0}$ is the time instant at which diffusion degradation starts to take place.

Then, the aging model considered here consists of Eqs. (2.21)-(2.23), (2.25)-(2.27) in Table 2.3 for $sr = \text{SEI}$, along with Eqs. (4.1),(4.2).

Remark 4.1.1. *Although the DFN model with thermal dynamics is a mature modeling framework for lithium-ion batteries, the field of aging modeling covers a wide spectrum of model derivations ranging from electrochemical principles to empirical functions. Such a plethora of models is due to the complexity and intertwined degradation mechanisms that occur within a battery cell. That is why we need to clarify our aging framework. Here we have chosen popular and at the same time diverse aging mechanisms that we consider particularly relevant.*

4.2 Modeling for State Estimation & Control

The DFN model with thermal and aging dynamics described in Section 4.1 consists of a coupled set of algebraic nonlinear partial-differential equations (PDEs). Although accurate for simulation, this complex model structure prevents its use in on-line scenarios of estimation/control. Therefore model reduction is required.

Different reduced-order models have been proposed in the literature, as referred in Section 2.3. However, most of those models are based on equivalent-circuit models, neglect relevant battery dynamics or loose in some degree the physical meaning they are intended to keep. In this scenario, we opted for deriving a reduced model that does not suffer from the last pitfalls, which exploits some existent reduced-order modeling efforts, together with the simplification of the DFN model. The way we perform model reduction is addressed in the following sections. More specifically, only one electrode is considered first for the exposition of the solid-phase diffusion equation, since the counter electrode corresponding equation is exactly the same but with a flip in the current sign. Then, the number of independent variables of the solid-phase diffusion equation is squeezed from (x, r, t) to (r, t) by focusing on a single spherical particle. The number of the remaining independent variables for both the solid and electrolyte-phase diffusion PDEs are further squeezed from $(\{r, x\}, t)$ to (t) by evaluating them at especially relevant boundary conditions. This procedure results in transcendental transfer functions that are later truncated through a Padé approximation. The obtained approximated transfer function is transformed into a state-space model based on an hydraulic equivalence. The material balance property of physical systems is then exploited to discard one of the electrodes in the battery cell model. Finally, the simplification of the thermal model, the output equation, the algebraic constraint arising from the aging dynamics and electrochemical constraints associated to degradation are discussed successively.

4.2.1 Diffusion Equations & Material Balance

Lithium-ions diffusion is one of the most relevant processes taking place inside a battery cell in both solid and electrolyte phases, while lithium has to be conserved according to the principle of mass conservation. These notions and associated equations are explored in the next subsections in order to derive a reduced-order electrochemical model for the lithium-ion diffusion process.

Solid-Phase Diffusion Equation

One common simplification of the DFN model is to neglect the x-spatial dependency of the state variables and to consider the entire electrode as a single spherical particle (i.e. the single-particle model, SPM). The scaling between both models relies on the equivalence between the surface area of the spherical particle and the active area of the porous electrode. The diffusion Eq. (2.6) resulting from Fick's law can be simplified by considering that the solid-phase diffusion coefficient is spatially constant and by using the change of variables $\bar{c}_s(r,t) = rc_s(r,t)$ [77], where $c_s(r,t)$ is the solid-phase concentration. The following diffusion equation with Dirichlet and Robin boundary conditions is then obtained[2]

$$\begin{cases} \dfrac{\partial \bar{c}_s}{\partial t}(r,t) = D_s \dfrac{\partial^2 \bar{c}_s}{\partial r^2}(r,t) \\ \quad \bar{c}_s(r,t)|_{r=0} = 0 \\ \quad R_s \dfrac{\partial \bar{c}_s}{\partial r}(r,t) - \bar{c}_s(r,t)\Big|_{r=R_s} = \dfrac{R_s^2}{D_s} j_n(t) \end{cases} \tag{4.3}$$

where $r \in [0, R_s]$, $t \geq 0$, and D_s and R_s are the diffusion coefficient and the particle radius, respectively. Assuming that the reaction rate is uniform along the x-axis, the pore-wall molar flux $j_n(t)$ is a function dependent on the current applied to the battery $I(t)$ given by

$$j_n(t) \approx \frac{1}{Fa_sL} I(t) \tag{4.4}$$

where F is Faraday's constant, L is the thickness of the electrode region and a_s is the specific interfacial area of each electrode. Taking the Laplace transform of Eq. (4.3) with respect to the time variable, solving the resulting ODE and setting $r = R_s$ (i.e. the spherical particle surface) yields the following solid-phase diffusion impedance equation [137]

$$\frac{C_{ss}(s)}{I(s)} = \frac{1}{Fa_sLc_{s,\max}} \frac{R_s \sinh(\alpha)}{D_s(\alpha \cosh(\alpha) - \sinh(\alpha))} \tag{4.5}$$

with $\alpha = R_s\sqrt{\frac{s}{D_s}}$. $C_{ss}(s)$ and $I(s)$ denote the Laplace transforms of $c_{ss}(t)$ and $I(t)$ respectively, where $c_{ss}(t) = c_s(r,t)|_{r=R_s}$ is the solid surface concentration and s is the Laplace variable.

Remark 4.2.1. *The system in Eq.* (4.5) *has a non integer order, i.e. irrational transfer function, with an infinite number of zeros* $-(k\pi\sqrt{D_s}R_s^{-1})^2$, $k \in \mathbb{N}$ *and poles* $-(\alpha_k\sqrt{D_s}R_s^{-1})^2$, *where* α_k *is the k-th root of* $\tanh\alpha = \alpha$.

[2]The remainder of this section adopts continuous-time with time variable t and the time derivative of χ denoted as $\dot{\chi}$, while the discrete-time variable is denoted as k in difference equations.

Electrolyte-Phase Diffusion Equation

Looking now at the electrolyte phase, the diffusion Eq. (2.9) can be simplified by considering a spatially constant electrolyte-phase diffusion coefficient. This is a strong assumption, since this coefficient does vary nonlinearly with electrolyte concentration as shown in Table 2.1. However, the resulting nonlinear PDE is too complex to obtain an analytical solution out of it, which is required to derive a transfer function. Similarly as for the solid-phase PDE, there might be a state transformation that renders a linear electrolyte-phase PDE, but we could not find one. Therefore, the constant parameter approximation is adopted here [21, 138, 139], which results in the following PDEs

TABLE 4.1: Electrolyte-phase diffusion partial differential equations.

	In-domain Equations	Boundary Conditions
Negative electrode	$\frac{\partial c_e^-}{\partial t} = \frac{D_{e,\text{eff}}^-}{\varepsilon_e^-}\frac{\partial^2 c_e^-}{\partial x^2} + \frac{a_s^-(1-t_c^0)}{\varepsilon_e^-} j_n^-$,	$\left\{ \begin{array}{c} \left.\frac{\partial c_e^-}{\partial x}\right\|_{x=0} = \left.\frac{\partial c_e^+}{\partial x}\right\|_{x=L} = 0 \\ D_{e,\text{eff}}^- \left.\frac{\partial c_e^-}{\partial x}\right\|_{x=L^-} = D_e^s \left.\frac{\partial c_e^s}{\partial x}\right\|_{x=L^-} \\ c_e^-\|_{x=L^-} = c_e^s\|_{x=L^-} \\ D_e^s \left.\frac{\partial c_e^s}{\partial x}\right\|_{x=L^{-s}} = D_{e,\text{eff}}^+ \left.\frac{\partial c_e^+}{\partial x}\right\|_{x=L^{-s}} \\ c_e^s\|_{x=L^{-s}} = c_e^+\|_{x=L^{-s}} \end{array} \right.$
Separator	$\frac{\partial c_e^s}{\partial t} = \frac{D_e^s}{\varepsilon_e^s}\frac{\partial^2 c_e^s}{\partial x^2}$,	
Positive electrode	$\frac{\partial c_e^+}{\partial t} = \frac{D_{e,\text{eff}}^+}{\varepsilon_e^+}\frac{\partial^2 c_e^+}{\partial x^2} + \frac{a_s^+(1-t_c^0)}{\varepsilon_e^+} j_n^+$	

where the spatio-temporal dependence (x,t) is not shown here for the sake of compactness, and $x \in [0, L]$ and $t \geq 0$. $D_{e,\text{eff}}$ is an effective coefficient that is a function of the electrolyte-phase diffusion coefficient D_e, and t_c^0 is the transference number. Notice that the in-domain equations and boundary conditions for each electrode domain are spanned in Table 4.1, while a general in-domain equation with terminal boundary conditions at $x = 0$ and $x = L$ are shown in Eq. (2.9) due to space limitations.

The approach proposed in [139] is leveraged here to analytically solve the electrolyte diffusion PDE of Table 4.1. The same uniform reaction rate assumption as in Eq. (4.4) for the pore-wall molar flux is used. Taking the Laplace transform of the negative electrode PDE in Table 4.1 with respect to the time variable, solving the resulting ODE and setting $x = 0$ (i.e. the current collector/negative electrode interface) yields the following electrolyte-phase impedance equation

$$\frac{C_e(s)}{I(s)} = \frac{N_c(s)}{D_c(s)} \tag{4.6}$$

where

$$\begin{aligned} N_c(s) \;=\; & -b^+\alpha^s\varepsilon_e^- D_e^s \sinh(\beta^+ L^+) \\ & + b^- \left(-\alpha^s\varepsilon_e^+ D_e^s \cosh(\beta^s L^s)\sinh(\beta^+ L^+)\right. \\ & - \alpha^+\varepsilon_e^s D_e^s \cosh(\beta^+ L^+)\sinh(\beta^s L^s) \\ & + \alpha^-\varepsilon_e^+ D_e^- \sinh(\beta^- L^-)\sinh(\beta^+ L^+)\sinh(\beta^s L^s) \\ & + \alpha^s\varepsilon_e^+ D_e^s \cosh(\beta^- L^-)\cosh(\beta^s L^s)\sinh(\beta^+ L^+) \\ & + \alpha^+\varepsilon_e^s D_e^s \cosh(\beta^- L^-)\cosh(\beta^+ L^+)\sinh(\beta^s L^s) \\ & \left. + \alpha^-\alpha^+\alpha^s D_e^- D_e^s \cosh(\beta^+ L^+)\cosh(\beta^s L^s)\sinh(\beta^- L^-)\right) \end{aligned} \tag{4.7}$$

$$\begin{aligned} D_c(s) \;=\; & \varepsilon_e^- s \left(\alpha^-\varepsilon_e^+ D_e^- \sinh(\beta^- L^-)\sinh(\beta^+ L^+)\sinh(\beta^s L^s)\right. \\ & + \alpha^+\varepsilon_e^s D_e^s \cosh(\beta^- L^-)\cosh(\beta^+ L^+)\sinh(\beta^s L^s) \\ & + \alpha^s\varepsilon_e^+ D_e^s \cosh(\beta^- L^-)\cosh(\beta^s L^s)\sinh(\beta^+ L^+) \\ & \left. + \alpha^-\alpha^+\alpha^s D_e^- D_e^s \cosh(\beta^+ L^+)\cosh(\beta^s L^s)\sinh(\beta^- L^-)\right) \end{aligned} \tag{4.8}$$

with $\beta^{\pm s} = \sqrt{\frac{\varepsilon_e^{\pm s} s}{D_e^{\pm s}}}$, $\alpha^{\pm s} = \sqrt{\frac{\varepsilon_e^{\pm s}}{D_e^{\pm s}}}$ and $b^{\pm} = \mp \frac{1-t_c^0}{FL^{\pm}A}$. $C_e(s)$ and $I(s)$ denote the Laplace transforms of $c_e(t)$ and $I(t)$ respectively, where $c_e(t) = c_e(x,t)|_{x=0}$ and s is the Laplace variable. The computation of the transfer function Eq. (4.6) following the line of [139] is exemplified in Appendix D.

Model-Order Reduction

The Padé expansion approximates functions as the quotient of two polynomials. Given the first $m+n+1$ terms of the Taylor series expansion $T(s)$ of a function $\frac{C(s)}{I(s)}$, two polynomials, one $P(s)$ of order m and one $Q(s)$ of order n can be obtained, such that $\frac{P(s)}{Q(s)}$ is the Padé approximation of order $[m/n]$. In contrast to the standard Padé approximation, here we first have to multiply by s, then compute the approximation and finally divide by s. This procedure is required because the expansion is about zero, where the functions $\frac{C(s)}{I(s)}$ are undefined [48]. Given that

$$sT(s) - s\frac{P(s)}{Q(s)} = 0$$

where $P(s) = p_0 + p_1 s + p_2 s^2 + \ldots + p_m s^m$ and $Q(s) = 1 + q_1 s + q_2 s^2 + \ldots + q_n s^n$, the polynomial coefficients are calculated by exploiting the Taylor's coefficients $a_i, i = 0, 1, \ldots, m+n$, such that

$$\begin{cases} a_0 = p_0 \\ a_1 + a_0 q_1 = p_1 \\ a_2 + a_1 q_1 + a_0 q_2 = p_2 \\ \vdots \\ a_m + a_{m-1} q_1 + \ldots + a_0 q_m = p_m \\ a_{m+1} + a_m q_1 + a_{m-1} q_2 + \ldots + a_{m-n+1} q_m = 0 \\ \vdots \\ a_{m+n} + a_{m+n-1} q_1 + \ldots + a_n q_m = 0. \end{cases} \tag{4.9}$$

The resulting transfer function $G_{\text{Pade}}(s)$ corresponds to

$$G_{\text{Pade}}(s) = p_0 \frac{P'(s)}{Q(s)} = \frac{p_0}{s} \frac{1 + p_1' s + p_2' s^2 + \ldots + p_m' s^m}{1 + q_1 s + q_2 s^2 + \ldots + q_n s^n} \tag{4.10}$$

where p_0 was taken as a common factor and thus $P'(s) = P(s)/p_0$. To be able to design a Kalman filter, which will be needed subsequently in Sections 5.1 and 5.3, a state-space representation is required. One way to go is to take the controllable canonical form of the transfer function $G_{\text{Pade}}(s)$ [48]. However, the state vector lacks physical meaning in such a representation, and therefore a linear transformation is required to recover the physics of the problem. One option to enforce a physics-based state vector is to resort to a different parameterization. Here, we opted for the

following n-tanks equivalent-hydraulic model (EHM)[3]

$$\begin{bmatrix}\beta_1\dot{q}_1\\ \beta_2\dot{q}_2\\ \beta_3\dot{q}_3\\ \vdots\\ \beta_n\dot{q}_n\end{bmatrix}=\begin{bmatrix}-g_{12} & g_{12} & 0 & \cdots & 0 & 0\\ g_{12} & -(g_{12}+g_{23}) & g_{23} & 0 & \cdots & 0\\ 0 & g_{23} & -(g_{23}+g_{34}) & g_{34} & \cdots & 0\\ \vdots & & & & & \\ 0 & \cdots & 0 & g_{n-2,n-1} & -(g_{n-2,n-1}+g_{n-1,n}) & g_{n-1,n}\\ 0 & 0 & \cdots & 0 & g_{n-1,n} & -g_{n-1,n}\end{bmatrix}\begin{bmatrix}q_1\\ q_2\\ q_3\\ \vdots\\ q_n\end{bmatrix}+[0\ 0\ 0\ \cdots\ 0\ \zeta_0]^{\mathrm{T}}u \tag{4.11}$$

which is depicted in Fig. 4.1.

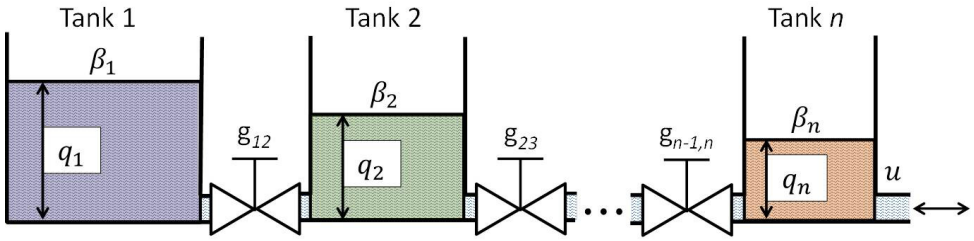

FIGURE 4.1: Equivalent-hydraulic model consisting of n tanks, where u, q_i, $g_{i,i+1}$ and β_i, $i = 1, \ldots, n$, are respectively the input current, tank level state, valve coefficient and tank cross-section area for a given number of tanks n.

The physical equivalence between batteries and tanks builds on the idea that the transportation phenomena taking place within an electrode spherical particle (see e.g. Fig. 4.2 below) or throughout the electrolyte solution can be represented as the mass flow among tanks with levels q_i, tank cross-section areas β_i and valve coefficients $g_{i,i+1}$ with $i = 1, \ldots, n$. The tank levels may be translated into relevant electrochemical states, such as the total lithium concentration state $c_{\text{bulk}} = \sum_{i=1}^{n} \beta_i q_i$ and the concentration state just adjacent to a lithium source (input) $c_{\text{surf}} = q_n$. The remaining tanks can be associated to successive layer concentrations within the bulk of the phases, e.g. $c_i = q_i, i = 2, \ldots, n-1$. Considering this change of variables, the new state vector is given by

$$x(t) = [c_{\text{bulk}}(t), c_2(t), \ldots, c_{n-1}(t), c_{\text{surf}}(t)]^{\mathrm{T}}, \tag{4.12}$$

[3]For compactness of notation the time argument (t) in $q(t)$ and $u(t)$ is dropped in the EHM state-space representation.

with the state-space model taking the form

$$\begin{bmatrix} \dot{c}_{\text{bulk}} \\ \dot{c}_2 \\ \dot{c}_3 \\ \vdots \\ \dot{c}_{\text{surf}} \end{bmatrix} = \begin{bmatrix} 0 & 0 & 0 & \cdots & 0 & 0 \\ \frac{g_{12}}{\beta_1\beta_2} - \left(\frac{g_{12}}{\beta_1} + \frac{g_{12}+g_{23}}{\beta_2}\right) & \frac{g_{23}}{\beta_2} & -\frac{g_{12}\beta_3}{\beta_1\beta_2} & -\frac{g_{12}\beta_4}{\beta_1\beta_2} & \cdots & -\frac{g_{12}\beta_n}{\beta_1\beta_2} \\ 0 & \frac{g_{23}}{\beta_3} & -\frac{(g_{23}+g_{34})}{\beta_3} & \frac{g_{34}}{\beta_3} & \cdots & 0 \\ \vdots & & & & & \\ 0 & \cdots & 0 & \frac{g_{n-2,n-1}}{\beta_{n-1}} & -\frac{g_{n-2,n-1}+g_{n-1,n}}{\beta_{n-1}} & \frac{g_{n-1,n}}{\beta_{n-1}} \\ 0 & 0 & \cdots & 0 & \frac{g_{n-1,n}}{\beta_n} & -\frac{g_{n-1,n}}{\beta_n} \end{bmatrix} \begin{bmatrix} c_{\text{bulk}} \\ c_2 \\ c_3 \\ \vdots \\ c_{\text{surf}} \end{bmatrix} \tag{4.13}$$

$$+ [\zeta_0 \ 0 \ 0 \ \cdots \ 0 \ \zeta_0/\beta_n]^{\mathrm{T}} u$$

$$y = [0 \ 0 \ \cdots \ 1] \, [c_{\text{bulk}}, c_2, c_3, \cdots, c_{\text{surf}}]^{\mathrm{T}}. \tag{4.14}$$

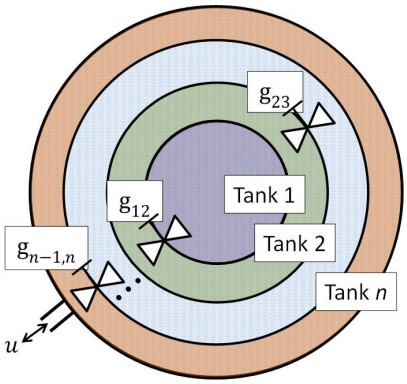

FIGURE 4.2: Equivalent-hydraulic model representing the spherical particle with n sections, where u and $g_{i,i+1}$ represent the input current and valve coefficient, respectively.

It can be transformed into the transfer function $G_{\text{EHM}}(s)$ through

$$G_{\text{EHM}}(s) = C_0(sI - A_0)^{-1}B_0 = \frac{\Pi(s)}{\Sigma(s)} = \zeta_0 \frac{\pi_0 + \pi_1 s + \pi_2 s^2 + \cdots + \pi_m s^m}{s\left(\sigma_0 + \sigma_1 s + \sigma_2 s^2 + \cdots + \sigma_n s^n\right)},$$

where $A_0 \in \mathbb{R}^{n\times n}$, $B_0 \in \mathbb{R}^{n\times 1}$ and $C_0 \in \mathbb{R}^{1\times n}$ are the state, input and output matrices, respectively. It turns out that $\pi_0 = \sigma_0$, and therefore $G_{\text{EHM}}(s)$ can be rewritten:

$$G'_{\text{EHM}}(s) = \frac{\Pi'(s)}{\Sigma'(s)} = \zeta_0 \frac{1 + \pi'_1 s + \pi'_2 s^2 + \cdots + \pi'_m s^m}{s\left(1 + \sigma'_1 s + \sigma'_2 s^2 + \cdots + \sigma'_n s^n\right)} \tag{4.15}$$

where $\Pi'(s) = \Pi(s)/\pi_0$ and $\Sigma'(s) = \Sigma(s)/\pi_0$. To obtain the EHM parameters, namely β_i, $g_{i,i+1}$ with $i = 1, \ldots, n$ and ζ_0, it is just a matter of equating the coefficients of $G_{\text{Pade}}(s)$ with the ones of $G'_{\text{EHM}}(s)$ and solving the following system of equations

$$\begin{cases} p_0 = \zeta_0 & \\ p'_1 = \pi'_1, & q'_1 = \sigma'_1 \\ \vdots & \vdots \\ p'_m = \pi'_m, & q'_m = \sigma'_m. \end{cases} \tag{4.16}$$

After completing this procedure, it was found that the EHM parameter $g_{i,i+1}$

relates to the lithium diffusion parameters through $g_{i,i+1} = \gamma_i \frac{D_s}{R_s^2}$ for the solid and $g_{i,i+1} = \delta_i D_e$ for the electrolyte-phase diffusion, where γ_i, δ_i and β_i are constants that depend on the system order.

The state-space representation of the EHM then takes the general form

$$\dot{x}_j(t) = A_j x_j(t) + B_j u(t) \tag{4.17}$$

where $j \in \{s, e\}$ for solid and electrolyte phases, respectively. The solid-phase diffusion state vector $x_s(t) \in \mathbb{R}^{n_s}$ is defined as

$$x_s(t) = [\mathrm{SOC}(t), c_{s,2}(t), \ldots, c_{s,n-1}(t), \mathrm{CSC}(t)]^{\mathrm{T}},$$

where $c_{\mathrm{bulk}}(t)$ and $c_{\mathrm{surf}}(t)$ of Eq. (4.12) were substituted by the state-of-charge $\mathrm{SOC}(t) = c_{\mathrm{bulk}}(t)$ and the critical-surface-concentration $\mathrm{CSC}(t) = c_{\mathrm{surf}}(t)/c_{s,\max}$, since these state variables are particularly relevant for a battery cell. The SOC reflects the amount of battery energy that is available at a given time instant, while the CSC directly impacts the battery voltage and therefore provides a measure of the battery power.

Remark 4.2.2. *Notice that the solid-phase diffusion variables $\bar{c}_s(x,t)$ and $c_{ss}(x,t)$ for the average and surface lithium concentration, respectively, of the DFN model in Eq.* (2.7) *map into the current reduced-order model framework for solid-phase diffusion as* $\mathrm{SOC}(t) = \bar{c}_s(t)/c_{s,\max}$ *and* $\mathrm{CSC}(t) = c_{ss}(t)/c_{s,\max}$ *without the x-spatial dependence as in the SPM. This relationship between both models comes handy when translating constraints, as it becomes apparent below.*

The electrolyte-phase diffusion state vector $x_e(t) \in \mathbb{R}^{n_e}$ is defined as

$$x_e(t) = [c_{eb}(t), c_{e,2}(t), \ldots, c_{e,n-1}(t), c_{es}(t)]^{\mathrm{T}},$$

where $c_{\mathrm{bulk}}(t)$ and $c_{\mathrm{surf}}(t)$ of Eq. (4.12) were replaced by $c_{eb}(t)$ and $c_{es}(t)$ for notational compactness, with each of them having a similar interpretation as SOC and CSC for the electrolyte phase, respectively. The input is the current applied to the battery $u(t) = I(t)$.

The state and input matrices, A_j and B_j respectively, are shown in Table 4.2 for different system orders. Increasing the model dimension (i.e. the order of the Padé approximation and the number of tanks) increases the model accuracy towards higher frequencies, which is evidenced in Fig. 4.3.

TABLE 4.2: State A_j and input B_j matrices for the diffusion equation of different orders, where $j \in \{s, e\}$ for solid and electrolyte phases, respectively.

Order	State Matrix A_j	Input Matrix B_j	
1st	0	ζ_0	(4.18)
2nd	$\begin{bmatrix} 0 & 0 \\ g\frac{\gamma}{\beta_1\beta_2} & -g\frac{\gamma}{\beta_1\beta_2} \end{bmatrix}$	$\zeta_0 \begin{bmatrix} 1 \\ \frac{1}{\beta_2} \end{bmatrix}$	(4.19)
3rd	$\begin{bmatrix} 0 & 0 & 0 \\ g\frac{\gamma_1}{\beta_1\beta_2} & -g\left(\frac{\gamma_1}{\beta_1} + \frac{\gamma_1+\gamma_2}{\beta_2}\right) & g\left(\frac{\gamma_2}{\beta_2} - \frac{\beta_3\gamma_1}{\beta_1\beta_2}\right) \\ 0 & g\frac{\gamma_2}{\beta_3} & -g\frac{\gamma_2}{\beta_3} \end{bmatrix}$	$\zeta_0 \begin{bmatrix} 1 \\ 0 \\ \frac{1}{\beta_3} \end{bmatrix}$	(4.20)

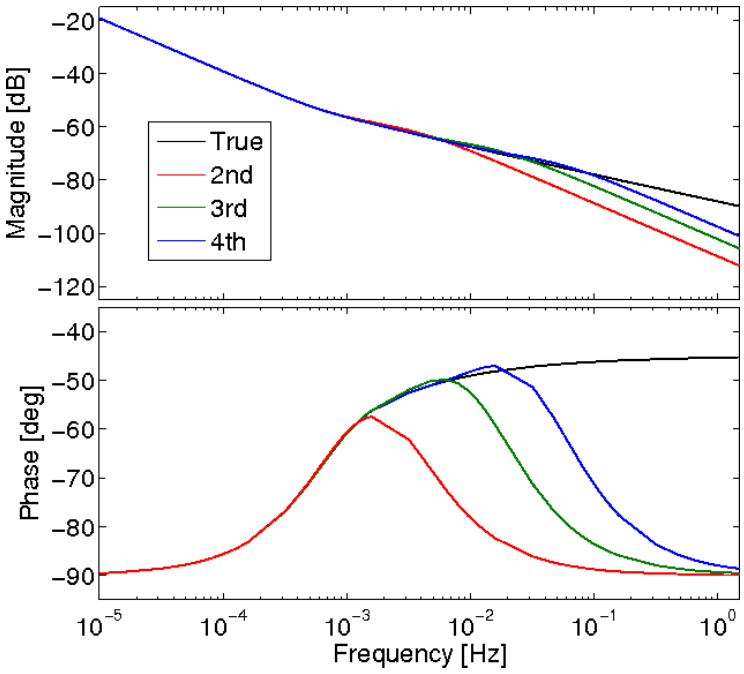

FIGURE 4.3: Bode plots of the irrational transfer function Eq. (4.5) in black, and from the 2nd to the 3rd-order Padé approximations of Eq. (4.17) and Table 4.2 in red, green and blue respectively.

Material Balance

Although the state estimation and control of the solid-phase lithium concentration in each electrode domain independently would be ideal to track electrode aging and handle it properly, this cannot be achieved with currently available sensors. It turns out that the entire state vector comprising positive and negative electrode concentrations is weakly observable from voltage measurements [44]. One way to tackle this issue is to simplify further the model by considering a single electrode while accounting for the counter electrode through material conservation [77]. The electrode with the limiting diffusion process (i.e. the one with slower dynamics), which is usually the negative electrode, is the one that is chosen. Moreover, the most popular negative electrodes are graphite-based, which are known to limit long term battery performance due to aging. This aspect further motivates its careful monitoring and control. Finally, given the fast dynamics of the positive electrode with respect to the negative, the solid-phase diffusion process taking place in the former can be seen as instantaneous. Therefore, the resulting approximation of the positive electrode dynamics is given by the following conditions

$$\begin{aligned} \mathrm{CSC}^{+}(t) &= \mathrm{SOC}^{+}(t) \\ \mathrm{SOC}^{+}(t) &= \rho_s \mathrm{SOC}(t) + \sigma_s. \end{aligned} \tag{4.21}$$

In line with the reference electrode for solid-phase diffusion, the negative electrode is also chosen to evaluate the electrolyte diffusion model. More specifically, the current collector/electrode boundary $x = 0$ is the selected location, since it corresponds to one of the voltage terminals. Similarly as with the solid-phase, the electrolyte concentration at the positive battery terminal is also obtained from material balance. However, the instantaneous diffusion assumption for the solid-phase concentration

does not hold for the electrolyte. Therefore, a direct link is drawn between the electrolyte surface concentrations of both electrode domains through material balance as:

$$c_{es}^{+}(t) = \rho_e c_{es}(t) + \sigma_e. \tag{4.22}$$

In both Eqs. (4.21) and (4.22), the states of the positive electrode are denoted by $\text{SOC}^{+}(t)$, $\text{CSC}^{+}(t)$ and $c_{es}^{+}(t)$, whereas $\text{SOC}(t)$, $\text{CSC}(t)$ and $c_{es}(t)$ are the states of the negative one obtained by dropping the superscript "$-$" for notational convenience. Parameters ρ_j and σ_j, with $j \in \{s, e\}$ for respectively solid and electrolyte phases, are constants given in Table 4.3, Eqs. (4.23),(4.24).

TABLE 4.3: Functions associated to the material balance and output equations.

Var	Function Eq.		Eq. involved
ρ_s, σ_s	$\rho_s = -\dfrac{c_{s,\max}^{-} R_s^{-} L^{-} a_s^{-}}{c_{s,\max}^{+} R_s^{+} L^{+} a_s^{+}}, \sigma_s = \dfrac{3 n_{s,0}^{Li}}{c_{s,\max}^{+} R_s^{+} L^{+} a_s^{+}}$	(4.23)	(4.21)
ρ_e, σ_e	$\rho_e = -\dfrac{\varepsilon_e^{-} L^{-}}{\varepsilon_e^{+} L^{+}}, \sigma_e = -\dfrac{\varepsilon_e^{s} L^{s}}{\varepsilon_e^{+} L^{+}} c_{e,0} + \dfrac{n_e^{Li}}{\varepsilon_e^{+} L^{+} A}$	(4.24)	(4.22)
$\eta_s^{+}(t)$	$\dfrac{R_g T_{bc}(t)}{\alpha_0 F} \sinh^{-1}\left(\dfrac{-1}{2 a_s^{+} L^{+} i_0^{+}} u(t)\right)$	(4.25)	(4.35)
$\eta_s^{-}(t)$	$\dfrac{R_g T_{bc}(t)}{\alpha_0 F} \sinh^{-1}\left(\dfrac{1}{2 a_s^{-} L^{-} i_0^{-}} u(t)\right)$	(4.26)	(4.35)
$i_0^{\pm}(t)$	$k_n^{\pm} c_{s,\max}^{\pm} \sqrt{c_e^{\pm}(t) \text{CSC}^{\pm}(t) \left(1 - \text{CSC}^{\pm}(t)\right)}$	(4.27)	(4.35)

[a] Φ could be D_s, D_e, k_n, κ or j_{sr}. [b] Taken from [26].

4.2.2 Thermal Equation

The thermal process described by Eqs. (2.18), (2.19) has a distributed nature due to the integral term in Eqs. (2.18). However, under the assumption of uniform pore-wall molar flux given by Eq. (4.4), the core temperature Eq. (2.18) [30] together with the same Eq. (2.19) are given by

$$\rho_c C_{pc} \frac{dT_{bc}}{dt}(t) = k_c \left(T_{bs}(t) - T_{bc}(t)\right) - I(t)\left(\Delta U_b^{\pm}(t) - T_{bc}(t) \Delta \frac{\partial U_b^{\pm}}{\partial T_{bc}}(t) - V(t)\right) \tag{4.28}$$

$$\rho_s C_{ps} \frac{dT_{bs}}{dt}(t) = k_c \left(T_{bc}(t) - T_{bs}(t)\right) + h_c \left(T_{\text{amb}} - T_{bs}(t)\right) \tag{4.29}$$

Thermal parameters h_c and k_c are convection and conduction coefficients, respectively, ρ_j and C_{pj}, $j \in \{c, s\}$ are the density and specific heat of core and surface variables respectively, and T_{amb} is the ambient temperature considered as constant. The difference between functions $\chi^{+}(t)$ and $\chi^{-}(t)$ for any function $\chi(t)$ is denoted as $\Delta\chi^{\pm}(t)$, while functions $U_b^{\pm}(\text{SOC}(t))$ and $\frac{\partial U_b^{\pm}}{\partial T_{bc}}(\text{SOC}(t))$ depend on the battery chemistry. Note that in Eq. (4.28) the explicit dependence of $U_b^{\pm}$ on SOC is not indicated for the sake of compactness. The general form of the thermal model is given by

$$\dot{x}_T(t) = A_T x_T(t) + f_T\left(u(t), x_T(t), \text{SOC}(t), V(t)\right) \tag{4.30}$$

where $x_T(t) \in \mathbb{R}^2$ is the temperature state vector given by $x_T(t) = [T_{bc}(t), T_{bs}(t)]^{\mathrm{T}}$ with T_{bc} and T_{bs} as the battery core and skin temperature, respectively, and the matrix and nonlinear function are given by

$$A_T = \begin{bmatrix} -\frac{k_c}{\rho_c C_{pc}} & \frac{k_c}{\rho_c C_{pc}} \\ \frac{k_c}{\rho_s C_{ps}} & -\frac{h_c + k_c}{\rho_s C_{ps}} \end{bmatrix}, \; f_T = \begin{bmatrix} \frac{1}{\rho_c C_{pc}} \left(\Delta U_b^{\pm}(t) - \Delta \frac{\partial U_b^{\pm}}{\partial T_{bc}}(t) T_{bc}(t) - V(t) \right) I(t) \\ \frac{1}{\rho_s C_{ps}} h_c T_{\mathrm{amb}} \end{bmatrix}. \tag{4.31}$$

4.2.3 State Space Model Summary

The representation of the state space model takes the form

$$\dot{x}(t) = A(x(t))x(t) + B_u u(t) + f_x(u(t), x(t), y(t)) \tag{4.32}$$

where $x(t) \in \mathbb{R}^n$ with $n = n_s + n_e + 2$ is the differential state vector defined as

$$x(t) = \left[x_s(t)^{\mathrm{T}}, x_e(t)^{\mathrm{T}}, x_T(t)^{\mathrm{T}} \right]^{\mathrm{T}},$$

$u(k) \in \mathbb{R}$ is the input vector $u(t) = I(t)$ and $y(t) \in \mathbb{R}^2$ is the output vector $y(t) = [V(t), T_{bs}(t)]^{\mathrm{T}}$. The matrices and functions of the state equation are given by

$$\begin{aligned} A(x(t)) &= \mathrm{diag}\left(A_s(x(t)), A_e(x(t)), A_T\right) \\ B_u &= [B_s^{\mathrm{T}}, B_e^{\mathrm{T}}, 0_{1\times 2}]^{\mathrm{T}} \\ f_x(u(t), x(t), y(t)) &= [0_{1\times(n_s+n_e)}, f_T^{\mathrm{T}}(u(t), x(t), y(t))]^{\mathrm{T}}. \end{aligned} \tag{4.33}$$

By abuse of notation, function f_T introduced in Eq. (4.30) is considered here only with three arguments as $x(t)$ includes $x_s(t)$ and $\mathrm{SOC}(t)$.

4.2.4 Output Equation

The internal states of a battery cell, namely the solid and electrolyte-phase concentrations along with the core temperature, cannot be directly measured using standard sensors available in daily life applications. Only voltage and surface temperature can be measured. The former is linked to the state vector via a nonlinear transformation.

The voltage of a battery cell is the electric potential difference between the positive and negative battery terminals given by Eq. (2.17) in Table 2.1. Solving Eq. (2.14) for $\phi_s^{\pm}$ and subtracting the negative potential from the positive potential results in

$$\begin{aligned} V(t) = &\left(U_s^+(x,t) + \eta_s^+(x,t) + \phi_e^+(x,t) + R_f^+ F j_n^+(x,t) \right) |_{x=L} \\ &- \left(U_s^-(x,t) + \eta_s^-(x,t) + \phi_e^-(x,t) + R_f^- F j_n^-(x,t) \right) |_{x=0} \end{aligned} \tag{4.34}$$

Assuming a uniform reaction rate along the battery thickness (as expressed by Eq. (4.4)), the spatial dependency of each variable can be neglected. Moreover, usually the negative electrode exhibits a thicker film surrounding the electrode and a larger associated resistance than that of the positive electrode, so that $R_f^+ \approx 0\ \Omega.\mathrm{m}^2$ and the superscript "-" can be dropped from R_f^-. The voltage output equation then takes the form

$$V(t) = \Delta U_s^{\pm}(t) + \Delta \eta_s^{\pm}(t) + \Delta \phi_e(t) - \frac{R_f}{a_s L} I(t) \tag{4.35}$$

which is a spatially independent and rearranged version of Eq. (4.34). The surface equilibrium potential functions $U_s^{\pm}(\mathrm{SOC(t)}, \mathrm{CSC(t)})$ depend on the battery chemistry,

while the surface overpotential functions $\eta_s^{\pm}(u(t), \mathrm{CSC}(t))$ are given in Table 4.3, Eqs. (4.25),(4.26). To obtain the electrolyte phase potential drop $\Delta\phi_e(u(t), c_e(t))$, the electrolyte potential Eq. (2.10) is simplified by three means: the electrolyte-phase ionic conductivity $\kappa_{e,\mathrm{eff}}$ is considered spatially constant [140, 141], the activity coefficient $f_{c/a}$ is assumed equal to 1 [138, 142], and the equation is linearized about the initial electrolyte concentration $c_{e,0}$ [143, 141]. Both the first and third approximations simplify the integration of the electric potential, just as the assumption of a constant electrolyte-phase diffusion coefficient eases the handling of the electrolyte-phase PDE. The second approximation is made due to the absence of experimental data [21, 142]. The resulting electrolyte phase potential is given by

$$\kappa_{e,\mathrm{eff}} \frac{\partial^2 \phi_e}{\partial x^2}(x,t) = -a_s F j_n(x,t) + \frac{2R_g T_{bc}(t)}{F c_{e,0}}(1 - t_c^0)\kappa_{e,\mathrm{eff}} \frac{\partial^2 c_e}{\partial x^2}(x,t). \tag{4.36}$$

Since the battery cell voltage response results from the potential difference between battery terminals, ϕ_e can be set to zero at $x = 0$ and only potential differences might be considered. Defining the electrolyte potential difference along the cell thickness as $\Delta\phi_e(t) = \phi_e^+(L,t) - \phi_e^-(0,t)$ and integrating directly Eq. (4.36), the following expression arises

$$\Delta\phi_e(t) = \frac{2R_g T_{bc}(t)}{F c_{e,0}}(1 - t_c^0)(c_{es}^+(t) - c_{es}(t)) - \frac{1}{\kappa_{e,\mathrm{eff}}}\left(\frac{L^+}{2(\varepsilon_e^+)^\epsilon} + \frac{L^s}{(\varepsilon_e^s)^\epsilon} + \frac{L^-}{2(\varepsilon_e^-)^\epsilon}\right) I(t) \tag{4.37}$$

where the assumption of uniform utilization has been used [140, 141].

The general form of the output voltage equation is given by

$$y_n(t) = h_n\left(u(t), x(t)\right) \tag{4.38}$$

where $y_n(t) \in \mathbb{R}$ with $y_n(t) = V(t)$, the subscript n stands for the main intercalation reaction, the input $u(t) = I(t)$, the state vector $x(t) = \left[x_s(t)^{\mathrm{T}}, x_e(t)^{\mathrm{T}}, x_T(t)^{\mathrm{T}}\right]^{\mathrm{T}}$ and the nonlinear function is

$$h_n\left(u(t), x(t)\right) = \Delta U_s^{\pm}(t) + \Delta\eta_s^{\pm}(t) + \Delta\phi_e(t) - \frac{R_f}{a_s L}u(t). \tag{4.39}$$

The general form of the output equation, i.e. where the surface temperature is accounted for, is then given by

$$y(t) = h_y\left(u(t), x(t)\right) \tag{4.40}$$

where $y(t) \in \mathbb{R}^2$ with $y(t) = [V(t), T_{bs}(t)]^{\mathrm{T}}$, and the associated nonlinear output function is given by

$$h_y\left(u(t), x(t)\right) = \left[h_n\left(u(t), x(t)\right),\ [0, 0, \ldots, 0, 1]x(t)\right]^{\mathrm{T}}. \tag{4.41}$$

4.2.5 Analysis of Aging

So far, no degradation mechanisms have been considered when deriving the diffusion, thermal and output equations in Sections 4.2.1-4.2.4. However, the model presented above has to be upgraded with parameter and equation dependencies in order to account for aging dynamics. These captured aging phenomena can be then used for SOH monitoring or to define unsafe regions that should be avoided during battery operation. We consider the degradation processes described in Section 2.2,

whereas the distributed nature of model equations and constraints in Section 2.3 for the DFN model is simplified in the present section. As we always want a physical interpretation of the model we are developing, we need first to understand aging before introducing the required model modifications.

Two different sources of battery degradation have been identified from the literature and are the subject of our studies. The first one is temporal-induced degradation or calendar aging, while the second one corresponds to operation-induced degradation associated to side reactions, either SEI growth or lithium plating. Depending on the nature of the side reaction, the degradation can be mitigated in more or less extent. An advanced battery-management system (BMS) should ideally be able to process the information about degradation and act accordingly. The present situation of a BMS is shown in Fig. 4.4, together with the role of an advanced BMS. Fig. 4.4(a) depicts an operating map built from measured variables, namely applied current and terminal voltage, while Fig. 4.4(b) portrays a similar map but based on unmeasurable electrochemical variables like solid-phase surface concentration and overpotential. Nowadays, a BMS imposes current and voltage restrictions that delimit an operating region given by the purple rectangle in the Fig. 4.4(a). Such region defines e.g. the purple polygon in Fig. 4.4(b), but it is conservative if compared with the safe region that results when the electrochemistry behind the degradation mechanisms is accounted for. This safe region is represented by the green rectangle in Fig. 4.4(b), which has a counterpart region in Fig. 4.4(a). The red region in both plots represents unsafe scenarios where battery degradation takes place. Notice how the advanced BMS enlarges the operating range of the present BMS by imposing electrochemical constraints directly linked to degradation mechanisms. However, other degradation mechanisms cannot be circumvented regardless the battery operation, which is depicted in Fig. 4.4(a) and (b) by the orange region overlapping the green region of safe operation. In such situations, degradation cannot be mitigated but its influence in the battery operation can be properly tracked. The fact of having different types of degradation motivates the BMS to possess different ways to handle them accordingly, namely to steer the system state to keep it inside the safe region while tracking unavoidable degradation.

In the following, the two referred types of degradation are considered. First, the unavoidable degradation mechanisms are detailed and an aging model is developed in order to track them. Secondly, the (possibly) mitigable degradation mechanisms are explained and electrochemical constraints meant to be avoided are derived.

Aging Model

This subsection presents the required model modifications so that an aging model consistent with the thermal and electrolyte enhanced EHM is obtained. This model aims at tracking battery aging caused by degradation mechanisms that cannot be avoided by no means. Whether the battery is used in a very conservative fashion or even not in use at all, the battery ages due to e.g. calendar aging and parasitic side reactions. Two sources of battery degradation are considered. First, purely temporal-induced degradation is accounted for via time-varying parameters, namely the diffusion coefficient $D_{s,\mathrm{ref}}$ and the film resistance R_f. These parameters are collected in the parameter vector $\theta(t) \in \mathbb{R}^2$ defined as

$$\theta(t) = [\theta_1(t), \theta_2(t)]^{\mathrm{T}},$$

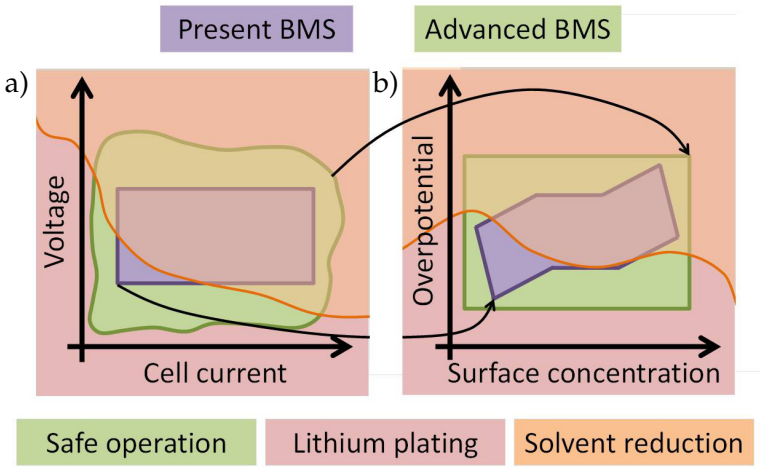

FIGURE 4.4: Present situation of a BMS (purple region) together with the ideal situation of an advanced BMS (green region) in terms of the operational envelope defined by the accounted constraints. The operating map is derived from a) measured variables and b) electrochemical variables. Safe operation region, region where lithium plating takes place and region where solvent reduction reaction occurs are represented by green, red and orange regions, respectively.

and their evolution is described by the empirical expressions given in Eqs. (4.1) and (4.2).

The second degradation source corresponds to the side reaction associated to SEI growth (orange area in Fig. 4.4). This mechanism is a mixture of temporal and operation-induced aging, i.e. the battery always degrades, but it does it faster as the power demand becomes larger. The fact that the battery degrades even with zero current will become clearer with the study of the system equilibrium points detailed below. It turns out that the SEI growth is a degradation mechanism that is difficult to mitigate for a "reasonable" use of the battery. The term "reasonable" is explained next with the help of Fig. 4.5. In the figure, the battery voltage is represented by the solid red curve associated to the right y-axis, whereas negative electrode potentials such as surface overpotential plus equilibrium potential $\eta_s^- + U_s^-$ and equilibrium U_s^-, SEI growth U_{SEI}^- and lithium plating U_{lp}^- potentials are respectively depicted by dashed and solid blue and dotted and dashed black curves associated to the left y-axis. Let us consider, for instance, a standard operating voltage window provided by battery manufacturers, i.e. from 2.5 V to 4.2 V, where the lower and upper cut-off voltage implies 0% and 100% SOC respectively. Side reactions such as SEI growth take place when the negative electrode potential $U_s^- + \eta_s^-$ drops below $U_{\text{SEI}} = 0.4$ V, which may occur when the battery SOC reaches 20% or the voltage V rises above 3.5 V (see Fig. 4.5). These limits can be even tighter depending on the chemistry and manufacturing process. This means that for mitigating the impact of SEI growth, the battery should be operated between 2.5 V and 3.5 V, which could translate in 0% and 20% SOC (recall that the mapping SOC $\mapsto V$ is not linear). This usage strategy could potentially increase battery life, but at the expense of imposing operating limits that are overly conservative. Imagine for example that you need to charge your phone every 30 min, assuming an average rate of discharge of C/2. This is not a "reasonable" use of the battery, which we then define as the battery operating window that offers the maximum autonomy to a given application, i.e. the maximum time without needing

to plug the battery in for recharging.

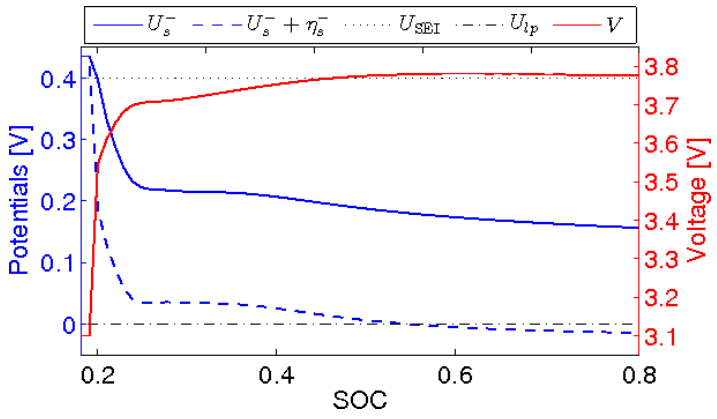

FIGURE 4.5: Galvanostatic charge of a graphite | LCO battery cell at 5C. The left y-axis portrays the different negative electrode potential contributions to the battery voltage, as well as the side reaction potentials. The right y-axis shows the battery voltage.

The principle behind side reactions is the following. When side reactions occur, not all the input current $I(t)$ contributes to the main intercalation reaction $j_n(t)$, and therefore Eq. (4.4) is not valid anymore. Instead, the current balance Eq. (2.21) has to be considered such that

$$j_n(t) + j_{\text{SEI}}(t) \approx \frac{1}{Fa_sL} I(t) \tag{4.42}$$

under the assumption of uniform reaction rate and considering SEI growth as the only side reaction (in accordance with Section 4.1). Eq. (4.42) can be written in a general form as

$$z(t) + d(t) = u(t) \tag{4.43}$$

where $u(t) = I(t)$ is the battery applied current, $z(t) = Fa_sLj_n(t)$ is the main reaction current and $d(t) = Fa_sLj_{\text{SEI}}(t)$ is the side reaction current. Both the main intercalation reaction and side reaction compete to take away a part of the current applied to the battery. The ratio of this current split is determined by the electric potential of each reaction. Let us define the voltage drop due to SEI growth with the nonlinear function

$$h_{\text{SEI}}\left(u(t), d(t), x(t)\right) = \Delta U_{\text{SEI}}(t) + \Delta\eta_{\text{SEI}}(t) + \Delta\phi_e(t) - \frac{R_f}{a_sL} u(t) \tag{4.44}$$

where the difference between functions $\chi^+(t)$ and $\chi_{\text{SEI}}(t)$ for any function $\chi(t)$ is denoted as $\Delta\chi_{\text{SEI}}(t)$, whereas U_{SEI} is a scalar that represents the equilibrium potential of the side reaction and $\eta_{\text{SEI}}(t)$ is the overpotential of the side reaction given by

$$\eta_{\text{SEI}}(t) = -\frac{R_g T_{bc}(t)}{\alpha_0 F} \ln\left(\frac{-1}{a_sLi_{\text{SEI},0}} d(t)\right). \tag{4.45}$$

Then Kirchhoff's law states the following relationship between electric potentials

$$h_n\left(z(t), x(t)\right) - h_{\text{SEI}}\left(u(t), d(t), x(t)\right) = 0 \tag{4.46}$$

where $h_n(z(t), x(t))$ is given by Eq. (4.39) with $z(t)$ replacing $u(t)$. Notice that Eq. (4.46) is a nonlinear algebraic constraint, whose algebraic state variable corresponds

to $z(t)$ (or $d(t)$ through Eq. (4.43)). This nonlinear model structure precludes the possibility of finding an explicit solution for either variable.

The distributed nature of the capacity loss Eq. (2.25) given by its integral term can be disregarded through the uniform reaction rate assumption. The capacity loss is then given by

$$\frac{dQ_{\text{loss}}}{dt}(t) = -\frac{Fa_sAL}{3600} j_{\text{SEI}}(t) \tag{4.47}$$

or in general form as

$$\dot{x}_Q(t) = A_Q x_Q(t) + B_Q d(t) \tag{4.48}$$

Since some amount of lithium is lost with time, the material balance of Eq. (4.21) has to be corrected. The initial amount of lithium in the solid phase $n_{s,0}^{Li}$ encoded in the parameter σ_s can be updated through

$$\sigma_s(t) = \frac{3}{c_{s,\max}^{+} R_s^{+} L^{+} a_s^{+}} \left(n_{s,0}^{Li} - \frac{3600}{F} Q_{\text{loss}}(t) \right).$$

Electrochemical Constraints

In contrast to the previous subsection where unavoidable degradation mechanisms are displayed, this subsection focuses on other degradation mechanisms that take place just outside the boundaries of "reasonable" operating windows (red area in Fig. 4.4). Compare, for instance, the negative electrode potential $U_s^- + \eta_s^-$ with SEI growth potential $U_{\text{SEI}} = 0.4$ V and lithium plating potential $U_{lp} = 0.0$ V. The growth of SEI layer and lithium plating happen when the negative electrode potential drops below the respective side reaction constant potential. While SEI growth occurs very early in the charging process (i.e. $U_s^- + \eta_s^- \leq U_{\text{SEI}}$), lithium platting takes place half way the charging process (i.e. $U_s^- + \eta_s^- \leq U_{lp}$) as shown in Fig. 4.5. Furthermore, although a steady-state battery[4] avoids these unsafe regions thanks to such operating conditions, nothing precludes a battery under dynamic operation to overstep these limits and to fall into possibly degrading operating modes. This issue becomes apparent in Fig. 4.5, where the battery at equilibrium is represented by the open-circuit potential U_s^-, the battery dynamic operation involves the additional effect of the surface overpotential η_s^- and the lithium plating potential is denoted by U_{lp}. Notice the positive gap between the negative electrode potential $U_s^- + \eta_s^-$ and the lithium plating potential U_{lp} at the beginning of the charge (before 0.5 SOC), but how this potential drops below the threshold at the end of the considered time horizon (after 0.5 SOC). Moreover, safe operating regions tend to shrink as the battery ages, which further promotes a faster battery degradation. These are the regions that we are interested in so that we can impose hard constraints and track their evolution to guarantee the battery safe operation.

Since the variables of the EHM have an explicit link with the ones of the DFN model as highlighted in Remark 4.2.2, it is possible to map constraints Eq. (2.32) into

[4] A battery is at equilibrium when the applied current is zero for a long enough period of time.

the following constraints for the EHM

$$\begin{cases} 0 \leq \mathrm{SOC}(t) \leq \bar{r}_{c_s}, & \text{(4.49a)} \\ 0 \leq \mathrm{CSC}(t) \leq \bar{r}_{c_s} & \text{(4.49b)} \\ \eta_{sr}^{-}(t) = \eta_s^{-}(t) + U^{-}(t) + \dfrac{R_f}{a_s L} I(t) - U_{sr}^{-} > 0 & \text{(4.49c)} \\ \eta_{sr}^{+}(t) = \eta_s^{+}(t) + U^{+}(t) + \dfrac{R_f}{a_s L} I(t) - U_{sr}^{+} < 0 & \text{(4.49d)} \end{cases}$$

where $\bar{r}_{c_s}$ is the upper bound of the $\mathrm{SOC}(t)$ and $\mathrm{CSC}(t)$, and $U_{sr}^{\pm}$ are scalars. This constraint mapping can be explained as follows. Since $\mathrm{SOC} = \bar{c}_s / c_{s,\max}$ and $\mathrm{CSC} = c_{ss} / c_{s,\max}$ (see Remark 4.2.2), constraints Eq. (2.32a) of the negative electrode can be rewritten as Eqs. (4.49a),(4.49b). The left-hand side of these inequalities are added because SOC and CSC are physically nonnegative quantities. Since the dynamics of the positive electrode are negligible, constraints Eq. (2.32b) of the positive electrode can be satisfied by controlling the negative ones, and therefore they are not necessary. Constraints Eqs. (4.49c),(4.49d) are obtained by substituting $\phi_s^{\pm} - \phi_e$ of Eq. (2.15) in Eqs. (2.32c),(2.32d) under the assumption of uniform reaction rate. Notice that electrolyte constraint Eq. (2.32e) requires the extension of the EHM to account for electrolyte dynamics. However, such constraint is not violated under the considered conditions. Extensive simulations have shown that the satisfaction of constraints Eq. (4.49) implies the satisfaction of constraints Eq. (2.32) for given values of $\bar{r}_{\mathrm{SOC}}$, $\bar{r}_{\mathrm{CSC}}$, and $U_{sr}^{\pm}$. This result is not surprising from the physical viewpoint since the EHM is derived by suitably neglecting the spatial distribution of the DFN variables.

As done with the different submodels introduced in the previous subsections, let us generalize the constraint set Eq. (4.49) as the set of linear constraints

$$S_j^{\mathrm{T}} x(k) \leq s_j, \quad j = 1, \ldots, n_c, \tag{4.50}$$

where n_c is the number of constraints. This kind of generalization allows us to end up with a general model structure in the next subsection. Notice that constraints such as Eqs. (4.49a) and (4.49b) are linear, while constraints of the form Eqs. (4.49c) and (4.49d) are typically nonlinear and may delimit a nonconvex region. However, nonlinear nonconvex constraints can be approximated by affine constraints of the form Eq. (4.50).

4.2.6 Summary of Reduced-Order Model with Constraints

The model presented in Sections 4.2.1-4.2.5 involves solid-phase diffusion dynamics, as in the original equivalent-hydraulic model (EHM) [52], but it also incorporates electrolyte-phase diffusion, thermal and aging dynamics. Therefore, it is referred to as *enhanced* EHM and it is denoted by *e*EHM.

The overall state equation of Section 4.2.3 with the aging dynamics of Section 4.2.5 can be written as

$$\begin{aligned} \dot{x}(t) &= A(x(t), \theta(t))x(t) + B_z z(t) + B_d d(t) + f_x(u(t), x(t), y(t)) & \text{(4.51)} \\ \dot{\theta}(t) &= f_\theta(t) & \text{(4.52)} \\ y(t) &= h_y(z(t), x(t), \theta(t)) & \text{(4.53)} \\ 0 &= h_n(z(t), x(t), \theta(t)) - h_{\mathrm{SEI}}(u(t), d(t), x(t), \theta(t)) & \text{(4.54)} \\ u(t) &= z(t) + d(t) & \text{(4.55)} \end{aligned}$$

where $x(t) \in \mathbb{R}^n$ with $n = n_s + n_e + 3$ is the differential state vector $x(t) = \left[x_s(t)^{\mathrm{T}}, x_e(t)^{\mathrm{T}}, x_T(t)^{\mathrm{T}}, x_Q(t)\right]^{\mathrm{T}}$, $u(k) \in \mathbb{R}$ is the input vector $u(t) = I(t)$, $y(t) \in \mathbb{R}^2$ is the output vector $y(t) = [V(t), T_s(t)]^{\mathrm{T}}$, $z(t) \in \mathbb{R}$ is the algebraic state vector $z(t) = Fa_sLj_n(t)$ and $\theta(t) \in \mathbb{R}^2$ is the parameter vector $\theta(t) = \left[D_s(t), R_f(t)\right]^{\mathrm{T}}$. The matrices and functions of the state Eq. (4.51) are given by

$$\begin{aligned} A(x(t),\theta(t)) &= \operatorname{diag}\left(A_s(x(t),\theta(t)), A_e(x(t)), A_T, A_Q\right) \\ B_z &= [B_s^{\mathrm{T}}, B_e^{\mathrm{T}}, 0_{1\times 3}]^{\mathrm{T}} \\ B_d &= [0_{1\times(n_s+n_e+2)}, B_Q]^{\mathrm{T}} \\ f_x(u(t),x(t),y(t)) &= [0_{1\times(n_s+n_e)}, f_T^{\mathrm{T}}(u(t),x(t),y(t)), 0]^{\mathrm{T}}, \end{aligned} \tag{4.56}$$

whereas the function for the parameter Eq. (4.52) is given by Eqs. (4.1) and (4.2). The output function for Eq. (4.53) is given by

$$h_y(z(t),x(t),\theta(t)) = \begin{bmatrix} \Delta U_s^{\pm}(t) + \Delta\eta_s^{\pm}(t) + \Delta\phi_e(t) - \frac{R_f(t)}{a_sL}u(t) \\ [0,0,\ldots,0,1]\,x(t) \end{bmatrix}, \tag{4.57}$$

while the equality constraint functions for Eq. (4.54) are given by:

$$\begin{aligned} h_{\mathrm{SEI}}(u(t),d(t),x(t),\theta(t)) &= \Delta U_{\mathrm{SEI}}(t) + \Delta\eta_{\mathrm{SEI}}(t) + \Delta\phi_e(t) - \frac{R_f}{a_sL}u(t) \\ h_n\left(z(t),x(t),\theta(t)\right) &= \Delta U_s^{\pm}(t) + \Delta\eta_s^{\pm}(t) + \Delta\phi_e(t) - \frac{R_f}{a_sL}u(t) \end{aligned} \tag{4.58}$$

By abuse of notation, the state matrix A and functions h_y, h_n and h_{SEI} of Eqs. (4.56)-(4.58) are considered here with an extra argument for $\theta(t)$, since time-varying parameters arise when calendar aging is accounted for.

The model Eqs. (4.51)-(4.58) is subject to inequality constraints associated to degradation mechanisms such as

$$S_j^{\mathrm{T}}x(t) \leq s_j, \;\; j = 1,\ldots,n_c. \tag{4.59}$$

These inequalities describe a region within which it is safe to operate the battery. These constraints are not embedded in the model, but they will be exploited to develop a constrained control scheme in Chapter 6 and 7 below.

4.2.7 Analysis of Equilibrium Points

One of the main tasks that an engineer is asked to do when controlling a plant is to analyze its stability, more precisely the stability of its equilibrium points. In our context, such analysis also renders the means to initialize the different electrochemical models (EHM, *e*EHM, DFN) that we use for simulation, estimation and control. A similar derivation as the one proposed in [76] to determine the equilibrium points of a battery model is retrieved, although with a different model.

Let us analyze the equilibrium points of the *e*EHM with no side reaction taking place, and denote the associated equilibrium variables with the superscript "$*$". At equilibrium, the integrator of Eq. (4.17) (see Table 4.2, Eqs. (4.18)-(4.20) for instance) yields a main reaction equilibrium current $j_n^* = 0$, which implies that the equilibrium current applied to the battery is $I^* = 0$ from Eq. (4.4). The rest of the state vector takes the form $\mathrm{SOC}^* = c_{s,2}^* = \ldots = c_{s,n-1}^* = \mathrm{CSC}^*$ and $c_{eb}^* = c_{e,2}^* = \ldots = c_{e,n-1}^* = c_{es}^*$ for the solid and electrolyte phase diffusion processes, respectively. Given that $I^* = 0$, the thermal equilibrium states are $T_{bc}^* = T_{bs}^* = T_{\mathrm{amb}}$ obtained from Eq. (4.30).

The last variable whose equilibrium needs to be defined is the output voltage given by the function $h_n(z(t), x(t))$ in Eq. (4.39). The terms $R_f u(t)$ and $\Delta\eta_s^{\pm}(t)$ given by Eqs. (4.25), (4.26) become zero for a zero input current. The function $\Delta\phi_e(t)$ is also zero in the case that $I = 0$ and $c_{es} = c_{es}^{+}$ (see Eq. (4.37)). The first equality follows from I^*, while the second can be obtained from the continuity boundary conditions for the electrolyte concentration of the original electrolyte-phase diffusion PDE of Table 4.1. Therefore, at equilibrium, it follows that $c_{es}^{+,*} = c_{es}^{*}$, which makes $\Delta\phi_e = 0$. The resulting output voltage equilibrium equation derived from Eq. (4.35) is given by

$$V^*(\mathrm{SOC}^*) = U_s^{+,*}(\mathrm{SOC}^*) - U_s^{-,*}(\rho_s \mathrm{SOC}^* + \sigma_s), \tag{4.60}$$

where the independent variable of each function has been made explicit in this equation. Under the assumption of strict monotonicity for the open-circuit potentials $U_s^{\pm}$ (which is usually the case), there is a set of solid-phase equilibrium concentrations that generate a unique set of equilibrium voltages. Therefore, there is an infinite set of equilibrium points [76]. This result is expected when analyzing the physics of the system, since its state consists of concentrations of lithium in the solid phase. Concentration is an intensive property that reflects a continuum between a minimum and a maximum value. Thus, whenever the current applied to the battery is zero and the concentration gradient is allowed to relax, the resulting state is an equilibrium point. Since the *e*EHM can be seen as a spatially discretized version of the DFN model, the equilibrium conditions resulting from the present analysis based on the former model can be extrapolated to the latter model.

If side reactions such as SEI growth is considered, Kirchhoff's law for both the main and the side reaction has to be included in the model. By explicitly expanding the functions of Eq. (4.46) and setting $u(t) = I^* = 0$, the following expression is obtained

$$U_s^{-}(x(t)) + \eta_s^{-}(z(t), x(t)) = U_{\mathrm{SEI}} + \eta_{\mathrm{SEI}}(d(t), x(t)) \tag{4.61}$$

with the side reaction current rate given by

$$j_{\mathrm{SEI}}(t) = -a_s L i_{\mathrm{SEI},0} \exp\left(-\frac{\alpha_0 F}{R_g T_{bc}(t)} \eta_{\mathrm{SEI}}(t)\right) \tag{4.62}$$

Three situations can be distinguished:

- If $U_s^{-}(x(t)) = U_{\mathrm{SEI}}$, the main and the side reactions are balanced, and therefore no side reaction takes place.
- If $U_s^{-}(x(t)) \neq U_{\mathrm{SEI}}$, side reactions occur in lesser or greater extent. Assuming that $U_{\mathrm{SEI}} \geq 0$ (which is usually the case), we have:
  - If $U_s^{-} + \eta_s^{-} > U_{\mathrm{SEI}} \implies \eta_{\mathrm{SEI}} > 0$ and the side reaction current rate given by Eq. (4.62) results in $|j_{\mathrm{SEI}}| < a_s L i_{\mathrm{SEI},0}$ mol·m^{-2}·s^{-1}. Notice that the bigger $\eta_{\mathrm{SEI}} > 0$, the smaller $|j_{\mathrm{SEI}}|$ (exponentially).
  - If $U_s^{-} + \eta_s^{-} < U_{\mathrm{SEI}} \implies \eta_{\mathrm{SEI}} < 0$ and the side reaction current rate of Eq. (4.62) results in $|j_{\mathrm{SEI}}| > a_s L i_{\mathrm{SEI},0}$ mol·m^{-2}·s^{-1}. Notice that the smaller $\eta_{\mathrm{SEI}} < 0$, the bigger j_{SEI} (exponentially).

These dependencies can be clearly seen in Fig. 4.6 for some values of the side reaction equation.

The side reaction has to be accompanied to some extent by the main reaction for Eq. (4.61) to hold. However, the total current applied to the battery cell can be the

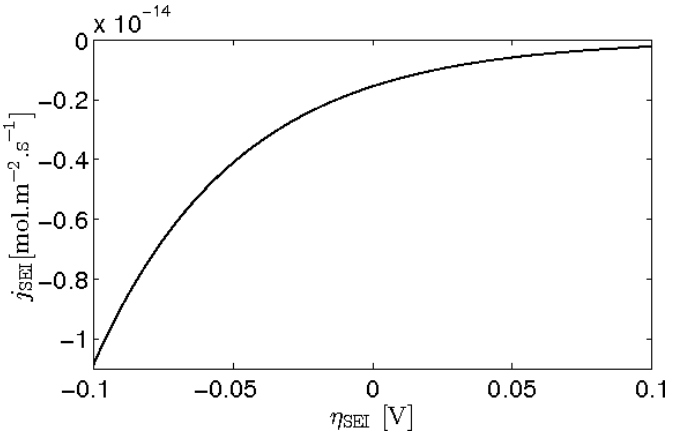

FIGURE 4.6: Dependence of side reaction current density due to SEI growth on surface overpotential.

equilibrium current $I^* = 0$ and both the main and the side reaction currents with opposite signs might be flowing through the system respecting $u^* = 0 = z(t) + d(t)$. This process exemplifies the self-discharge in batteries, and it tends to be low for lithium-ion chemistries (it is a function of the side reaction exchange current density $i_{\text{SEI},0}$). However, from the above analysis follows that side reactions such as SEI growth are diminished when $\eta_{\text{SEI}} > 0$ (see Fig. 4.6), implying that $U_s^- + \eta_s^- > U_{\text{SEI}}$ which holds for low battery voltages (see Fig. 4.5). Therefore, self-discharge can be mitigated by storing the batteries at low state-of-charges. The presence of self-discharge translates in a slight persistent perturbation of the equilibrium presented above (i.e. the one without side reaction). Taking the SOC as an example, the previous SOC^* takes the form $\text{SOC}^* + \tilde{\text{SOC}}^*$, with $\tilde{\text{SOC}}^*$ as a perturbation due to the presence of side reactions.

4.2.8 Discretization for Implementation

The *e*EHM described throughout this section, whose general structure is given in Eqs. (4.51)-(4.55), is in continuous-time domain. However, the digital implementation of estimators and controllers that come up in the next Chapter 5 to 7 requires a discrete-time version of this *e*EHM. The simplest way to discretize such a nonlinear system is through Euler approximation, which yields a discrete-time *e*EHM of the following form

$$
\begin{aligned}
x(k+1) &= A^d(x(k),\theta(k))x(k) + B_z^d z(k) + B_d^d d(k) + f_x^d(u(k),x(k),y(k)) && (4.63)\\
\theta(k+1) &= \theta(k) + f_\theta^d(\theta(k),k) && (4.64)\\
y(k) &= h_y\left(z(k),x(k),\theta(k)\right) && (4.65)\\
0 &= h_n(z(k),x(k),\theta(k)) - h_{\text{SEI}}(d(k),x(k),\theta(k)) && (4.66)\\
u(k) &= z(k) + d(k) && (4.67)
\end{aligned}
$$

where the superscript d in Eqs. (4.63),(4.64) denote discrete-time matrices and functions. With an abuse of notation, we consider the same variables for the difference state $x(k)$, parameter $\theta(k)$, output $y(k)$ and algebraic state $z(k)$ vectors for the continuous-time system Eqs. (4.51)-(4.55) and the discrete-time system Eqs. (4.63)-(4.67). $x(k) \in \mathbb{R}^n$ with $n = n_s + n_e + 3$ is the dynamic state vector $x(k) =$

$\left[x_s(k)^{\mathrm{T}}, x_e(k)^{\mathrm{T}}, x_T(k)^{\mathrm{T}}, x_Q(k)\right]^{\mathrm{T}}$, $u(k) \in \mathbb{R}$ is the input vector $u(k) = I(k)$, $y(k) \in \mathbb{R}^2$ is the output vector $y(k) = [V(k), T_{bs}(k)]^{\mathrm{T}}$, $z(k) \in \mathbb{R}$ is the algebraic state vector $z(k) = Fa_sLj_n(k)$ and $\theta(k) \in \mathbb{R}^2$ is the parameter vector $\theta(k) = \left[D_s(k), R_f(k)\right]^{\mathrm{T}}$. The discrete-time version of the state and parameter matrices and functions in Eqs. (4.63),(4.64) are given by

$$\begin{aligned} A^d(x(k),\theta(k)) &= I_d + T_s A(x(k),\theta(k)) \\ B_z^d &= T_s B_z \\ B_d^d &= T_s B_d \\ f_x^d(u(k),x(k),y(k)) &= T_s f_x(u(k),x(k),y(k)) \\ f_\theta^d(\theta(k),k) &= T_s f_\theta(\theta(k),k) \end{aligned}$$

where I_d is an identity matrix with appropriate dimensions, T_s is the sampling period and the concatenation of matrices and functions are given by

$$A(x(k),\theta(k)) = \operatorname{diag}\left(A_s(x(k),\theta(k)), A_e(x(k)), A_T, A_Q\right) \tag{4.68}$$

$$B_z = [B_s^{\mathrm{T}}, B_e^{\mathrm{T}}, 0_{1\times 3}]^{\mathrm{T}} \tag{4.69}$$

$$B_d = [0_{1\times(n_s+n_e+2)}, B_Q]^{\mathrm{T}} \tag{4.70}$$

$$f_x(u(k),x(k),y(k)) = [0_{1\times(n_s+n_e)}, f_T^{\mathrm{T}}(u(k),x(k),y(k)), 0]^{\mathrm{T}} \tag{4.71}$$

The function of the parameter Eq. (4.64) is given by the discrete-time version of Eqs. (4.1) and (4.2). In the next chapters however, the superscript d in the system model Eqs. (4.63)-(4.64) is dropped for the sake of simplicity.

The output function for Eq. (4.65) follows, taking the form

$$h_y(z(k),x(k),\theta(k)) = \begin{bmatrix} \Delta U_s^{\pm}(k) + \Delta\eta_s^{\pm}(k) + \Delta\phi_e(k) - \frac{R_f}{a_sL}(k)u(k) \\ [0,0,\ldots,0,1]\,x(k) \end{bmatrix}, \tag{4.72}$$

and the equality constraint functions for Eq. (4.66) as

$$\begin{aligned} h_{\mathrm{SEI}}(u(k),d(k),x(k),\theta(k)) &= \Delta U_{\mathrm{SEI}}(k) + \Delta\eta_{\mathrm{SEI}}(k) + \Delta\phi_e(k) - \tfrac{R_f}{a_sL}u(k) \\ h_n\left(z(k),x(k),\theta(k)\right) &= \Delta U_s^{\pm}(k) + \Delta\eta_s^{\pm}(k) + \Delta\phi_e(k) - \tfrac{R_f}{a_sL}u(k). \end{aligned} \tag{4.73}$$

The resulting model Eqs. (4.63)-(4.73) is a nonlinear difference algebraic equation (NLDAE) system. Similarly as the continuous-time model, the model Eqs. (4.63)-(4.73) is subject to the inequality constraints given by

$$S_j^{\mathrm{T}} x(k) \leq s_j, \;\; j = 1,\ldots,n_c. \tag{4.74}$$

4.3 Concluding Remarks

This chapter has introduced the framework used to develop different battery electrochemical models. These models differ in complexity and accuracy. The most accurate model is the DFN model with thermal and aging dynamics, which is exploited as a battery cell simulator. However, its complexity precludes its use for estimation/control. Model-order reduction has been performed in the different subsystems comprising the DFN model, namely solid and electrolyte-phase diffusion equations, thermal, aging and output equations. The resulting model is denoted as *e*EHM. Although the EHM and its extension by adding dynamics to the model is not new, the link between this model and the electrochemical ones has been drawn

here for the first time. This link renders an easy to interpret model that is totally transparent from the physical viewpoint in terms of states and parameters. This is particularly relevant for state and SOH estimation. Electrochemical constraints associated to battery degradation have also been defined for the reduced model. Although these degradation-related constraints are directly borrowed from the literature, their combination with unavoidable degradation mechanisms and the different ways of handling both of them are a novelty that comes out from this work. The state of equilibrium of the resulting reduced-order electrochemical model has been studied under healthy and faulty conditions. This analysis can be extended to higher-order models such as the DFN model, providing a way to initialize the associated states. Furthermore, it gives us insight into the impact of degradation processes even under zero input current. Finally, a discrete-time version of the *e*EHM is derived, which will be necessary when monitoring and controlling the battery. The proposed *e*EHM is conceived to be scalable and modular. The former characteristic means that the order of the solid and electrolyte-phase diffusion subsystems can be increased according to the model accuracy specification. The latter characteristic translates in the possibility of considering specific subsystems and neglecting others. Such assets will be explored in the following chapters for supervisory control.

Chapter 5

System Identification & Fault Detection and Isolation

Following the state of the art of Sections 2.4 to 2.6, a battery monitoring and diagnosis system is developed in this chapter, which is structured as follows. On the one hand, Section 5.1 introduces an extended Kalman filter along with parameter identification methods for SOH estimation (green block in Fig. 5.1). This state and parameter estimation strategy is validated through both a high-fidelity battery cell simulator and real battery experiments in Section 5.2. On the other hand, Section 5.3 presents an unscented Kalman filter to generate residuals to diagnose sensor faults (blue block in Fig. 5.1). This fault diagnosis system has been validated via simulation so far, and the results are presented in Section 5.4. Although the SOH monitoring and the sensor FDI system are two different pieces of work, they can be combined so that the monitoring system has these two distinctive features. The light red block in Fig. 5.1 corresponds to the output feedback controller developed in Chapters 6 and 7 for safe and fast battery changing. The common element tying all the pieces of this work together is the state observer (orange block in Fig. 5.1).

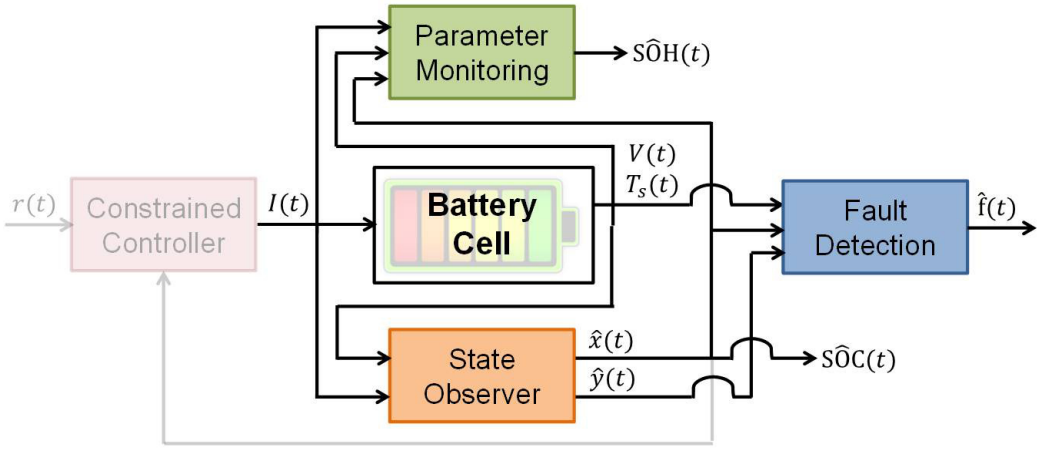

FIGURE 5.1: Block diagram of the monitoring system for a battery cell.

5.1 State/Parameter Estimation for SOH

This section deals with the estimation problem of providing battery SOH indicators based on changes in the model parameters. Two groups of parameters are sorted out, namely parameters that change according to operating conditions, and

the ones that change due to aging. We resort to a mix of on-line and batch parameter identification approaches to respectively handle each group of parameters, which are coupled with an observer for state estimation. The standard extended Kalman filter (EKF) of Section 2.4 is modified to account for state constraints (orange block in Fig. 5.2). For the on-line identification, the EKF state vector is augmented with unknown and slowly time-varying parameters to perform joint state/parameter estimation. For the batch identification, the EKF state estimate is further exploited to periodically identify parameter changes through instrumental variable (green "SRIVC" block in Fig. 5.2) and least squares (green "LS" block in Fig. 5.2) methods. This procedure results in capacity and power fade SOH indicators. In the event that only parameter changes due to operating conditions are expected, on-line parameter monitoring through a state observer should be performed. Conversely, if only parameter changes due to aging are expected, the batch parameter identification can be pursued.

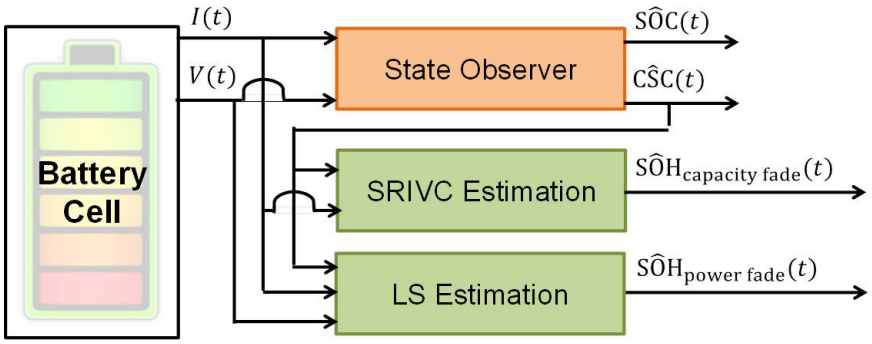

FIGURE 5.2: Block diagram of the identification scheme.

5.1.1 Constrained Extended Kalman Filter

In this early work, a simplified version of the system Eqs. (4.63)-(4.67) was considered. First, the electrolyte diffusion and thermal dynamics are neglected in the state Eq. (4.63), and only the solid-phase diffusion dynamics are considered (i.e. $x(k) = x_s(k)$) through a third-order EHM. Secondly, in contrast to the parameter vector $\theta(k) = [D_s(k), R_f(k)]^{\mathrm{T}}$ and function $f_\theta(\theta(k), k)$ in Eq. (4.64) whose component-wise functional forms come from Eqs. (4.1),(4.2), here the parameter vector comprises $\theta_1(k) = g_s(k) = R_s^{-2} D_s$ and $\theta_2(k) = R_f(k)$, whose dynamic evolution is represented by slowly time-varying processes as $f_\theta(\theta(k), k) = [\theta_1(k), \theta_2(k)]^{\mathrm{T}}$. This choice for the parameter evolution is motivated by the ignorance regarding expected functional forms for parameter variations associated to degradation and the fact that aging is a slow process. Thirdly, by neglecting degradation mechanisms via $d(k) = 0$ (i.e. $u(k) = z(k) = I(k)$), the algebraic Eqs. (4.66),(4.67) disappear and the DAE model becomes an ODE model. Finally, noise sources are introduced. The resulting model has the following form[1]

$$\begin{aligned} x_s(k+1) &= A_s(\theta(k))x_s(k) + B_s u(k) + w_n(k) \\ \theta(k+1) &= \theta(k) + w_{n,\theta}(k) \\ y_n(k) &= h_n\left(u(k), x_s(k), \theta(k)\right) + v_n(k) \end{aligned} \tag{5.1}$$

[1]Although the solid-phase diffusion state matrix $A_s(x(k), \theta)$ has both the state and parameter vectors as arguments in the general model Eq. (4.68), the simplified model considered here makes this matrix to be only dependent on the parameters. For convenience in the presentation, we use the same notation in both cases, and just drop the independent term in Eq. (5.1).

which, after augmenting the state vector $x_s(k)$ with the parameter vector $\theta(k)$ denoted as $x_{s\theta}(k) \in \mathbb{R}^5$ given by $x_{s\theta}(k) = [x_s(k), \theta(k)]^{\mathrm{T}}$, takes the equivalent form[2]

$$x_{s\theta}(k+1) = A_{s\theta}(x_{s\theta}(k))x_{s\theta}(k) + B_{s\theta}u(k) + w_{s\theta}(k) \tag{5.2}$$
$$y_n(k) = h_n(u(k), x_{s\theta}(k)) + v_n(k) \tag{5.3}$$

where $x_s(k) \in \mathbb{R}^3$ is the solid-phase diffusion state vector $x_s(k) = [\mathrm{SOC}(k), c_{s,2}(k), \mathrm{CSC}(k)]^{\mathrm{T}}$, $\theta(k) \in \mathbb{R}^2$ is the parameter vector $\theta(k) = \left[g_s(k), R_f(k)\right]^{\mathrm{T}}$, $u(k) \in \mathbb{R}$ is the battery current input vector $u(k) = I(k)$, $y_n(k) \in \mathbb{R}$ is the battery voltage output vector $y_n(k) = V(k)$, $w_{s\theta}(k) \in \mathbb{R}^5$ results from the concatenation of the process $w_n(k) \in \mathbb{R}^3$ and parameter $w_{n,\theta}(k) \in \mathbb{R}^2$ noise sequences, i.e. $w_{s\theta}(k) = [w_n(k), w_{n,\theta}(k)]^{\mathrm{T}}$, and $v_n(k) \in \mathbb{R}$ is a measurement noise sequence. These noise sequences are normally distributed, zero-mean mutually uncorrelated white noise sequences with covariance matrix

$$\mathbb{E}\left(\begin{bmatrix} w_{s\theta}(k) \\ v_n(k) \end{bmatrix} \left[w_{s\theta}(l)^{\mathrm{T}} v_n(l)^{\mathrm{T}}\right]\right) = \begin{bmatrix} Q_{s\theta} & 0 \\ 0 & R \end{bmatrix} \delta_{kl} \tag{5.4}$$

where $\mathbb{E}$ is the expectation operator and δ_{kl} is the Kronecker delta function. The state $A_s(x_{s\theta}(k)) \in \mathbb{R}^{5\times5}$ and input $B_s \in \mathbb{R}^{5\times1}$ matrices in Eq. (5.3) are equivalent to the ones of Table 4.2 but with a time-varying parameter $g_s(k)$ and the system state augmented with $\theta(k)$, i.e.

$$A_{s\theta}(x_{s\theta}(k)) = \begin{bmatrix} 1 & 0 & 0 & 0 & 0 \\ g_s(k)\frac{\gamma_1}{\beta_1\beta_2} & 1 - g_s(k)\left(\frac{\gamma_1}{\beta_1} + \frac{\gamma_1+\gamma_2}{\beta_2}\right) & g_s(k)\left(\frac{\gamma_2}{\beta_2} - \frac{\beta_3\gamma_1}{\beta_1\beta_2}\right) & 0 & 0 \\ 0 & g_s(k)\frac{\gamma_2}{\beta_3} & 1 - g_s(k)\frac{\gamma_2}{\beta_3} & 0 & 0 \\ 0 & 0 & 0 & g_s(k) & 0 \\ 0 & 0 & 0 & 0 & R_f(k) \end{bmatrix} \tag{5.5}$$

$$B_{s\theta} = \zeta_0 \begin{bmatrix} 1 & 0 & \frac{1}{\beta_3} & 0 & 0 \end{bmatrix}^{\mathrm{T}}, \tag{5.6}$$

whereas the nonlinear output function $h_n\left(u(k), x_{s\theta}(k)\right)$ is given in Eq. (4.39), whose dependency on the underlying parameter vector $\theta(k)$ can be made explicit as

$$h_n\left(u(k), x_{s\theta}(k)\right) = \Delta U_s^{\pm}(k) + \Delta\eta_s^{\pm}(k) + \Delta\phi_e(k) - \frac{R_f(k)}{a_s L}u(k). \tag{5.7}$$

Since this model neglects electrolyte dynamics, the electrolyte potential drop $\Delta\phi_e(k)$ reduces to

$$\Delta\phi_e(k) = -\frac{1}{2\kappa_{e,\mathrm{eff}}}\left(\frac{L^+}{(\varepsilon_e^+)^\epsilon} + 2\frac{L^s}{(\varepsilon_e^s)^\epsilon} + \frac{L^-}{(\varepsilon_e^-)^\epsilon}\right) I(k). \tag{5.8}$$

Remark 5.1.1. *The electrolyte-phase electric potential drop of Eq.* (5.8) *results from a simplification of the discrete version of Eq.* (4.37)*. By considering a constant electrolyte concentration, the first term in the right-hand side of Eq.* (4.37) *becomes zero.*

[2]Since the state vector has been augmented here with the parameters, the state matrix $A_s(\theta(k))$ and the output function $h_n\left(u(k), x_s(k), \theta(k)\right)$ in Eq. (5.1) now depend on the augmented state vector $x_{s\theta}(k)$ in model Eqs. (5.2),(5.3). For convenience in the presentation, we do not change notation despite this modification.

Before describing the state estimation procedure for model Eqs. (5.2),(5.3), the model is complemented by accounting for physical constraints, namely:

$$\begin{array}{l} 0 \leq x_s(k) \leq 1 \\ 0 \leq \theta(k) \end{array} \tag{5.9}$$

Remark 5.1.2. *The complete set of constraints for the solid-phase diffusion process involves the whole solid-phase diffusion state vector such as* $0 \leq x_s(k) \leq 1$*. Some of these constraints might be redundant from the physical viewpoint, since if the surface state is constrained as* $0 \leq \mathrm{CSC}(k) \leq 1$*, there is no way that the internal states violate their inequality constraints. However, the evolution of the state estimate is not governed only by the physics of the process. It is affected by the modeling uncertainties, the level of excitation, the initial estimation error and the noise level notably. Therefore, considering the entire constraint set such as in Eq.* (5.9) *ensures that the state estimates retain a physical sense.*

To perform state estimation while enforcing constraints Eq. (5.9) on the estimated state, the standard EKF of Table 3.2 has to be modified accordingly. A constrained EKF with estimate projection is used here. This is a direct extension of the Kalman filter with state constraints presented in [144] . To apply this method, first note that, given the definition of the state variables in Eq. (5.2), the constraints Eq. (5.9) can be rewritten in the form

$$S_j^{\mathrm{T}} x_{s\theta}(k) \leq s_j, \;\; j = 1, \ldots, 8 \tag{5.10}$$

where $S_1 = -[1\ 0_{1\times 4}]^{\mathrm{T}}$, $S_2 = -S_1$, $S_3 = -[0\ 1\ 0_{1\times 3}]^{\mathrm{T}}$, $S_4 = -S_3$, $S_5 = -[0_{1\times 2}\ 1\ 0_{1\times 2}]^{\mathrm{T}}$, $S_6 = -S_5$, $S_7 = -[0_{1\times 3}\ 1\ 0]^{\mathrm{T}}$, $S_8 = -[0_{1\times 4}\ 1]^{\mathrm{T}}$, and $s_1 = s_3 = s_5 = 1$ and $s_2 = s_4 = s_6 = s_7 = s_8 = 0$.

Now, at any time instant, only a subset of the constraints Eq. (5.10) will be active. In particular, only one of the first pair, second pair and third pair of constraints can be active at a given time. Let $(S_j^{ac})^{\mathrm{T}}$ and s_j^{ac} denote the matrix and vector made of the rows of S_j^{T} and s_j corresponding to the active constraints. Furthermore, let $\hat{x}_{s\theta}(k)$ denote the state estimate at time k given measurements up to time $k-1$, and let $\hat{x}_{s\theta}^{+}(k)$ denote its constrained counterpart. Then the projection step in the Kalman filter amounts to solving the following optimization problem:

$$\begin{array}{rl} \hat{x}_{s\theta}^{+}(k) = & \arg\min_{x_{s\theta}(k)} (x_{s\theta}(k) - \hat{x}_{s\theta}(k))^{\mathrm{T}} (x_{s\theta}(k) - \hat{x}_{s\theta}(k)) \\ & \text{s.t. } (S_j^{ac})^{\mathrm{T}} x_{s\theta}(k) = s_j^{ac}. \end{array} \tag{5.11}$$

This yields the following solution

$$\hat{x}_{s\theta}^{+}(k) = \hat{x}_{s\theta}(k) - S_j^{ac}((S_j^{ac})^{\mathrm{T}} S_j^{ac})^{-1}((S_j^{ac})^{\mathrm{T}} \hat{x}_{s\theta}(k) - s_j^{ac}).$$

The complete EKF algorithm with state projection is summarized in Table 5.1 for system Eqs. (5.2),(5.3) with $f_{s\theta}(x_{s\theta}(k)) = A_{s\theta}(x_{s\theta}(k))x_{s\theta}(k)$.

The initialization step in Table 5.1 involves setting the state estimate $\hat{x}_{s\theta}(0) = \left[\hat{\mathrm{SOC}}(0), \hat{c}_{s,2}(0), \hat{\mathrm{CSC}}(0), \hat{g}_s(0), \hat{R}_f(0)\right]^{\mathrm{T}}$ and the variance of the state estimation error $P(0)$. Initialization of the state elements comprising the solid concentration is straightforward by assuming that the battery cell was at rest (zero current) during a long enough period of time before its use. This condition ensures equilibrium where $\mathrm{SOC}(0) = c_{s,2}(0) = \mathrm{CSC}(0)$, which can be estimated by inverting the open circuit voltage (OCV) function. Initialization of the uncertain parameters θ relies on the knowledge of the battery chemistry. Parameter g_s can be initialized with a reasonable *a priori* estimate of the diffusion time constant τ_s, since $g_s = \tau_s^{-1}$. Parameter R_f can

TABLE 5.1: Extended Kalman filter with state constraints[†].

Initialization: for $k = 0$ set

$\hat{x}_{s\theta,0} = \mathbb{E}[x_{s\theta,0}]$, $P_0 = \mathbb{E}[(x_{s\theta,0} - \hat{x}_{s\theta,0})(x_{s\theta,0} - \hat{x}_{s\theta,0})^{\mathrm{T}}]$

At each time instant compute:

Time-update:

$$\hat{x}^{-}_{s\theta,k} = f_{s\theta}(\hat{x}^{+}_{s\theta,k-1}) + B_{s\theta}u_{k-1} \tag{5.12}$$

$$P^{-}_{k} = F_{k-1}P_{k-1}F^{\mathrm{T}}_{k-1} + Q_{s\theta} \tag{5.13}$$

$$\hat{y}_{n,k} = h_n(u_k, \hat{x}^{-}_{s\theta,k}) \tag{5.14}$$

Measurement-update

$$\hat{x}_{s\theta,k} = \hat{x}^{-}_{s\theta,k} + K_k\,(y_{n,k} - \hat{y}_{n,k}) \tag{5.15}$$

$$\hat{x}^{+}_{s\theta,k} = \hat{x}_{s\theta,k} - S^{ac}_j((S^{ac}_j)^{\mathrm{T}}S^{ac}_j)^{-1}((S^{ac}_j)^{\mathrm{T}}\hat{x}_{s\theta,k} - s^{ac}_j) \tag{5.16}$$

$$K_k = P^{-}_k H^{\mathrm{T}}_k \left(H_k P^{-}_k H^{\mathrm{T}}_k + R\right)^{-1} \tag{5.17}$$

$$P_k = P^{-}_k - K_k \left(H_k P^{-}_k H^{\mathrm{T}}_k + R\right) K^{\mathrm{T}}_k \tag{5.18}$$

where $F_k = \left.\dfrac{\partial f_{s\theta}(x_{s\theta,k})}{\partial x_{s\theta,k}}\right|_{x_{s\theta,k}=\hat{x}_{s\theta,k}}$, $H_k = \left.\dfrac{\partial h_n(u_k, x_{s\theta,k})}{\partial x_{s\theta,k}}\right|_{x_{s\theta,k}=\hat{x}_{s\theta,k}}$

[†]For compactness, the time argument is set as an index.

be initialized e.g. with a value around 1 $\Omega{\cdot}\mathrm{m}^2$. Finally, $P(0)$ is chosen as a diagonal matrix. Its diagonal elements are taken as tuning parameters in order to ensure an appropriate trade-off between convergence speed and "noise level" on the estimate. The variance matrix $Q_{s\theta}$ is also used as a tuning parameter, since it accounts for model inaccuracies that are difficult to quantify.

The EKF of Table 5.1 provides the means to estimate the internal state of the battery cell while adapting the operation-induced parameter changes. However, a lithium-ion battery is also prone to suffer degradation, in which case the tracking of aging-induced parameter changes is required. In the next section, we introduce parameter identification techniques that allow to process a batch of data in order to estimate aging parameters. In contrast to permanent monitoring at each sample time, periodic monitoring using a batch of data can be exploited due to the characteristic slow dynamics of aging mechanisms. In this way, unnecessary computational burden is avoided.

5.1.2 The SRIVC & LS Methods

An important issue that is not well recognized in the literature, except for [99], is that battery aging is a slow phenomenon as stressed above. Therefore, there is a time-scale separation between parameter estimation and state estimation that can be exploited. It suffices to evaluate the aging level periodically without necessarily performing a permanent monitoring. Some identification methods require specific battery tests, i.e. battery operation has to be interrupted for battery health assessment. Other methods involve an excessive computational burden due to nonlinear (even nonconvex) optimization problems. Instead, we resort to algorithms that keep the simplicity of least squares estimation, and develop a two-step procedure to ensure time separation between states and aging dynamics. Hence, SOH indicators are not subject to short term transients and they only capture the monotonic variation due to

aging [87]. This can be beneficial since otherwise SOH indicators are overly sensitive to noise or operating point changes.

Besides the way in which aging dynamics are accounted for as mentioned in the previous paragraph, there are intrinsic flaws in the parameter estimation methods presented in the literature. Most of them, covered in Section 2.5, are based on the least squares method, which involves two drawbacks: 1) the initialization of these methods requires some *a priori* knowledge of the unknown parameters, and 2) they produce biased estimates in presence of colored noise. These pitfalls can be circumvented by resorting notably to instrumental variable (IV) methods [145, 128, 146], which provide unbiased estimates regardless of the noise type and initial parameter uncertainty.

In the following, two parameter identification techniques are explained. The first one exploits the dynamic EHM Eq. (5.2), corresponding to the solid-phase diffusion process, to estimate the electrode diffusion time constant $\tau_s = D_s^{-1}R_s^2$. The second one exploits the output Eq. (5.3), corresponding to the electrochemical reaction process, to estimate the film resistance R_f around the electrode. The former and latter parameters are related to capacity and power fade of the battery, respectively.

Estimation of the Diffusion Time Constant

As discussed in Section 3.2, the parameter identification problem is based on model Eq. (4.10). This model has constant parameters in contrast to model Eq. (5.2). The battery is thus assumed to operate around a given current intensity along the considered data set. A third-order model is considered, which is in line with the model order selected in [140] for the solid-phase diffusion model. Such model order selection results from the frequency response of the model and the frequency content of the input signal, which happens to be driving cycles in [140]. The estimation problem now boils down to estimating parameters R_s and D_s in

$$\frac{CSC(s)}{I(s)} \approx \frac{1}{Fa_s Lc_{s,\max}} \frac{21R_s^3 s^2 + 1260R_s D_s s + 10395R_s^{-1}D_s^2}{s(R_s^4 s^2 + 189R_s^2 D_s s + 3465D_s^2)} \tag{5.19}$$

given the measurements

$$\hat{\text{CSC}}(t_k) = \text{CSC}(t_k) + v_{n1}(t_k) \tag{5.20}$$

provided by the EKF of Section 5.1.1, with $t_k = kT_s$, T_s the sampling period. $v_{n1}(t_k)$ is a noise source that notably accounts for the estimation error of the EKF. This noise is assumed to be uncorrelated with the input data. As the EKF relies on the nonlinear model Eqs. (5.2),(5.3) and its error covariance matrix changes with time, the additive noise of the state estimation is not granted to be white and it is heteroscedastic[3]. Special attention to this feature is then necessary.

The above stated parameter estimation problem does not directly fall into a standard continuous-time parameter estimation problem in the prediction error framework since:

(a) The transfer function has a pole at the origin.

(b) The parameters of interest D_s and R_s appear nonlinearly in Eq. (5.19).

These issues prohibit the direct use of the standard SRIVC method of Table 3.5. However, the issues can be overcome by first removing the unstable part of the transfer

[3] An heteroscedastic noise is a noise whose variance varies with time.

function through data pre-filtering with a state-variable filter (SVF). Secondly, the resulting transfer function is identified by using instrumental variable (IV) techniques. Finally the nonlinear function in the coefficients D_s and R_s can be turned into a linear form to obtain the capacity fade SOH indicator.

Starting with the SVF, it yields the filtered quantities $\mathrm{CSC_f}(s)$, $I_\mathrm{f}(s)$, $\hat{\mathrm{CSC}}_\mathrm{f}(t_k)$ and $v_{n1,\mathrm{f}}(t_k)$ defined as

$$\mathrm{CSC_f}(s) = \frac{s}{s+\nabla}\mathrm{CSC}(s) \quad \text{and} \quad I_\mathrm{f}(s) = \frac{1}{s+\nabla}I(s) \tag{5.21}$$

$$\hat{\mathrm{CSC}}_\mathrm{f}(t_k) = \frac{s}{s+\nabla}\hat{\mathrm{CSC}}(t_k) \quad \text{and} \quad v_{n1,\mathrm{f}}(t_k) = \frac{s}{s+\nabla}(\hat{\mathrm{CSC}}(t_k) - \mathrm{CSC}(t_k)) \tag{5.22}$$

where the cutoff frequency ∇ should be properly chosen to keep the relevant frequency range of the third-order Padé approximation.

Based on the new set of signals Eqs. (5.21) and (5.22), the filtering operation transforms model Eq. (5.19) and the associated measurement equation into:

$$\frac{\mathrm{CSC_f}(s)}{I_\mathrm{f}(s)} = \frac{1}{Fa_sLc_{s,\max}}\frac{21R_s^3s^2 + 1260R_sD_ss + 10395R_s^{-1}D_s^2}{R_s^4s^2 + 189R_s^2D_ss + 3465D_s^2} \tag{5.23}$$

$$\hat{\mathrm{CSC}}_\mathrm{f}(t_k) = \mathrm{CSC_f}(t_k) + v_{n1,\mathrm{f}}(t_k). \tag{5.24}$$

This filtering operation *a priori* accounts for the pole at the origin, rendering a stable system in Eq. (5.23). Similarly to $v_{n1}(t_k)$ in Eq. (5.20), $v_{n1,\mathrm{f}}(t_k)$ in Eq. (5.24) is an heteroscedastic colored noise.

Moving now to the IV-based estimation of parameters D_s and R_s in Eq. (5.23), let us first rewrite the model as:

$$\mathrm{CSC_f}(s) = \frac{B(s,\theta_\mathrm{coef})}{A(s,\theta_\mathrm{coef})}\alpha I_\mathrm{f}(s) \tag{5.25}$$

where $A(s,\theta_\mathrm{coef})$ and $B(s,\theta_\mathrm{coef})$ respectively stand for

$$\begin{cases} B(s,\theta_\mathrm{coef}) = b_2s^2 + b_1s + b_0 & \text{(5.26a)} \\ A(s,\theta_\mathrm{coef}) = s^2 + a_1s + a_0 & \text{(5.26b)} \end{cases}$$

with $\theta_\mathrm{coef} = [a_1 \;\; a_0 \;\; b_2 \;\; b_1 \;\; b_0]^\mathrm{T}$ and $\alpha = 1/(Fa_sLc_{s,\max})$. The constant $Fa_sLc_{s,\max}$ involves geometric parameters assumed to be known, although the method could be extended to the case where this is not true. Comparing Eq. (5.25) and Eq. (5.23) directly yields the expressions for the unknown parameters:

$$\begin{gathered} a_1 = 189R_s^{-2}D_s, \;\; a_0 = 3465R_s^{-4}D_s^2, \\ b_2 = 21R_s^{-1}, \;\; b_1 = 1260R_s^{-3}D_s \;\text{ and }\; b_0 = 10395R_s^{-5}D_s^2 \end{gathered} \tag{5.27}$$

The identification of the parameter vector θ_coef from Eqs. (5.24), (5.25) cannot be solved by the least-squares approach because the output measurements are corrupted by colored noise. In this scenario, the least squares approach would give biased estimates [128]. Therefore, the so-called simplified refined instrumental variable for continuous-time systems (SRIVC) method [146] is used here. The corresponding algorithm is summarized in Table 5.2. It returns both an estimate of θ_coef, $\hat{\theta}_\mathrm{coef}$, and of the variance of this estimate, $\hat{\sigma}^2_{\hat{\theta}_\mathrm{coef}} = \mathrm{diag}(P_{\theta_\mathrm{coef}})$ [147].

The last step of the procedure consists in recovering the physical parameter estimate $\hat{\theta}_\mathrm{phys} = \left[\hat{R}_s \; \hat{D}_s\right]$. Taking the logarithm of θ_coef component-wise in Eq. (5.27)

TABLE 5.2: The simplified refined instrumental variable method for continuous-time systems for the parameter identification of the transfer function Eq. (5.19) given the measurements Eq. (5.20)†.

Initialization: given the data sequences $Y_{t_N} = \{y_{t_N}, y_{t_{N-1}}, \ldots, y_{t_0}, u_{t_N}, u_{t_{N-1}}, \ldots, u_{t_0}\}$
At iteration $j = 0$ compute

$$\text{LS} - \text{SVF estimate}: \quad \hat{\theta}_0 = \left(\sum_{k=0}^{N} \varphi_{t_k}^{\mathrm{T}} \varphi_{t_k} \right)^{-1} \left(\sum_{k=0}^{N} \varphi_{t_k}^{\mathrm{T}} \mathrm{Y}_{t_k} \right)$$

$$\text{with } \varphi_{t_k} = \frac{1}{(s+\nabla)^2} \left[s^2 \alpha I_{\mathrm{f}},\ s\alpha I_{\mathrm{f}},\ \alpha I_{\mathrm{f}},\ -sC\hat{S}C_{\mathrm{f}},\ -C\hat{S}C_{\mathrm{f}} \right]_{t=t_k}$$

$$\text{and } \mathrm{Y}_{t_k} = \left. \frac{s^2}{(s+\nabla)^2} C\hat{S}C_{\mathrm{f}} \right|_{t=t_k}$$

For iteration $j = 1, 2, \ldots$ compute

$$\text{Auxiliary output}: \quad C\mathring{S}C_{\mathrm{f}}(s) = \frac{B(s, \hat{\theta}_j)}{A(s, \hat{\theta}_j)} \alpha I_{\mathrm{f}}(s)$$

$$\text{Instrumental vector}: \zeta_{t_k} = \frac{1}{A(s, \hat{\theta}_j)} \left[s^2 \alpha I_{\mathrm{f}},\ s\alpha I_{\mathrm{f}},\ \alpha I_{\mathrm{f}},\ -sC\mathring{S}C_{\mathrm{f}},\ -C\mathring{S}C_{\mathrm{f}} \right]_{t=t_k}$$

$$\text{Regressor vector}: \quad \varphi_{t_k} = \frac{1}{A(s, \hat{\theta}_j)} \left[s^2 \alpha I_{\mathrm{f}},\ s\alpha I_{\mathrm{f}},\ \alpha I_{\mathrm{f}},\ -sC\hat{S}C_{\mathrm{f}},\ -C\hat{S}C_{\mathrm{f}} \right]_{t=t_k}$$

$$\text{IV estimate}: \quad \hat{\theta}_{j+1} = \left(\sum_{k=0}^{N} \zeta_{t_k}^{\mathrm{T}} \varphi_{t_k} \right)^{-1} \left(\sum_{k=0}^{N} \zeta_{t_k}^{\mathrm{T}} \mathrm{Y}_{t_k} \right)$$

$$\text{with } \mathrm{Y}_{t_k} = \left. \frac{s^2}{A(s, \hat{\theta}_j)} C\hat{S}C_{\mathrm{f}} \right|_{t=t_k}$$

If convergence occurs according to a user-specified criterion,
e.g. $\frac{||\theta_{j+1} - \theta_j||}{||\theta_j||} < \mu$, or the maximum number of iterations is reached,
then stop, else set $j = j + 1$
Output:
An estimate of the parameter vector θ, $\hat{\theta}$, and the associated error covariance matrix:

$$\text{Error covariance matrix}: \quad P_\theta = \sigma_{v_{n1}}^2 \left(\sum_{k=0}^{N} \zeta_{t_k}^{\mathrm{T}} \zeta_{t_k} \right)^{-1}$$

†For compactness, the time argument is set as an index.

results in:

$$\log_{10} \hat{\theta}_{\text{coef}} = M_1 \log_{10}(\hat{\theta}_{\text{phys}}) + M_2 \tag{5.28}$$

where M_1 and M_2 are given by

$$M_1 = \begin{bmatrix} -2 & 1 \\ -4 & 2 \\ -1 & 0 \\ -3 & 1 \\ -5 & 2 \end{bmatrix} \text{ and } M_2 = \begin{bmatrix} \log_{10}(189) \\ \log_{10}(3465) \\ \log_{10}(21) \\ \log_{10}(1260) \\ \log_{10}(10395) \end{bmatrix}. \tag{5.29}$$

From Eq. (5.28), the following least squares estimate of θ_{phys} (in logarithmic scale) can be obtained:

$$\log_{10}(\hat{\theta}_{\text{phys}}) = \left(M_1^{\text{T}} M_1\right)^{-1} M_1^{\text{T}} \left(\log_{10} \hat{\theta}_{\text{coef}} - M_2\right) \tag{5.30}$$

which provides the means to estimate D_s and R_s, whose respective variances $\hat{\sigma}^2_{D_s}$ and $\hat{\sigma}^2_{R_s}$ come from the error propagation of $\hat{\sigma}^2_{\theta_{\text{coef}}}$. Both estimates can be lumped together in order to have an estimate of the solid-phase diffusion time constant τ_s.

It might be argued that the particle radius R_s is not expected to vary with time and its value could be known in advance through the physical characterization of the battery electrodes. However, its simultaneous estimation along with the solid-phase diffusion coefficient D_s is convenient. Indeed, it was observed that it reduces the estimation error while providing an accuracy indication of the overall estimation. For its part, the solid-phase diffusion coefficient D_s, and therefore the diffusion time constant τ_s, may change in the short term with operating conditions and in the long term with aging [10]. To distinguish between operation-induced and aging-induced parameter changes for a given battery, the following approach could be used. Firstly, parameter estimates are determined at the beginning of the battery life for a set of operating conditions covering the operating range. This yields a set of values $\hat{\tau}_{s,i}(0), i = 1, \ldots, n_{oc}$ where n_{oc} stands for the number of operating conditions. Next, new parameter estimates $\hat{\tau}_{sc,j}$ are determined regularly from current data in a given operating condition, say the j-th one. A suitable SOH indicator is then deduced as

$$\text{SOH} = \frac{\hat{\tau}_{sc,j} - \hat{\tau}_{s,j}(0)}{\hat{\tau}_{s,j}(0)}.$$

Estimation of the Film Resistance

The identification of R_f is simpler than the previous identification of τ_s since it involves the static electrochemical reaction process in contrast to the dynamic solid-phase diffusion process. The output voltage equation given in Eq. (5.3) can be rewritten in the following linear form

$$\text{Y}_2(t_k) = R_f \varphi_2(t_k) + v_{n2}(t_k) \tag{5.31}$$

where

$$\begin{cases} \text{Y}_2(t_k) = y_n(t_k) - \eta_s^+(t_k) + \eta_s^-(t_k) - U^+(t_k) - \Delta\phi_e(t_k) \\ \varphi_2(t_k) = -\dfrac{1}{a_s L} I(t_k) \end{cases}$$

The stated estimation problem can be solved within the output error minimization framework through a least squares (LS) method. The parameter estimate for the film resistance $\hat{R}_f$ is given by

$$\hat{R}_f = \left(\sum_{k=0}^{N} \varphi_2(t_k)^{\text{T}} \varphi_2(t_k)\right)^{-1} \left(\sum_{k=0}^{N} \varphi_2(t_k)^{\text{T}} \text{Y}_2(t_k)\right) \tag{5.33}$$

whose variance can be computed through

$$\hat{\sigma}^2_{R_f} = \sigma^2_{v_{n2}} \left(\sum_{k=0}^{N} \varphi_2(t_k)^{\mathrm{T}} \varphi_2(t_k) \right)^{-1} \tag{5.34}$$

where $\sigma^2_{v_{n2}}$ is the residual variance.

5.2 Validation of State/Parameter Estimation for SOH

During regular battery operation, the available (measurable) information is limited to current, voltage and surface temperature. Therefore, before applying the state/parameter estimation strategies proposed in Section 5.1 to an experimental setup, they are first validated via simulation. This allows us to perfectly know all the battery cell internal states and parameters. Then, experimental validation is carried out with data coming from a LFP half battery cell.

5.2.1 Validation Through Simulation

The SOH indicator proposed in Section 5.1 is now studied using a LFP half battery cell, which is simulated resorting to the DFN model described in Section 2.3. As a half battery cell is considered, the negative electrode OCP corresponding to the lithium metal foil is set to $U^- = 0$ V [21] while i_0^- is a constant. Moreover, two specific features traditionally associated to LFP electrodes are introduced in the DFN modeling framework in the form of parameter variations. On the one hand, a C-rate dependent solid-phase diffusion coefficient $D_s(I(t))$ [57, 148] represents a variable solid-phase diffusion coefficient [54, 55]. On the other hand, a contact-resistance distribution [55, 67] R_f reflects resistive-reactant effects [57, 59, 67]. This distribution is uniform over the interval $[0.835, 1.660]\Omega{\cdot}\mathrm{m}^2$, and it was introduced in a discrete way into the DFN model by associating to each considered spherical particle a contact-resistance sampled from the distribution. The solid-phase diffusion process of the DFN model is implemented through a fifth-order Padé approximation while discretizing all the other PDEs with a central difference method. The system of nonlinear equations is solved using Newton's method at each time step. The parameter values used to set up the simulator are given in the Table C.1, Appendix C.

The input current profile feed to the simulator is the same type as the one used in the experiments of the next Section 5.2.2 below. This profile consists of a series of galvanostatic charge/discharge consecutive steps with three different C-rates: C/5, C/2 and 1C (see Fig. 5.3(a)). For convenience, the charge/discharge cycles that share the same C-rate are called here cycle blocks and each set of charge/discharge cycles within each block is denoted as a period. Therefore, the considered input profile has three cycle blocks made of 3, 5 and 10 periods respectively. The voltage sequence obtained from the simulator (see Fig. 5.3(b), solid black line) was corrupted with a white noise sequence with variance $\sigma^2 = 1$ mV^2.

Before implementing the EKF, we verify in simulation if the stochastic stability conditions provided by Theorem 3.1.2 hold true. This theorem is applied to model Eqs. (5.2),(5.3), which has been modified according to the considered half battery cell, i.e. it is expressed in terms of the LFP positive electrode. The same current profile described above is used. The first condition holds for such a profile, while the second condition is easy to prove from model Eqs. (5.2),(5.3). In order to verify the third condition, the procedure outlined in [125] was followed based on numerical simulations.

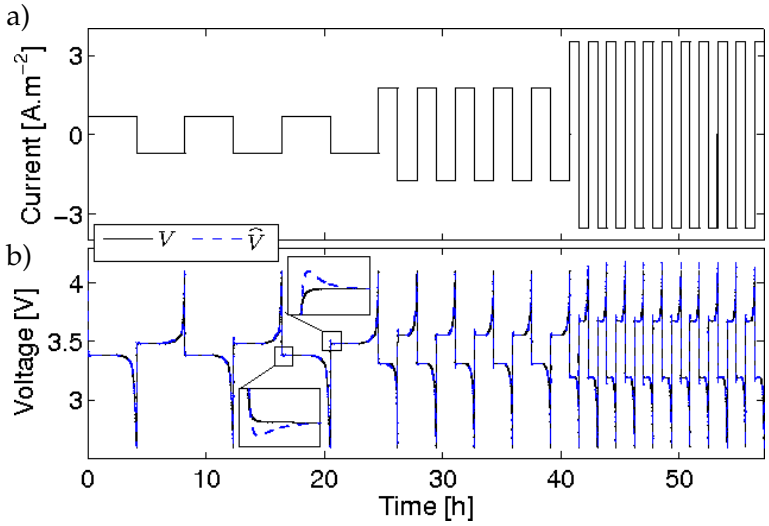

FIGURE 5.3: a) Series of galvanostatic charge/discharge current profile of C/5, C/2 and 1C consecutive cycles; b) simulated voltage (noise free as solid black curve) and predicted voltage (dashed blue curve).

The simulator was set up with the parameters and initial conditions given in Table C.1, Appendix C. Three cases were considered for different filter initializations and measurement noise variance, namely 1) small initial error and small measurement noise, 2) small initial error and large measurement noise, and 3) large initial error and small measurement noise. The values of $P(0)$ and $Q_{s\theta}$ were kept constant for all the cases, namely

$$\begin{aligned} \text{diag}(P(0)) &= \left[10^{-10}, 10^{-10}, 10^{-10}, 10^{-17}, 10^{-9}\right] \\ \text{diag}(Q_{s\theta}) &= \left[10^{-21}, 10^{-19}, 10^{-13}, 10^{-21}, 10^{-10}\right], \end{aligned} \tag{5.35}$$

whereas Table 5.3 summarizes the value of each variable per considered case. The units of P and $Q_{s\theta}$ in Eq. (5.35) are coherent with the units of the state vector.

TABLE 5.3: Initial estimates and measurement noise variance for the stochastic stability study.

Case	$\hat{x}_{s\theta,0}$ [-,-,-,s^{-1},Ω·m^2]	R [mV^2]
1	$\left[[0.41, 0.41, 15.78] \cdot 10^{-2}, 1.92 \cdot 10^{-5}, 1.3\right]^{\mathrm{T}}$	10^{-2}
2	$\left[[0.41, 0.41, 15.78] \cdot 10^{-2}, 1.92 \cdot 10^{-5}, 1.3\right]^{\mathrm{T}}$	10^{2}
3	$\left[[50.00, 50.00, 50.00] \cdot 10^{-2}, 19.20 \cdot 10^{-5}, 1.0\right]^{\mathrm{T}}$	10^{-2}

The simulation results are shown in Fig. 5.4. The input current profile together with the noiseless output voltage are shown in Fig. 5.4(a), whereas the simulated and estimated CSC and the associated estimation error are depicted in Figs. 5.4(b) and (c), respectively. The changes in C-rate are clearly observed in Fig. 5.4(c). The best scenario is case 1, where the state estimate tracks well the simulated state and the error remains close to zero. Cases 1 and 2 share the same state initialization. In both cases, as soon as a different current density kicks in, the estimate suddenly drifts apart. Although the transient error is higher for the estimate of case 1, this estimate converges faster than the one of case 2 given the smaller measurement noise and hence the higher filter gain of case 1. Cases 1 and 3 have the same measurement noise variance, but the higher initial error of case 3 causes its estimation error to be

larger than in the other two cases for the first two applied currents. Nevertheless, this error is considerably reduced for the last applied C-rate to the extent that the estimation error of case 3 is similar to the one of case 1 once the large initial error transient is overcome. Thus, it is observed that the estimation error remains bounded for large initial error or large measurement noise given the $P(0)$ and $Q_{s\theta}$ provided in Eq. (5.35).

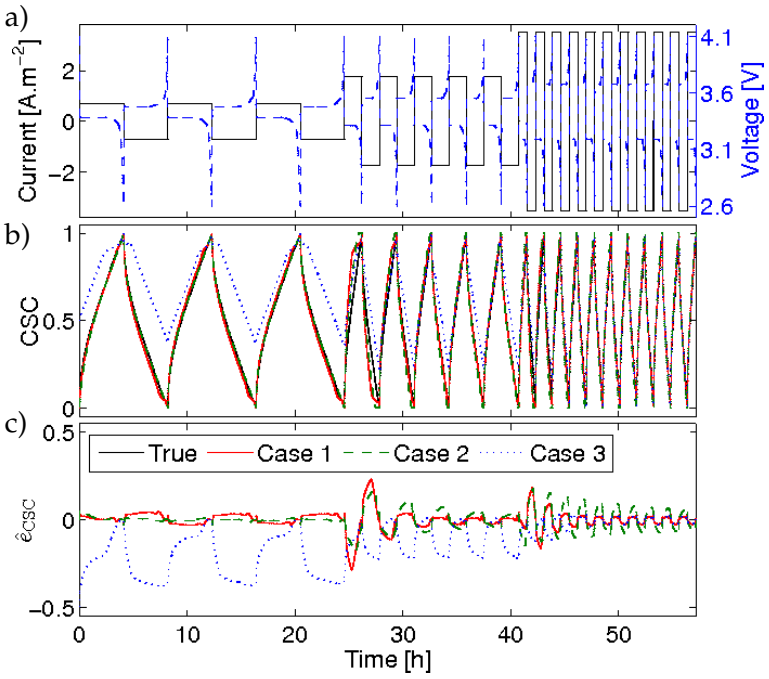

FIGURE 5.4: Stochastic stability simulation study considering three cases, namely: 1) small initial error and small measurement noise (solid red curve), 2) small initial error and large measurement noise (dashed green curve), and 3) large initial error and small measurement noise (dotted blue curve). The plotted signals are a) series of galvanostatic charge/discharge current profile of C/5, C/2 and 1C consecutive cycles, and associated voltage (noise free simulation); b) simulated (solid black curve) and estimated CSC; c) estimation error of CSC.

Now that the constrained EKF has been proven to be stochastically stable, we are in position to confidently use it. The initial conditions and tuning parameters used for setting the EKF are

$$\begin{aligned} \hat{x}_{s\theta}(0) &= \left[[0.19, 0.19, 0.19] \cdot 10^{-2}, 6.40 \cdot 10^{-6}, 1.30\right]^{\mathrm{T}}, \\ \mathrm{diag}(P(0)) &= \left[10^{-10}, 10^{-10}, 10^{-10}, 10^{-17}, 10^{-9}\right], \\ \mathrm{diag}(Q_{s\theta}) &= \left[10^{-21}, 10^{-19}, 10^{-13}, 10^{-21}, 10^{-10}\right], \end{aligned} \tag{5.36}$$

where $\left[\hat{\mathrm{SOC}}(0), \hat{c}_{s,2}(0), \hat{\mathrm{CSC}}(0)\right]$ were obtained by inverting the OCV function taken from [148]. Regarding the parameters, g_s $(= R_s^{-2} D_s)$ was initialized with a value of $D_s = 10^{-17}$ m^2·s^{-1} within the range reported in the literature, i.e. $[10^{-22}, 10^{-14}]$ m^2·s^{-1} [67], along with a particle radius of $R_s = 1.25 \cdot 10^{-6}$ m provided by the manufacturer. For its part, R_f was initialized by comparing the voltage drop at the onset of the voltage-capacity curve of the synthetic data with that obtained from the EHM Eqs. (5.2),(5.3). The measurement noise variance R was set to 10^{-2} mV^2, which is two orders of magnitude less than the actual noise value, to improve convergence

speed.

Some guidelines coming from the physics of the problem were followed in order to set the process noise variance matrix. First of all, the solid phase concentration state estimates within each charge/discharge cycle have to be smooth; no abrupt changes are allowed. Moreover, the CSC estimate has to cover all its possible range, from 0 to 1, since this ensures that the battery-cell voltage achieves the maximum and minimum cut-off voltages. The transient of these state estimates should vanish in one period. The g_s estimate has to slowly vary between cycles and blocks, and to exhibit some convergence trend at the end of each block. The R_f estimate is responsible for the ohmic drop of the voltage within the intermediate composition region, and therefore it has to ensure that the filtered output voltage is as close as possible to the measured voltage.

The state estimation results are shown in Fig. 5.5 for SOC and Fig. 5.6 for CSC. Fig. 5.5(a) shows the simulated and predicted SOC, whereas Fig. 5.5(b) portrays the estimation error that is incurred. The same convention is used in Figs. 5.6(a)-(b) for the CSC. From the figures it follows an overall good match after transient between simulated and predicted battery internal states. Most of the transient dynamics of the filter appear in the first period of each cycle block, with estimation errors as large as [0.20, 0.17, 0.12] for SOC and [0.41, 0.29, 0.18] for CSC during C/5, C/2 and 1C, respectively. After these first periods, the estimation error converges towards zero, remaining smaller than 0.09 for both states. The predicted voltage coming from the EKF based on the EHM Eqs. (5.2),(5.3) is shown in Fig. 5.3(a).

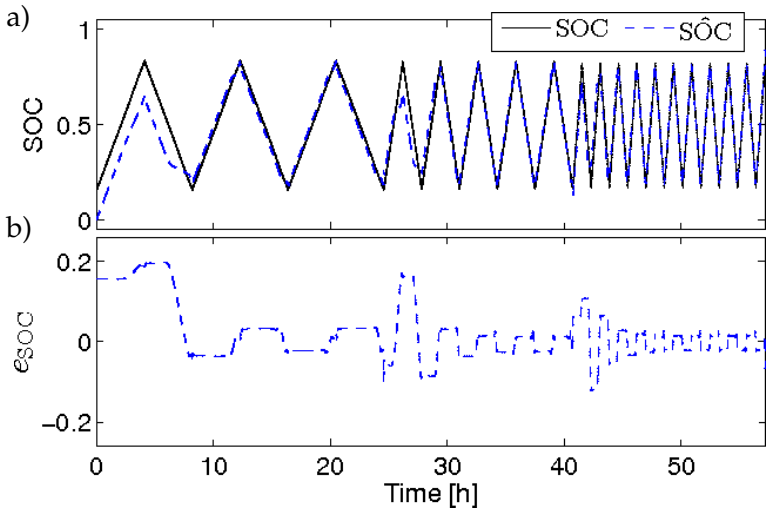

FIGURE 5.5: State estimation study: a) simulated (solid black curve) and predicted SOC (dashed blue curve); b) SOC estimation error.

The parameter estimation results are displayed in Fig. 5.7, where both the fixed parametric values of the simulation and the parametric time evolution of the estimation are shown. Fig. 5.7(a) corresponds to the parameter g_s while Fig. 5.7(b) corresponds to the film resistance R_f, where the bounds (minimum and maximum values) on the contact-resistance distribution R_r are represented by the solid and dashed black constant curves. From 5.7(a) follows that $\hat{g}_s$ exhibits a monotonic increase within the considered time horizon and in turn within each cycle block. Within each block, the g_s estimate moves towards its true value specified in the simulator ($g_s = R_s^{-2} D_s$, see Table C.1, Appendix C) but it requires more periods to converge as the C-rate increases. For its part, two resistive contributions can be

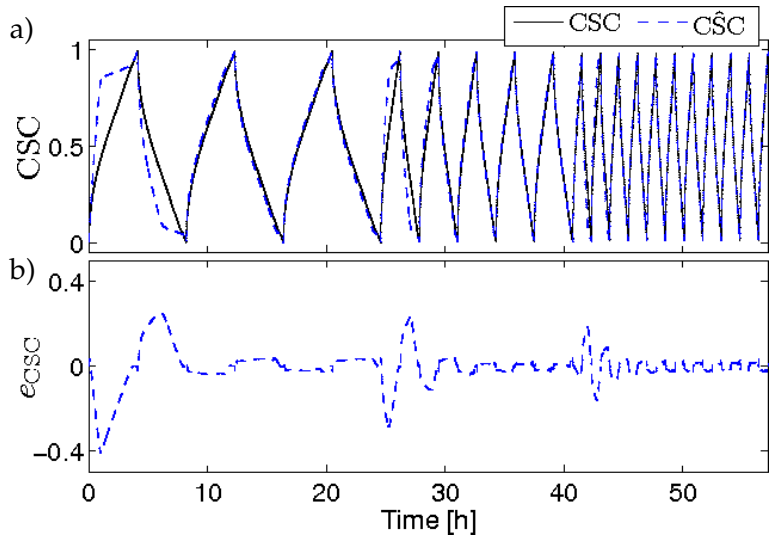

FIGURE 5.6: State estimation study: a) simulated (solid black curve) and predicted CSC (dashed blue curve); b) CSC estimation error.

ascribed to $\hat{R}_f$ in Fig. 5.7(b). The first one is a constant resistance along the considered time horizon, whereas the second one is a resistance that increases non-linearly (in contrast with the proposition in [140]) in the extreme composition regions at each charge/discharge cycle, i.e. where the nonlinearities prevail. The former and the latter contributions can be associated to a film resistance and the LFP resistive reactant feature, respectively. While the film resistance contribution remains within the R_r bounds $(0.835, 1.660)$ $\Omega.\text{m}^2$, the resistive-reactant contribution tends to overstep these bounds by forming the spikes clearly observed in the figure. These spikes are artifacts that cause a small overpotential in the filtered output (inset plot), but it is corrected within seconds (less than 10 s). These artifacts might be avoided by modifying the tuning parameters of the filter, but it would render a slower convergence.

The CSC estimate coming from the EKF is now used to obtain a refined estimate parameter set $\hat{\theta}_{\text{phys}} = [\, \hat{D}_s,\ \hat{R}_s \,]$ and $\hat{R}_f$ for each C-rate. The SRIVC estimation was carried out using the available data after removing the transient, i.e. the first 1, 2 and 4 periods for C/5, C/2 and 1C, respectively. The need to account for longer transient periods as the current rate increases comes from the fact that both current and diffusion coefficient are approximately doubled simultaneously. Table 5.4 shows the D_s and R_s refined estimates, along with their standard deviation. By comparing these results with the true values (Table C.1, Appendix C), it is observed that the diffusion coefficient exhibits relative errors of 15%, 9% and 13%, while the particle radius presents relative errors of 10%, 4% and 9% for C/5, C/2 and 1C, respectively. This error level is acceptable in the considered framework aiming at SOH monitoring as will be justified below.

In spite of the gap between estimated and true parameters, their standard deviations do not reflect such a difference. This issue can be explained in terms of modeling error. Indeed, the parameter estimation procedure relies on a single-particle third-order model (for both the Kalman filter and the SRIVC method), while the simulator relies on a multi-particle higher-order model (fifth-order model). In order to exhibit that the misfit stems from modeling uncertainties, the fit goodness, defined

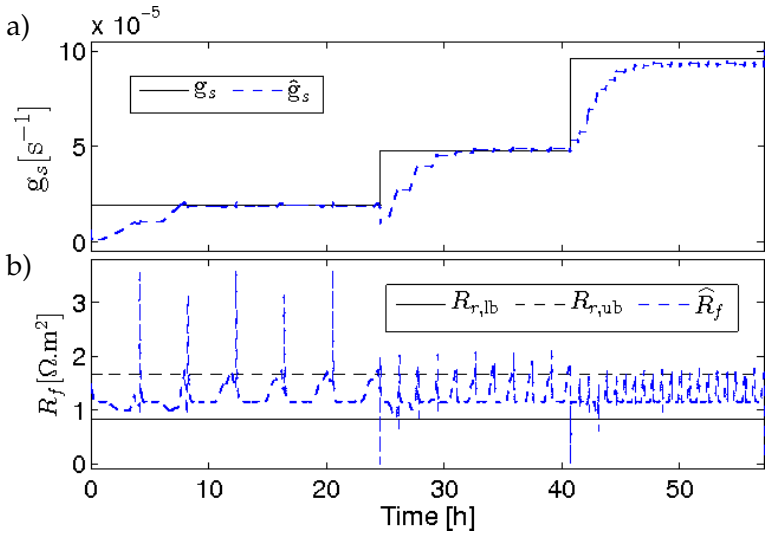

FIGURE 5.7: State estimation study: a) fixed (solid black curve) and predicted g_s (dashed blue curve); b) solid and dashed black lines respectively depict the lower and upper bound of the contact-resistance distribution R_r while dashed blue curve is the predicted R_f.

TABLE 5.4: Results obtained using the SRIVC method for the estimation of D_s and R_s, and the LS method for the estimation of R_f on each cycle block of simulated data.

C-rate	$\hat{D}_s \cdot 10^{17}$	$\hat{\sigma}_{D_s} \cdot 10^{19}$	$\hat{R}_s \cdot 10^{6}$	$\hat{\sigma}_{R_s} \cdot 10^{9}$	$\hat{R}_f$	$\hat{\sigma}_{R_f} \cdot 10^{5}$
	$[m^2 \cdot s^{-1}]$		[m]		$[\Omega \cdot m^2]$	
C/5	2.55	1	1.127	3	1.2951	10
C/2	6.83	5	1.201	5	1.26830	4
1C	13.0	14	1.357	8	1.23295	2

by the following metric, is evaluated:

$$\text{Fit} = 100\left(1 - \frac{\parallel \hat{\text{CSC}} - \text{CSC} \parallel}{\parallel \hat{\text{CSC}} - \bar{\text{CSC}} \parallel}\right) \tag{5.37}$$

where $\parallel \cdot \parallel$ denotes the 2-norm, $\hat{\text{CSC}}$ is the EKF estimate of the surface concentration, $\bar{\text{CSC}}$ is the mean of $\hat{\text{CSC}}$ and CSC is captured from the third-order Padé approximation Eq. (5.19). CSC is evaluated twice, respectively with the estimated parameters $\hat{\theta}_{\text{phys}}$ from Table 5.4, and with the true parameters $\theta = [D_s, R_s]$ from Table C.1, Appendix C, which results in the values of the fit reported in Table 5.5. In both cases the fit has the same order of magnitude, demonstrating that modeling uncertainties rather than parameter estimation is the main source of misfit.

The R_f refined estimates obtained using the LS method and the associated standard deviation are also shown in Table 5.4, where it can be seen that the film resistance estimates are within the considered contact-resistance range (Table C.1, Appendix C).

In order to have a benchmark to compare the simulation results on SOH estimation obtained from the SRIVC method, the widely popular least squares estimation method is now used to estimate the same parameter set $\theta_{\text{phys}} = [D_s, R_s]$. This method has been already used to tackle similar battery parameter identification problems as

TABLE 5.5: Fit results obtained from comparing the EKF estimation with the Padé approximation model using the true (θ) and estimated ($\hat{\theta}_{\text{phys}}$) parameters.

C-rate [h^{-1}] \ Fit [%]	θ	$\hat{\theta}_{\text{phys}}$
C/5	81	86
C/2	79	84
1C	79	72

the one considered here [87, 91, 77]. The parameter estimates obtained from the LS method are denoted as $\hat{D}_s^{\text{LS}}$ and $\hat{R}_s^{\text{LS}}$, which are shown in Table 5.6 together with their associated standard deviation. In contrast to the SRIVC method, the LS parameter estimates for D_s and R_s exhibit a bigger error with respect to the true values (Table C.1, Appendix C). The diffusion coefficient shows relative errors of 62%, 88% and 96% whereas the particle radius incurs in 25%, 40% and 100% of relative error for C/5, C/2 and 1C, respectively. Not only these estimates are more biased than the ones obtained through SRIVC method, but they are also inconsistent since the wrong trend can be seen as the magnitude of the current applied to the battery becomes larger. It is worth recalling that the true value of D_s increases with battery current while R_s is constant throughout the simulation studies, which are trends revealed by the SRIVC method despite some offset in the actual value of the estimated parameters. Indeed, in presence of colored noise on the output data, the LS method applied to continuous-time systems is known to provide biased estimated parameters [128].

TABLE 5.6: Results obtained using the LS method for the estimation of D_s and R_s on each cycle block of simulated data.

C-rate	$\hat{D}_s^{\text{LS}} \cdot 10^{17}$	$\hat{\sigma}_{D_s^{\text{LS}}} \cdot 10^{19}$	$\hat{R}_s^{\text{LS}} \cdot 10^{6}$	$\hat{\sigma}_{R_s^{\text{LS}}} \cdot 10^{9}$
	[$m^2 \cdot s^{-1}$]		[m]	
C/5	1.15	5	0.933	20
C/2	0.88	4	0.755	20
1C	0.66	1	0.002	0.01

The above results demonstrate that the proposed approach is able to detect parameter changes in the order of 100% with less than 15% of relative error (for e.g. D_s at C/5) once the transient has vanished. Given the simplicity of the third-order model compared to the target system, the obtained results are satisfactory. Even though the results focus on parameter changes of a LFP battery cell during regular operation, the considered parameters are directly related with aging processes and their evolution reflects the SOH of most lithium-ion batteries. Indeed, magnitude changes of more than 70% and 400% are expected for D_s and R_f, respectively, after 360-500 operating cycles [37, 82, 83, 84]. Therefore the methodology is suitable for SOH monitoring. The proposed approach is now tested in the light of experimental data in the next section.

5.2.2 Experimental Validation

After the validation through simulation, we had the opportunity to get experimental data from a LFP half battery cell gathered by Prof. Alexandre Léonard at the Department of Chemical Engineering, Université de Liège. Such data was exploited to assess the performance of the proposed approach. This section introduces the

experimental setup and testing conditions, followed by the discussion of the obtained results.

Setup and Testing Conditions

The considered positive electrode consists of lithium iron phosphate, $LiFePO_4$ (LFP), as active material provided by beLife/Prayon (Pholicat FE100). Slurries containing LFP, binder and conducting carbon (Timcal C-nergy Super C65) in weight ratios 75:5:20 respectively were coated on Al acting as current collector. After drying at 60°C overnight, the coated electrodes were weighted, giving access to the mass of active material with good accuracy (≈ 2 mg·cm^{-2}). These electrodes were then dried under vacuum ($2 \cdot 10^3$ Pa) during 2 h and introduced in a glovebox (M-Braun) under argon atmosphere for half-cell assembly.

To evaluate the electrochemical behavior, the formed electrodes were assembled in CR2032 coin-cells, with 2 Celgard® separators (25 μm thickness and 16 mm diameter each) soaked with 80 μL of electrolyte (lithium hexafluorophosphate, $LiPF_6$ 1 mol·L^{-1} in an ethylene carbonate:diethyl carbonate – 1:1 mixture). 15-mm diameter metallic lithium disks were used as reference- and counter-electrode (half-cell design). The half-cells were then tested in galvanostatic cycling mode on a BioLogic VMP3 multichannel potentiostat at 25°C in a temperature-controlled climate chamber. Galvanostatic charge/discharge was carried out at C-rates of C/5, C/2 and 1C between 2.0 and 4.2 V vs. Li^+/Li. The equilibrium potential of the material was obtained from the average of charge and discharge curves at a C-rate of C/100. The maximum experimental capacity of the material was 155 mAh·g^{-1}.

Results and Discussion

A set of current and voltage data was gathered from the above introduced experiment. Notice that both the simulation of Section 5.2.1 and the experiments of the current section share the same type of input current profile. The only difference is in the last cycle block of the experimental data, where five periods are considered instead of ten (see Fig. 5.8(a) and (b) for measured current and voltage, respectively, coming from the LFP half battery cell).

The same procedure for state initialization and parameter tuning outlined in the simulation Section 5.2.1 to set up the constrained EKF was followed in the experiments. Nevertheless, the OCP function used with experimental data was the one obtained from LFP half battery cell measurements at C/100. The measured OCP was fitted using a nonlinear least squares method and its functional form is given by Eq. (C.1), Appendix C. The initial state and tuning parameter values were the following

$$\begin{aligned} \hat{x}_{s\theta}(0) &= \left[[8.41, 8.41, 8.41] \cdot 10^{-4}, 6.40 \cdot 10^{-6}, 1.00\right]^{\mathrm{T}}, \\ \mathrm{diag}(P(0)) &= \left[10^{-10}, 10^{-10}, 10^{-10}, 10^{-17}, 10^{-9}\right], \\ \mathrm{diag}(Q_{s\theta}) &= \left[10^{-12}, 10^{-13}, 10^{-14}, 10^{-22}, 10^{-12}\right], \end{aligned} \tag{5.38}$$

where the first three components of the state vector are dimensionless, and the fourth and fifth components are associated to the inverse of the diffusion time constant $[\mathrm{s}^{-1}]$ and an ohmic resistance $[\Omega \cdot \mathrm{m}^2]$, respectively. The units of P and $Q_{s\theta}$ are coherent with the units of the state vector. While the variance of the measured voltage was found to be between $(1.1, 14.2) \cdot 10^{-1}$ mV^2 according to the considered cycle block, the measurement noise variance was set to a smaller value of 10^{-2} mV^2 to improve convergence speed.

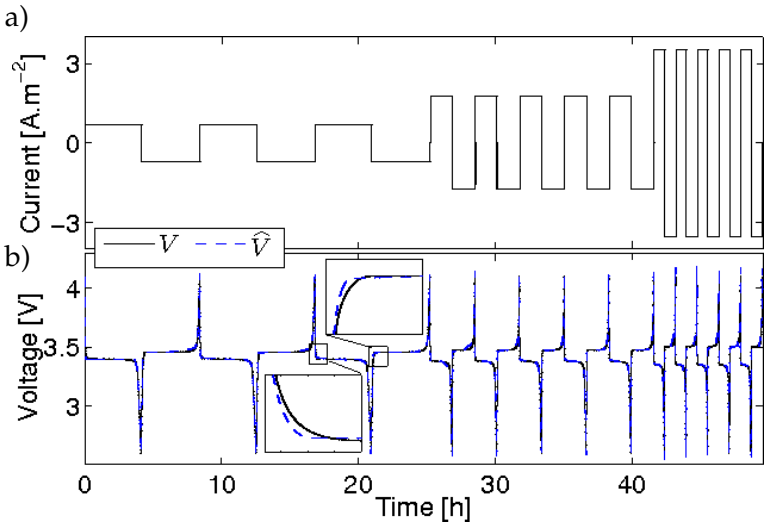

FIGURE 5.8: a) Series of galvanostatic charge/discharge current profile of C/5, C/2 and 1C consecutive cycles carried out at 25°C between 2.0 and 4.2 V; b) experimental (solid black curve) and predicted voltage (dashed blue curve).

Fig. 5.9(a) presents the rightly initialized Coulomb-counted SOC and the SOC estimated by the filter, whereas Fig. 5.9(b) shows the estimated CSC. Although the CSC estimate covers the entire range of allowed values (0 and 1, respectively), the SOC estimate exhibits a smaller operating range (from approximately 0.2 to 0.8). This cyclic behavior can be ascribed to the slow diffusion dynamics of the LFP chemistry, which results in a difference between the lithium concentration at the outer shell and the inner core of the spherical particle model. The resulting model output voltage is shown in Fig. 5.8(b).

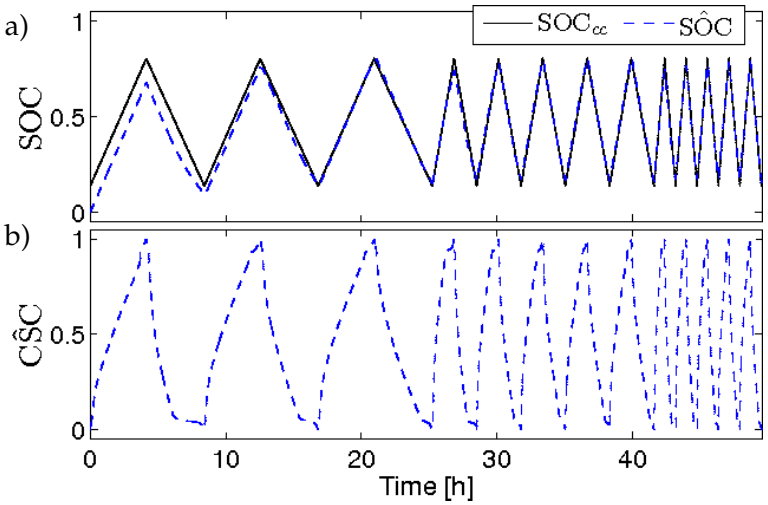

FIGURE 5.9: State estimation study: a) Coulomb-counted (solid black curve) and estimated SOC (dashed blue curve); b) estimated CSC.

Fig. 5.10(a) and (b) shows the tracking of the uncertain parameters, namely g_s and R_f respectively, together with the mean value of a contact resistance determined

experimentally $\bar{R}_r$. The estimated g_s follows a similar trend as in the simulation Section 5.2.1. Considering a constant particle radius, it can be argued that the diffusion coefficient changes not only with C-rate but even within each cycle block. Nevertheless, the simulation in Section 5.2.1 showed that g_s time-variation within each block is due to the transient in the estimate and not because of an actual parameter variation.

With regard to the other parameter, the film resistance, there are multiple ways to obtain a reference value from experimental data [31, 149]. Here, this experimental value was computed using the following expression:

$$\bar{R}_r = a_s L \frac{\Delta V}{\Delta I}, \tag{5.39}$$

where ΔV is the first potential drop at the onset of the discharge voltage curve as soon as a current is applied, and ΔI is the current magnitude that causes such a voltage change. The R_f estimate coming from the filter underestimates the contact resistance with respect to the reference value $\bar{R}_r$. However, $\bar{R}_r$ might be larger than the real impedance of the battery since it was computed just after the current flip from charge to discharge. Therefore, effects such as concentration gradients might be included in $\bar{R}_r$. Even if $\bar{R}_r$ is an overestimation, its order of magnitude and decreasing trend as the current rate increases coincides with those ones of the $\hat{R}_f$. The same two contributions observed in the simulation Section 5.2.1 are exhibited by the R_f estimate, namely the film resistance and the resistive-reactant feature. Moreover, this estimate also shows similar spikes as the ones observed in simulation. Nonetheless, these spikes have smaller magnitude than in simulation, which also reduces the fictitious overpotential in the filtered output (inset plot in Fig. 5.8(b)). Again, the spikes are artifacts made up by the filter given the tuning parameters.

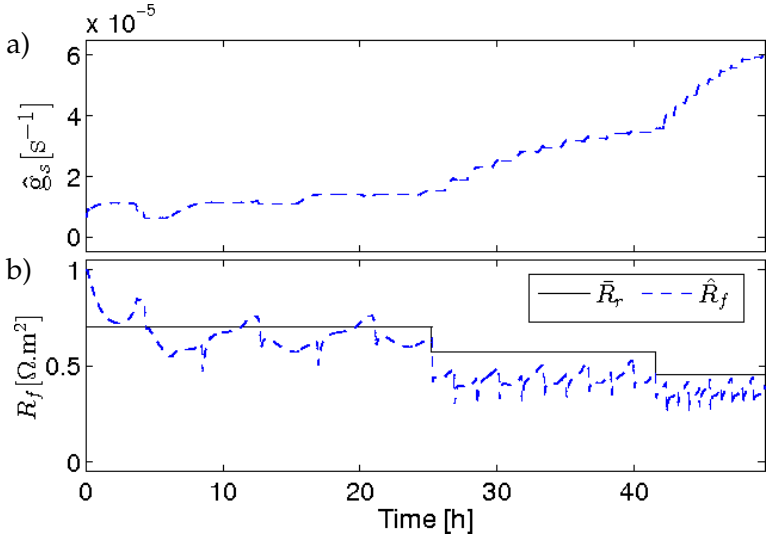

FIGURE 5.10: State estimation study: a) estimated g_s; b) experimentally determined contact resistance mean $\bar{R}_r$ (solid black curve) and estimated R_f (dashed blue curve).

In contrast to other modeling efforts, the EHM Eqs. (5.2),(5.3) used here does not embed any special feature or mechanism limitation, such as bulk-related rate [54, 55] or resistive-reactant rate limitations [57, 59, 67]. This model relies on few assumptions and gives "freedom" to these parameters, that in turn govern the controversial electrochemical mechanism of LFP electrode operation (see Section 2.3). The slowly

time-varying parameters are expected to adjust their values according to the data, revealing the underlying electrochemical mechanism instead of imposing it. This is only possible in a state/parameter estimation setting.

The SRIVC method is now used to split $\hat{g}_s$ into its contributions $\hat{D}_s$ and $\hat{R}_s$. The data was pretreated similarly as in simulation Section 5.2.1, by removing the first 1, 2 and 4 transient periods for C/5, C/2 and 1C, respectively. The obtained refined estimates and associated standard deviations are shown in Table 5.7. As expected, $\hat{D}_s$ increases for each cycle block, whereas $\hat{R}_s$ can be considered as constant. Therefore, the $\hat{g}_s$ dynamics can be mainly ascribed to D_s. This further motivates the notion of a C-rate dependent diffusion coefficient [57] to describe the rate capability of LFP electrodes. Given these results, it seems clear that the electrochemical reaction is facilitated at the bulk diffusion level with higher current densities.

TABLE 5.7: Results obtained using the SRIVC method for the estimation of D_s and R_s, and the LS method for the estimation of R_f on each cycle block of experimental data.

C-rate	$\hat{D}_s \cdot 10^{17}$	$\frac{\hat{\sigma}_{D_s}}{\cdot 10^{19}}$	$\hat{R}_s \cdot 10^{6}$	$\frac{\hat{\sigma}_{R_s}}{\cdot 10^{8}}$	$\hat{R}_f$	$\frac{\hat{\sigma}_{R_f}}{\cdot 10^{5}}$
	$[\mathrm{m}^2 \cdot \mathrm{s}^{-1}]$		[m]		$[\Omega \cdot \mathrm{m}^2]$	
C/5	1.15	4	2.42	1	0.5961	10
C/2	5.09	3	2.19	2	0.38591	4
1C	28.0	20	2.3	10	0.31090	3

The particle radius R_s refined estimate is c.a. $2.30 \cdot 10^{-6}$ m in contrast with the value of $1.25 \cdot 10^{-6}$ m provided by the manufacturer. This discrepancy can be explained in terms of the real infinite-dimensional system and the considered reduced-order model. While LFP electrodes are comprised by a particle-size distribution within a range of c.a. $(0.1, 2.0) \cdot 10^{-6}$ m, the reduced-order model is based on a single-particle approach. Therefore, the particle radius estimate should be considered as an apparent one describing LFP crystals agglomeration. Considering the radius of agglomerates as the characteristic diffusion length renders larger values of diffusion coefficient [150].

Finally, the film resistance parameter variation is obtained using the LS method and it is shown in Table 5.7. The overall trend of the film resistance estimate is to decrease its value as the C-rate increases, suggesting that the reaction becomes easier at the surface reaction level besides the bulk diffusion level assessed above.

5.3 State/Parameter Estimation for Battery Monitoring & FDI

This section deals with the diagnosis problem of internal and sensor faults occurring simultaneously in a battery. As opposed to the EKF in Section 5.1, this section focuses on an unscented Kalman filter for state/parameter estimation (orange block in Fig. 5.11) and it motivates this observer upgrade first. More specifically, a dual unscented Kalman filter is proposed in this section, followed by a FDI system for internal and sensor faults. The standard UKF of Section 2.4 is modified to account for the nonlinear algebraic constraint arising from side reactions taking place. The state observer provides residuals (blue "residual generator" block in Fig. 5.11), which are statistically post-processed with a log-likelihood ratio algorithm (blue "decision system" block in Fig. 5.11) to determine whether a sensor fault has occurred. This procedure enables the detection and isolation of both internal faults, such as capacity and power fade, and sensor faults, for voltage and temperature measurements.

It is worth stressing that while the work in Section 5.1 aims at SOH tracking, the work in this section aims at sensor fault diagnosis while accounting for model uncertainty of SOH-related parameters. Both pieces of work are not mutually exclusive by no means, and future contributions should combine these two ingredients in an unified framework.

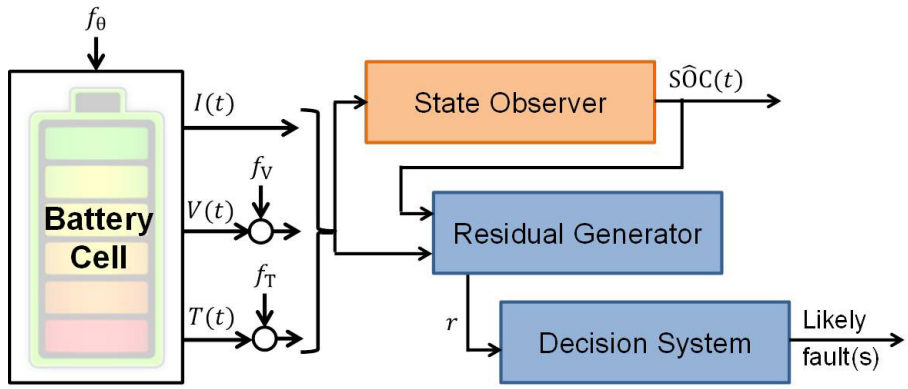

FIGURE 5.11: Block diagram of the fault detection and isolation scheme.

5.3.1 From the EKF to the UKF

The previous Section 5.1.1 introduced an EKF as a basis for the state estimation of a lithium-ion battery. Although simple and widely used in engineering, the EKF comes associated with intrinsic errors due to the model linearization it relies on. One way to improve upon the EKF is to resort to another Kalman-based nonlinear filter, namely the unscented Kalman filter (UKF). In contrast to the EKF, the UKF avoids linearization by approximating the probability distribution of the state random variable, and it propagates such sampled distribution through the true nonlinear system. To see the advantages of using the UKF over the EKF when a lithium-ion battery model is concerned, let us take two of the most nonlinear transformations of the *e*EHM of Section 4.2, namely the core temperature and voltage equations given

by:

$$V = \Delta U_s^{\pm} + \Delta \eta_s^{\pm} + \Delta \phi_e - R_f F I \tag{5.40}$$

$$T_{bc}^{+1} = T_{bc} + \frac{T_s}{\rho_c C_{pc}} \left(k_c \left(T_{bs} - T_{bc} \right) - I \left(\Delta U_b^{\pm} - T_{bc} \Delta \frac{\partial U_b^{\pm}}{\partial T_{bc}} - V \right) \right) \tag{5.41}$$

where the time argument has been dropped for each state variable, Eq. (5.40) and the right-hand side of Eq. (5.41) are referred to the k time instant, while the variable T_{bc}^{+1} in Eq. (5.41) is referred to the $k+1$ time instant. The sampling time is represented by T_s. Both Eqs. (5.40),(5.41) depend on a state vector of the form $x_{sT} = [\text{SOC}, \text{CSC}, T_{bc}, T_{bs}]^{\text{T}}$. However, let us fix $\text{SOC} = 0.50$ and $T_{bs} = 298$ K in order to have two nonlinear functions dependent on two state variables only, namely $x = [\text{CSC}, T_{bc}]^{\text{T}}$. The nonlinear transformation Eqs. (5.40),(5.41) can be written in general form as

$$y_{nl} = h_{nl}(x), \tag{5.42}$$

where $y_{nl} = [V, T_{bc}^{+1}]^{\text{T}}$. The true mean and covariance of the random variable x subject to the nonlinear transformation Eq. (5.42) are respectively given by

$$\begin{aligned} \bar{y}_{nl} &= \mathbb{E}[h_{nl}(x)] \\ P_{nl} &= \mathbb{E}[(y_{nl} - \bar{y}_{nl})(y_{nl} - \bar{y}_{nl})^{\text{T}}]. \end{aligned} \tag{5.43}$$

For the sake of illustration, let us assume that CSC and T_{bc} are independent random variables, whose mean and variance are respectively denoted by $\bar{x} = [\bar{\text{CSC}}, \bar{T}_{bc}]^{\text{T}}$ and $P_x = \text{diag}\{[\sigma_{\text{CSC}}^2, \sigma_{T_{bc}}^2]\}$. Considering the first-order linearization of Eq. (5.42) and taking the expected value of both sides yields

$$\bar{y}_l \approx h_{nl}(\bar{x}) \tag{5.44}$$

with an associated covariance matrix given by

$$P_l \approx \left(\left. \frac{\partial h}{\partial x} \right|_{\bar{x}} \right) P_x \left(\left. \frac{\partial h}{\partial x} \right|_{\bar{x}} \right)^{\text{T}}. \tag{5.45}$$

Finally, the unscented transform (UT) generates a set of $2n+1$ sigma points (see Section 3.1.3), with $n = 2$ for system Eqs. (5.40),(5.41), according to

$$\mathcal{X} = \left[\bar{x} \;\; \bar{x} + \left(\sqrt{nP} \right)_l \;\; \bar{x} - \left(\sqrt{nP} \right)_l \right], \;\; l = 1, \ldots, n \tag{5.46}$$

where n is the dimension of x and $(\cdot)_l$ is the l-th column of the matrix. The mean approximation is obtained by transforming the sigma points of Eq. (5.46) using the nonlinear function in Eq. (5.42) as

$$\mathcal{Y} = h_{nl}(\mathcal{X}), \tag{5.47}$$

and then taking the weighted sum of the transformed sigma points according to

$$\bar{y}_{\text{UT}} = \sum_{l=0}^{2n} W_l \mathcal{Y}_l \tag{5.48}$$

with $W_0 = 0$ and $W_l = 1/(2n)$, $l = 1, \ldots, 2n$. The associated covariance matrix is given by

$$P_{\mathrm{UT}} = \sum_{l=0}^{2n} W_l \left(\mathcal{Y}_l - \bar{y}_{\mathrm{UT}}\right) \left(\mathcal{Y}_l - \bar{y}_{\mathrm{UT}}\right)^{\mathrm{T}}. \tag{5.49}$$

In general, it is difficult to transform a probability density function through a nonlinear function. Exact analytic nonlinear transformations with indicated mean and variance can only be obtained for simple transformations such as polar-to-rectangular coordinate transformation [121]. For the nonlinear system at hand Eq. (5.42), we exploit simulation to show what happens to random variables when propagated through the system. For this end, 10^4 sample points are generated randomly for CSC and T_{bc}, which are assumed to be normally distributed. Three cases are considered, namely 1) nominal case, 2) high mean CSC case and 3) high mean and variance T_{bc} case. The mean and standard deviation values used for each case are shown in Table 5.8.

TABLE 5.8: Mean and standard deviation values of the random variables used to simulate model Eqs. (5.40),(5.41).

Case	$\bar{\mathrm{CSC}}$	σ_{CSC}	$\bar{T}_{bc}$ [K]	$\sigma_{T_{bc}}$ [K]
1	0.50	0.01	298	0.5
2	0.95	0.01	298	0.5
3	0.50	0.01	318	7

The results obtained for cases 1-3 in Table 5.8 are depicted in Figs. 5.12(a)-(c), respectively. The gray points denoted as "PD" correspond to the sampled *a posteriori* probability distribution. The empirical estimate of the mean and covariance at the output of the nonlinearity, together with the mean and covariance approximated via linearization and unscented transformation, are shown in the figure with symbols and ellipses of red, green and blue colors, respectively. As shown in Fig. 5.12(a), in nominal conditions of SOC = 50% and ambient temperature of 25°C (case 1), the mean and covariance estimates obtained from linearization and the unscented transformation are very close to those of the nonlinear system. However, when the mean of the first and second state variables is increased towards more extreme conditions and their associated variance are stretched over a wider operating range (cases 2 and 3), the difference between the considered approximations becomes more accentuated. In such situations, the linearized approximation suffers a considerable mean bias with respect to that of the empirical mean, which is not so marked for the unscented transform mean as seen in Figs. 5.12(b)-(c). Therefore, the UKF is able to approximate nonlinear functions with a higher accuracy than the EKF, which implies that the battery states can be confidently estimated in a wider operating range by using such UKF.

5.3.2 The Dual Unscented Kalman Filter for NLDAE Systems

In contrast to the previous Section (5.1), the specific model Eqs. (5.2),(5.3) is dropped and the more general *e*EHM Eqs. (4.63)-(4.67) is recovered including state, parameter, output and algebraic equations. Compared to the model of the previous section that was able to handle mild applied currents (less than 1C), this more complex model allows one to obtain reliable state estimates over a wider operating range, as was observed in the experiments later described in Chapter 7. Moreover, this model also includes a more descriptive side reaction model typically associated to

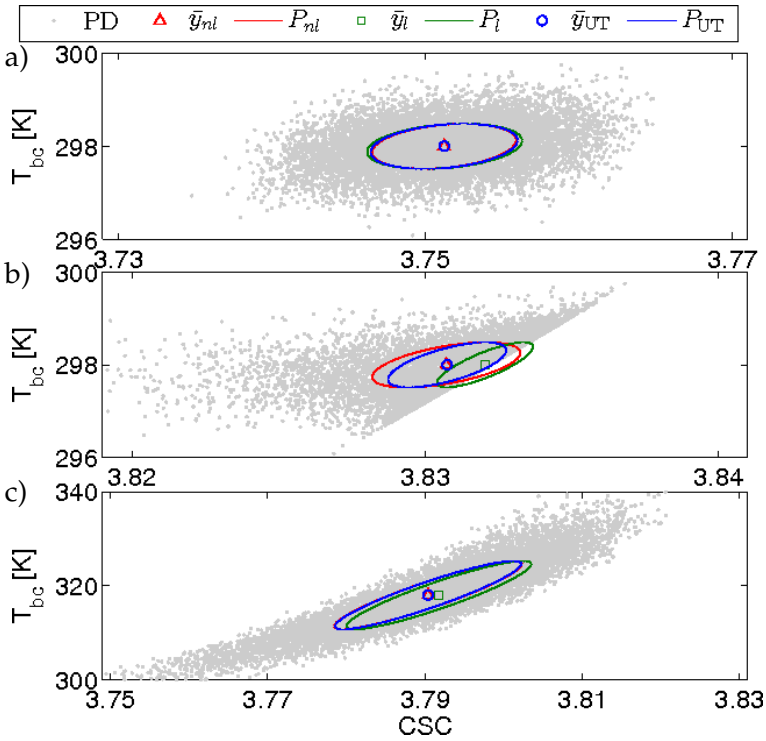

FIGURE 5.12: Nonlinear (in red), linearized (in green) and unscented transformed (blue) mean (symbol) and covariance (curve) of normally distributed random variables for a) case 1, b) case 2 and c) case 3 in Table 5.8. The gray dots correspond to the sampled probability distribution of the random variable.

negative electrode degradation processes. This *e*EHM is based on a third-order EHM for the solid-phase diffusion dynamics of the state Eq. (4.63) such as the one used in Section 5.1.1. The extra model dynamics rely on a second-order EHM for the electrolyte-phase diffusion dynamics, and thermal and aging submodels following from Sections 4.2.2 and 4.2.5 in discrete-time. For the aging models, both parametric changes and algebraic constraints are considered. This model choice preserves the nonlinear difference algebraic equation (NLDAE) model Eqs. (4.63)-(4.67). After including the noise sources in a more general framework than in Section 5.1.1, the resulting model has the following form

$$x(k+1) = A(x(k),\theta(k))x(k) + B_z z(k) + B_d d(k) + f_x(u(k),x(k),y(k)) + w_n(k) \quad (5.50)$$
$$\theta(k+1) = f_\theta(\theta(k),k,w_{n,\theta}(k)) \quad (5.51)$$
$$y(k) = h_y\left(z(k),x(k),\theta(k),v_n(k)\right) \quad (5.52)$$
$$0 = h_n(z(k),x(k),\theta(k)) - h_{\text{SEI}}(d(k),x(k),\theta(k)) \quad (5.53)$$
$$u(k) = z(k) + d(k) \quad (5.54)$$

where $x(k) \in \mathbb{R}^8$ is the difference state vector $x(k) = \left[x_s(k)^{\mathrm{T}}, x_e(k)^{\mathrm{T}}, x_T(k)^{\mathrm{T}}, x_Q(k)\right]^{\mathrm{T}}$, $u(k) \in \mathbb{R}$ is the input vector $u(k) = I(k)$, $y(k) \in \mathbb{R}^2$ is the output vector $y(k) = [V(k), T_{bs}(k)]^{\mathrm{T}}$, $z(k) \in \mathbb{R}$ is the algebraic state vector $z(k) = Fa_s Lj_n(k)$ and $\theta(k) \in \mathbb{R}^2$ is the parameter vector $\theta(k) = [\theta_1(k), \theta_2(k)]^{\mathrm{T}}$. Unlike the parameter vector of Section 5.1 defined over the physically meaningful variables D_s and R_f, now the parameter vector θ corresponds to perturbed or normalized versions of the physical variables

like $\theta_1(k)D_{s,\text{ref}}$ and $\theta_2(k)R_f$, where $D_{s,\text{ref}}$ and R_f stand for the value of the given variable at the beginning of the battery life (while $D_{s,\text{ref}}$ changes with aging, D_s depends on $D_{s,\text{ref}}(k)$ and $T_{bc}(k)$ according to the Arrhenius Eq. (2.20)). Therefore, a given change in the physical parameters is reflected in the variables comprised in $\theta(k)$. Process, parameter and measurement noise sequences are respectively denoted by $w_n(k) \in \mathbb{R}^8$, $w_{n,\theta}(k) \in \mathbb{R}^2$ and $v_n(k) \in \mathbb{R}^2$. These noise sequences are normally distributed, zero-mean mutually uncorrelated white noise sequences with covariance matrix

$$\mathbb{E}\left(\begin{bmatrix} w_n(k) \\ w_{n,\theta}(k) \\ v_n(k) \end{bmatrix} \begin{bmatrix} w_n(l)^{\mathrm{T}} w_{n,\theta}(l)^{\mathrm{T}} v_n(l)^{\mathrm{T}} \end{bmatrix}\right) = \begin{bmatrix} Q & 0 & 0 \\ 0 & Q_\theta & 0 \\ 0 & 0 & R \end{bmatrix} \delta_{kl}. \tag{5.55}$$

The state $A(x(k),\theta(k))$, input B_z and disturbance B_d matrices, as well as state $f_x(u(k),x(k),y(k))$, output $h_y(z(k),x(k),\theta(k))$ and algebraic $h_n(z(k),x(k),\theta(k))$, $h_{\text{SEI}}(d(k),x(k),\theta(k))$ nonlinear functions are given in Section 4.2.8. The parameter function $f_\theta(\theta(k),k)$ takes the form $f_\theta(\theta(k),k) = \theta(k)$. As aging is a slow process, the parameter θ is modeled as a constant subject to changes due to the noise term. To clarify how the parameter vector $\theta(k)$ enters in the system model, the solid-phase diffusion matrix $A_s(x(k),\theta(k))$ and the main reaction output equation $h_n(u(k),x(k),\theta(k))$ dependent on $\theta(k)$ are reported in the following:

$$A_s(x(k),\theta(k)) = \begin{bmatrix} 1 & 0 & 0 \\ \theta_1(k)g_s(k)\frac{\gamma_1}{\beta_1\beta_2} & 1-\theta_1(k)g_s(k)\left(\frac{\gamma_1}{\beta_1}+\frac{\gamma_1+\gamma_2}{\beta_2}\right) & \theta_1(k)g_s(k)\left(\frac{\gamma_2}{\beta_2}-\frac{\beta_3\gamma_1}{\beta_1\beta_2}\right) \\ 0 & \theta_1(k)g_s(k)\frac{\gamma_2}{\beta_3} & 1-\theta_1(k)g_s(k)\frac{\gamma_2}{\beta_3} \end{bmatrix} \tag{5.56}$$

for the state matrix and

$$h_n\left(u(k),x(k),\theta(k)\right) = \Delta U_s^{\pm}(k) + \Delta\eta_s^{\pm}(k) + \Delta\phi_e(k) - \theta_2(k)\frac{R_f}{a_s L}u(k) \tag{5.57}$$

for the output function. The time variation of $g_s(k)$ comes from its dependency on the core temperature state variable as referred above for D_s ($g_s(k) = \tau_s(k)^{-1} = R_s^{-2}D_s(k)$).

The just introduced *e*EHM Eqs. (5.50)-(5.54) is now exploited to design a state observer. The estimation of the parameter vector θ provides parameter-based SOH indicatiors, while state estimation will result in state estimates used for battery monitoring and in residuals. Since the UKF provides a more accurate estimation of the mean and variance of a random variable subject to a nonlinear transformation as shown in Section 5.3.1, we opted for this observer over the EKF of Section 5.1.1. Time-varying parameters are tracked through dual estimation, which is preferred over the joint estimation used in Section 5.1.1 given its lower computational burden due to smaller covariance matrices. These computational savings are at the expense of neglecting (possible) correlations between state and parameters. This dual estimation approach is however convenient in order to possibly account for different time scales between state and parameter dynamics.

While the dual UKF is recognized as the most suitable approach for our specific estimation problem, there is one last issue that needs to be tackled, namely the NLDAE system model Eqs. (5.50)-(5.54). This model contrasts with the ordinary difference equation estimation problem solved in the previous section. Different approaches have been proposed in the literature to deal with the state estimation problem of NLDAE systems. As there is no classical way to handle these systems,

to the best of our knowledge, and no solution has been proposed in the battery community, these approaches have not been included in the State of the Art, Chapter 2 and the Prerequisite Material, Chapter 3. Nonetheless, other communities like power systems are obliged to deal with this type of systems, and therefore we resort to their contributions on the topic. The following joint state and parameter estimation for NLDAE systems found in the literature are worth mentioning:

(a) Nonlinear moving horizon observer handling constraints [151].

(b) Constrained ensemble Kalman filter [152].

(c) Extended Kalman filters based on an ODE model deduced from the NLDAE model by elimination of the algebraic state [153, 154].

(d) Unscented Kalman filter [154].

Approaches like (a) and (b) come associated with high computational burden. The EKF in (c) is prone to accumulate linearization errors, which might be significant in the case of batteries at high and low SOC and temperatures as shown in Section 5.3.1. The UKF in (d) resorts to a DAE solver and provides a trade-off between complexity and accuracy. The UKF algorithm proposed below departs from the above methods in two ways:

- First, it uses a dual framework to solve the state/parameter estimation.
- Second, it handles the nonlinear algebraic equation in a different way as described below.

The corresponding algorithm is presented in Table 5.9 for system Eqs. (5.50)-(5.54) with

$$\begin{aligned} f(u(k), z(k), x(k), \theta(k), y(k), w_n(k)) \; = \; & A(x(k), \theta(k))x(k) + B_z z(k) \\ & + B_d d(k) + f_x(u(k), x(k), y(k)) + w_n(k). \end{aligned}$$

For the dual framework, a second output equation must be introduced to handle the measurement update for the parameter vector (see Eq. (5.75) in Table 5.9 below). This output equation can be written as

$$\delta(k+1) = h_n\left(z(k+1), x(k+1), \theta(k)\right) + v_n(k+1) + v_{n,\theta}(k+1), \tag{5.58}$$

where $v_{n,\theta}(k)$ is a white noise sequence of variance matrix R_θ and

$$x(k+1) = A(x(k), \theta(k))x(k) + B_z z(k) + B_d d(k) + f_x(u(k), x(k), y(k)) + w_n(k).$$

Notice that Eq. (5.58) is a copy of the voltage component of the output Eq. (5.52) with a fictitious noise $v_{n,\theta}(k)$, where the nonlinear function $h_n\left(z(k+1), x(k+1), \theta(k)\right)$ is evaluated with the parameter $\theta(k)$ in both the state and the output functions. The output Eq. (5.58) considers the previous states $x(k), z(k), d(k)$ as a given (known) inputs.

Secondly, contrary to the methods presented in the above references, the system Eqs. (5.50)-(5.54) is not linearized in order to eliminate the algebraic state, nor solved as a DAE system at each time step. An alternative method that turns out to limit the computational burden while keeping a similar estimate quality for the battery application is considered. The algebraic state $z(k)$ characterizing the current split between main ($z(k)$) and side reactions ($d(k) = u(k) - z(k)$) is estimated by solving

the nonlinear optimization problem Eqs. (5.61) and (5.66) in Table 5.9 below through the trust-region-reflective method. This could be interpreted as "peaking up" the random variable around its mean, i.e. $P_z \to 0$ [155] where P_z is the covariance matrix of z). This approach decouples the difference and algebraic state estimation while avoiding linearization errors. The resulting estimator is then able to exploit Euler discretization to solve an ODE model, which speeds up computation when compared to solving the DAEs, without significantly sacrificing state and parameter estimation accuracy. The resulting UKF is able to handle NLDAEs of index 1[4]. The gain in computation burden essentially results from the fact that the algebraic equation is solved only once to get the average of the algebraic state distribution, instead of solving it for each sigma-point.

5.3.3 Fault Detection and Isolation

In contrast to other contributions in the field of FDI systems for lithium-ion batteries described in Section 2.6, we consider multiple process and sensor faults simultaneously. The dual UKF of the previous Section 5.3.2 provides an estimation of both the system state and SOH-related parameters. By monitoring the temporal evolution of variables as the state $Q_{\text{loss}}(k)$ and parameters $\theta(k)$ and comparing them with their nominal value, fault diagnosis for internal faults can be achieved. Magnitude changes of 100% and 400% could be expected for $D_{s,\text{ref}}$ and R_f, and 30% loss of capacity after 500 operating cycles [37].

The same UKF of Section 5.3.2 also generates residuals of the form

$$\nu(k) = y(k) - \hat{y}(k), \tag{5.78}$$

which can be exploited for sensor fault detection and isolation using the tools introduced in Section 3.3. Here, the generalized likelihood ratio (GLR) algorithm [130] is used as statistical test to detect a change in the residual mean. Thus, when the GLR decision function Eq. (3.84) is compared with a threshold $\bar{h}$, it provides the required criterion to distinguish between the hypotheses of Eq. (3.82).

[4]The DAE system has to be differentiated once to transform it into an explicit ODE system [154].

TABLE 5.9: The dual unscented Kalman filter algorithm for the considered NLDAE system [156, 126]†.

Initialization: for $k = 0$, set

$\hat{x}_0 = \mathbb{E}[x_0], \quad P_0 = \mathbb{E}[(x_0 - \hat{x}_0)(x_0 - \hat{x}_0)^{\mathrm{T}}]$

$\hat{x}_0^a = \mathbb{E}[x_0^a] = [\hat{x}_0^{\mathrm{T}} \;\; 0 \;\; 0]^{\mathrm{T}}$

$P_0^a = \mathbb{E}[(x_0^a - \hat{x}_0^a)(x_0^a - \hat{x}_0^a)^{\mathrm{T}}] = \mathrm{diag}(P_0, Q, R)$

$\hat{\theta}_0 = \mathbb{E}[\theta_0], \quad P_{\theta,0} = \mathbb{E}[(\theta_0 - \hat{\theta}_0)(\theta_0 - \hat{\theta}_0)^{\mathrm{T}}]$

Computation: for $k = 1, 2, \ldots$ compute

Sigma points:

$$\mathcal{X}_{k-1}^a = \left[\hat{x}_{k-1}^a \;\; \hat{x}_{k-1}^a + \gamma\sqrt{P_{k-1}^a} \;\; \hat{x}_{k-1}^a - \gamma\sqrt{P_{k-1}^a}\right] \tag{5.59}$$

$$\Theta_{k-1} = \left[\hat{\theta}_{k-1} \;\; \hat{\theta}_{k-1} + \gamma\sqrt{P_{\theta,k-1}} \;\; \hat{\theta}_{k-1} - \gamma\sqrt{P_{\theta,k-1}}\right] \tag{5.60}$$

Algebraic state estimation:

$$\begin{aligned} &\hat{z}_{k-1} = \arg\min_{z_{k-1}} \| e_{k-1} \|_2^2 \\ &\text{s.t. } e_{k-1} = h_n\left(z_{k-1}, \hat{x}_{k-1}, \hat{\theta}_{k-1}\right) - h_{\mathrm{SEI}}\left(d_{k-1}, \hat{x}_{k-1}, \hat{\theta}_{k-1}\right) \end{aligned} \tag{5.61}$$

Time-update:

$$\mathcal{X}_{k|k-1}^x = f\left(u_{k-1}, \hat{z}_{k-1}, \mathcal{X}_{k-1}^x, \hat{\theta}_k^-, \hat{y}_{k-1}, \mathcal{X}_{k-1}^w\right) \tag{5.62}$$

$$\hat{x}_k^- = \sum_{l=0}^{2n_{ax}} W_l^{(m)} \mathcal{X}_{l,k|k-1}^x, \quad \hat{\theta}_k^- = \hat{\theta}_{k-1} \tag{5.63}$$

$$P_k^- = \sum_{l=0}^{2n_{ax}} W_l^{(c)} \left(\mathcal{X}_{l,k|k-1}^x - \hat{x}_k^-\right)\left(\mathcal{X}_{l,k|k-1}^x - \hat{x}_k^-\right)^{\mathrm{T}} \tag{5.64}$$

$$P_{\theta,k}^- = P_{\theta,k-1} + Q_\theta \tag{5.65}$$

Algebraic state prediction :

$$\begin{aligned} &\hat{z}_k^- = \mathrm{argmin}_{z_k} \| e_k^- \|_2^2 \\ &\text{s.t. } e_k^- = h_n\left(z_k, \hat{x}_k^-, \hat{\theta}_k^-\right) - h_{\mathrm{SEI}}\left(d_k, \hat{x}_k^-, \hat{\theta}_k^-\right) \end{aligned} \tag{5.66}$$

$$\mathcal{Y}_{k|k-1} = h_y\left(\hat{z}_k^-, \mathcal{X}_{k|k-1}^x, \hat{\theta}_k^-, \mathcal{X}_{k-1}^v\right) \tag{5.67}$$

$$\Delta_{k|k-1} = h_n\left(\hat{z}_k^-, f\left(u_{k-1}, \hat{z}_{k-1}, \hat{x}_{k-1}, \Theta_{k-1}, y_{k-1}, \bar{w}_{k-1}\right), \Theta_{k-1}, \bar{v}_k\right) \tag{5.68}$$

$$\hat{y}_k = \sum_{l=0}^{2n_{ax}} W_l^{(m)} \mathcal{Y}_{l,k|k-1}, \quad \hat{\delta}_k = \sum_{l=0}^{2n_{a\theta}} W_l^{(m)} \Delta_{l,k|k-1} \tag{5.69}$$

Measurement-update

$$P_{y,k} = \sum_{l=0}^{2n_{ax}} W_l^{(c)} \left(\mathcal{Y}_{l,k|k-1} - \hat{y}_k\right)\left(\mathcal{Y}_{l,k|k-1} - \hat{y}_k\right)^{\mathrm{T}} \tag{5.70}$$

$$P_{\delta,k} = \sum_{l=0}^{2n_{a\theta}} W_l^{(c)} \left(\Delta_{l,k|k-1} - \hat{\delta}_k\right)\left(\Delta_{l,k|k-1} - \hat{\delta}_k\right)^{\mathrm{T}} + R_\theta \tag{5.71}$$

$$P_{xy,k} = \sum_{l=0}^{2n_{ax}} W_l^{(c)} \left(\mathcal{X}_{l,k|k-1}^x - \hat{x}_k^-\right)\left(\mathcal{Y}_{l,k|k-1} - \hat{y}_k\right)^{\mathrm{T}} \tag{5.72}$$

$$P_{\theta\delta,k} = \sum_{l=0}^{2n_{a\theta}} W_l^{(c)} \left(\Theta_{l,k|k-1} - \hat{\theta}_k^-\right)\left(\Delta_{l,k|k-1} - \hat{\delta}_k\right)^{\mathrm{T}} \tag{5.73}$$

$$K_k = P_{xy,k} P_{y,k}^{-1}, \quad K_{\theta,k} = P_{\theta\delta,k} P_{\delta,k}^{-1} \tag{5.74}$$

$$\hat{x}_k = \hat{x}_k^- + K_k\left(y_k - \hat{y}_k\right), \quad \hat{\theta}_k = \hat{\theta}_k^- + K_{\theta,k}\left(y_k - \hat{\delta}_k\right) \tag{5.75}$$

$$P_k = P_k^- - K_k P_{y,k} K_k^{\mathrm{T}}, \quad P_{\theta,k} = P_{\theta,k}^- - K_{\theta,k} P_{\delta,k} K_{\theta,k}^{\mathrm{T}} \tag{5.76}$$

Parameters for x and θ

$$\begin{aligned} &\gamma = \sqrt{n_a + \lambda}, \quad \lambda = \alpha^2(n_a + \kappa) - n_a \\ &W_0^{(m)} = \tfrac{\lambda}{n_a+\lambda}, \quad W_0^{(c)} = \tfrac{\lambda}{n_a+\lambda} + 1 - \alpha^2 + \beta \\ &W_l^{(m)} = W_l^{(c)} = \tfrac{1}{2(n_a+\lambda)}, \; l = 1, \ldots, 2n_a, n_a = 2n + p \end{aligned} \tag{5.77}$$

†For compactness, the time argument is set as an index.

5.4 Validation of State/Parameter Estimation for Battery Monitoring & FDI

Similarly as in Section 5.2, the first step for validating the approach proposed in Section 5.3 is to carry out simulations. The obtained results are shown in this section. In contrast to the estimation strategy for SOH monitoring of Section 5.1, the estimation strategy for FDI could not be experimentally validated in the present work, but it remains as a pending task for future work.

The battery internal and sensor FDI system is assessed through a simulated graphite | LCO battery cell based on the *e*EHM described in Section 4.2. The parameter values used to set up the simulator are the ones provided in Table C.2, Appendix C [157]. This model is solved using the interior-reflective Newton's method at each time step. The current profile is a positive and negative square wave with resting periods of 100 s in-between each pulse. The pattern of the total current $u(k)$ applied to the battery is very similar to the one of the main reaction current (algebraic state $z(k)$) shown in Fig. 5.13 given the small side reaction rate, i.e. $d(k) \approx 0 \rightarrow u(k) \approx z(k)$.

Remark 5.4.1. *Notice that the previous Section 5.2.1 has shown a good agreement between the state estimation based on a EHM and the true state values coming from the DFN model for low applied currents (equal or less than 1C). Although we are aware that a strict validation requires an accurate simulator and experiments, at this point we think that it is reasonable to exploit the low computational burden of reduced-order models to validate our approach.*

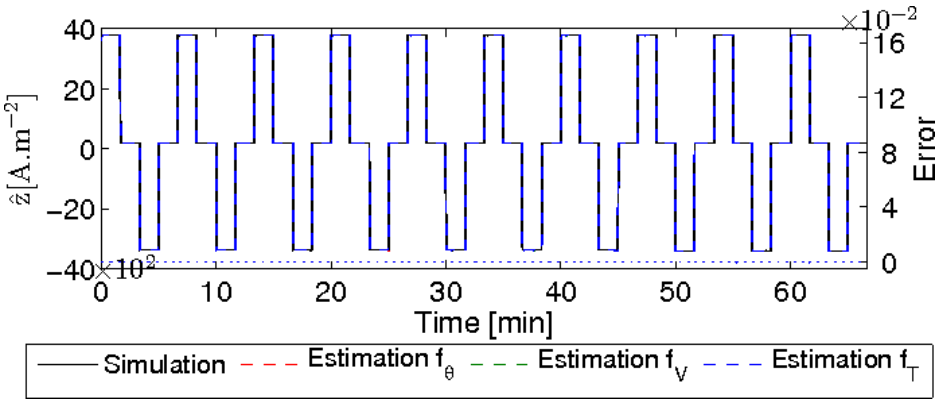

FIGURE 5.13: Primary reaction current state ($\hat{z}$) estimated with the dual UKF in the left y-axis, where solid black and dashed red, green and blue (overlapping) curves represent the scenarios of fault-free, internal faults, voltage sensor fault and surface temperature sensor fault, respectively. The right y-axis corresponds to the associated estimation error (dotted blue curve).

A white noise sequence with variance $\text{diag}(R) = [R_1, R_2]^{\text{T}}$, $R_1 = 10$ mV^2 and $R_2 = 10^2$ mK^2 was added to the output signals obtained from simulation. Although the input signal is also corrupted by noise in real applications, it could be accommodated in the proposed UKF framework and we assume a noiseless current here. Both system and sensor faults are considered in three different scenarios, namely:

- Case 1: process faults comprising capacity and power fade.
- Case 2: voltage sensor fault.
- Case 3: temperature sensor fault.

Within process faults, capacity fade Q_{loss} due to side reactions starts to happen from the very beginning of the battery utilization [37], it increases linearly over time and it is always present. The other two process faults, namely capacity fade due to aging and power fade, are injected as drifts in the parameters $D_{s,\text{ref}}$ and R_f respectively, according to Eqs. (4.1) and (4.2). These assumed aging-induced parameter variations contrast with the additional operation-induced parameter changes considered in the previous Section 5.1. The latter are not required by the battery chemistry explored in the current section. These equations of degradation have been slightly modified to evidence an accelerated aging process within the considered time horizon. Both faults are considered simultaneously since it is the most likely situation. Within sensor faults, a bias is injected in both voltage and surface temperature measured signals. These sensor faults are considered independently of each other since it is the most likely situation. The equation numbers describing parameter drifts, sensor fault magnitudes f and time instants $\tau_{\text{f},0}$ of fault injection are given in Table 5.10 for each variable.

TABLE 5.10: Equations describing parameter drift, sensor fault magnitudes and fault injection time instants for each variable.

	Q_{loss}	$D_{s,\text{ref}}$	R_f	V	T_{bs}
(Eq.),f	(2.25)	(4.2)	(4.1)	10^{-2} V	10^{-1} K
$\tau_{\text{f},0}$ [min]	0.00	36.67	23.33	35.00	25.00

A similar procedure for state initialization and parameter tuning outlined in the previous Section 5.2.1 to set up the constrained EKF was followed for the dual UKF. The tuning parameter values were the following

$$\begin{aligned}
&\hat{x}(0) = \left[1_3^{\text{T}} \cdot 0.67, 1_2^{\text{T}} \cdot 10^3, 1_2^{\text{T}} \cdot 298, 0\right]^{\text{T}} \\
&\text{diag}(P_0) = 1_8^{\text{T}} \cdot 10^{-14}, \qquad \text{diag}(Q) = 1_8^{\text{T}} \cdot 10^{-16} \\
&\text{diag}(P_{\theta,0}) = [10^{-3}, 10^{-8}]^{\text{T}}, \quad \text{diag}(Q_\theta) = 1_2^{\text{T}} \cdot 10^{-4} \\
&\alpha_x = 0.01, \quad \beta_x = 2, \quad \kappa_x = 3 - n_{ax} = -15 \\
&\alpha_\theta = 0.1, \quad \beta_\theta = 2, \quad \kappa_\theta = 3 - n_{a\theta} = 1
\end{aligned} \tag{5.79}$$

where the first three components of the state vector are dimensionless, the second two components are associated to the electrolyte-phase concentration $[\text{mol} \cdot \text{m}^{-3}]$, the third two components are thermal states [K] and the last component is capacity loss [Ah]. The units of P and Q are coherent with the units of the state vector. The units of the parameter vector are defined as $[\text{s}^{-1}]$ and $[\Omega \cdot \text{m}^2]$ for the first and second component related to the inverse of the diffusion time constant and an ohmic resistance, respectively. The units of P_θ and Q_θ are coherent with the units of the parameter vector.

Fig. 5.13 shows the estimation of the algebraic state, while its state estimation error is represented by the dotted blue curve at the bottom of this plot, with the associated y-axis on the right. Fig. 5.14 depicts the estimation of the dynamic states of the main reaction, namely the solid-phase diffusion states in Fig. 5.14(a), the electrolyte-phase diffusion states in Fig. 5.14(b) and the thermal states in Fig. 5.14(c). The dynamic state of the side reaction, i.e. the capacity fade state, is shown in Fig. 5.15(a). The obtained results are considered as satisfactory for every injected fault. Indeed, the estimation performed over the different faulty scenarios is so close to each other and to the actual states (solid black curves) that the curves overlap even for the considered parameter faults (dashed red curves), voltage sensor fault (dashed green curves) and temperature sensor fault (dashed blue curves). Thus, the considered faults do not

affect significantly the state estimate to be used for battery monitoring. Let us see whether they can be detected in such an early stage.

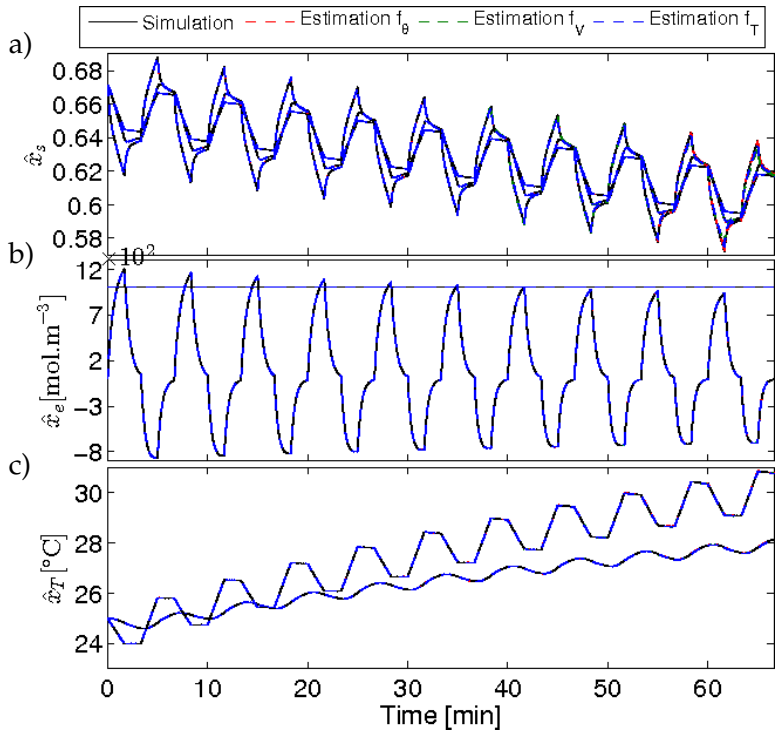

FIGURE 5.14: State estimation study: a) solid-phase diffusion states; b) electrolyte-phase diffusion states; c) thermal states. Solid black and dashed red, green and blue (overlapping) curves represent the scenarios of fault-free, internal faults, voltage sensor fault and surface temperature sensor fault, respectively.

Fig. 5.15(b) shows the estimation of the normalized slow time-varying parameters, namely the capacity fade due to aging on the left y-axis and the power fade on the right y-axis. When only internal faults take place, the parameter estimates (dashed red curves) try to track the actual parameter changes (solid black curves). The estimation of the power fade, $\hat{\theta}_2$, is closer to the actual power fade when compared with the aging-induced capacity fade estimation, $\hat{\theta}_1$. This might be related to the sensitivity of the voltage output function, which is higher for the film resistance R_f than for the diffusion coefficient D_s under the considered operating conditions. When only a voltage sensor fault occurs, both capacity and power fade estimates start to oscillate (dashed green curves). When only a temperature sensor fault occurs, neither the capacity nor the power fade estimates considerably move from their operating points (dashed blue curves). Therefore, the parameter estimation is more sensitive to voltage changes than to temperature changes. The detection and isolation of the latter two faults can be achieved by processing each residual given by

$$\begin{aligned} \nu_V(k) &= V(k) - \hat{V}(k) \\ \nu_T(k) &= T_{bs}(k) - \hat{T}_{bs}(k) \end{aligned} \tag{5.80}$$

through a GLR algorithm Eq. (3.84).

Figs. 5.16 and 5.17 show residual information associated to voltage and temperature sensors, respectively. Fig. 5.16(a) and 5.17(a) depict the generated residuals

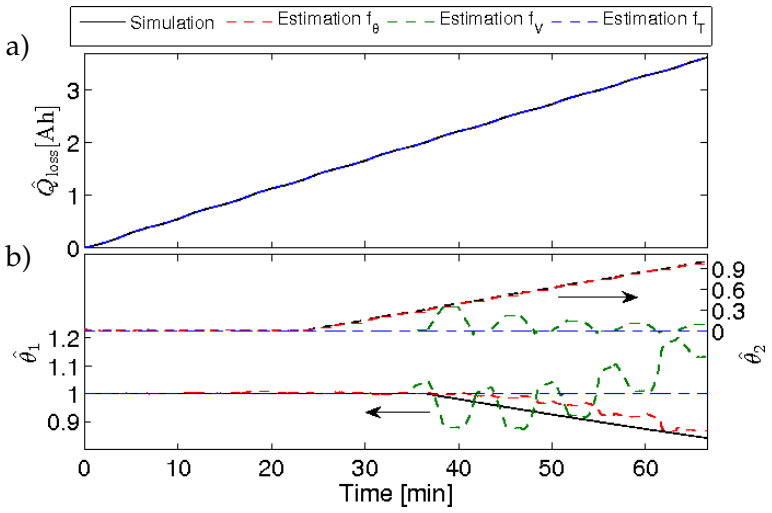

FIGURE 5.15: State estimation study: a) capacity fade state; b) normalized aging parameters, namely rate capability and power fade on the left and right y-axis, respectively. Solid black and dashed red, green and blue curves represent the scenarios of fault-free, internal faults, voltage sensor fault and surface temperature sensor fault, respectively.

$\nu(k)$, whereas 5.16(b) and 5.17(b) portray the decision functions $g_{GLR}(k)$ associated to each residual for each respective sensor. For setting the GLR parameters, the residual mean and variance for the healthy condition are estimated from a residual sequence obtained in healthy operation. Besides, the window size is chosen as $M = 5$. This window size ensures fast change detection of abrupt faults with a low computational burden. Should the signal-to-noise ratio decrease, a longer window size would be needed resulting in larger computational costs. When only internal faults take place (solid red curves), the residual sequences do not exhibit a significant change in the mean and none of the GLR functions exceed the preselected threshold (dashed black curves). This threshold is 2×10^2, which was chosen through simulation to ensure fast detection and absence of false alarm in the considered data set. Thus, hypothesis 0 in Eq. (3.82) associated to a healthy operation can be declared. When a given sensor fault occurs (green and blue curves), the residual sequence associated to that fault exhibits an evident change in the mean, which translates into the GLR function exceeding its threshold. Thus, hypothesis 1 in Eq. (3.82) associated to a faulty operation can be flagged. Notice that voltage and temperature faults can be distinguished from each other since each residual only reacts to a fault occurring to its associated sensor.

5.5 Concluding Remarks

This chapter has dealt with the state and parameter estimation problem towards SOH monitoring and sensor fault diagnosis. Two battery systems were considered, namely a LFP half battery cell and a graphite | LCO battery cell. On the one hand, special features of the LFP electrode, such as a solid-phase diffusion process dependent on the operating condition and a contact-resistance distribution, have been accounted for. On the other hand, a more thorough degradation model associated to side reactions and SEI growth in the graphite electrode has been considered for the graphite | LCO battery.

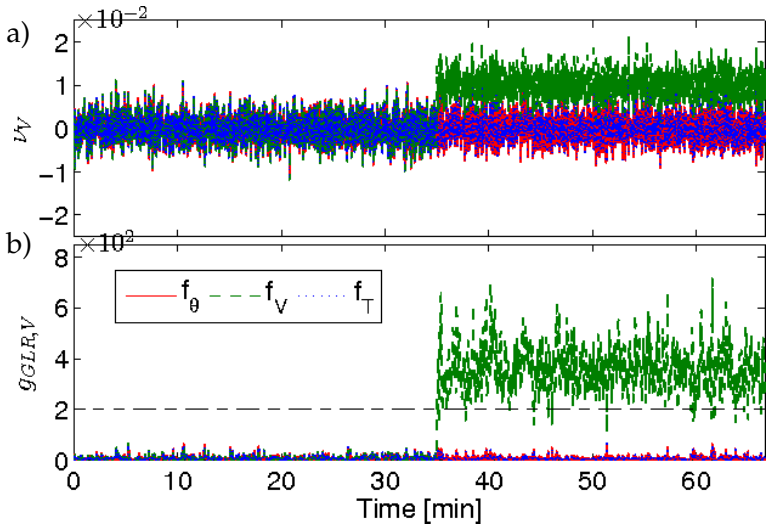

FIGURE 5.16: Fault detection study considering the voltage sensor: a) generated residuals and b) associated GLR decision function. Solid red, dashed green and dotted blue curves represent the scenarios of internal faults, voltage sensor fault and surface temperature sensor fault, respectively.

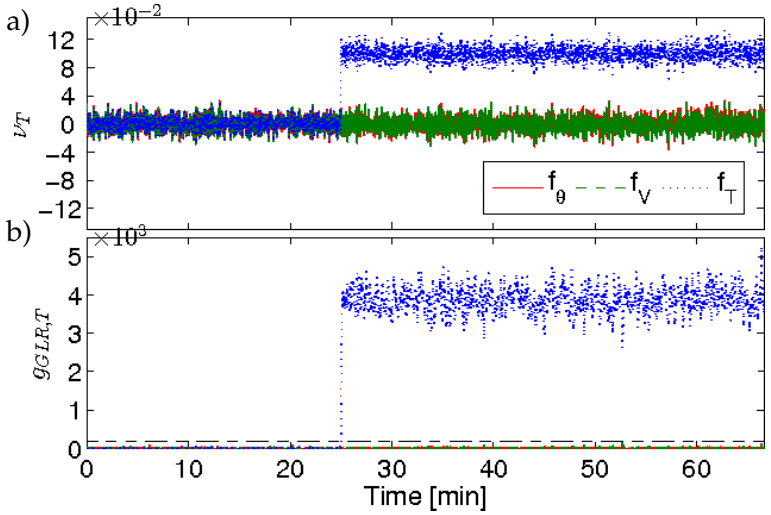

FIGURE 5.17: Fault detection study considering the surface temperature: a) generated residuals and b) associated GLR decision function. Solid red, dashed green and dotted blue curves represent the scenarios of internal faults, voltage sensor fault and surface temperature sensor fault, respectively.

Two approaches for SOH monitoring and sensor FDI have been presented independently, but both have strengths and weaknesses and they could be merged into a single solution. Different models and state observers were explored, which vary in complexity and accuracy. Within the modeling framework, a simple third-order EHM was used as a basis to design an EKF for SOH monitoring, whereas a more sophisticated *e*EHM including electrolyte diffusion, thermal and aging dynamics was exploited to design an UKF. While the EHM has been proven to be accurate at low currents (less than 1C), the *e*EHM can be confidently used in more demanding

operating conditions such as larger currents. This is particularly relevant for fast charging, which is discussed in the next two Chapters 6 and 7. However, the side reactions of the *e*EHM considered here makes it a DAE system, which complicates its handling for estimation and control.

Within the estimation framework, the EKF is computationally cheap and simple to implement, but it requires Jacobians that might be not trivial for large systems and it inherently comes associated with linearization errors. The UKF overcomes these issues while being able to accommodate noise corrupting the input signal. Moreover, a dual estimation is preferred over a joint estimation given the computational savings and the possibility of directly exploiting the time-scale separation between battery regular dynamics and aging dynamics for estimation update.

In the first contribution, periodic SOH indicators for capacity and power fade have been derived. An EKF is used to estimate the internal state of the battery, which is exploited for SOH estimation by parameter identification techniques such as SRIVC and LS methods. The former method provides unbiased parameter estimates in spite of the presence of (possibly colored) noise and wrong initial parameters. These aspects are in sharp contrast with the widely popular LS methods for estimating unknown parameters of dynamic systems. In the second contribution, the model operating region was enlarged by considering additional battery dynamics, and the resulting model was used to design an UKF to provide SOH estimates related to accelerated aging and residuals to assess sensor faults. It is shown that residuals made of the output estimation errors provide an early detection and isolation of voltage and temperature sensor faults, while the state and parameter estimates allow distinguishing between capacity and power fade. For the considered small fault magnitudes the internal faults and sensor faults turn out to be decoupled.

Besides the intrinsic advantages of models like EHM and *e*EHM, joint and dual estimation, and EKF and UKF observers in terms of computation and accuracy, the two proposed approaches have the add-on monitoring units that deserve some comments. The EHM-based EKF is able to discern between operation-induced and aging-induced parameter changes thanks to the periodic parameter identification scheme, to which the second proposed approach is blind. The *e*EHM-based UKF is, for its part, able to assess sensor faults, to which the first proposed approach is unaware of. Having these two features around a given state observer would be the most robust solution for SOH monitoring and sensor diagnosis.

Chapter 6

Fast Charging Constrained Control

While the previous Chapter 5 focused on the monitoring part of the battery supervisory control system (light green and blue blocks in Fig. 6.1), this chapter is centered around the constrained control strategy for battery fast charging (red block in Fig. 6.1). A state observer is again needed to access the internal state of the battery (orange block in Fig. 6.1). The present chapter is structured as follows. Section 6.1 describes all the theoretical development and implementation issues involved when deriving a reference governor to solve the constrained control problem for battery charge. Section 6.2 follows to validate the proposed approach using a detailed battery cell simulator and compares its performance with commercial CCCV charging strategies. The validation step in this chapter is restricted to testing the fast charging features of the proposed controller via simulated short-term cycling. However, Chapter 7 goes one step further by studying the safe charging capabilities, on top of the fast charging ones, that the proposed controller is able to deliver. This is assessed through long-term cycling experiments.

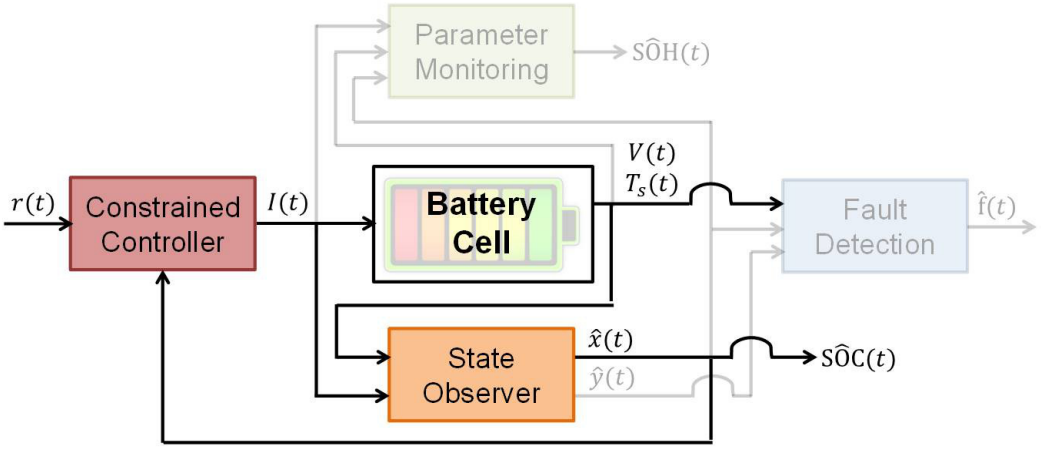

FIGURE 6.1: Block diagram of the control system for a battery cell.

6.1 State Feedback Constrained Control

After exploring state and parameter estimation for SOH monitoring and fault diagnosis in Chapter 5, it is time to close the loop and control the battery operation. More specifically, we aim at charging the battery faster and healthier than commercial charging protocols. While the current chapter focuses on the fast charging, the next chapter adds the healthy management of such charging. We achieve this through

electrochemical modeling and constrained control. It is worth pointing out that we restrict ourselves to using computationally cheap solutions if compared with e.g. MPC schemes, so that we eventually could test our methods on board. Such kind of solutions are based on reference governor (RG) schemes. However, the standard scalar RG of Section 3.4 is modified to handle OR constraints that typically characterize degradation mechanisms (red "reference governor" block in Fig. 6.2). The modified RG acts on a battery that has been pre-stabilized using a linear quadratic regulator (LQR) with integral action (red "K_x" and "K_i" blocks in Fig. 6.2). This state feedback controller needs to be coupled with a state observer (orange block in Fig. 6.2) to come up with an output feedback controller, since the system state is unknown.

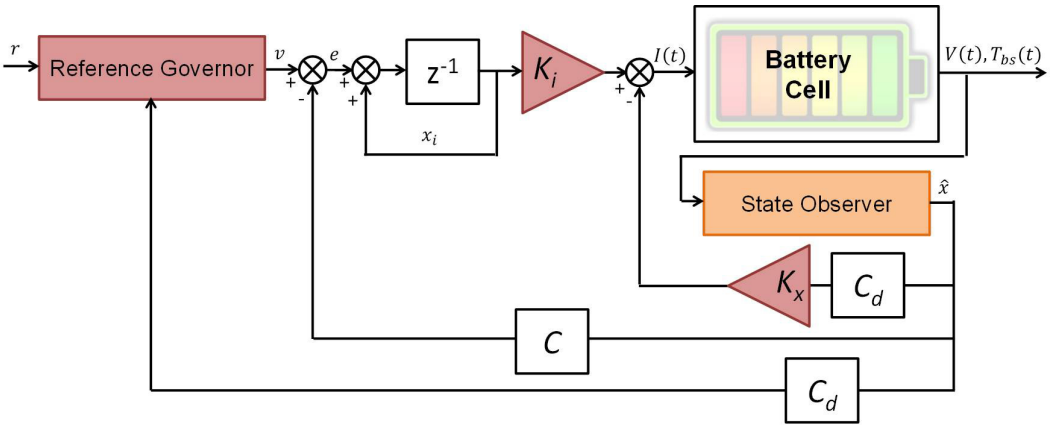

FIGURE 6.2: Block diagram of the optimal constrained control scheme.

6.1.1 Pre-Stabilization

This preliminary work on fast charging control uses an alternative version of the system Eqs. (4.63)-(4.74) that has been simplified and modified according to the problem needs. First, only the solid-phase diffusion dynamics are accounted for in the state Eq. (4.63) through a second-order EHM, which translates in $x(k) = x_s(k)$. Secondly, no unknown parameters are considered, which means that Eq. (4.64) is dropped. Thirdly, the nonlinear output voltage function (first component of Eq. (4.65)) is replaced by the SOC(k) measurement through $C_s = [1\ 0]$. Fourthly, the algebraic functions Eqs. (4.66),(4.67) are disregarded by neglecting degradation mechanisms, which makes the DAE model become an ODE model. The resulting model replacing Eqs. (4.63)-(4.73) takes the form

$$x_s(k+1) = A_s x_s(k) + B_s u(k) \tag{6.1}$$
$$y_s(k) = C_s x_s(k) \tag{6.2}$$

where $x_s(k) \in \mathbb{R}^2$ is the solid-phase diffusion state vector $x_s(k) = [\text{SOC}(k),\ \text{CSC}(k)]^{\text{T}}$, $u(k) \in \mathbb{R}$ is the battery current input vector $u(k) = I(k)$ and $y_s(k) \in \mathbb{R}$ is the battery state-of-charge $y_s(k) = \text{SOC}(k)$. Finally, the convex inequality constraints Eq. (4.74) of system Eqs. (4.63)-(4.67) are substituted by a more general nonconvex counterpart (OR constraints) for the simplified system Eqs. (6.1),(6.2), which are closer to the original constraint set Eq. (2.32). This constraint reformulation is explored in the next section.

The system Eqs. (6.1),(6.2) is equivalent to the system Eq. (3.86) for which the standard SRG was derived. Therefore, we can pre-stabilize the system using a similar LQR controller with integral action as in Section 3.4. Resorting to the same state feedback control law of Eqs. (3.90),(3.91) given by

$$u(k) = -\begin{bmatrix} K_x & K_i \end{bmatrix} \begin{bmatrix} x_s(k) \\ x_i(k) \end{bmatrix} \tag{6.3}$$

the closed-loop system takes the form of Eqs. (3.93),(3.94), which is retrieved here for convenience, i.e.

$$x_{cl}(k+1) = A_{cl}x_{cl}(k) + B_{cl}v(k) \tag{6.4}$$

where the closed-loop state vector is $x_{cl}(k) = \begin{bmatrix} x_s(k)^{\mathrm{T}}, & x_i(k) \end{bmatrix}^{\mathrm{T}}$, and the state and input matrices are respectively given by

$$A_{cl} = \begin{bmatrix} A_s - B_s K_x & -B_s K_i \\ -B_i C_s & A_s \end{bmatrix}, \quad B_{cl} = \begin{bmatrix} 0 \\ B_i \end{bmatrix}, \tag{6.5}$$

with $A_i = 1$ and $B_i = 1$.

6.1.2 Electrochemical Constraints Reformulation

Before designing the desired Reference Governor scheme, the electrochemical constraints Eq. (4.49) derived from the original constraints Eq. (2.32) have to be rewritten in terms of the closed-loop system Eqs. (6.4),(6.5). Instead of considering a convex set as in Eq. (4.74), we generalize here the inequality constraints Eq. (4.49) through a set of nonconvex constraints. Such set consists of both linear and nonlinear nonconvex constraints. The linear constraints Eqs. (4.49a),(4.49b) can be expressed as

$$S_j^{\mathrm{T}} x_{cl}(k) \quad \leq \quad s_j, \;\; j = 1, ..., 4 \tag{6.6}$$

where $S_1 = -[1\ 0\ 0]^{\mathrm{T}}$, $S_2 = -S_1$, $S_3 = -[0\ 1\ 0]^{\mathrm{T}}$, $S_4 = -S_3$, and $s_1 = 0$, $s_2 = \bar{r}_{c_s}$, $s_3 = 0$, and $s_4 = \bar{r}_{c_s}$. These linear constraints are depicted in Fig. 6.3(a) as dashed blue curves denoted with numbers 1-4 within blue circle symbols. The admissible region given by the lower bounds of Eqs. (4.49a),(4.49b) is shown in green in Fig. 6.3(b), and similarly in Fig. 6.3(c) for the upper bounds of Eqs. (4.49a),(4.49b).

The remaining DFN constraints Eqs. (2.32c)-(2.32e) are accounted for by considering the static characteristic of the battery cell on the plane $(\mathrm{CSC} - I)$. This is carried out through the simulation of the DFN model, by specifying a discharged battery cell as initial condition and galvanostatically charging the cell at different C-rates until the boundary of any given constraint Eqs. (2.32c)-(2.32e) is reached. Such procedure provides possibly nonconvex constraints $I \geq g(\mathrm{CSC})$, see e.g. the red area in Fig. 6.3(a) delimited by curves denoted with numbers 5 and 6 within cyan diamond symbols. These nonconvex constraints can be typically inner-approximated as the union of linear constraints of the form $I \geq a_{j,i}\mathrm{CSC} + b_{j,i}$. For example, Fig. 6.3(a) depicts the linear approximations of the nonconvex constraint as dashed purple curves denoted with numbers 5,1-2 and 6,1-2 within purple circle symbols. The linear constraints 5,2 and 6,2 are the same, and the different constraints are paired such that they delimit OR regions. For instance, the union of linear constraints 5,1 and 5,2 gives the admissible area colored with green in Fig. 6.3(d), and similarly in Fig. 6.3(e) for constraints 6,1 and 6,2. The union of these linear constraints can be mathematically

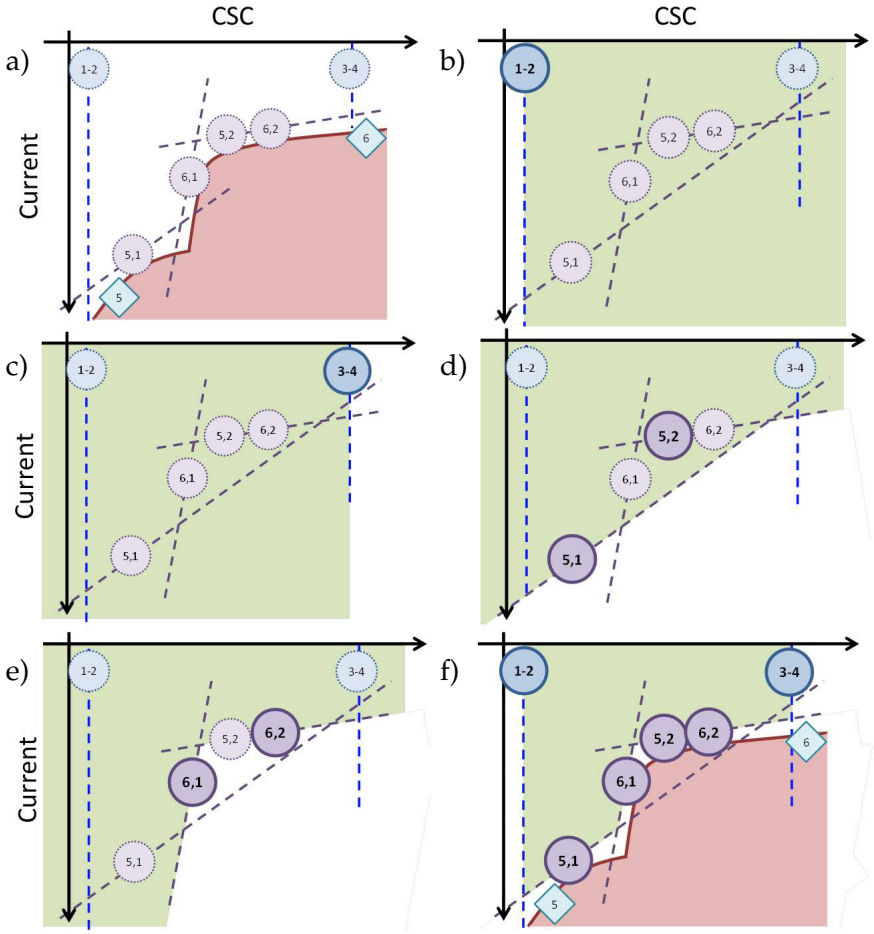

FIGURE 6.3: Electrochemical constraints mapping, where a) nonlinear nonconvex operating region delimited by constraint boundaries; admissible area for b) lower and c) upper bounds of constraint Eqs. (4.49a),(4.49b); union of linear approximations of constraint Eqs. (2.32c)-(2.32e), i.e. d) lines 5,1 and 5,2 and e) lines 6,1 and 6,2; and f) resulting admissible (green) and unsafe (red) regions resulting from the intersection of all the approximated constraints.

written as

$$\bigvee_{i=1}^{2} \left(S_{j,i}^{\mathrm{T}} x_{cl}(k) \leq s_{j,i} \right), \; j = 5,6 \tag{6.7}$$

where the use of the control law Eq. (6.3) makes the expression only dependent on the closed-loop state, $S_{j,i}^{\mathrm{T}} \triangleq a_{j,i}[0 \;\; 1 \;\; 0] - [K_x \;\; -K_i]$ and the scalars $s_{j,i} = -b_{j,i}$ for $j = \{5,6\}, i = \{1,2\}$. Thus, the overall constrained region given by the originally linear constraints and the nonconvex constraints approximated as the union of linear constraints can be defined as

$$\begin{cases} S_j^{\mathrm{T}} x_{cl}(k) \leq s_j, & j = 1,...,4 \\ \bigvee_{i=1}^{2} \left(S_{j,i}^{\mathrm{T}} x_{cl}(k) \leq s_{j,i} \right), & j = 5,6 \end{cases} \quad \forall k > 0. \tag{6.8}$$

The admissible region of the battery operation is then described by the intersection of the union of constraints as shown in Fig. 6.3(f), which can be represented by the

operators AND and OR in generic and compact form as

$$\bigwedge_{j=1}^{c_c} \bigvee_{i=1}^{n_{c,j}} \left(S_{j,i}^{\mathrm{T}} x_{cl}(k) \leq s_{j,i} \right), \forall k \geq 0 \tag{6.9}$$

where c_c is the total number of constraints. In the case of Eq. (6.8), $n_{c,j} = 1$, $S_{j,1} = S_j$ and $s_{j,1} = s_j$ for $j = 1, \ldots, 4$, whereas $n_{c,j} = 2$ for $j = 5, 6$.

6.1.3 The Reference Governor with OR Constraints

Inspired by the SRG described in Section 3.4, this work extends the SRG so it can handle a nonconvex set defined by OR-constraints of the form Eq. (6.9). As with the SRG, the principle behind this modified RG is to compute at each time instant the applied reference $v(k)$ such that if it is kept constant from the time instant k onward, the future state trajectory will never violate the constraints, i.e.

$$\bigwedge_{j=1}^{c_c} \bigvee_{i=1}^{n_{c,j}} S_{j,i}^{\mathrm{T}} \hat{x}_{cl}(\ell | x_{cl}(k), v(k)) \leq s_{j,i}, \quad \ell = 0, ..., \infty, \tag{6.10}$$

where $\hat{x}_{cl}(\ell | x_{cl}, v)$ is the ℓ step ahead prediction previously defined in Eq. (3.97) but repeated here for convenience:

$$\hat{x}_{cl}(\ell | x_{cl}, v) = A_{cl}^{\ell} x_{cl} + (I - A_{cl})^{-1} (I - A_{cl}^{\ell}) B_{cl} v.$$

Since this time we have the OR-constraints in Eq. (6.9), the inner approximation of O_∞ obtained for the case of the SRG [135] is no longer valid. The following lemma shows how to compute an arbitrarily tight finitely-computable approximation $\tilde{O}_\infty$.

Lemma 6.1.1. *Consider the linear system Eq.* (6.4)*, where $A_{cl} \in \mathbb{R}^{n \times n}$ is Schur, and a set of constraints Eq.* (6.9)*. If constraints Eq.* (6.9) *define a compact set in $\mathbb{R}^n$, then for any arbitrarily small $\epsilon > 0$, it is possible to compute a finite integer ℓ^* such that*

$$\tilde{O}_\infty = \left\{ (x_{cl}, v) | \bigwedge_{\ell=0}^{\ell^*} \bigwedge_{j=1}^{c_c} \bigvee_{i=1}^{n_{c,j}} H_{x,\ell,j,i}^{\mathrm{T}} x_{cl} + H_{v,\ell,j,i}^{\mathrm{T}} v \leq h_{j,i} \right\} \cap O_\epsilon \tag{6.11}$$

is an inner approximation of O_∞, where $H_{x,\ell,j,i}^{\mathrm{T}} = S_{j,i}^{\mathrm{T}} A_{cl}^{\ell}$, $H_{v,\ell,j,i}^{\mathrm{T}} = S_{j,i}^{\mathrm{T}} (I - A_{cl})^{-1} (I - A_{cl}^{\ell}) B_{cl}$, $h_{j,i} = s_{j,i}$ and

$$O_\epsilon = \left\{ (x_{cl}, v) | \bigwedge_{j=1}^{c_c} \bigvee_{i=1}^{n_{c,j}} H_{v,j,i}^{\mathrm{T}} v \leq (1 - \epsilon) h_{j,i}, \right\} \tag{6.12}$$

with $H_{v,j,i}^{\mathrm{T}} = S_{j,i}^{\mathrm{T}} (I - A_{cl})^{-1} B_{cl}$.

Proof. See Appendix B. □

Following the SRG, the scalar $\kappa(k) \in [0, 1]$ that provides the best approximation of the desired reference $r(k)$ along the line segment $v(k-1)$ and $r(k)$ ensuring

$(x_{cl}(k), v(k)) \in \tilde{O}_\infty$ is the solution of the optimization problem given by

$$\kappa(k) = \max_{\kappa \in [0,1]} . \ \kappa \tag{6.13}$$

$$\text{s.t.} \bigwedge_{\ell=0}^{\ell^*+1} \bigwedge_{j=1}^{c_c} \bigvee_{i=1}^{n_{c,j}} (\alpha_{j,i}^{\ell} \kappa \leq \beta_{j,i}^{\ell}) \tag{6.14}$$

where $\alpha_{j,i}^{\ell} \triangleq H_{v,\ell,j,i}^{\mathrm{T}}(r(k) - v(k-1))$ and $\beta_{j,i}^{\ell} \triangleq h_{j,i} - H_{x,\ell,j,i}^{\mathrm{T}} x_{\mathrm{cl}}(k) - H_{v,\ell,j,i}^{\mathrm{T}} v(k-1)$ for $\ell = 0, ..., \ell^*$ and $\alpha_{j,i}^{\ell^*+1} \triangleq H_{v,j,i}^{\mathrm{T}}(r(k) - v(k-1))$ and $\beta_{j,i}^{\ell^*+1} \triangleq h_{j,i} - H_{v,j,i}^{\mathrm{T}} v(k-1)$. As with the SRG, the command to be applied to the system is given by

$$v(k) = v(k-1) + \kappa(k)(r(k) - v(k-1)). \tag{6.15}$$

At this point, using the same arguments as for the standard RG it is possible to prove the following result.

Theorem 6.1.2. *Consider a linear system Eq.* (6.4) *subject to constraints Eq.* (6.9) *under the usual RG assumptions that $A_{cl} \in \mathbb{R}^{n \times n}$ is Schur and that at time $k = 0$ the applied reference $v(0)$ is such that $(x_{cl}(0), v(0)) \in \tilde{O}_\infty$. Then if the applied reference is Eq.* (6.15) *where $\kappa(k)$ is computed using Eqs.* (6.13),(6.14)*:*

- *At each time step k, the optimization problem Eqs.* (6.13),(6.14) *always admits at least one solution and the constraints Eq.* (6.9) *are satisfied.*
- *If $r(k)$ is kept constant over time, i.e. $r(k) = r$ and if $(0, v(0) + \kappa(r - v(0))) \in O_\varepsilon, \forall \kappa \in [0, 1]$ then $v(k)$ will converge to r.*

Proof. See [158]. □

Let us now build an efficient solution for the above optimization problem. Considering a generic constraint with indices ℓ, j, i

$$\alpha_{j,i}^{\ell} \kappa \leq \beta_{j,i}^{\ell}, \tag{6.16}$$

four cases are possible:

C1 - If $\alpha_{j,i}^{\ell}, \beta_{j,i}^{\ell} > 0$, any positive κ such that $\kappa \leq \min\{\underline{\kappa}_{j,i}^{\ell}, 1\}$ where $\underline{\kappa}_{j,i}^{\ell} \triangleq \beta_{j,i}^{\ell} / \alpha_{j,i}^{\ell}$ is an admissible solution.

C2 - If $\alpha_{j,i}^{\ell} \leq 0, \beta_{j,i}^{\ell} > 0$, then any $\kappa \leq \underline{\kappa}_{j,i}^{\ell} \triangleq 1$ is an admissible solution.

C3 - If $\alpha_{j,i}^{\ell} < 0, \beta_{j,i}^{\ell} < 0$, then any positive value κ such that $\kappa \geq \bar{\kappa}_{j,i}^{\ell} \triangleq \beta_{j,i}^{\ell} / \alpha_{j,i}^{\ell}$ is an admissible solution if $\bar{\kappa}_{j,i}^{\ell} \leq 1$.

C4 - There is no solution for κ in all other cases.

Notice that case C1 and C2 match the two cases considered for the SRG development in Section 3.4. The remaining cases are added here due to the nature of the OR constraints. Keeping in mind the four cases C1-C4, let us explore the nature of the OR operation over index i for fixed indices ℓ, j, i.e.

$$\bigvee_{i=1}^{n_{c,j}} (\alpha_{j,i}^{\ell} \kappa \leq \beta_{j,i}^{\ell}). \tag{6.17}$$

The admissible region in terms of κ assumes then the form

$$(\kappa \leq \underline{\kappa}_j^\ell) \vee (\kappa \geq \bar{\kappa}_j^\ell) \tag{6.18}$$

where

$$\underline{\kappa}_j^\ell = \max_{i=1,\ldots,n_{c,j}} \underline{\kappa}_{j,i}^\ell \text{ and } \bar{\kappa}_j^\ell = \min_{i=1,\ldots,n_{c,j}} \bar{\kappa}_{j,i}^\ell \tag{6.19}$$

using the convention that if $\underline{\kappa}_{j,i}^\ell$ or $\bar{\kappa}_{j,i}^\ell$ are not defined, they are not considered. Due to recursive feasibility, $\kappa = 0$ is always an admissible solution for the optimization problem Eq. (6.13). This implies that for at least one i the case C1 or C2 apply, and thus $\underline{\kappa}_j^\ell$ is always defined. Conversely, $\bar{\kappa}_j^\ell$ in case C3 might or might not be defined. This analysis translates in two possibilities depending on whether the admissible region defined by the OR constraints with indices ℓ, j is equivalent to the single κ-inequality at the left of Eq. (6.18) or both κ-inequalities in Eq. (6.18) are necessary. Further classifying the set of all indices (ℓ, j) in terms of these two possibilities yields

$$\Sigma_1 = \{(\ell, j) : \kappa \leq \underline{\kappa}_j^\ell\} \text{ and } \Sigma_2 = \{(\ell, j) : \kappa \leq \underline{\kappa}_j^\ell \vee \kappa \geq \bar{\kappa}_j^\ell\} \tag{6.20}$$

depending on the fact that at least one $\bar{\kappa}_{j,i}^\ell$ is defined or not. In the special case where $\bar{\kappa}_j^\ell \leq \underline{\kappa}_j^\ell$, it is convenient to rewrite the condition as $\kappa \leq \underline{\kappa}_j^\ell = 1$. The two groups of indices in Eq. (6.20) can be exploited to rewrite constraint Eq. (6.14) as follows:

$$\left(\bigwedge_{(\ell,j)\in\Sigma_1} (\kappa \leq \underline{\kappa}_j^\ell) \right) \wedge \left(\bigwedge_{(\ell,j)\in\Sigma_2} (\kappa \leq \underline{\kappa}_j^\ell) \vee (\kappa \geq \bar{\kappa}_j^\ell) \right)$$

or by defining $\underline{\kappa}_{\Sigma_1} \triangleq \min_{(\ell,j)\in\Sigma_1} \underline{\kappa}_j^\ell$, the following simplified version is obtained:

$$(\kappa \leq \underline{\kappa}_{\Sigma_1}) \wedge \left(\bigwedge_{(\ell,j)\in\Sigma_2} (\kappa \leq \underline{\kappa}_j^\ell) \vee (\kappa \geq \bar{\kappa}_j^\ell) \right). \tag{6.21}$$

The maximum $\kappa(k)$ satisfying Eq. (6.21) can be computed according to the following simple algorithm:

Algorithm 6.1.1. *Computation of κ for the RG with OR constraints.*

1. *IF $\bar{\kappa}_j^\ell \leq \underline{\kappa}_{\Sigma_1}$ for any $(\ell, j) \in \Sigma_2$*
   - 1.1 $\kappa(k) = \underline{\kappa}_{\Sigma_1}$;
   - 1.2 *STOP.*
2. *ELSE, for any $(\ell, j) \in \Sigma_2$ such that $\bar{\kappa}_j^\ell > \underline{\kappa}_{\Sigma_1}$*
   - 2.1 *Set* $\underline{\kappa}_{\Sigma_1} = \min\{\underline{\kappa}_{\Sigma_1}, \underline{\kappa}_j^\ell\}$
   - 2.2 *Update* $\Sigma_2 = \Sigma_2 \setminus \{(\ell, j)\}$
3. *GO TO 1.*

Remark 6.1.3. *This algorithm solves a maximization problem for the scalar κ in the presence of nonconvex constraints without using any optimization solver. The numerical operations involved do not require any special software nor particularly performing hardware for its real-time implementation (this is in opposition to the high computational requirements involved*

when solving nonconvex optimization problems using more standard control schemes such as MPC).

6.1.4 Digital Implementation

The constrained state feedback control approach presented in sections (6.1.1)-(6.1.3) exploits the linear structure of the model state equation in Eq. (6.1) and relies on the perfect knowledge of the internal state of the system. However, this is not realistic since only a nonlinear combination of the state can be gathered from an operating battery. A state observer is used to bypass this issue, resorting to an extended Kalman filter given its simplicity and low computational cost compared with other nonlinear estimators.

The system dynamics are based on the state Eq. (6.1), while the measurement equation corresponds to the nonlinear output Eq. (4.65) representing the voltage measurement in contrast to the linear output Eq. (6.2). Indeed, SOC cannot be measured directly in a precise way. After adding the process $w_n(k)$ and measurement $v_n(k)$ noise sources, the resulting model takes the form

$$x_s(k+1) = A_s x_s(k) + B_s u(k) + w_n(k) \tag{6.22}$$

$$y_n(k) = h_n\left(u(k), x_s(k)\right) + v_n(k) \tag{6.23}$$

where $x_s(k) \in \mathbb{R}^2$ is the solid-phase diffusion state vector $x_s(k) = [\mathrm{SOC}(k),\ \mathrm{CSC}(k)]^{\mathrm{T}}$, $u(k) \in \mathbb{R}$ is the battery current input vector $u(k) = I(k)$, $y(k) \in \mathbb{R}$ is the battery voltage output vector $y_n(k) = V(k)$, $w_n(k) \in \mathbb{R}^2$ and $v_n(k) \in \mathbb{R}$ are process and measurement white noise sequences, respectively, with the classical noise assumptions, and the nonlinear output function is given by

$$h_n(u(k), x_s(k)) = \Delta U_s^{\pm}(k) + \Delta\eta_s^{\pm}(k) + \Delta\phi_e(k) - \frac{R_f}{a_s L}u(k). \tag{6.24}$$

The standard EKF of Table 3.2 is directly used as state estimator, where the state estimate is denoted by $\hat{x}_s(k)$. Thus, the true state $x_s(k)$ is replaced in the control law Eq. (6.3) by the estimated state $\hat{x}_s(k)$.

6.2 Simulation Results

To evaluate the effectiveness of the RG with OR constraints proposed in Section 6.1, we tested it in simulation on two battery cells differing in chemistry, namely graphite | LCO and graphite | LMO. The DFN model described in Section 2.3 is simulated using a third-order Padé approximation for the solid-phase diffusion equations, whereas all the other partial differential and algebraic equations are discretized with the central difference method. The battery parameters for each chemistry are provided in Table C.2, Appendix C [22, 157, 159]. Each battery cell chemistry has an associated set of constraints Eqs. (2.32), whose parameter values are reported in Table 6.1.

Trespassing a constraint induces a specific degradation mechanism. If inequalities Eqs. (2.32a)-(2.32b) are violated, the graphite electrode deposits lithium [160], the LCO electrode is transformed towards inactive phases and oxygen is released [161], and the LMO electrode becomes structurally unstable and more vulnerable to degradation [162]. If constraints Eqs. (2.32c)-(2.32d) are violated, lithium plating side reaction takes place in the graphite electrode [10] and both LCO and LMO positive

TABLE 6.1: Values for the DFN model constraints Eqs. (2.32) associated to degradation mechanisms.

Parameter	Graphite	LCO	LMO
$r_{c_s}{}^a$	1.00	0.50	0.20
U_{sr} (V)	0.00	4.30	4.20
$\underline{r}_{c_e}$ (mol·m^{-3})	1.00	1.00	1.00

[a] $\bar{r}_{c_s}$ for graphite, $\underline{r}_{c_s}$ for LCO, LMO.

electrodes undergo solvent oxidation [160, 35], which is critical for the LMO electrode since it involves acid generation, active material dissolution [163], and manganese deposition in the graphite electrode [164]. Finally, if inequalities Eqs. (2.32e) are violated, the amount of lithium in the electrolyte is depleted, which may increase the internal battery impedance.

As detailed in Section 6.1.2, constraints Eq. (2.32) are mapped into constraints Eq. (4.49) for the closed-loop system Eqs. (6.4),(6.5) with compactly written constraints Eq. (6.9). The specific vector and scalar values defining the constraints Eq. (6.9) for each considered battery are reported in Table 6.2. Two aspects should be highlighted. First, recall that only the negative electrode is modeled through the EHM embedded in system Eq. (6.4) given its slower dynamics when compared to the positive electrode. This just means that the degradation limiting electrode is the latter one, since its state will reach the associated constraint boundary sooner. However, material balance allows to map the constraints of the positive electrode into the negative electrode, which ensures that both electrodes respect their constraints. By constraining the negative electrode with the values of Table 6.2, which are smaller than the theoretical values reported in Table 6.1, we are able to keep the positive electrode within its constraint boundaries of Table 6.1. Secondly, the number of constraints differs for the two battery chemistries because they come associated with different nonconvex regions, and therefore different inner approximations are required (see red areas in Fig. 6.4). Instead of taking linear approximations that are tangent to the nonlinear functions wrapping the nonconvex regions, a certain margin (orange area) is left between the nonlinear constraints (delimiting the red area) and the linear approximations (delimiting the green area) to account for model mismatch. Extensive numerical simulations have demonstrated that for the reported values, the satisfaction of constraints Eqs. (6.9) in system Eqs. (6.4),(6.5) always ensures the satisfaction of constraints Eqs. (2.32) on the DFN model, even in presence of the uncertainty resulting from the difference between the DFN and the EHM.

TABLE 6.2: Values for the constraints Eq. (6.9).

Graphite | LCO				Graphite | LMO			
$s_{1,1}$	0	$s_{2,1}$	0.712	$s_{1,1}$	0	$s_{2,1}$	0.622
$s_{3,1}$	0	$s_{4,1}$	0.712	$s_{3,1}$	0	$s_{4,1}$	0.622
$s_{5,1}$	-9.33	$s_{5,2}$	-2.59	$s_{5,1}$	-17.28	$s_{5,2}$	-5.76
-	-	-	-	$s_{6,1}$	-33.6	$s_{6,2}$	-5.76
$a_{5,1}$	22.47	$a_{5,2}$	0	$a_{5,1}$	24	$a_{5,2}$	7.2
-	-	-	-	$a_{6,1}$	96	$a_{6,2}$	7.2

For the model-based estimation and control, the second-order EHM Eq. (5.1) is used with constant parameters $\theta(k) = \theta$, where $g_s = 2.60 \cdot 10^{-3}$ s^{-1}, $\gamma_s = 8.81 \cdot 10^{-6}$ C^{-1} and $\beta_s = 0.70$ for both battery chemistries. These parameters are directly derived

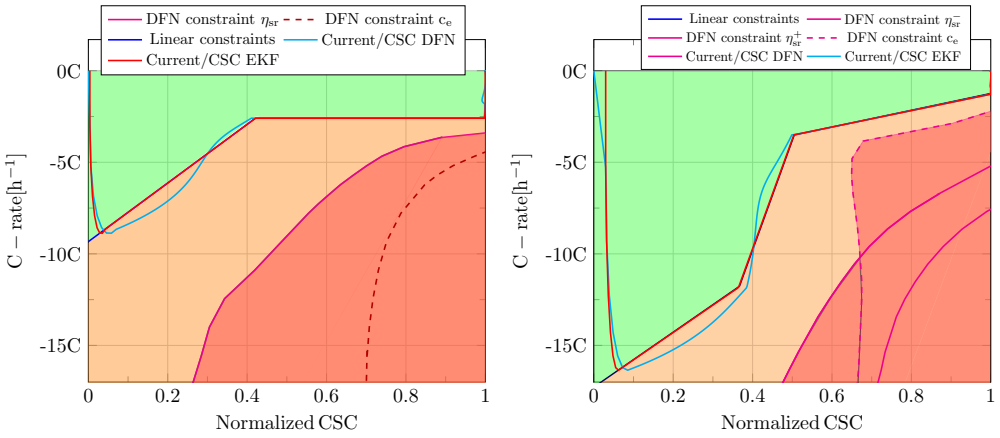

(a) LCO battery cell with $\eta_{sr}^+ = 4.3$ V (b) LMO battery cell with $\eta_{sr}^+ = 4.2$ V

FIGURE 6.4: DFN model critical conditions for η_{sr}^+ at the positive electrode/separator interface (electrode dependent), $\eta_{sr}^- = 0.0$ V at the negative electrode/separator interface and $c_e = 1.0$ mol·m^{-3} at the current collector/negative electrode interface (common for both batteries). The green, orange and red regions represent the admissible, safety margin and unsafe operating regions, respectively. The solid red and cyan curves represent the DFN simulator states and the EKF state estimates, respectively.

from the DFN model given the explicit relationship between this model and the EHM. Both battery chemistries have the same parameter set because they share the same negative electrode. The internal state of the battery is estimated using an extended Kalman filter (EKF), which was tuned with the following parameters:

$$\begin{aligned} \hat{x}_s(0) &= [3.89, 3.89] \cdot 10^{-2} \\ \text{diag}(P(0)) &= 1_2 \cdot 10^{-9} \\ \text{diag}(Q) &= \left[10^{-13}, 10^{-11}\right] \\ R &= 10^{-6} \end{aligned} \tag{6.25}$$

where the state vector is dimensionless, as well as $\text{diag}(P)$ and $\text{diag}(Q)$, while the unit of R is $[\text{V}^2]$. Such state estimate is exploited by the optimal LQR state feedback with integral action, which pre-stabilizes the system with respect to the state-of-charge. The LQR controller is designed by selecting suitable Q_c and R_c values, i.e. $Q_c = 10^3 \cdot I_d$ and $R_c = 10^{-4}$, which results in the matrices $K_x = [2.8137 \;\; 0.0066] \cdot 10^4$ and $K_i = -2.7833 \cdot 10^3$. The control sampling period is 1 s.

The results of the RG with OR constraints in terms of input and state trajectories are shown in Figs. 6.4(a) and 6.4(b) for LCO and LMO, respectively. The DFN model (actual) state is represented by the solid cyan curve, while the EKF state estimate corresponds to the solid red curve. For both chemistries, the actual state drifts from the state estimate during the high current stage of the charging process. While the state estimate is perfectly riding the linear constraints once it achieves them, the actual state overshoots the first constraint after the maximum current is applied. Then, it stays within the safety area for a while and it goes back to the safe operating region, to end up riding the constraint until the charging process is finished. This behavior is due to model mismatch, which increases with the current magnitude given the assumptions involved to derive the EHM. Indeed, the assumptions of constant electrolyte and thermal dynamics are harder to meet as the current rate increases. The safety margin has been tuned to enforce constraint satisfaction regardless model

mismatch.

Let us now compare the improvements of the proposed approach with the commercially available and widely used CCCV charging strategy. The virtual batteries are charged with a 2C CC until the upper cut-off voltages are reached (4.06 V and 3.96 V for LCO and LMO, respectively), followed by a CV charge. Figs. 6.5(a) and 6.5(b) show current and voltage profiles, respectively, for LCO and LMO batteries subject to CCCV and the RG with OR constraints charging strategies. The CCCV profile introduces a constant amount of energy during the CC stage (30 min for 2C), after which the CV stage takes over and gradually reduces the current rate to zero. Meanwhile, the RG increases the input current at the beginning of charging and it keeps it higher than e.g. 2C for most part of the charging process. This fact explains the fast charging capabilities of the RG with OR constraints. But more importantly, the proposed RG is healthier for battery charging, since it avoids the violation of constraints associated to battery degradation as pointed out in Fig. 6.4. Notice how the RG also enables safe incursions beyond the upper cut-off voltage specified for the CCCV strategy. This result proves the point that voltage operating windows are not really aligned with any specific degradation mechanism.

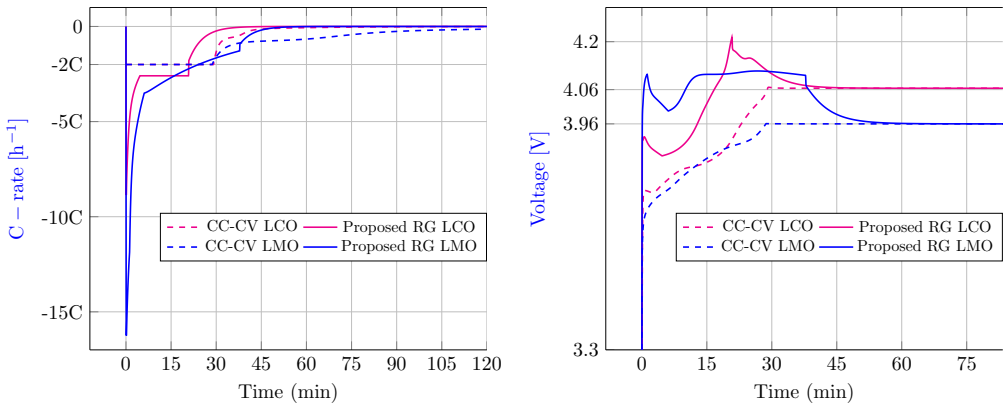

(a) Current profile.

(b) Voltage profile.

FIGURE 6.5: Current and voltage profiles from the DFN simulator using CCCV (as dashed curves) and the proposed RG method (as solid curves) for LCO (in magenta) and LMO (in blue).

Although current and voltage are easy to measure and provide relevant information of the operation state of the battery, we are more concerned about the constrained internal states. The temporal evolution of the constrained variables in Eqs. (2.32) are shown in Fig. 6.6 for both tested charging strategies. Fig. 6.6(a) shows the SOC evolution. For LCO, the RG with OR constraints takes 35 min to achieve 99.5% SOC, while the CCCV strategy requires more than twice that time (90 min) for the same SOC level. Such charging time difference becomes even greater for the LMO cell, needing 48 min for the proposed RG to reach 99.5% SOC level whereas CCCV strategy only gets up to 87% after 120 min of charging. This is due to the different diffusion time constants τ_s^+ of each positive electrode, namely $\tau_{s,\text{LCO}}^+ = 7.23$ s and $\tau_{s,\text{LMO}}^+ = 722.50$ s. A similar trend can also be seen in the CSC evolution of Fig. 6.6(b), but with faster dynamics. It is interesting to inspect the SOC^+ evolution (see Fig. 6.6(c)), since it shows how the satisfaction of the negative electrode constraints guarantees the satisfaction of constraints in the positive electrode ($\underline{r}_{c_s^+} \geq 0.50$ for LCO and $\underline{r}_{c_s^+} \geq 0.20$ for LMO). Finally, the electrolyte concentration c_e as well as the positive and negative side reaction overpotentials $\eta_{sr}^{\pm}$ are depicted in Figs. 6.6(d)-6.6(f). In contrast to the

CCCV, the RG with OR constraints pushes more the performance of both batteries by forcing these variables to go closer to the constraint boundaries (namely $c_e \geq 1.0$ mol·m^{-3}, $\eta_{sr}^{-} > 0.0$ V and $\eta_{sr}^{+} < 0.0$ V), especially at the beginning of the charging process.

These simulation results show that LCO and LMO batteries can be charged more than twice as fast by using the RG with OR constraints when compared to conventional charging strategies. At the same time, the proposed RG copes with electrochemical constraints associated to degradation mechanisms, which are supposed to limit battery performance in the long run.

6.3 Concluding Remarks

This chapter develops a novel RG scheme able to handle nonconvex constraints, namely constraints that can be characterized by an OR logical operator. This modified version of the RG is based on a reduced-order electrochemical model, and it is designed to respect nonconvex electrochemical constraints associated to battery degradation. This RG acts on a plant that is pre-stabilized through a LQR controller, and it has access to the battery internal state thanks to an EKF. The proposed approach has been proven to charge lithium-ion batteries faster than commercial CCCV charging strategies in a simulation environment. This has been corroborated for two different battery chemistries, namely LCO and LMO. However, the proposed RG also ensures the satisfaction of constraints related with battery aging, which makes us expect that this feedback charge strategy is also able to extend battery life beyond what is achieved using CCCV protocols. The next Chapter 7 explores the validity of the last claim in the light of experiments.

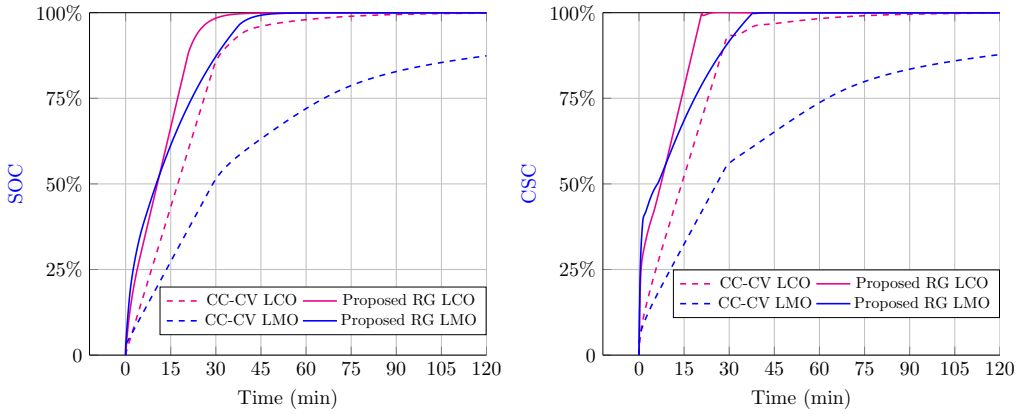

(a) SOC evolution.

(b) CSC evolution.

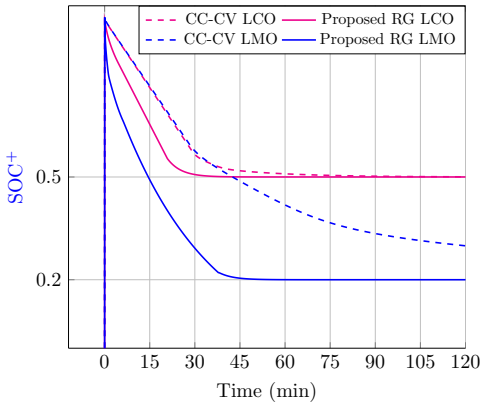

(c) SOC^+ evolution.

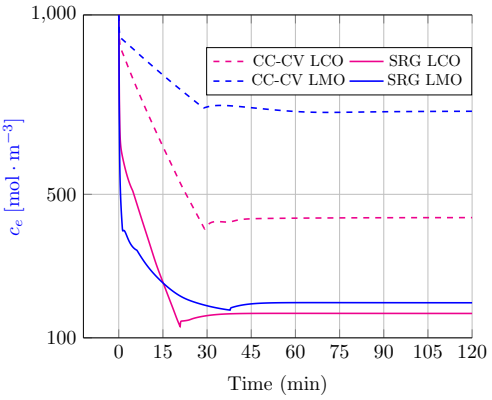

(d) c_e evolution.

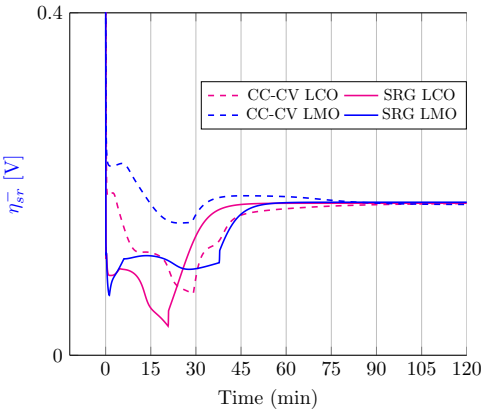

(e) η_{sr}^- evolution.

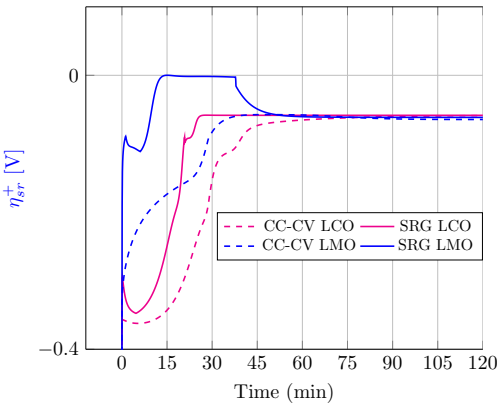

(f) η_{sr}^+ evolution.

FIGURE 6.6: Profiles of the constrained variables from the DFN simulator using CCCV (as dashed curves) and the proposed RG method (as solid curves) for LCO (in magenta) and LMO (in blue).

Chapter 7

Safe & Fast Charging Control

This last chapter extends the previous Chapter 6 by further validating the proposed charging strategy based on the reference governor with OR constraints. In contrast to the previous Chapter 6 that used simulation and short term cycling to test fast charging capabilities, the current chapter resorts to experiments and long-term cycling to assess the safe and fast charging features of the proposed approach. This approach is compared with a benchmark coming from the industry, which is the most widely used commercial solution for charging batteries, namely the CCCV protocol. This chapter structure is the following. Section 7.1 introduces different practical issues that we faced when implementing the RG with OR constraints in the experimental setup, along with the different ways we solved such issues. Section 7.2 is entirely devoted to show and analyze the obtained experimental results.

7.1 Output Feedback Constrained Control

While Chapter 6 served us to test fast charging using a reduced-order model, a modified version of the standard RG and electrochemical constraints associated to battery degradation, we still need to check if battery aging can be reduced compared to commercial charging protocols. The current chapter aims at validating the control scheme proposed in the previous chapter via long-term cycling experiments. Whereas all the required theoretic development of the modified RG is provided in Chapter 6, here special care is taken regarding the model and the state estimator.

7.1.1 Model Identification

The electrochemical parameters of the DFN model for the lithium nickel-cobalt-aluminum oxide (NCA) battery cell used in this study were previously identified through sensitivity-based optimal experiment design [90]. The model identification in [90] was carried out at low C-rates and constant temperature. The identified parameters are shown in Table C, Appendix C.3. However, fast charging strategies presumably excite electrolyte and thermal dynamics. To elucidate this issue, a 2C CC charge experiment was conducted with a NCA battery cell, and the current profile (in C-rate) is shown in Fig. 7.1(a). The associated voltage V_{exp} and surface temperature $T_{bs,\text{exp}}$ response of the battery are represented by the solid black curves in Fig. 7.1(b), (c), respectively. The first aspect to notice from a visual inspection of Fig. 7.1 is that, under the considered charging condition, the surface temperature is not constant. As a matter of fact, it rises up to c.a. 38°C from an ambient temperature of 25°C. It is apparent that the isothermal assumption for the model of the previous Chapter 6 is not fulfilled in this case. Thus, a more complex model is required.

Let us consider a more general model than the one used in Section 6.1.1 by simplifying the original model Eqs. (4.63)-(4.73) differently. Instead of only considering a

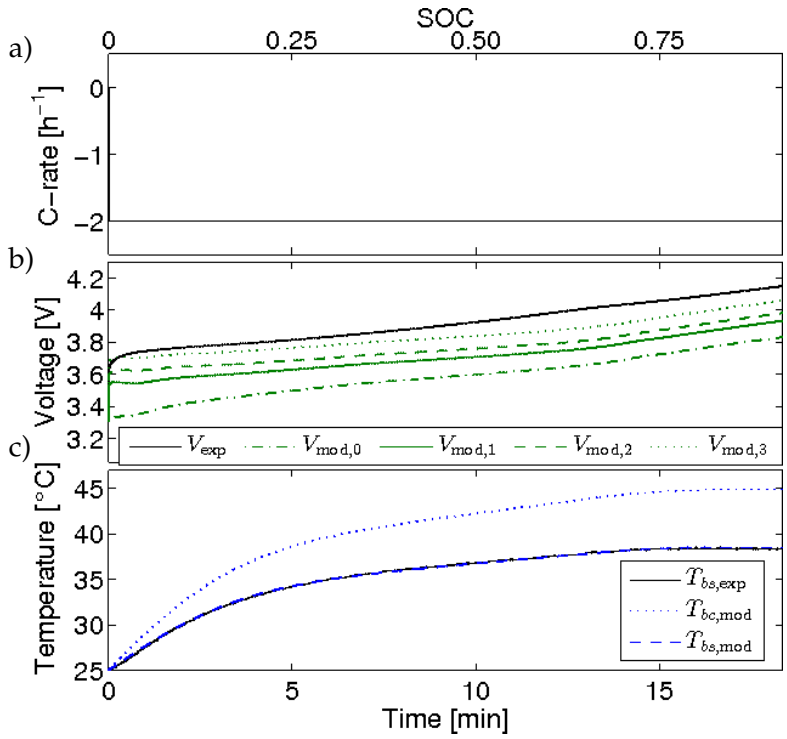

FIGURE 7.1: a) 2C CC applied current at 25°C, and associated response of the battery in terms of b) voltage and c) surface temperature. Different system models are also shown in the voltage plots, namely V_{exp} is the experimental voltage; $V_{\text{mod},0}$ is the battery OCV; $V_{\text{mod},1}$ is the surface overpotential; $V_{\text{mod},2}$ is the electrolyte potential drop; and $V_{\text{mod},3}$ is an ohmic resistance potential drop. The temperature plots show the experimental surface temperature $T_{bs,\text{exp}}$ and the modeled core $T_{bc,\text{mod}}$ and surface temperatures $T_{bs,\text{mod}}$.

two-state EHM for the solid-phase diffusion dynamics in the state Eq. (4.63), here we include a second-order EHM for the electrolyte-phase diffusion and a second-order model for thermal dynamics, but also exclude capacity loss. Secondly, all model parameters are considered to be known *a priori*, so Eq. (4.64) is dropped. Thirdly, no side reaction is accounted for, which allows us to cancel Eqs. (4.66),(4.67). The resulting model replacing Eqs. (4.63)-(4.73) takes the form

$$x_{seT}(k+1) = A(x_{seT}(k))x_{seT}(k) + Bu(k) + f_x(u(k), x_{seT}(k), y(k)) \tag{7.1}$$
$$y(k) = h_y\left(u(k), x_{seT}(k)\right) \tag{7.2}$$

where $x_{seT}(k) \in \mathbb{R}^6$ is the state vector $x_{seT}(k) = \left[x_s(k)^{\mathrm{T}}, x_e(k)^{\mathrm{T}}, x_T(k)^{\mathrm{T}}\right]^{\mathrm{T}}$, $u(k) \in \mathbb{R}$ is the input vector $u(k) = I(k)$, $y(k) \in \mathbb{R}^2$ is the output vector $y(k) = \left[V(k), T_{bs}(k)\right]^{\mathrm{T}}$ and the remaining matrices and functions are given in Eqs. (4.68)-(4.73) with $B = B_z$ and dropping the capacity fade state.

Since the work of [90] has not covered thermal dynamics yet, a complete identification of the thermal submodel was required. The thermal model embedded in the state Eq. (7.1) comes from Eq. (4.30) in discrete-time form with a sampling period $T_s = 1$ s, i.e.

$$x_T(k+1) = A_T x_T(k) + f_T\left(u(k), x_T(k), \text{SOC}(k), V(k)\right), \tag{7.3}$$

where $x_T(k) \in \mathbb{R}^2$ is the temperature state vector given by $x_T(k) = [T_{bc}(k), T_{bs}(k)]^{\mathrm{T}}$ and the state matrix and nonlinear function are given by

$$A_T = \begin{bmatrix} 1 - \frac{k_c}{\rho_c C_{pc}} & \frac{k_c}{\rho_c C_{pc}} \\ \frac{k_c}{\rho_s C_{ps}} & 1 - \frac{h_c + k_c}{\rho_s C_{ps}} \end{bmatrix}, \; f_T = \begin{bmatrix} \frac{1}{\rho_c C_{pc}} \left(\Delta U_b^{\pm}(k) - V(k) \right) u(k) \\ \frac{1}{\rho_s C_{ps}} h_c T_{\mathrm{amb}} \end{bmatrix}, \tag{7.4}$$

where the term $\frac{\partial U_b^{\pm}}{\partial T_{bc}}$ in Eq. (4.30) is set to zero given its typically small value. Notice that in the way that the thermal model Eqs. (7.3),(7.4) is written, it only depends on the thermal states $x_T(k)$, the input current $I(k)$ and the terminal voltage $V(k)$, since the SOC(k) can be determined by Coulomb counting. Therefore, the identification of the thermal model can be done independently of the identification of the electrochemical model as pointed out in [31]. A particle swarm optimization (PSO) algorithm [165] was used to identify the parameter set of the thermal model $\theta_T = [\rho_c C_{pc},\ k_c,\ h_c]^{\mathrm{T}}$. The PSO algorithm solves the following optimization problem

$$\min_{\theta_T} . \; \sqrt{\frac{1}{n_d} \sum_{i=1}^{n_d} |T_{bs,i} - \hat{T}_{bs,i}|^2} \tag{7.5}$$

$$\text{s.t.} \quad \text{Eqs. (7.3), (7.4)} \qquad \underline{\theta}_T \leq \theta_T \leq \overline{\theta}_T \tag{7.6}$$

where T_{bs} and $\hat{T}_{bs}$ are the measured and model predicted surface temperatures, respectively, n_d is the number of data points and $\underline{\theta}_T$ and $\overline{\theta}_T$ are lower and upper bounds for the thermal parameters, respectively. The identified parameter set $\hat{\theta}_T$ is shown in Table C.3, Appendix C. The simulated temperature response of the identified thermal model is depicted in Fig. 7.1(c), along with the experimental surface temperature $T_{bs,\mathrm{exp}}$. Both the surface $T_{bs,\mathrm{mod}}$ and the core $T_{bc,\mathrm{mod}}$ temperatures predicted by the model are shown in the figure, from which it follows a good model match for the surface temperature dynamics.

Now that a thermal model has been obtained, the next step is to study the voltage mismatch between the experiments and the electrochemical model. The model parameters identified in [90] for the full-order model are mapped into the reduced-order electrochemical model given the relationship between the DFN model and the *e*EHM shown in Chapter 4. The first component of the output Eq. (7.2) is the voltage component, whose difference variables can be expanded in order to get

$$y_n(k) = (U_s^+(k) - U_s^-(k)) + (\eta_s^+(k) - \eta_s^-(k)) + \Delta\phi_e(k) - \frac{R_f}{a_s L} u(k). \tag{7.7}$$

Besides the experimental voltage, Fig. 7.1(b) shows four different simulated voltage responses to highlight the contribution of each term within the voltage Eq. (7.7). The voltage responses represented in Fig. 7.1(b) are: $V_{\mathrm{mod},0}$ is the battery OCV, i.e. the first term in parentheses in the right-hand side of Eq. (7.7); $V_{\mathrm{mod},1}$ adds the second term in parentheses of the equation corresponding to the surface overpotential; $V_{\mathrm{mod},2}$ adds the third term in the equation, the electrolyte potential drop; $V_{\mathrm{mod},3}$ adds the last term of the equation corresponding to an ohmic resistance potential drop. The latter contribution is used to reduce the gap between the measured voltage V_{exp} and the voltage predicted by the model. However, a good match between experimental and measured voltage cannot be obtained even with the addition of this latter contribution as seen in Fig. 7.1(b). Therefore, we decided to transfer this voltage mismatch problem from modeling to state observer design by considering R_f

as an extra state with slow dynamics, which is detailed in Section 7.1.3 below.

Remark 7.1.1. *Instead of considering R_f as a lumped parameter, a thorough identification of the electrolyte submodel would also reduce model mismatch. However, some attempts to follow this second road using the 2C CC charging profile of Fig. 7.1 were fruitless. This issue might be related to lack of excitation of the system input. Moreover, R_f is still expected to be required for reducing model mismatch even with a properly identified (at high C-rates) electrolyte submodel. Therefore, the electrolyte parameters found by [90] (at low C-rates) were the ones considered and R_f was directly used to account for model uncertainty in the filter design.*

This section shows that the solid-phase diffusion dynamics exploited in Chapter 6 are not sufficient to describe the considered NCA battery cell during 2C CC charge, i.e. fast charging conditions. In terms of voltage, electrolyte-phase diffusion dynamics and an ohmic potential drop are required to reduce model mismatch. Notice that if the voltage predicted by the model is below the real one, a state observer would continually over-estimate the state-of-charge (SOC). This is easily seen with the help of the upper x-axis in Fig. 7.1 representing battery SOC. Consider model 1 in Fig. 7.1(b), which accounts for the OCV and surface overpotential only. At e.g. 0.75 SOC, the voltage $V_{\text{mod},1} \approx 3.8$ V, while the real voltage measured from the battery $V_{\text{exp}} \approx 3.8$ V with an associated SOC of approximately 0.25. This gap between SOCs would make the state observer to report a larger SOC than the real one due to model mismatch. This was observed in simulation, where the EHM-based EKF provided an overestimated SOC with respect to the true state value coming from the NCA battery simulator based on the DFN model. In terms of temperature, the skin temperature can increase above 35°C (more than 10°C temperature difference with respect to ambient temperature), whereas the internal temperature is certainly higher than that value due to heat generation. Although the measurement of the internal temperature is needed for a proper model validation as done in [31] , the temperature inside the battery can be as high as 45°C according to our model. Hence, battery internal temperature should also be monitored to avoid safety hazards and thermal runaways, which is left for future work.

All the aforementioned considerations might improve state estimation at the expense of a nonlinear model Eqs. (7.1),(7.2). This aspect conflicts with the linear state dynamics exploited in Chapter 6 for constrained control. Therefore, in contrast to the previous chapter where the same simple model is used for both estimation and control, here we use two different models that differ in complexity. The first model is the nonlinear model Eqs. (7.1),(7.2) aiming at providing reliable state estimates to the control scheme, whereas the second one is the simpler linear time invariant (LTI) model Eqs. (6.1),(6.2) to come up with suitable control laws. Both the state estimation approach and the constrained control approach are successively introduced in the next sections.

7.1.2 The Reference Governor with OR Constraints

In order to implement the same solution as in Chapter 6 for constrained control based on a pre-stabilizing LQR controller and a RG scheme that guarantees constraint satisfaction, a LTI model is required. It turns out that the model Eqs. (6.1),(6.2) exploited in Chapter 6 is a particularization of the more general nonlinear model Eqs. (7.1),(7.2). By considering electrolyte-phase diffusion and thermal dynamics as constant in state Eq. (7.1), and replacing the nonlinear function in the output Eq. (7.2) by the SOC(k) measurement via $C_s = [1 \;\; 0]$, the model Eqs. (7.1),(7.2) reduces to the

model Eqs. (6.1),(6.2). For convenience, the model Eqs. (6.1),(6.2) is recovered here

$$x_s(k+1) = A_s x_s(k) + B_s u(k) \tag{7.8}$$
$$y_s(k) = C_s x_s(k) \tag{7.9}$$

where $x_s(k) \in \mathbb{R}^2$ is the solid-phase diffusion state vector $x_s(k) = [\text{SOC}(k),\ \text{CSC}(k)]^\text{T}$, $u(k) \in \mathbb{R}$ is the battery current input vector $u(k) = I(k)$ and $y_s(k) \in \mathbb{R}$ is the battery state-of-charge $y_s(k) = \text{SOC}(k)$. This model is exploited in a similar manner as in Chapter 6 to synthesize an optimal and constrained controller, namely to pre-stabilize the system through a LQR with integral action as in section 6.1.1 and to enforce constraint satisfaction via the proposed RG as in section 6.1.3.

Remark 7.1.2. *Notice that the state vector for estimation contains more information than the one considered for control purposes, given the more detailed model used. This approach was preferred in order to keep the computational complexity of the control scheme relatively low. If temperature constraints to avoid thermal runaways need to be considered, the proposed control scheme has to be extended to account for the additional nonlinear thermal dynamics. Anyways, since the internal temperature of the battery is estimated, a naive approach would be to disconnect the input current if an abnormal thermal behaviour is detected. Accounting for thermal constraints is left as future work.*

7.1.3 The Extended Kalman Filter

In order to have access to the state vector of the battery, an extended Kalman filter is designed based on the nonlinear model Eqs. (7.1),(7.2). This model is augmented with an uncertain parameter $\theta(k) = R_f(k)$ that adds a potential drop to the voltage equation, which is intended to reduce the voltage mismatch discussed in Section 7.1.1. Process $w_n(k)$ and measurement $v_n(k)$ noise sequences have also been introduced, resulting in the following model

$$x_{seT\theta}(k+1) = A(x_{seT\theta}(k))x_{seT\theta}(k) + Bu(k) + f_x(u(k), x_{seT\theta}(k), y(k)) + w_n(k) \tag{7.10}$$
$$y(k) = h_y\left(u(k), x_{seT\theta}(k)\right) + v_n(k) \tag{7.11}$$

where $x_{seT\theta}(k), w_n(k) \in \mathbb{R}^7$ are the augmented state and process noise vectors defined as $x_{seT\theta}(k) = \left[x_s(k)^\text{T}, x_e(k)^\text{T}, x_T(k)^\text{T}, \theta(k)\right]^\text{T}$ and $w_n(k) = [w_{n,seT}(k), w_{n,\theta}(k)]^\text{T}$, respectively. $u(k) \in \mathbb{R}$ is the input vector $u(k) = I(k)$, $y(k), v_n(k) \in \mathbb{R}^2$ are the output and measurement noise vectors where the former vector is defined as $y(k) = [V(k), T_{bs}(k)]^\text{T}$, and $\theta(k) \in \mathbb{R}$ is the parameter vector $\theta(k) = R_f(k)$. The noise sources are white noise sequences with the classical noise assumptions. The standard EKF of Table 3.2 is directly used as state estimator, where the state estimate is denoted by $\hat{x}_{seT\theta}(k)$. To replace the true state $x_s(k)$ with the state estimate in the control scheme, a linear transformation C_{lt} such as

$$C_{lt} = \begin{bmatrix} 1 & 0 & 0 & 0 & 0 & 0 & 0 \\ 0 & 1 & 0 & 0 & 0 & 0 & 0 \end{bmatrix} \tag{7.12}$$

is required. Therefore, through $\hat{x}_s(k) = C_{lt}\hat{x}_{seT\theta}(k)$ we select the subset of the EKF state estimates corresponding to the solid-phase diffusion states, and then the true state $x_s(k)$ is replaced in the control law by the estimated state $\hat{x}_s(k)$.

7.2 Experimental Results

After validating in simulation the RG with OR constraints for fast charging in Section 6.2, the next step is to validate it experimentally through long-term cycling in order to assess the presumed safe charging capabilities of the proposed approach. We had the opportunity to start a collaboration with Prof. Scott Moura, who leads the Energy, Controls Applications Lab (eCAL) at UC Berkeley. Through this collaboration, we had the privilege of exploiting the facilities of eCAL to carry out the required tests. The experimental setup and testing conditions are introduced first, followed by the implementation aspects associated to the closed-loop battery control and a discussion of the obtained results next.

7.2.1 Setup and Testing Conditions

Aging tests were carried out on Panasonic 2.7 Ah 18650 lithium nickel-cobalt-aluminum oxide (NCA) battery cells. The battery nominal capacity is the one used whenever a C-rate is reported. Cycling aging tests (CAT), as well as reference performance tests (RPT), were performed successively, and the flow chart of these experiments is shown in Fig. 7.2. In the scheme, CC stands for constant current, CV for constant voltage, and SRPT and LRPT for short and long RPT, respectively. The current, voltage and surface temperature data was collected by a battery tester (SBT2050, PEC, Belgium) every 1 s. The ambient temperature was set to 25 °C through an environmental chamber (BTX-475, Espec, Japan).

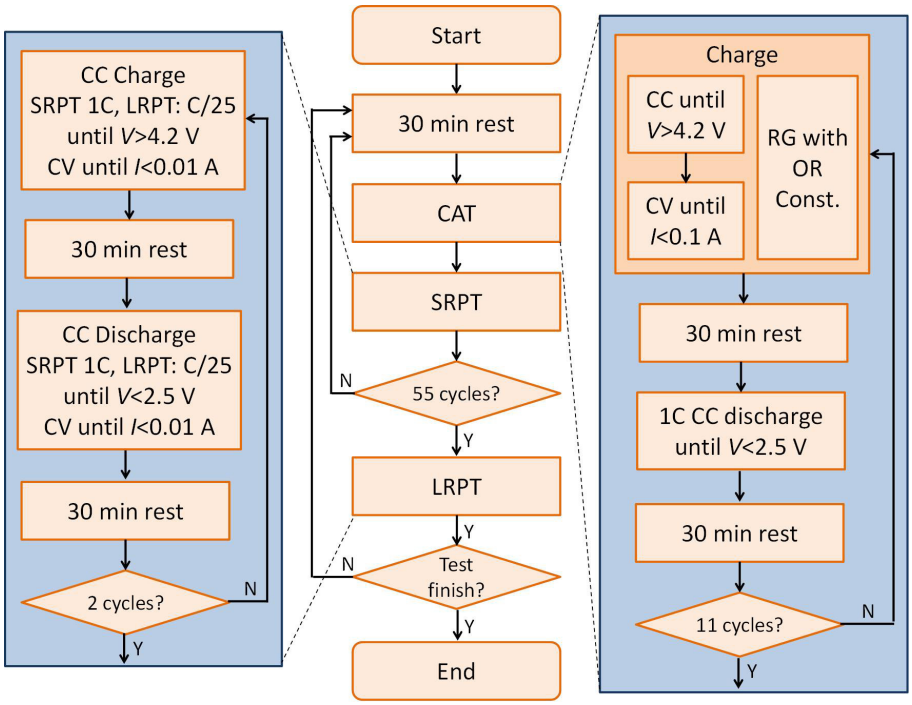

FIGURE 7.2: Flow chart of the cycling aging (CAT) and reference performance (RPT) tests.

The CATs (see right column of Fig. 7.2) consist of 11 cycles with four steps each. The first step changes according to the studied charging strategy, namely 1C CCCV, 2C CCCV and RG with OR constraints. The second and fourth steps correspond to resting periods, while in the third step the battery undergoes discharge using

the same policy for all scenarios. The batteries were cycled for 110 cycles using CCCV commercial charging strategies and 99 cycles using the proposed RG charging strategy. The reason for this discrepancy is explained below.

The RPTs consist of 2 cycles with four steps each (see left column of Fig. 7.2). Similarly as the CATs, the second and fourth steps are resting periods, but in contrast to the CATs, both charge (first step) and discharge (third step) are conducted using CCCV at the same given C-rate. Two different RPTs are considered, namely a SRPT after each CAT and a LRPT after 5 consecutive CATs. The main difference in operation between both RPTs is the C-rate used, and consequently the testing time. SRPT involved 1C currents while LRPT involved C/25 currents, which means approximately 2 h vs. 2 days of testing for each RPT. For its part, different outcomes are expected from both RPTs, since lower C-rates allow to determine a cell capacity that is closer to the total available capacity. However, an error of less than 2% is incurred by using 1C with respect to C/25 for the considered battery cell. Therefore, the SRPT is the one used to provide the real battery capacity, and it is simply denoted as RPT from now on. The batteries aged with commercial charging strategies were subjected to 10 RPTs, while the ones aged with the proposed RG charging strategy were evaluated through 9 RPTs. The difference in cycling and RPTs between these two sets of charging strategies is due to the difficulties to keep the RG properly working after the 99th cycle as discussed in Section 7.2.3 below.

In order to assess capacity fade, power fade and charging time through the CAT and RPT, the following metrics are used. The battery capacity Q_b is estimated using Coulomb-counting, which together with its associated estimation error δQ_b are given by

$$Q_b = \int_{t_0}^{t_f} I(t)dt, \quad \delta Q_b = (t_f - t_0)\delta I + I(t_f)T_s + I(t_0)T_s, \tag{7.13}$$

where t_0 and t_f are respectively the initial and final time of the experiment and T_s is the sampling period. The battery resistance R_b and its associated estimation error δR_b are determined through

$$R_b = \frac{\Delta V}{\Delta I}, \quad \delta R_b = \left(\left| \frac{\delta V}{\Delta V} \right| + \left| \frac{\delta I}{\Delta I} \right| \right) R_b, \tag{7.14}$$

where ΔV is the first potential rise/drop at the onset of the charge/discharge voltage curves as soon as a current is applied after rest, and ΔI is the current magnitude that causes such a voltage change.

It is important to highlight that the full charge of a battery is an asymptotic process, whatever charging technique is used. Therefore, thresholds have to be used to define when a battery is fully charged. In the case of a CCCV charging strategy, the threshold is defined at the CV stage in terms of cut-off current value. For both the 1C and 2C CCCV considered here, the current threshold for the CV phase is 0.1 A. In the case of the RG with OR constraints charging strategy, the references of current and voltage do not exist anymore, but a SOC reference is used. To define a cut-off SOC value, a brand new battery cell was charged using a CCCV profile with C/2 CC up to 4.2 V, after which a CV charge took place until the current fell below 0.1 A. Then, the battery was left at rest for 2 h while recording the battery voltage. By doing so, we have access to the final state of the battery and the results are shown in Fig. 7.3. The battery voltage drops from 4.2 V during the CV phase up to 4.176 V after the rest period. In terms of the RG, the 4.2 V corresponds to the target maximum voltage or SOC reference, whereas the 4.176 V is the equilibrium voltage that actually reflects how much energy has been stored in the battery. The latter voltage provides the cut-off

SOC value. Translating these voltage limits to SOC through OCV function inversion, the SOC reference is 0.9308 and the cut-off SOC is 0.9175 to achieve a similar level of charge as the CCCV. The final charge time t_f is then directly obtained from the tester chronometer and the associated estimation error δt_f corresponds to the sampling time of the data

$$\delta t_f = T_s. \tag{7.15}$$

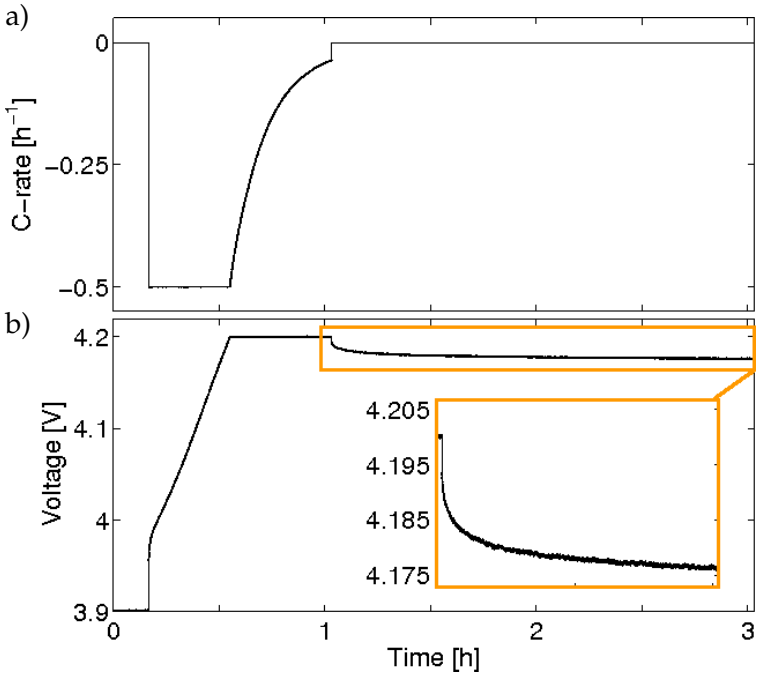

FIGURE 7.3: a) Current and b) voltage response of a battery subject to C/2 CCCV charging profile at 25°C.

As the battery ages, the battery capacity decreases. In order to have a fair comparison between CCCV and RG charging strategies, the SOC reference of the RG is proportionally compensated with the capacity fade associated to the 1C CCCV strategy after each batch of CATs.

The accuracy of each sensor used by the battery tester to gather data is given in Table 7.1. This information is provided in the specifications and calibration documentation of the battery tester.

TABLE 7.1: Instrumentation accuracy of the battery tester, namely current, voltage and temperature sensor, as well as data sampling time.

δI [A]	δV [V]	δT [°C]	T_s [s]
$2 \cdot 10^{-3}$	$2 \cdot 10^{-3}$	1	1

Along this chapter, linear regressions are fitted to the data to stress the trend of a given variable with respect to aging. To identify their coefficients and associated error, we first write a first-order polynomial in regression form as

$$Y_p = \Phi\theta_p + \epsilon, \tag{7.16}$$

where Φ is the regressor or Vandermonde matrix formed as $\Phi = [x_p,\ 1_{n_d \times 1}]$, $x_p = [x_{c,1}, x_{c,2}, \ldots, x_{c,n_d}]^{\mathrm{T}}$ is the data of the independent variable, n_d is the number of data points, $\theta_p = [a_1,\ a_0]^{\mathrm{T}}$ is the parameter vector of the coefficients to be estimated, $Y_p = [y_{c,1},\ y_{c,2},\ \ldots,\ y_{c,n_d}]^{\mathrm{T}}$ is the vector formed by the data of the dependent variable and ϵ is a noise source. Then, an estimation of θ_p, i.e. $\hat{\theta}_p$, can be obtained through

$$\hat{\theta}_p = (\Phi^{\mathrm{T}}\Phi)^{-1}(\Phi^{\mathrm{T}}Y_p), \tag{7.17}$$

whose variance is given by

$$\sigma^2_{\theta_p} = \sigma^2_{\epsilon}(\Phi^{\mathrm{T}}\Phi)^{-1} \tag{7.18}$$

where σ^2_{ϵ} is the noise variance.

The goodness of a fit is evaluated in terms of the coefficient of determination R^2 given by

$$R^2 = \frac{\sum_{i=1}^{n_d} \left(\hat{y}_{c,i} - \bar{y}_c\right)^2}{\sum_{i=1}^{n_d} \left(y_{c,i} - \bar{y}_c\right)^2} \tag{7.19}$$

where $y_c, \hat{y}_c$ and $\bar{y}_c$ denote the measured variable, and the predicted and the mean of the predicted variable obtained from the identified linear model, respectively.

For convenience in referencing, the CAT is divided into cycles, blocks and stages. Each charge and discharge process is considered as a *half-cycle*, while a charge/discharge operation is considered as a *cycle*. The set of 11 consecutive cycles after and before each SRPT form a *cycle block*, while the set of 5 blocks (55 cycles) after and before each LRPT is denoted as a *cycle stage*.

Remark 7.2.1. *There are different standards related to lithium-ion batteries. They are organized according to applications and topics. The former category includes portable (power tools, e-bikes), automotive (electrically propelled vehicles, such as mopeds, motorcycles, road/traction vehicles), stationary, grid-integrated and space (space vehicles) applications, whereas the latter involves performance, durability, reliability and safety of batteries, as well as their transportation, storage and handling, sustainability and environmental impact, materials and resource efficiency [166, 167, 168, 169]. Relevant standards for electric vehicle performance tests include, for instance, ISO 12405/1-4 [170, 171, 172, 173]and ICE 62660/1-2 [174, 175], while a compilation of standards that extend upon these aspects by accounting for durability assessment has been recently reported [166]. However, in an attempt to keep a general framework throughout this dissertation (application independent), generic cycling aging tests consisting of battery full charge-discharge were used. Moreover, the reference performance tests have also been tailored to our needs if compared with other standards or authors [176, 177, 178]. Nonetheless, the same tests are used to assess the performance of the different charging protocols, which constitutes a fair comparison.*

7.2.2 Closed-loop Implementation

The implementation of the feedback charge strategy based on the RG with OR constraints as proposed here involved the interfacing among different software and hardware components. A schematic representation is shown in Fig. 7.4. The main hardware components surrounding the battery cell under study are the ones introduced in the previous Section 7.2.1, namely the thermal chamber and the battery tester. Notice that if the switch box, denoted by "sw" in the figure, is in the position 0, the battery tester acts directly on the battery cell and no ancillaries are required. Thus, the battery tester provides the charge/discharge protocols that are available in its library, or custom made profiles such as drive cycles can also be loaded. However,

all the input profiles can only be fed into the battery in open-loop. To circumvent this limitation, the peripheral components comprised by MATLAB/Simulink and dSPACE (MicroAutoBox II 1401/1501) come into play. By switching from position 0 to position 1 the switch box, the MwareClient allows the dSPACE card to take the control of the charge/discharge operation. Nevertheless, such permission expires as soon as a given condition is met or a given battery tester restriction is violated, e.g. maximum time or voltage reached.

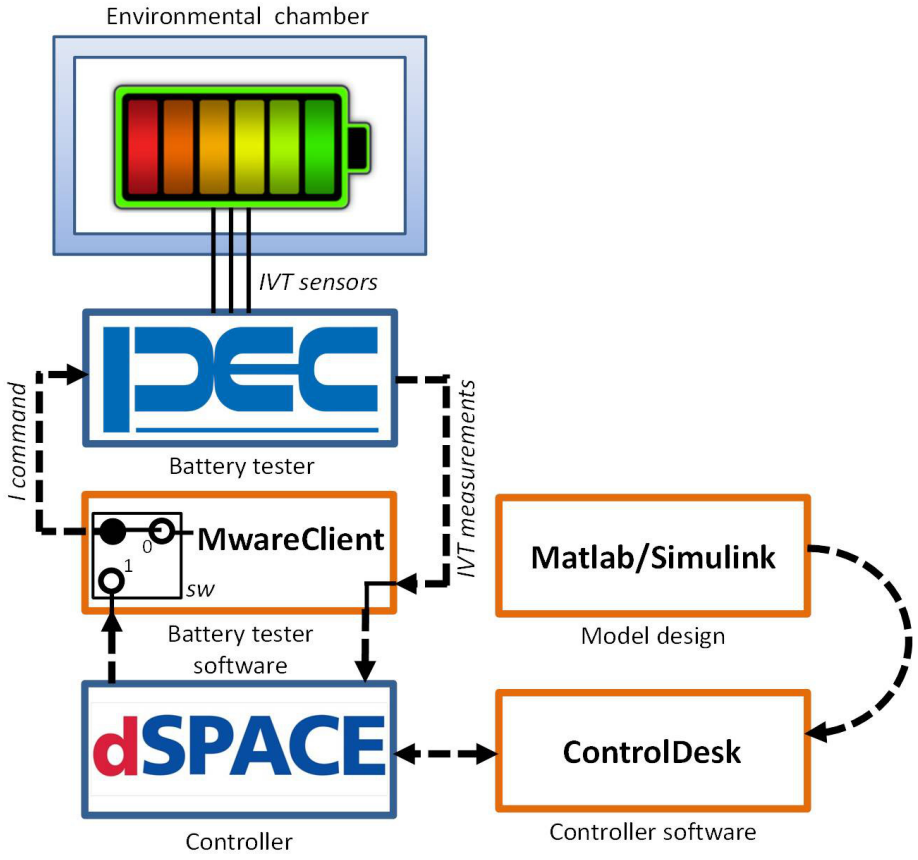

FIGURE 7.4: Schematic representation of the experimental layout needed to implement the charging strategy based on the proposed RG with OR constraints scheme.

The interplay between the MwareClient and dSPACE is the following. The battery tester acts as a master controller, and the overall charge/discharge regime is specified in its software as a sequence of steps, e.g. charge, resting time, discharge, resting time, charge, and so on. Within this regime, the charging steps of the sequence are devoted for the action of the dSPACE card, although the test always has to comply with the restrictions imposed in the battery tester. The RG-based charging strategy is only active during this designated time period. At the end of the charge, the dSPACE card passes the baton back to the battery tester. Then, the latter performs a resting time, a battery discharge and another resting time. In the meanwhile, the dSPACE card is still active in the background and it is able to read the information of the battery tester. This situation allows the EKF to be permanently online and to track the battery state even during rest periods and discharge sequences. After the second resting time, dSPACE card takes over, it resets the RG scheme, the LQR controller and the integral

action and conducts the battery charge again. Then, the cycle is repeated as many times as needed.

A pre-requisite to close the loop in this manner is to have the proposed control scheme written in Simulink. Fig. 7.5 shows a diagram of the Simulink model used for the ultimate test of the feedback charge strategy. There are four main blocks, namely the "battery plant," the "overvoltage protection", the "EKF" and the control law, where the latter does not appear as a single block in the figure but it includes the "RG with OR constraints" block, the "LQR gain" and the "integrator" for the error between the desired and applied references. Three other blocks are shown in the figure, namely one denoted as "sign adjustment" and the other two as "switching logic". The battery plant block is cancelled for online test. The protection against overvoltage matches the maximum voltage of 4.4 V allowed by the battery tester. The RG with OR constraints of Section 7.1.2 and the EKF of Section 7.1.3 are encoded in the blocks tagged with the corresponding names. The remaining blocks are devised to deal with intrinsic issues of this implementation. For instance, the "switching logic 1" block receives voltage and SOC information coming from the battery tester and the EKF, respectively. The voltage information allows the dSPACE card to know when the minimum voltage is reached at the end of discharge, and to count the rest period so that it knows when is its time to take the battery control. The SOC information is exploited to stop the charging process once the cut-off SOC is reached. The "sign adjustment" block corrects the current readings that the dSPACE card gets when the battery tester controls the battery operation, since the current magnitude is correct but not its sign. Finally, the "switching logic 2" block allows to feedback the solid-state diffusion states augmented with the integral action during the designated charging period.

7.2.3 Results and Discussion

In the following, the results obtained for the different charging strategies are introduced and compared. Commercial strategies such as 1C CCCV and 2C CCCV are contrasted with the proposed RG with OR constraints strategy in terms of e.g. remaining capacity, resistance increase and charging time during prolonged cycling.

Commercial Charging Strategies: 1C vs 2C CCCV Comparison

Before entering into the details of the results obtained for the RG with OR constraints and how they compared with traditional commercial CCCV charging strategies, the two CCCV strategies used here should be contrasted. Fig. 7.6 shows the results of the cycle aging tests (CAT) obtained when using 1C (green curves) and 2C (blue curves) CCCV strategies[1]. A total of 2 cycle stages, 10 cycle blocks and 110 cycles are presented. The results for the reference performance tests (RPT) are also shown after every 11 cycles (green and blue ○ symbols for 1C and 2C, respectively), whose positions are marked with dashed orange vertical lines. Fig. 7.6(a) shows the CAT charge/discharge capacity through the solid curves, Fig. 7.6(b) shows the resistance increase for charge/discharge, and Fig. 7.6(c) shows the charging time evolution, all in function of the half cycle number. Notice that there are two curves for each charging C-rate in Figs. 7.6(a) and (c), a solid curve above a dashed curve in each plot. The dashed curve represents the capacity and charge time of the CC charging

[1]In the following, the "CCCV" tag of the commercial charging strategies is dropped to avoid unnecessary repetition. When referring to 1C and 2C, it is assumed that it is always the CCCV strategy unless otherwise stated.

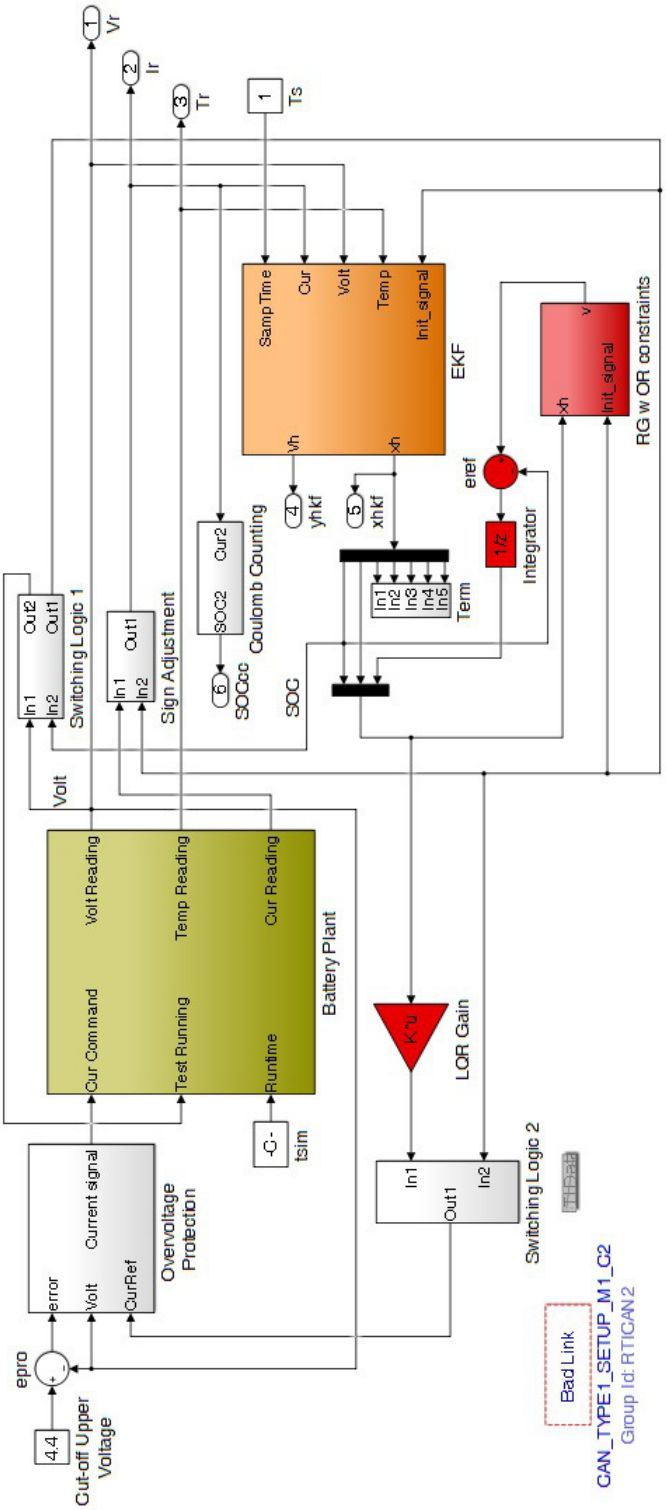

FIGURE 7.5: Simulink diagram for the implementation of the proposed RG with OR constraints charging strategy.

phase of the CCCV strategy, whereas the remaining portion of capacity/charge time up to the solid curve corresponds to the CV charging phase. Finally, the RPT results show two sets of symbols, namely ● and ○ to represent charge and discharge variables, respectively. After computing the error bars associated to each variable

using Eqs. (7.13),(7.14) and plotting them in Fig. 7.6, we verified that the incurred error is typically small. Therefore, we do not include error bars in the subsequent plots to avoid clumsiness.

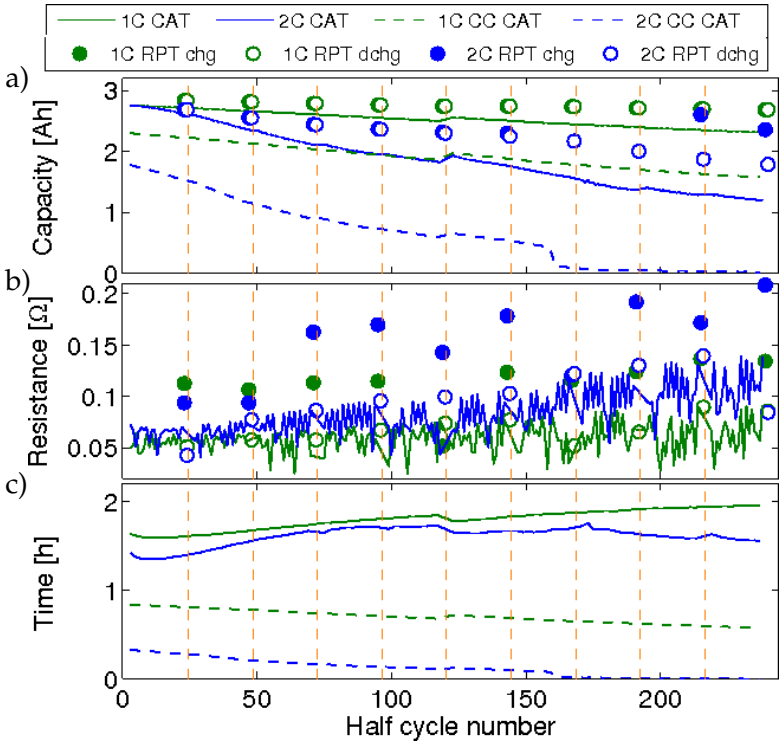

FIGURE 7.6: Performance comparison between two commercial charging strategies, namely 1C CCCV (in green) and 2C CCCV (in blue), in terms of a) retained capacity, b) resistance increase and c) charge time. Both CATs (curves) and RPTs (symbols) are shown. Dashed and solid curves respectively represent variables for the CC and the CCCV stage of a CCCV charging strategy. Symbols ● and ○ represent charge (chg) and discharge (dchg) variables, respectively.

As the battery cells age, the capacity tends to drop monotonically due to aging mechanisms taking place within the battery. Fig. 7.6(a) shows the cyclic capacity reduction for both 1C and 2C charging strategies as cycles go by. However, the monotonicity in capacity fade is broken whenever a RPT is carried out (every 11 cycles). The same figure also shows how the same cyclic capacity decreases faster when the C-rate is increased from 1C to 2C. Such capacity is an apparent one, since it is not all the available capacity of the battery cell. A capacity measure that is closer to the real capacity is accessed by the RPT, which also declines as the C-rate becomes larger. From the figure follows that both cells age at different rates. This is easily evidenced by fitting to the data a linear function of the form

$$y_Q = a_1 x_c + a_0 \,, \tag{7.20}$$

where x_c stands for the half cycle number and y_Q for the capacity. A total of four different fits are computed, one per C-rate and stage. The estimated parameter set and associated standard deviations are obtained through Eqs. (7.17) and (7.18), respectively, which are reported in Table 7.2 together with the coefficient of determination or R^2 value calculated according to Eq. (7.19).

The degrees of decay/growth in a given fit show the battery degradation rate. For the 1C case, the linear trend of the second stage has a smaller slope than the first one, which implies that degradation slows down as the battery cell ages under 1C. For the 2C case, the slope of the line associated to the first stage is fourfold larger than that for the 1C case, evidencing accelerated degradation when the C-rate is doubled. During the second stage, the 2C case exhibits an even faster degradation with respect to the first stage.

TABLE 7.2: Fitting parameters of the linear function Eq. (7.20) describing the retained capacity for a battery subject to 1C and 2C CCCV charging strategies. The fitted data is the RPT points of Fig. 7.6(a), and a set of parameters is obtained for each C-rate and cycle stage.

C-rate/Stage	a_1	σ_{a_1}	a_0	σ_{a_0}	R^2
	$\cdot 10^4$				
1/1	-9.5	0.2	2.853	0.001	0.9987
1/2	-6.5	0.2	2.836	0.004	0.9957
2/1	-40	3	2.75	0.03	0.9746
2/2	-50	3	2.98	0.05	0.9878

Aside from capacity loss, another important indicator of aging is resistance increase as shown in Fig. 7.6(b). Both cyclic and RPT resistances are represented for both 1C and 2C charging strategies. However, the resistance results are not as clean as the capacity results introduced above in terms of monotonicity. This may be related to the nature of the two variables: while capacity is an integrator over time, the resistance is an approximated quantity that is computed using only two data points for voltage and current as $\Delta V/\Delta I$. Therefore, different disturbances such as measurement noise, as well as the resistance dependence of temperature and SOC, may affect its determination greatly. Regardless these difficulties, the resistance increase with battery aging can still be spotted in the plot. A linear regression model similar to that one of capacity fade Eq. (7.20) was used to fit the data of the figure, i.e.

$$y_R = a_1 x_c + a_0 \tag{7.21}$$

where y_R represents the resistance. A total of four different fits are obtained, one per C-rate and charge/discharge mode, whose parameters, standard deviations and R^2 values are presented in Table 7.3. The y-intercepts for each charge/discharge mode are very close to each other, which means that both batteries have similar resistance at the beginning of the CAT. For each C-rate, the charge resistance (low SOC) is larger than the discharge resistance (high SOC). In the case of 1C charge, the standard deviation of the slope parameter is as large as the value of the parameter itself, which may indicate overfitting. Indeed, a constant value is enough to describe the battery resistance for 1C charge, with $a_0 = (11 \pm 1) \cdot 10^{-2}\ \Omega$. While 1C charge induces a constant power degradation, the 2C charge involves a significant degradation rate. For the discharge process, the 2C exhibits approximately twofold the power degradation rate of 1C discharge.

Looking at the charging time in Fig. 7.6(c), 2C is 13% faster (13 min) than 1C to fully charge the battery at the beginning of life (2nd cycle). Then, as the battery capacity fades with age, charging time increases for both 1C and 2C charging strategies. The 2C strategy achieves a minimum charging time at cycle 5 (1.35 h). From this point onwards, the charging time difference with respect to 1C decreases up to 4% (4 min) at the 33rd cycle. Then, the charging time difference starts to increase again and

TABLE 7.3: Fitting parameters of the linear function Eq. (7.21) describing the resistance increase for a battery subject to 1C and 2C CCCV charging strategies. The fitted data is the RPT points of Fig. 7.6(b), and a set of parameters is obtained for each C-rate and charge/discharge mode.

C-rate	a_1	σ_{a_1}	a_0	σ_{a_0}	R^2
	$\cdot 10^4$		$\cdot 10^2$		
1C Charge	1	1	10	2	0.1701
1C Discharge	1.3	0.4	5	0.6	0.5127
2C Charge	4	1	10	2	0.5580
2C Discharge	2.8	0.9	6	1	0.5219

it achieves a maximum of 20% (24 min) close to the end of the considered horizon (109th cycle). However, at this point the cell under 2C has lost 37% of its original capacity compared to the 6% capacity fade of 1C. Therefore, the cell is charging much faster because it is actually charging 31% less capacity. It turns out that most of the charging done with 2C at the end of the considered time horizon is done by the CV phase, as it can be seen by the dashed blue curve close to zero in Fig. 7.6(c). This phase is known to consume a considerable amount of time.

The RG with OR constraints

As an alternative to commercial CCCV charging strategies, here we propose a feedback charge strategy that reduces the charging time while accounting for battery degradation. Such claims are now tested in the light of experiments. In this section, the estimation results obtained from the EKF are first discussed, followed by a brief discussion of the control results coming from the RG with OR constraints[2].

The parameters used to tune the EKF were the following:

$$\begin{aligned} \hat{x}(0) &= \left[[3.89, 3.89] \cdot 10^{-2}, [1.27, 1.27] \cdot 10^{3}, 10^{-3}, 298, 298\right] \\ \text{diag}(P(0)) &= \left[10^{-9}, 10^{-9}, 10^{-1}, 10^{-1}, 10^{-10}, 10^{-5}, 10^{-5}\right] \\ \text{diag}(Q) &= \left[10^{-13}, 10^{-11}, 10^{-5}, 10^{-5}, 10^{-11}, 10^{-9}, 10^{-9}\right] \\ \text{diag}(R) &= \left[10^{-6}, 10^{-4}\right] \end{aligned} \tag{7.22}$$

where the first two components of the state vector are dimensionless, the second two components are associated to the electrolyte-phase concentration $[\text{mol} \cdot \text{m}^{-3}]$, the fifth component is an ohmic resistance $[\Omega \cdot \text{m}^2]$ and the last two components are thermal states [K]. The units of P and Q are coherent with the units of the state vector, while the units of $\text{diag}(R)$ are $[\text{V}^2]$ and $[\text{K}^2]$ for the first and second component, respectively. The LQR controller is designed by selecting suitable Q_c and R_c values as $Q_c = 10^2 \cdot I_d$ and $R_c = 10^{-3}$, yielding the matrices $K_x = [9.9129 \cdot 10^3,\ 1.3957]$ and $K_i = -3.0619 \cdot 10^2$.

The available measurements from the PEC tester are current, voltage and surface temperature, which are represented by the solid black curves in Figs. 7.7(a)-(c), respectively, for the first cycle block of CAT. This same restricted sensing is the typical situation in daily life applications such as electric vehicles and household energy storage systems. However, internal state estimates can be obtained from the battery

[2]From now on, the tag "with OR constraints" accompanying the RG is dropped to avoid unnecessary repetition. The RG scheme involves both the LQR controller with integral action providing fast charging capabilities and the RG handling the satisfaction of constraints. The RG denotes the entire feedback control scheme for battery charge unless otherwise stated.

by exploiting the same set of measurements along with specialized software. Here, the EKF of Section 7.1.3 is embedded in a Simulink model and loaded to the processor of a dSPACE card as explained in Section 7.2.2. The latter piece of hardware would be replaced by a microcontroller in a real application. Figs. 7.7(b)-(c) present in dashed red curves the predicted voltage and temperature, respectively. Aside from the surface temperature, the model-based estimator also provides information about the core temperature of the battery cell in the dotted red curve.

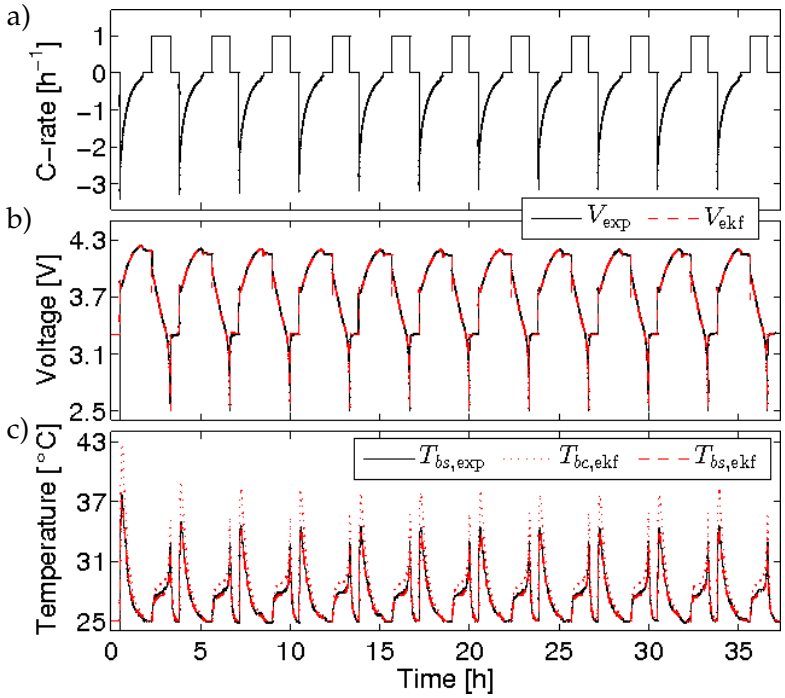

FIGURE 7.7: Measurements gathered from the PEC tester for the first cycle block of CAT, namely a) current, b) voltage (V_{exp}) and c) surface temperature ($T_{bs,\text{exp}}$). Superimposed to these signals are the voltage (V_{ekf}) and both surface ($T_{bs,\text{ekf}}$) and core temperature ($T_{bc,\text{ekf}}$) predicted by the EKF.

As it can be seen in Fig. 7.7(a), the input profile that solves the LQR problem while accounting for aging constraints starts with a large spike charging current (in the order of 3C) followed by a gradual decrease towards zero current. After each charge, the battery is discharged under 1C CC conditions. This cycle is repeated 11 times for each cycle block. In contrast to CCCV charging, the RG does not impose any restriction in voltage, thus allowing voltage incursions beyond traditional upper cut-off voltages of 4.2 V recommended by battery manufacturers. For the case at hand, the voltage in Fig. 7.7(b) can be as high as 4.24 V. The last aspect that deserves special attention in Fig. 7.7(c) is the thermal gradient that builds up within the battery cell. Up to 5°C difference can exist between the core and the surface temperature of the cell. Battery internal temperature monitoring is very important to avoid thermal runaways and maintain the battery safe operation.

Other internal states that can be accessed with the EKF are diffusion-related states, such as SOC and CSC (solid and dashed curves in Fig. 7.8(a), respectively) for the solid-phase diffusion and c_{eb} and c_{es} (solid and dashed curves in Fig. 7.8(b), respectively) for the electrolyte-phase diffusion, along with the film ohmic resistance (Fig. 7.8(c)).

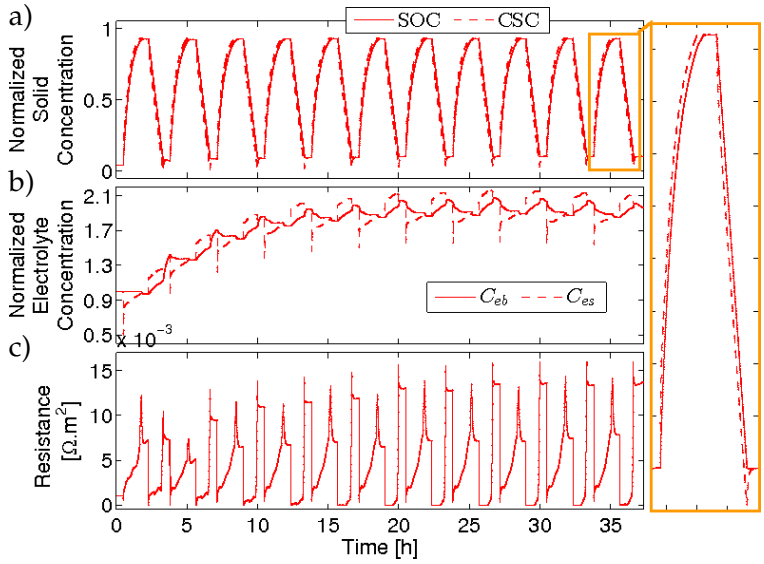

FIGURE 7.8: EKF estimated internal state of the battery cell during the first cycle block, namely a) solid (SOC and CSC) and b) electrolyte-phase (C_{eb} and C_{es}) diffusion states, and c) film resistance. The figure inset is a close-up of the solid-phase diffusion state at the last cycle.

Led by the cyclic behavior of the input current profile, the SOC oscillates between minimum and maximum values of 0.10 and 0.93, respectively. The SOC follows the CSC with a delay, since the former state is a low pass filter of the latter. Whereas both SOC and CSC reach the maximum charge simultaneously, note how the CSC undershoots by 0.07 the minimum charge after the CC discharge (Fig. 7.8 inset). Such shoots can be harmful for the battery since they can cause overcharge and overdischarge during CC charging and discharging, respectively. The two considered charging strategies, namely commercial CCCV and proposed RG, avoid these operating situations, but the RG does it in a less conservative manner as it will be verified below. The periodic behavior is also exhibited by the remaining states. However, electrolyte-phase diffusion states seem to change the operating point from 0.9 to 1.9 after 20 h. This result might be ascribed to wrong initial conditions, since good initial estimates (i.e. close to the real states) are more difficult to obtain for these states than for e.g. the solid-phase diffusion states. As discussed in the modeling Section 7.1.1, a contact resistance was required as an extra state to reduce the gap between predicted and measured voltage. This resistance should be seen as a lumped parameter that gathers the model mismatch incurred by using a low C-rate identified model to handle high C-rate scenarios. Two resistive contributions can be identified, namely high frequency spikes and low frequency baseline. The former contribution might be ascribed to charge transfer unmodeled effects, while the latter might be caused by ohmic resistance. The resulting polarization tends to increase during both charge and discharge processes, with a mean value of $5 \cdot 10^{-3}$ $\Omega.m^2$ and a standard deviation of $4 \cdot 10^{-3}$ $\Omega.m^2$.

The EKF state estimates introduced above are exploited downstream by a LQR for fast charging and a RG for ensuring constraint compliance. Both the desired reference r and the applied reference v are shown in Fig. 7.9(a), together with the real SOC. Notice that the RG is only operative during the charging process, while the SOC estimation takes place all the time. Both the applied SOC reference and the real SOC coincide perfectly during battery charge, while the applied SOC reference tends to the

desired SOC reference as the time elapses. For its part, the gain $\kappa(k)$ computed using Algorithm 6.1.1 is shown in Fig. 7.9(b). The value of κ starts with its highest value of 0.04 at the beginning of the charge during a single sampling time, and then it is reduced to a mean value of 10^{-3} with a standard deviation of $4 \cdot 10^{-4}$. This indicates that the charging process is more demanding (closer to the desired reference) at the beginning of the charge, since the battery initial operating point is the farthest away from the aging constraints. As the charge proceeds, the rate at which $v(k)$ tends to $r(k)$ decreases ($\kappa(k)$ decreases).

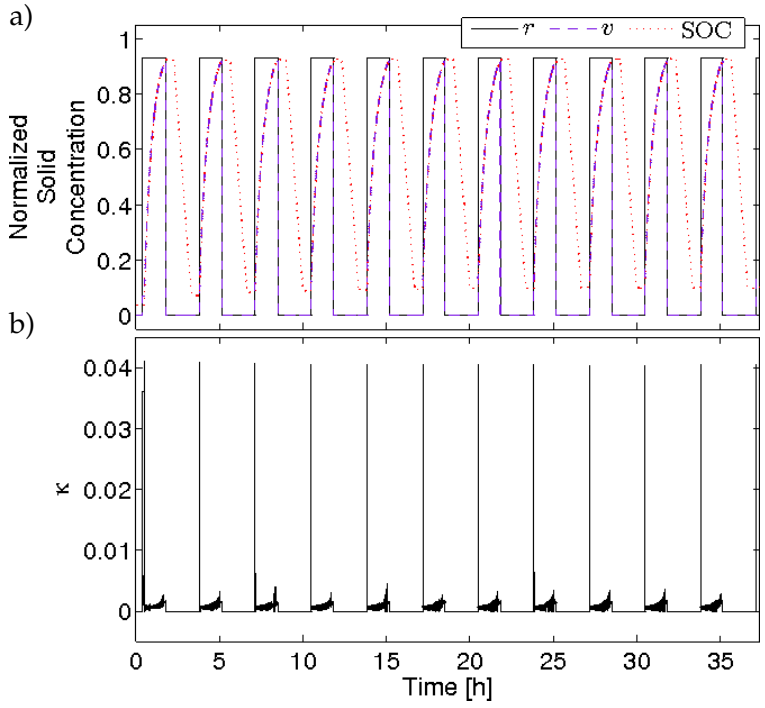

FIGURE 7.9: Signals generated by the RG during the first cycle block, namely a) desired reference r and applied reference v, together with real SOC, and b) gain κ.

Evidence that supports the aforementioned argument can be found in the $I-$CSC map shown in Fig. 7.10. The dashed black curve is the constraint boundary, above of which lies the admissible region. The charging process starts from the pair $(I(0), \text{CSC}(0))$, where $I(0) = 0$ and $\text{CSC}(0)$ a small value ($\text{CSC}(0)$ determines battery voltage, and $\text{CSC}(0) = \text{SOC}(0)$ under equilibrium assumption). From there, the RG rapidly increases the input current in few time steps up to reaching the constraint. From that point onwards, the optimal policy is to ride the constraint until the battery is fully charged.

Commercial Charging Strategies vs RG Comparison

Now that the commercial charging strategies have been introduced and the RG framework has been set, their performances are compared in terms of capacity fade, power fade and charging time. To avoid having too scattered data, the RG is first contrasted with the 1C given the similar results obtained for both. Afterwards, the 2C is also considered.

Building a similar plot as in Fig. 7.6 but replacing the 2C data by the RG data yields Fig. 7.11. In contrast to the previous figure where the 2 complete cycle stages

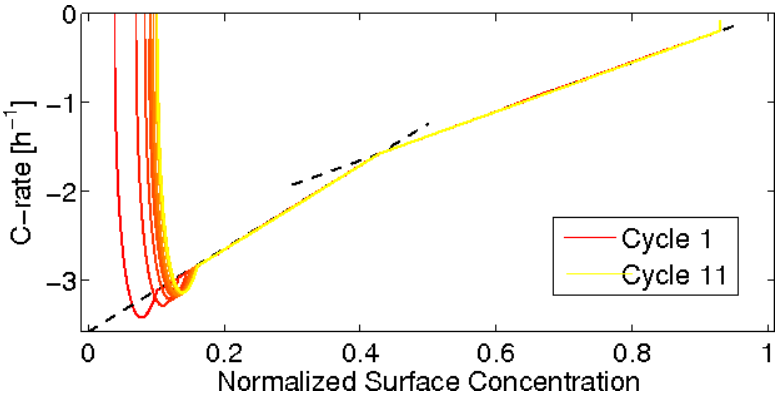

FIGURE 7.10: *I*-CSC plane portraying the trajectories followed by the battery system state under the charging protocol generated from the RG during the first cycle block. The red-yellow color gradient reflects the cycle number from 1 to 11.

(i.e. 5 cycle blocks each stage) were shown, here the 2nd cycle stage comprises 4 cycle blocks. Therefore, a total of 9 cycle blocks and 99 cycles are presented. The 10th cycle block was avoided due to the difficulty of keeping the RG working properly, which is discussed below. Also, dashed black curves have been added in Fig. 7.11(a) to show the desired SOC reference used at each cycle block. Aside from that, this figure contains the same information as the previous one: Fig. 7.11(a) portrays the charge/discharge cyclic capacity and Fig. 7.11(b) the resistance increase, both along with RPTs every 11 cycles, and Fig. 7.11(c) presents the charging time evolution, all as a function of the cycle number. The 1C and the RG results are depicted in green and red colors, respectively. The figure inset remarks the discharge capacity RPT results, where the x and y-axis scales are not shown to avoid a clumsy plot, but they follow from the main plot.

In terms of cyclic capacity performance, the first obvious difference between the two charging strategies is that the RG does not follow the linear trend obtained using 1C throughout the entire CAT (see Fig. 7.11(a)). However, the RG results do show some trend within most of the cycle blocks. When compared to 1C, the RG generally overcharges the battery at the beginning of a given cycle block, but it gradually undercharges it forming an arc shape. The arc behavior may be explained in terms of the EKF dynamic convergence. The most marked exceptions to this general behavior are cycle blocks 2 and 9. Results in block 2 might be ascribed to keeping the same SOC reference as block 1, while results in block 9 might be due to a lack of proper aging adaptation by both the observer and the controller. The figure inset shows the RPT results in terms of capacity, where it can be seen how the RG ages less the battery at the beginning (up to 50% less) and for most part of the aging test compared to 1C. However, the difference in degradation varies from cycle block to cycle block and the trend is even inverted for the last two cycle blocks. During block 9, the RG degrades up to 50% more the battery compared to 1C. A proposal to explain this result is given below. Similarly as before, the linear regression model Eq. (7.20) is fitted to the RPT data points, which are depicted in the figure inset. Two curves are fitted for RPT discharge capacity, one per cycle stage, whose parameters, standard deviations and R^2 values are presented in Table 7.4. For the first cycle stage of the RG, the slope of the linear trend is similar to that of the 1C (see Table 7.2). However, as opposed to 1C that exhibits a reduction in the rate of degradation during the second cycle stage, the

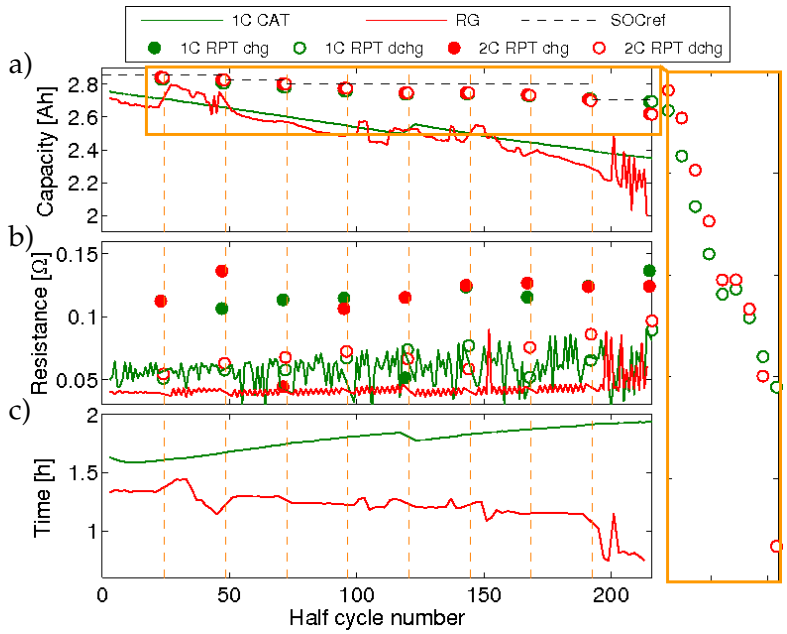

FIGURE 7.11: Performance comparison between 1C CCCV commercial (in green) and proposed RG (in red) charging strategies in terms of a) retained capacity, b) resistance increase and c) charge time. Both CATs (curves) and RPTs (symbols) are shown. The dashed black lines represent the reference SOC used at each cycle block. Symbols ● and ○ represent charge (chg) and discharge (dchg) variables, respectively. The figure inset highlights the difference between the RPTs for each charging strategy.

rate of capacity fade for the RG is doubled at such stage.

TABLE 7.4: Fitting parameters of the linear function Eqs. (7.20) and (7.21) describing the retained capacity and resistance increase for a battery subject to the proposed RG charging strategy. The fitted data is the RPT points of Fig. 7.11(a), and a set of parameters is obtained for each cycle stage and charge/discharge mode.

Variable (Stage)	a_1 $\cdot 10^4$	σ_{a_1}	a_0	σ_{a_0}	R^2
Capacity (1)	−9.8	0.6	2.869	0.005	0.9868
Capacity (2)	−17	4	3.02	0.07	0.8790
Charge Resistance	1	1	0.10	0.02	0.1063
Discharge Resistance	1.7	0.4	0.051	0.006	0.6666

The results of the resistance increase are shown in Fig. 7.11(b). As before, it is difficult to discern any pattern from the cyclic resistance, but the RPT resistance data can be fitted to a linear model in order to highlight the battery resistance growth with cycle number. Table 7.4 also shows the parameters associated to such fit, one parameter set for each charge/discharge mode. Interestingly, the curve fits for the RG and the one for 1C shown in Table 7.3 are very close. During the first cycle stage for the RG, the standard deviation of the slope parameter is as large as the parameter value itself. As happened with the 1C, a constant value of $a_0 = (11 \pm 1) \cdot 10^{-2}\ \Omega$ is sufficient to represent this ohmic resistance. The main difference between the RG and

the 1C fits comes from the discharge resistance (high SOC) that has a higher increase rate for the RG than for the 1C. This might be ascribed to the higher voltages reached by the battery under RG control, where the resistance may be larger.

Even though Fig. 7.11(a) shows the RG degrading less the battery at the beginning of the CAT while degrading it more at the end when compared to 1C, the charging time is another story. From Fig. 7.11(c) follows that the RG systematically outperforms the 1C in terms of charging time, even for cycle block 2 where RG considerably overcharges the battery cyclic capacity with respect to 1C. At the beginning of life (2nd cycle), RG charges the battery 18% faster (18 min) than the 1C. As the battery ages and as previously discussed, the 1C charging time increases, but the RG seems to slightly decrease the charging time as the cycles elapse. The minimum difference in charging time between both strategies is of 11% (11 min) taking place in the 14th cycle, while the maximum one occurs in the last cycle (99th) with 61% difference (71 min). The downside is the remaining capacity, that for this last cycle is of 92% for the RG compared to the 95% of the 1C. At this point, the cell is charged faster using the RG because it is actually charging less due to capacity fade. But looking at the previous cycle block 8, the remaining capacity for both charging strategies is 95% approximately and the RG is on average 39% faster (44 min) than 1C.

Now that all the three charging strategies have been introduced and analyzed, let us bring them all together in Fig. 7.12. The color code used to represent the results for each strategy follows from the previous plots, namely green, blue and red for 1C, 2C and RG, respectively. Figs. 7.12(a)-(b) show the charge/discharge cyclic capacity and resistance as a function of the cycle number for the three considered charging strategies. Whereas the capacity and resistance evolution is similar for 1C and RG, it becomes evident from the figure that 2C is able to charge less (see the CAT) and degrade more (see the capacity and resistance RPT) the battery from cycle to cycle. More interestingly, despite charging less cyclic capacity due to aging, the 2C charging strategy is not able to beat the RG in terms of charging time as shown in Fig. 7.12(c). At the beginning, 1C, 2C and RG take 98 min, 85 min and 80 min, respectively, to fill up with the same amount of charge (2.7 Ah) a fresh battery (2nd cycle). During 88 charge/discharge cycles, these three strategies respectively require on average 105 min, 96 min and 75 min to complete the battery charge. After the 88 cycles, the strategies respectively age 4.9%, 29.7% and 5.2% of the battery capacity. Therefore, the RG seems to be a suitable solution for both the short and long term battery operation by charging on average 23% faster than 2C while aging the battery at a similar rate than 1C. A proper adaptation of the proposed feedback charge strategy might show its advantages beyond the considered 88 cycles.

The fact of charging more in less time can be easily seen by plotting the ratio between the cyclic capacity divided by the charging time. The result is a *charging speed* with units [Ah·h^{-1}]. Fig 7.13(a) shows the charging speed for the three considered charging strategies. The RG indeed charges more and faster than its commercial CCCV competitors. Another relevant way of accommodating data is to plot the capacity evolution as a function of charge/discharge throughput. With this representation, short cycling (e.g. between 20-80% SOC) that would increase both battery life and number of (short) cycles is penalized. Fig. 7.13(b) shows the cyclic capacity with respect to the throughput, which makes evident the deterioration of the battery utilization under 2C. For its part, both 1C and RG seem to have a similar performance up to 400 Ah throughput, after which the RG degrades more the battery cell. It is also important to mention that 1C finishes with slightly more throughput than the other strategies, i.e. this battery has been more used.

After discussing how the different charging strategies work, let us propose some

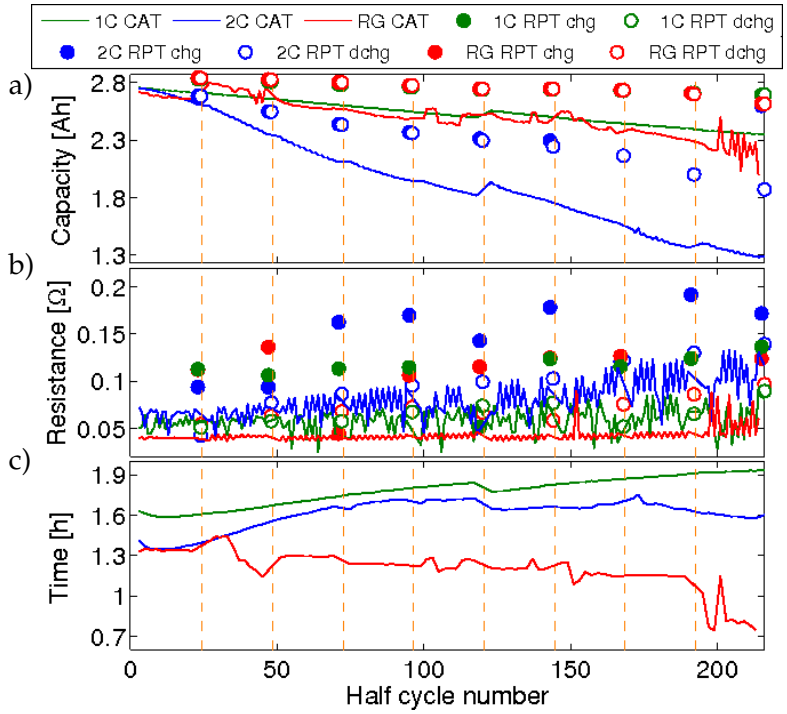

FIGURE 7.12: Performance comparison between two commercial charging strategies, namely 1C CCCV (in green) and 2C CCCV (in blue), and the proposed RG (in red) charging strategy in terms of a) retained capacity, b) resistance increase and c) charge time. Both CATs (curves) and RPTs (symbols) are shown. Symbols ● and ○ represent charge (chg) and discharge (dchg) variables, respectively.

ideas to explain why the RG outperforms a 2C CCCV charge in terms of charging time and retained capacity. To do that, it is required to enter into the details of the charge/discharge profiles themselves for the three strategies. Figs. 7.14(a)-(c) show the current, voltage and surface temperature, respectively, for the first cycle block of the CAT. The results for the 1C, 2C and RG are represented by solid green, dashed blue and dotted red curves, respectively. Given a problem with the thermocouple, the temperature for 1C could not be recorded for this cycling test. The figure inset shows a close-up of the 2nd cycle.

Since the RG is the strategy that charges the fastest the battery, the 1C results lag behind it followed by the 2C results as it can be seen in Fig. 7.14. However, by taking the results of the 2nd cycle and aligning them from the start produces the figure inset. The inset in Fig. 7.14(a) shows how the CCCV strategy seems to approach the RG one as the C-rate increases. However, the current during the CV phase of the CCCV seems to decay faster than the current reduction imposed by the electrochemical constraints for the RG. A faster decay in the current magnitude translates in more time required to charge the battery to a similar level than that charged by the RG. This aspect explains why the RG is able to defeat the commercial strategies in terms of charging time. The inset of Fig. 7.14(b) portrays the associated voltage response. The RG generates a voltage that lies in-between the one imposed by the other two charging strategies. Anyhow, whereas the CV phase in the commercial strategies enforces a maximum voltage to be kept constant until the end of charge, the RG does not have such limitation. Actually, explorations beyond the typical 4.2 V upper cut-off voltage of commercial chargers are allowed and do occur when the RG is

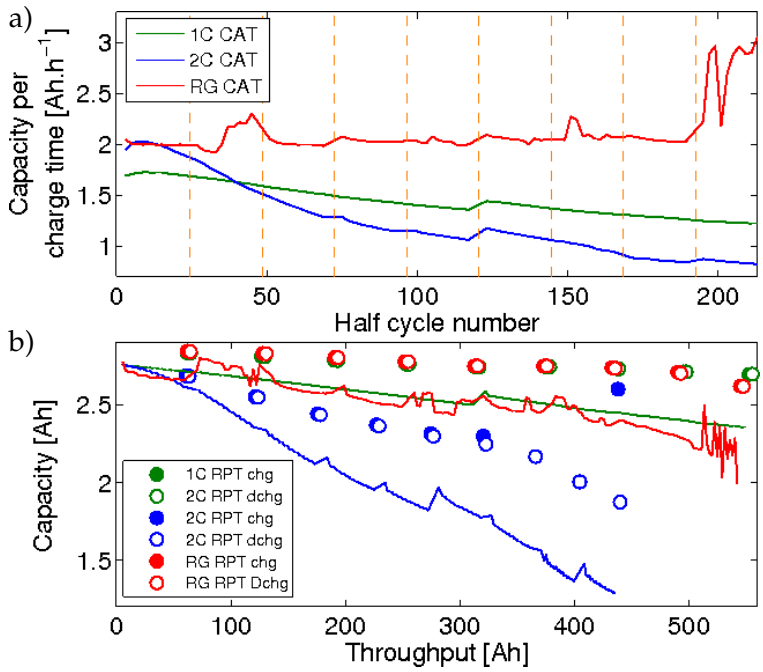

FIGURE 7.13: Performance comparison between two commercial charging strategies, namely 1C CCCV (in green) and 2C CCCV (in blue), and the proposed RG (in red) charging strategy in terms of a) charging speed and b) capacity evolution with charge/discharge throughput. Both CATs (curves) and RPTs (symbols) are shown. Symbols ● and ○ represent charge (chg) and discharge (dchg) variables, respectively.

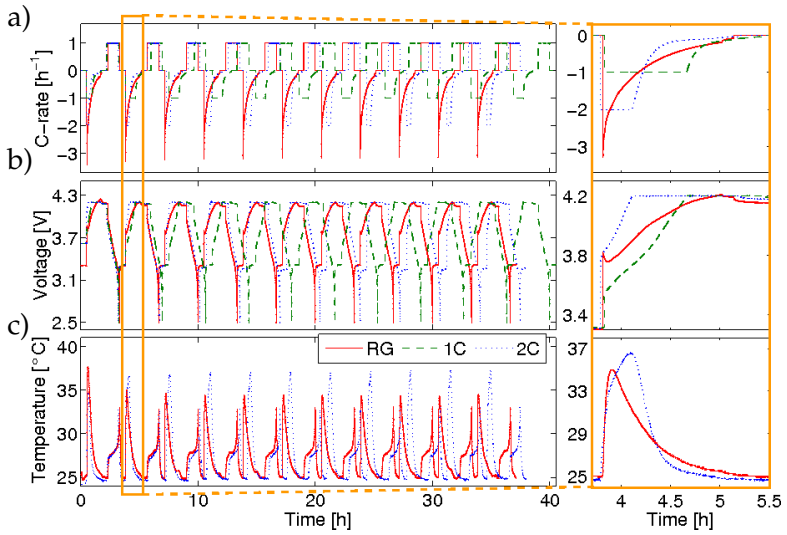

FIGURE 7.14: a) Current, b) voltage and c) surface temperature profiles from the 1st cycle block of a battery cell subject to different charging strategies, namely 1C CCCV (dashed green curves), 2C CCCV (dotted blue curves) and proposed RG (solid red curves). The figure inset is a close-up of the three signals during the 2nd charge cycle.

used. The last inset of Fig. 7.14(c) shows the associated thermal response. A change in the temperature profile is easily spotted from 2C to RG charge, with the former

reaching higher temperatures than the latter. The 2C heats up the cell during the CC phase, after which the CV phase takes over and the temperature decreases. In contrast, the RG induces heat generation during the spike of maximum current, after which the heat starts to gradually dissipate. Both aspects voltage and temperature combined might explain the RG performance in terms of aging. Although the RG allows incursions to high voltages, such operating conditions last for short time periods. Overall, the battery stays at a lower voltage during RG charging than during commercial charging (specially evident in the 2C case). Similarly, the battery is cooled down sooner and faster during RG charging than during 2C charging. These two stress factors might be the responsible ones for more side reactions taking place when the cell is charged under 2C, which yields a more degraded battery over time.

Even though Fig. 7.14 is helpful in giving hints to explain why the RG outperforms commercial charging, long term data is required to assess aging. Figs. 7.15(a)-(c) show the current, voltage and surface temperature, respectively, for the 5th cycle of each of the 9 cycle blocks of the CAT. The results for the 1C, 2C and RG are represented by dashed green-olive, dotted pink-blue and solid red-yellow curves, respectively, where the first-second color implies first-last cycle block, and the color gradient reflects the cycle blocks in-between. Since the temperature profiles are the most difficult to discern among charging strategies, small arrows are used to point the way in which each profile set moves with aging. The most significant change of the current profile is observed for the commercial strategies (see Fig. 7.15(a)). As cycle blocks pass, the CC phase of the CCCV charge is shortened and the current decay during the CV phase becomes slower. This explains why the charging time increases with aging for the commercial charging. For its part, the current profiles generated by the RG slightly move to smaller currents, but always keeping a similar decay rate for the charge current at each cycle. This fact explains the higher charge speed of the RG with respect to commercial charging. The temporal reduction of the CC phase of CCCV strategies is also reflected in the voltage response of the battery (see Fig. 7.15(b)). For the RG, the obtained maximum voltages are usually above the upper cut-off voltage used by CCCV strategies. As mentioned above, even if higher voltages are reached using the RG, the battery spends less time in this condition when compared to the 2C strategy that is almost pure 4.2 V CV for the last aging cycles. As the battery ages, the voltage response obtained using the RG after each cycle block seems to lie down at the top of the previous cycle block voltage response, whereas higher voltages are reached. This means that aging makes the battery to operate at higher voltages if the RG is used, which likely translates in the more degraded battery observed in the long run (99 cycles). This behavior may be corrected by a proper aging adaptation of the proposed control scheme. Finally, the thermal response of the battery is different for the three considered charging strategies (see Fig. 7.15(c)). While the battery under 1C tends to increase and shift its maximum temperature peak to the left, the battery under 2C also displaces its peak to the left but it is increased until half of the considered time horizon to decrease again from that point onwards. The left displacement of the maximum temperature peak for commercial charging follows the CC shortened time as battery ages. The temperature reduction for the 2C at the end of the time horizon is due to a very short CC phase (from 75 s to 24 s in the last three cycle blocks) and a CV phase quickly reducing the charge current (see inset in Fig. 7.15(a)). For its part, the maximum temperature peak resulting from the RG implementation does not shift sideways but stands still, while increasing in magnitude as the battery ages. The maximum temperature among cycle blocks is achieved in the last block, where the voltage achieves the 4.4 V upper limit of the tester.

Several factors are well known to increase the degradation rate of batteries. Some

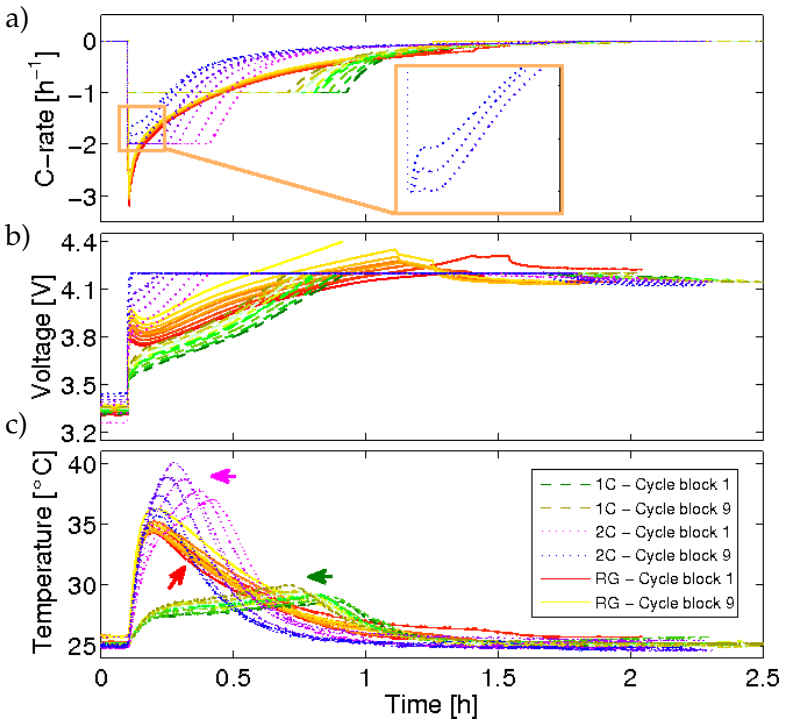

FIGURE 7.15: a) Current, b) voltage and c) surface temperature profiles from the 5th cycle per cycle block of a battery cell subject to different charging strategies, namely 1C CCCV (dashed green-olive curves), 2C CCCV (dotted pink-blue curves) and proposed RG (solid red-yellow curves). The first-second color corresponds to first-last cycle block, the color gradient reflects the cycle blocks in-between and the arrows in plot c) highlight the evolution of the thermal profile with cycle blocks. The figure inset is a close-up of the charging currents for the last cycle blocks during 2C CCCV charge.

of these factors are high currents, extreme voltages (either low or high) and high temperatures. A glance over some specifically picked cycles was given above, regarding how the charging strategies promoted these factors to occur and the impact of them in battery life. However, Fig. 7.16 provides the entire picture of the evolution of these stress factors with cycling. Fig. 7.16(a) shows the maximum current reached during each charging strategy through the green, blue and red solid curves for 1C, 2C and RG, respectively, while the average current (including the CV phase for CCCV strategies) is represented by the green, blue and red dashed curves for 1C, 2C and RG, respectively. The maximum current for commercial strategies corresponds to the CC phase current (1C and 2C in this case), but the RG achieves C-rates higher than 3C for almost every cycle. Moreover, as the time elapses, the average current of the RG is considerably constant around 0.7C, whereas the one of the commercial strategies can be as low as 0.4C and 0.3C for 1C and 2C, respectively. These two results put high current to the test as a stress factor, while confirming that the RG is faster in charging batteries than other strategies because it actually induces higher charging C-rates. Fig. 7.16(b) shows the maximum voltage reached for the RG through the solid red curve while the final voltage just before relaxation is depicted with the dashed red curve (for the commercial strategies, maximum and final voltages differ in less than 1 mV and correspond to the CV phase voltage of 4.2 V. Therefore, solid and dashed curves overlap around 4.2 V for both 1C and 2C). Both voltages tend to increase with

aging, and their difference also seems to increase. Even if the RG forces the battery to reach higher voltages, the time spent in this condition is less than the time at 4.2 V CV provided by the 2C strategy (see Fig. 7.15(b)). Looking now at the temperature, Fig. 7.16(c) shows the maximum temperature reached during each charging strategy through green, blue and red solid curves for 1C, 2C and RG, respectively. The use of 2C charging makes the battery surface hotter than any other strategy, reaching temperatures up to 40°C (the manufacturer specifies a maximum temperature of 45°C for these battery cells). The RG produces surface temperatures around 35°C, whereas the 1C keeps the cells around 30°C. Although the RG cell can have 5°C of difference with respect to the 1C cell, such difference does not seem to be reflected in the aging of the first part of the aging tests. Overall, it seems that traditionally considered stress factors such as high currents, voltages and temperatures are not *per se* degrading more the battery, but it is the time spent on stressful conditions that induces violation of electrochemical constraints and battery degradation.

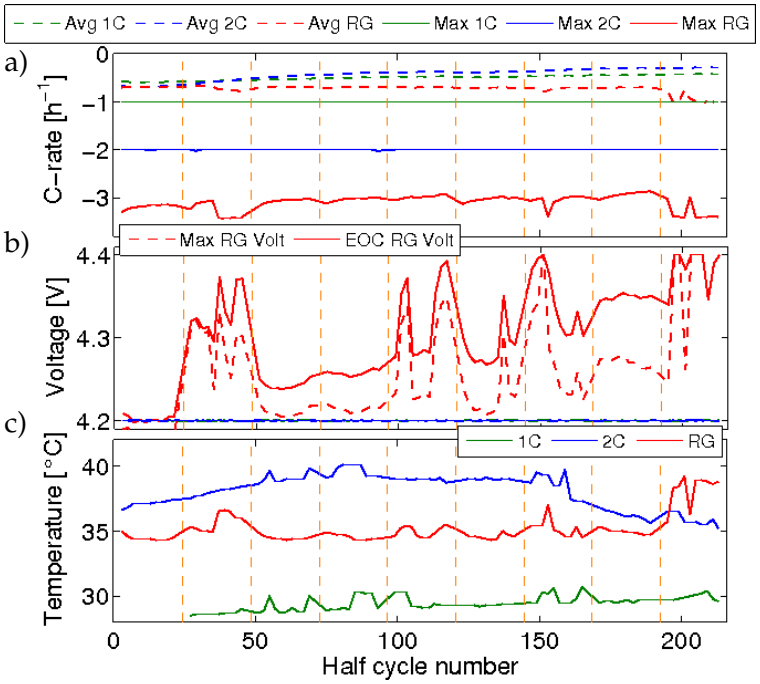

FIGURE 7.16: Common stress factors considered for lithium-ion batteries, namely a) maximum (solid curves) and average (dashed curves) applied current, b) maximum (dashed curves, denoted as "max") and end of charge voltage (solid curves, denoted as "EOC") and c) maximum surface temperature. Green, blue and red curves correspond to 1C CCCV, 2C CCCV and proposed RG, respectively.

To conclude this section, let us highlight a possible correlation among the commercial 1C and 2C CCCV charging strategies and the proposed RG charging strategy in terms of capacity fade. To this end, Fig. 7.17 depicts the retained capacity for each evaluated charging strategy paired with each other, i.e. 1C with 2C, RG with 2C and 1C with RG. A diagonal dashed black line is also shown, which indicates a high correlation between variables. From the figure follows on the one hand that 1C and the RG are highly correlated in terms of capacity fade, and the correlation decreases as the retained capacity decreases, or what is the same as aging progresses. On the other hand, 2C is less correlated to 1C and the RG, and such correlation is reduced as

the battery degrades. Therefore, the degradation mechanisms that promote capacity fade associated to 1C and RG charging might be related, while 2C charging induces a different aging response compared to the other charging strategies. To elucidate the type of degradation that occurs inside the battery however, a postmortem analysis should be carried out through specific electrochemical tests but this aspect is outside the scope of this dissertation.

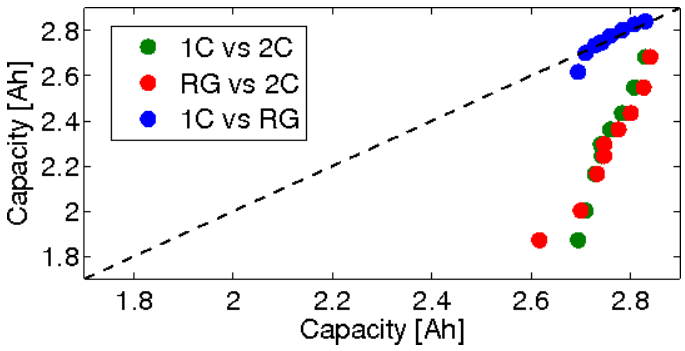

FIGURE 7.17: Capacity fade correlation plot obtained by pairing the retained capacity of each charging strategy with each other, namely 1C vs 2C (green), RG vs 2C (red) and 1C vs RG (blue).

7.3 Concluding Remarks

This chapter extends the previous one by considering experimental scenarios of prolonged battery aging. The first step towards implementation is to identify a sufficiently accurate electrochemical model for the battery at hand. Although most of the electrochemical parameters were previously estimated elsewhere, a model upgrade was necessary to account for extra dynamics that are typically excited during fast charging. This meant to go back to the design table and to test different models in simulation, while contrasting their predictions with experimental data. From this model re-design came out an *e*EHM, whose thermal parameters were identified here. While the EKF was designed on the basis of this *e*EHM, the RG was tuned on the basis of an approximation of this model resulting in a simple EHM. Once the feedback charge strategy was validated in simulation using the DFN model as a virtual battery, this strategy was written in simulink and tested on the real plant through the interfacing between MATLAB, dSPACE and the PEC tester.

The proposed RG charging strategy is compared to commercially available CCCV charging strategies with different C-rates, namely 1C and 2C. It turns out that the proposed RG strategy is able to charge faster and healthier the considered lithium-ion battery. The reasons behind such successful performance might be related to increasing the input current at the beginning of the charging process, while reducing it by riding the electrochemical constraints associated to battery degradation. This charging strategy allows safe incursions beyond upper cut-off voltages usually imposed by CCCV methods. It also reduces the time in which the battery is subject to this high voltage conditions when compared to CCCV strategies. Overall, the average current magnitude supplied by the RG is larger than that used by 1C and 2C CCCV, whereas the surface temperature is constantly larger than that induced by 1C CCCV. Despite these stress factors, the RG is able to provide a similar battery life (5.2% capacity fade) as the 1C CCCV (4.9% capacity fade) after 88 charge/discharge cycles while charging

faster the battery (75 min vs 105 min on average for RG and 1C CCCV, respectively). Adaptation to aging for the observer and the controller of the RG scheme may prove beneficial to improve its performance beyond the point reached at the moment of writing this thesis.

Chapter 8

Final Remarks

This last chapter wraps up this thesis with a brief summary in Section 8.1, the conclusions we have reached in the course of this work in Section 8.2 and some proposed future lines of research in Section 8.3.

8.1 Thesis Summary

This thesis proposed an electrochemical modeling framework and degradation-related constraints that, when embedded in diagnostic and control systems, proved to be accurate for the monitoring and performant for the operation of the battery while extending its lifetime. The recognition of the added value obtained from the tandem of first-principles models and control theoretic tools might consolidate a leap forward in the development of advanced battery management systems. More specifically, the proposed schemes for state-of-health tracking and safe and fast charging were successfully validated experimentally. The scheme for sensor fault diagnosis remains to be validated via experiments. The fine-grained control offers the possibility to operate the battery closer to the limits defined by degradation mechanisms and not arbitrarily set based on a countless number of experiments and heuristics. The immediate potential implications are smaller, lighter and cheaper batteries able to outperform nowadays batteries while keeping reliability and safety in high priority.

Chapters 2 and 3 provide the current state of knowledge concerning the different topics covered in this thesis as well as the standard control theoretic tools used as a basis to develop the different proposed solutions.

In Chapter 4, a thorough description of different electrochemical models that vary in model order and degree of detail is provided. The well-known DFN model is used as a benchmark to test the different monitoring and control strategies. The solid and electrolyte-phase diffusion parts of this model were simplified based on physical notions, e.g. by assuming a single spherical particle instead of multiple particles or a uniform reaction rate along the battery thickness. This model reduction yields an equivalent-hydraulic model. Both a thermal and aging models are also derived and coupled with the hydraulic model, which is finally complemented with a nonlinear output equation corresponding to the battery voltage. A careful analysis of degradation mechanisms showed that some of these mechanisms cannot be avoided for regular battery operation, such as calendar aging and solid-electrolyte interphase growth. However, some other sources of degradation such as lithium plating can be mitigated through suitable control policies. The knowledge of the degradation limits is exploited to come up with a set of electrochemical constraints intended to avoid the intrinsic conservatism of control strategies nowadays and to extend the lifetime of the battery.

Chapter 5 introduces diagnostic systems through two different approaches. On the one hand, the meeting point in-between these two approaches is that they both require

state observers to achieve their specific goal. On the other hand, the approaches differ in the following aspects. The first approach aims at providing parameter-based state-of-health (SOH) indicators to track battery aging, which is recognized to be a slow process compared to battery dynamics. Thus, system identification techniques are leveraged to estimate capacity and power fade from a batch of data meant to be periodically collected. The state estimation is performed by a joint state/parameter constrained extended Kalman filter. Besides battery monitoring of aging processes, the second approach aims at diagnosing voltage and temperature sensor faults. To this end, observer-based residuals are generated and evaluated via statistical change detection algorithms. The state estimation is performed by a dual state/parameter unscented Kalman filter for a differential algebraic equation system. Both approaches were devised to be complementary.

Chapter 6 describes a feedback charge strategy based on electrochemical models for the fast and health-conscious charge of lithium-ion batteries. First, the battery cell is pre-stabilized by means of a linear quadratic regulator which is tuned to charge the battery as fast as possible. Then, the set of electrochemical constraints associated to battery degradation is enforced through a modified reference governor able to handle OR constraints. For the digital implementation of this feedback controller, a state observer is designed. The fast charging capabilities of the proposed approach are first validated via simulation considering two different battery chemistries. This approach is further tested in Chapter 7 via long-term battery cycling experiments. Given the high C-rate conditions of fast charging and the considered battery cell, the reduced-order electrochemical model used previously needs to be enhanced with electrolyte and thermal dynamics in order to obtain a sufficiently accurate state estimate. The resulting model is used to design an extended Kalman filter. The latter provides the solid-phase diffusion state estimates to the modified reference governor, which generates a suitable control policy capable of complying with constraints. The proposed approach outperforms widely used commercial charging strategies in terms of both capacity retention and charging time.

In summary, the different contributions presented in this thesis have shown a great potential for improving battery systems through advanced management systems. These systems are based on electrochemical models and involve different tasks, such as battery state-of-charge and state-of-health monitoring, sensor fault detection and isolation and fast and health-conscious feedback charge control. Some of the proposed solutions were tested in simulation, while some others have been exhaustively tested with devoted experiments for the first time, to the best of the author's knowledge. Through all these capabilities, the new management system should be able to reduce battery price and size, and improve battery performance, safety and life expectancy.

As it could be seen, throughout Chapters 4-7 several electrochemical parametric models, state observers, parameter estimators coupled with a fault detection and isolation system or a closed-loop controller were considered. In order to have a clear picture of all the aforementioned contributions and the different pieces comprising them, a summary is provided in Table 8.1. The first column states the different features that a given contribution can have, whereas the first row heading denotes each contribution objective. The entries of the first four columns of the table show all the four contributions with their respective features. The electrochemical models differ on the number of states used to describe the solid-phase diffusion dynamics (2 or 3 states), as well as whether the model was enhanced with thermal, electrolyte and aging dynamics. Degradation mechanisms consisted of capacity, rate capability and power fade, which were associated to variables as Q_{loss} and $\theta = [D_s,\ R_f]$, respectively. State observers encompassed joint extended Kalman filter (jEKF) and dual unscented

Kalman filter (dUKF). Finally, parameter estimation, fault detection and isolation (FDI) diagnosis and closed-loop control were carried out by exploiting the simplified refined instrumental variable method for continuous-time systems (SRIVC) and least squares (LS) methods, the generalized likelihood ratio (GLR) algorithm and a reference governor (RG) with OR constraints, respectively. The chapter/section number corresponding to each contribution in this thesis is indicated in the last row of the table. The last column with the heading "All" highlights the ideal scenario (and perhaps future work) where all the different components developed at each stage of this work are combined together.

TABLE 8.1: Summary of the different contributions proposed throughout this thesis.

Feature\Focus	Estimation	FDI	Control	Control	All
Model	EHM3	*e*EHM3	EHM2	*e*EHM2	*e*EHM2
Aging	θ	θ, Q_{loss}	-	θ_2	θ, Q_{loss}
Observer	jEKF	dUKF	EKF	jEKF	UKF
Estimator	SRIVC/LS	-	-	-	SRIVC/LS
FDI Algorithm	-	GLR	-	-	GLR
Controller	-	-	RG	RG	RG
Chap/Sec	Sec. 5.1	Sec. 5.3	Chap. 6	Chap. 7	Sec. 8.3

8.2 Conclusions

This thesis presented a complete framework for lithium-ion battery monitoring and control, and the conclusions that can be drawn from this work are the following.

- Electrochemical models have been proven highly useful to improve the current state of battery systems. Although this type of models are typically too complex to be loaded into microcontrollers for estimation and control purposes, reduced-order electrochemical models able to keep relevant battery dynamics can be obtained and were derived in this work. This modeling framework is beneficial for deducing state-of-health indicators and degradation-related constraints.

- A diagnostic system for state-of-health monitoring and sensor fault detection and isolation was proposed. On the one hand, simulations showed that the state-of-health estimator detected 100% changes of capacity fade with 15% maximum error, while the power fade caused by a contact-resistance distribution was estimated to be within the distribution bounds. The applicability of this approach was also assessed with experimental data. On the other hand, simulations revealed that internal faults and sensor faults turn out to be decoupled for small fault magnitudes. Therefore, the battery state-of-health and voltage and temperature sensor faults can be successfully detected and isolated.

- Feedback charge strategies for lithium-ion batteries were derived from constrained control. These strategies are based on electrochemical models with degradation-related constraints. When tested in simulation, the proposed approaches proved to be very effective in charging different batteries faster than commercial charging strategies such as CCCV. When tested in long-term battery cycling experiments, the approach outperformed widely used commercial charging strategies such as CCCV in terms of charging time and capacity fade.

While the proposed approach charges a battery in 75 min and reduces its capacity in 5.2% after 88 cycles, a 2C CCCV needs 96 min to charge the battery and incurs in 29.7% of capacity fade after the same number of cycles. Actually, the capacity fade of this approach was comparable to the 4.9% of 1C CCCV, but the latter takes up to 105 min to charge the battery. Therefore, the combination of electrochemical modeling with constraints associated to degradation, state observers and constrained controllers have a great potential to improve battery systems.

8.3 Future Research Directions

This work has covered modeling, monitoring and control problems related to lithium-ion batteries while proposing solutions that hopefully add up a small grain of sand to create the Sahara Desert (i.e. it advances the research field one step further). Moreover, this work allowed us to identify some open issues in the field of battery management. We sketch the most relevant future research directions in the following lines.

This thesis has introduced different notions for the monitoring and control of batteries. However, many of the approaches proposed here have been proven to work in simulation and experimental setups, but no concrete mathematical proofs have been provided. We believe that aspects such as the convergence properties of the dual unscented Kalman filter for nonlinear differential algebraic equations of Section 5.3.2, the small coupling between internal faults and sensor faults of Section 5.3.3 and the separation principle for the feedback charge strategy of Section 6.1 can be proven under suitable hypotheses.

State-of-health indicators have been developed through the study of the different possible degradation mechanisms that can occur within a battery system. General aging sources likely to appear in batteries were accounted for. However, our approach was by no means exhaustive and we considered degradation mechanisms that differ in their mathematical description. Other battery degradation sources can be added to this framework, such as electrode particle stress and loss of active material, and some of the ones included here can be dropped if not considered relevant for a given battery chemistry and operating conditions.

A diagnosis system has been proposed to monitor the state of health of the battery and to assess the state of the sensors deployed for gathering measurements. Although both tasks were tackled separately, an advanced battery management system is expected to have both capabilities simultaneously. Therefore, the combination of these two aspects in a proper way remains as an interesting topic that is worth exploring in the future. This would make the diagnosis system robust to internal battery faults related to aging as well as sensor faults.

The feedback charge strategy proposed in this thesis has proven helpful to improve battery performance by reducing charge time, increasing lifespan and avoiding unsafe operating regions. We believe that we have reached a lower bound and these results can be further improved if the closed-loop control scheme adapts to aging and accounts for thermal dynamics. To this end, the first step is to analyze the data already gathered in order to identify the most likely degradation mechanisms taking place inside the battery. From that knowledge, the model parameters of the state observer and the controller can be updated in real time to account for degradation. On the other hand, the dynamics corresponding to battery temperature should also be considered in the closed-loop system. Extending the proposed control scheme

to accommodate thermal dynamics would allow to modify the input current such that thermal constraints are not violated. This approach can be proven beneficial to further reduce the typically temperature-dependent degradation mechanisms.

Another interesting road to explore is to consider a late lumping approach for the partial differential equations describing the system, as studied in [77] for instance. To hold the infinite-dimensional description of the system for estimation and control design would keep the eigenvalue structure of the problem while untangling the control synthesis from the discretization technique used for implementation. Thus, there is no need to reanalyze the system and the control scheme can be preserved even if a different discretization is needed. Extending the different control schemes proposed here to infinite dimensions is appealing from the theoretical viewpoint, although the high dimensionality of this kind of problems involves serious challenges that need to be addressed.

Although we have focused on the battery charge problem given its relevance nowadays, the discharge problem should also be addressed in the future. To this end, a battery pack needs to be considered and the interaction among battery cells accounted for. Then, the problem of managing the entire pack in terms of short term and long term operation has to be explored when the battery is subject to unknown discharge loads (typical of electric vehicles or household demand). Furthermore, the charging scheme proposed here should also be modified to suit this new scenario.

Appendix A

List of Publications

A.1. L.D. Couto, J. Schorsch, N. Job, A. Léonard and M. Kinnaert. "SOH Estimation for Li-Ion Batteries based on an Equivalent-Hydraulic Model: A LFP Application". *Journal of Energy Storage*, 21:259-271, 2019.

A.2. L.D. Couto, J. Schorsch, M.M. Nicotra and M. Kinnaert. "SOC and SOH estimation for Li-ion batteries based on an equivalent hydraulic model. Part I: SOC and surface concentration estimation". In *2016 American Control Conference*. Boston, MA, USA. pp. 4022-4028

A.3. J. Schorsch, L.D. Couto and M. Kinnaert. "SOC and SOH estimation for Li-ion battery based on an equivalent hydraulic model. Part II: SOH power fade estimation". In *2016 American Control Conference*. Boston, MA, USA. pp. 4029-4034.

A.4. L.D. Couto and M. Kinnaert. "Internal and Sensor Fault Detection and Isolation for Li-ion Batteries". In *Proceedings of 10th IFAC Symposium on Fault Detection, Supervision and Safety of Technical Processes*. Warsaw, Poland, 2018.

A.5. R. Romagnoli, L.D. Couto, M. Kinnaert and E. Garone. "A Feedback Charge Strategy for Li-Ion Battery Cells based on Reference Governor". To appear in *Journal of Process Control*.

A.6. R. Romagnoli, L.D. Couto, M. Kinnaert and E. Garone. "Control of the State-of-Charge of a Li-Ion Battery Cell via Reference Governor". In *2017 International Federation of Automatic Control World Congress*. Toulouse, France. 50.1, pp. 13747-13753. Rated among the best papers. Invited for journal extension.

A.7. L.D. Couto and M. Kinnaert. "Partition-Based Unscented Kalman Filter for Reconfigurable Battery Pack State Estimation Using an Electrochemical Model", In *2018 American Control Conference*. Milwaukee, WI, USA. pp. 3122-3128.

A.8. R. Romagnoli, L.D. Couto, M.M. Nicotra, M. Kinnaert and E. Garone. "Computationally-Efficient Constrained Control of the State-of-Charge of a Li-ion Battery Cell". In *2017 IEEE 56th Annual Conference on Decision and Control*. Melbourne, Australia. pp. 1433-1439.

A.9. A. Romero, L.D. Couto, A. Goldar and E. Garone. "Economic optimal control of a hybrid energy supply system for household applications under lithium-ion battery degradation". Submitted to *Journal of Power Sources*.

A.10. D. Zhang, S. Dey, L.D. Couto and S.J. Moura. "Battery Adaptive Observer for a Single Particle Model with Intercalation-Induced Stress". Provisionally accepted in *IEEE Transactions on Control Systems Technology*.

A.11. J. Schorsch, C.C. Castro, L.D. Couto, C. Nobre and M. Kinnaert. "Optimal control for fermentative production of fructo-oligosaccharides in fed-batch bioreactor". Provisionally accepted in *Journal of Process Control*.

Appendix B

$\tilde{O}_\infty$ Computation in the Case of OR-Constraints

This appendix presents the proof of Lemma 6.1.1 on how to compute an arbitrarily tight finitely-computable approximation $\tilde{O}_\infty$. The proof is inspired by [116] and it is borrowed from Ref. A5 in Appendix A. Since the matrix A_{cl} is Schur, given a constant reference v and the corresponding steady state $x_v = (I - A_{cl})^{-1}B_{cl}v$, a Lyapunov function in the form

$$V(x_{cl}, x_v) = (x_{cl} - x_v)^{\mathrm{T}} P (x_{cl} - x_v), \quad P > 0,$$

exists such that

$$V(x_{cl}(k+1), x_v) - V(x_{cl}(k), x_v) \leq -(x_{cl}(k) - x_v)^{\mathrm{T}} Q (x_{cl}(k) - x_v). \tag{B.1}$$

with $Q > 0$. According to Eq. (6.9), the set of admissible states is

$$X = \left\{ x_{cl} \in \mathbb{R}^n | \bigwedge_{j=1}^{c_c} \bigvee_{i=1}^{n_{c,j}} S_{j,i}^{\mathrm{T}} x_{cl} \leq s_{j,i} \right\}. \tag{B.2}$$

According to the definition of O_ϵ, the set of admissible equilibria x_v is

$$X_v = \left\{ x_v \in \mathbb{R}^n \left| \exists v \in \mathbb{R}^m : x_v = (I - A_{cl})^{-1} B_{cl} v \text{ and } \bigwedge_{j=1}^{c_c} \bigvee_{i=1}^{n_{c,j}} S_{j,i}^{\mathrm{T}} x_v \leq (1-\epsilon) s_{j,i} \right. \right\}. \tag{B.3}$$

At this point since: i) X and X_v are compact sets; and ii) since X_v is contained in the interior of X, the following two quantities exist:

- The maximum possible value of the Lyapunov function for any feasible $x \in X$ and any feasible $x_v \in X_v$

$$V_{\max} \triangleq \max_{\substack{x_{cl} \in X \\ x_v \in X}} V(x_{cl}, x_v)$$

- The minimum value that the Lyapunov function must have so that at least one state of the associated Lyapunov level set is able to violate the constraints if $x_v \in X_v$, i.e.

$$V_{\min} \triangleq \min_{\substack{x_{cl} \notin X \\ x_v \in X_v}} V(x_{cl}, x_v)$$

The important consideration here is that, if at a given time k: i) the Lypunov function $V(x_{cl}(k), x_v)$ is less than $V_{\min}$; ii) $x_v \in X_v$; and iii) if v is kept constant from k onward,

then, because of invariance, constraints are always satisfied in the future and then there is no need to check the constraints. At this point to conclude the proof it is enough to notice that because of Eq. (B.1) whenever $V(x_{cl}, x_v) > V_{\min}$, the one step variation always decreases of at least a nonzero quantity $\Delta V_{\min}$ defined as

$$\Delta V_{\min} \triangleq \begin{cases} \min_{e \in \mathbb{R}^n} e^{\mathrm{T}} Q e \\ \text{s.t.} \\ \quad e^{\mathrm{T}} P e \geq V_{\min} \end{cases}.$$

As a consequence, for any $x_{cl} \in X$ and $x_v \in X_v$, after at most a finite number of predictions ℓ^* there is no need to check the constraints. The integer ℓ^* can be defined as

$$\ell^* \triangleq \left\lceil \frac{V_{\max} - V_{\min}}{\Delta V_{\min}} \right\rceil$$

Note that Eqs. (6.11),(6.12) ensure that $x_{cl}(k) \in X$ and $x_v \in X$.

Appendix C

Battery Model Parameters for Simulation

This appendix introduces tables with the parameter values used for the different battery cell chemistries considered in this thesis for numerical simulation. Table C.1 corresponds to a LFP half battery cell. Table C.2 shows the parameters for a graphite | LCO and a graphite | LMO battery cells. Table C.3 corresponds to a graphite | NCA battery cell.

TABLE C.1: List of parameters for the LFP half battery cell [148] used in Section 5.2 to set up the DFN-based simulator.

Symbol	Units	Value
Design adjustable parameters		
A^b	m^2	1.13×10^{-4}
L^b	m	5×10^{-5}
${\varepsilon_s}^b$	-	0.14
${R_s}^b$	m	1.25×10^{-6}
${a_s}^b$	m^{-1}	3.36×10^5
${\bar{c}_e}^a$	$\mathrm{mol{\cdot}m}^{-3}$	10^3
L^{sb}	m	5×10^{-5}
Electrode parameters		
$D_s(I(t))^d$	$\mathrm{m}^2.\mathrm{s}^{-1}$	3×10^{-17} 7.5×10^{-17} 15×10^{-17}
${c_{s,\max}}^c$	$\mathrm{mol{\cdot}m}^{-3}$	22806
k_n^{+a}	$\mathrm{A{\cdot}m}^{2.5}{\cdot}\mathrm{mol}^{-1.5}$	4×10^{-5}
i_0^{-c}	$\mathrm{A{\cdot}m}^{-2}$	19.0
${\alpha_0}^a$	-	0.5
${\sigma_s}^b$	$\mathrm{S{\cdot}m}^{-1}$	6.75
R_r	$\Omega{\cdot}\mathrm{m}^2$	$(0.835, 1.660)$
U^+	V	^{c}

[a]Assumed [b]Measured [c]Taken from [148]
[d]Set according to the C-rate (C/5, C/2 and 1C, successively)

TABLE C.2: List of parameters used for setting up the DFN-based simulator used in Section 5.4 and Chapter 6 for a graphite | LCO [157] and a graphite | LMO [22, 157, 159] battery cell.

Symbol	Units	Graphite	Separator	LCO	LMO
		Design adjustable parameters			
A	m^2		1		
L	m	70×10^{-6}	25×10^{-6}	70×10^{-6}	
ε_s	-	0.55		0.5052	0.63
ε_e	-	0.4382	0.45	0.3	0.3
ϵ	-		1.5		
n_s^{Li}	mol		1.75		
R_s	m	12.5×10^{-6}		8.5×10^{-6}	8.5×10^{-6}
a_s	m^{-1}	1.32×10^5		1.78×10^5	2.22×10^5
		Electrode parameters			
D_s	$m^2 \cdot s^{-1}$	5.5×10^{-14}		1×10^{-11}	1×10^{-13}
$c_{s,\max}$	$mol \cdot m^{-3}$	30555		51555	22860
k_n	$A \cdot m^{2.5} \cdot mol^{-1.5}$	1.70×10^{-6}		6.43×10^{-6}	2.26×10^{-6}
α_0		0.5		0.5	
σ_s	$S \cdot m^{-1}$	100		10	3.8
R_c	$\Omega \cdot m^2$	1×10^{-5}		5×10^{-5}	2.5×10^{-3}
t_c^0	-		0.4		
U	V		[a]		[b]

[a]Taken from [157] [b]Taken from [22]

TABLE C.3: List of parameters used for setting up the DFN-based simulator used in Chapter 7 for a graphite | NCA battery cell [90].

Symbol	Units	Graphite	Separator	NCA
		Design adjustable parameters		
A	m^2		1	
L	m	79×10^{-6}	80×10^{-6}	61.5×10^{-6}
ε_s	-	0.54		0.67
ε_e	-	0.18	0.50	0.33
ϵ	-		1.5	
n_s^{Li}	mol		1.89	
R_s	m	14.9×10^{-6}		8.7×10^{-6}
a_s	m^{-1}	1.09×10^5		2.29×10^5
		Electrode parameters		
D_s	$m^2 \cdot s^{-1}$	1.44×10^{-14}		1.41×10^{-13}
$c_{s,\max}$	$mol \cdot m^{-3}$	37100		51000
k_n	$A \cdot m^{2.5} \cdot mol^{-1.5}$	1.70×10^{-6}		2.35×10^{-6}
α_0		0.5		0.5
σ_s	$S \cdot m^{-1}$	500		500
R_c	$\Omega \cdot m^2$	10^{-5}		10^{-5}
t_c^0	-		0.363	
U	V		[a]	

[a]Taken from [90]

The OCP function obtained by fitting the experimental data of Section 5.2 is shown in Eq. (C.1) below. The measurements were taken from a LFP half battery cell subject

to C/100 CC, and the fit was obtained by using the nonlinear least squares method. The OCP functional form is the following:

$$\begin{aligned} U^{+} = & -0.01284\mathrm{y} + 0.2766\left(1+\exp(896\mathrm{y})\right)^{-1} \\ & +0.7715\left(1+\exp(113.3(\mathrm{y}-0.002127))\right)^{-1} \\ & -0.192\left(1+(\exp(-107(\mathrm{y}-0.015)))\right)^{-1} \\ & +0.4515\left(1+\exp(-108.7((1-\mathrm{y})-0.03279))\right)^{-1} \\ & +0.8637\left(1+\exp(-90.71(1-\mathrm{y}))\right)^{-1} + 2.312 \end{aligned} \tag{C.1}$$

Appendix D

Computation of Electrolyte-Phase Diffusion Model

The reduced-order model for the lithium-ion diffusion taking place throughout the electrolyte phase of the battery system is derived here. The approach proposed in [139] is leveraged to analytically solve the electrolyte-phase diffusion PDEs as it was previously shown in Ref. A7 in Appendix A. These PDEs are given by

$$\frac{\partial c_e}{\partial t}(x,t) = \frac{D_{e,\text{eff}}}{\varepsilon_e}\frac{\partial^2 c_e}{\partial x^2}(x,t) + \frac{a_s(1-t_c^0)}{\varepsilon_e} j_n(x,t) \tag{D.1}$$

where c_e is the electrolyte concentration that covers the entire battery cell thickness. Eq. (D.1) takes the stated form within the positive $(+)$ and negative $(-)$ electrode spatial domains, while $\varepsilon_e = 1$ and $j_n = 0$ within the separator (s) domain. The boundary conditions that guarantee a zero flux of lithium ions outside the system and continuity of ion flux and electrolyte concentration throughout the cell thickness are given by

$$\begin{cases} \dfrac{\partial c_e^-}{\partial x}(x,t)\Big|_{x=0} = \dfrac{\partial c_e^+}{\partial x}(x,t)\Big|_{x=L} = 0 & \text{(D.2a)} \\ D_{e,\text{eff}}^- \dfrac{\partial c_e^-}{\partial x}(x,t)\Big|_{x=L^-} = D_{e,\text{eff}}^s \dfrac{\partial c_e^s}{\partial x}(x,t)\Big|_{x=L^-} & \text{(D.2b)} \\ c_e^-(x,t)\big|_{x=L^-} = c_e^s(x,t)\big|_{x=L^-} & \text{(D.2c)} \\ D_{e,\text{eff}}^s \dfrac{\partial c_e^s}{\partial x}(x,t)\Big|_{x=L^{-s}} = D_{e,\text{eff}}^+ \dfrac{\partial c_e^+}{\partial x}(x,t)\Big|_{x=L^{-s}} & \text{(D.2d)} \\ c_e^s(x,t)\big|_{x=L^{-s}} = c_e^+(x,t)\big|_{x=L^{-s}}\,. & \text{(D.2e)} \end{cases}$$

Expanding Eq. (D.1) with superindices to denote spatial domains and taking the Laplace transform to eliminate the time derivative results in

$$s\varepsilon_e^{\pm s} C_e^{\pm s}(x,s) - D_{e,\text{eff}}^{\pm s}\frac{\mathrm{d}^2 C_e^{\pm s}}{\mathrm{d}x^2}(x,s) + b^{\pm} I(s) = 0 \tag{D.3}$$

where $b^{\pm} = \mp\frac{1-t_c^0}{FL^{\pm}A}$, the pore-wall molar flux has been replaced by the uniform utilization $j_n(x,t)^{\pm} \approx \frac{I(t)}{Fa_s^{\pm}L^{\pm}}$, $C_e(x,s)$ and $I(s)$ are the Laplace transforms of $c_e(x,t)$ and $I(t)$ respectively, with s as the Laplace variable. The solution of Eq. (D.3) is

$$C_e^{\pm s}(x,s) = K_1^{\pm s}\exp(\beta^{\pm s}x) + K_2^{\pm s}\exp(-\beta^{\pm s}x) + \frac{b^{\pm}}{\varepsilon_e^{\pm s}s} I(s) \tag{D.4}$$

where $\beta^{\pm s} = \sqrt{\frac{\varepsilon_e^{\pm s} s}{D_e^{\pm s}}}$. Substituting Eq. (D.4) into boundary conditions Eqs. (D.2) (after taking the Laplace transform of these conditions) produces six linear equations with unknown constants $\{K_1^+, K_2^+, K_1^-, K_2^-, K_1^s, K_2^s\}$. After solving such system and evaluating it at the current collector/negative electrode interface $x = 0$, the following transcendental transfer function is obtained:

$$\frac{C_e(s)}{I(s)} = \frac{N_c(s)}{D_c(s)} \tag{D.5}$$

with

$$\begin{aligned} N_c(s) \;=\; & -b^+\alpha^s\varepsilon_e^- D_e^s \sinh(\beta^+ L^+) \\ & +b^- \left(-\alpha^s\varepsilon_e^+ D_e^s \cosh(\beta^s L^s)\sinh(\beta^+ L^+)\right. \\ & -\alpha^+\varepsilon_e^s D_e^s \cosh(\beta^+ L^+)\sinh(\beta^s L^s) \\ & +\alpha^-\varepsilon_e^+ D_e^- \sinh(\beta^- L^-)\sinh(\beta^+ L^+)\sinh(\beta^s L^s) \\ & +\alpha^s\varepsilon_e^+ D_e^s \cosh(\beta^- L^-)\cosh(\beta^s L^s)\sinh(\beta^+ L^+) \\ & +\alpha^+\varepsilon_e^s D_e^s \cosh(\beta^- L^-)\cosh(\beta^+ L^+)\sinh(\beta^s L^s) \\ & \left.+\alpha^-\alpha^+\alpha^s D_e^- D_e^s \cosh(\beta^+ L^+)\cosh(\beta^s L^s)\sinh(\beta^- L^-)\right) \end{aligned} \tag{D.6}$$

$$\begin{aligned} D_c(s) \;=\; & \varepsilon_e^- s\left(\alpha^-\varepsilon_e^+ D_e^- \sinh(\beta^- L^-)\sinh(\beta^+ L^+)\sinh(\beta^s L^s)\right. \\ & +\alpha^+\varepsilon_e^s D_e^s \cosh(\beta^- L^-)\cosh(\beta^+ L^+)\sinh(\beta^s L^s) \\ & +\alpha^s\varepsilon_e^+ D_e^s \cosh(\beta^- L^-)\cosh(\beta^s L^s)\sinh(\beta^+ L^+) \\ & \left.+\alpha^-\alpha^+\alpha^s D_e^- D_e^s \cosh(\beta^+ L^+)\cosh(\beta^s L^s)\sinh(\beta^- L^-)\right) \end{aligned} \tag{D.7}$$

where $\beta^{\pm s}$ is as previously defined and $\alpha^{\pm s} = \sqrt{\frac{\varepsilon_e^{\pm s}}{D_e^{\pm s}}}$. Only the negative electrode external boundary $x = 0$ is taken to evaluate the electrolyte diffusion. Such electrode choice is in line with the reference electrode for solid-phase diffusion while the external boundary location is taken since it corresponds to one of the voltage terminals.

The transfer function Eq. (D.5) is truncated through a second-order Padé approximation and parameterized as an equivalent-hydraulic model such as

$$\frac{C_e(s)}{I(s)} = \gamma_e \frac{\beta_e s + g_e}{s(\beta_e(1-\beta_e)s + g_e)} \tag{D.8}$$

which is finally rewritten in state-space form and discretized in time (sampling period $T_s = 1$ s) via Euler's approximation to get the following EHM

$$c_e(k+1) = \begin{bmatrix} 1 & 0 \\ \frac{g_e}{\beta_e(1-\beta_e)} & 1 - \frac{g_e}{\beta_e(1-\beta_e)} \end{bmatrix} c_e(k) + \begin{bmatrix} \gamma_e \\ \frac{\gamma_e}{1-\beta_e} \end{bmatrix} I(k) \tag{D.9}$$

with the state vector $c_e(k) = [c_{eb}(k), c_{es}(k)]^{\mathrm{T}}$.

Bibliography

[1] P. Patel. “New battery tech launches in drones [news]”. In: *IEEE Spectrum* 55 (7) (2018), pp. 7–9.

[2] T. Baxter. *Samsung reflects on exploding battery debacle, consumer trust*. Electronic Article. 2017.

[3] C. Davies. *Calls for lithium battery review after Boeing Dreamliner fire at Heathrow*. Electronic Article. 2015.

[4] FAA. *Lithium Batteries & Lithium Battery-Powered Devices*. Report. Federal Aviation Administration, 2018.

[5] R. Clark and A. Thomas. *Addressing the Safety Issues Related to Air Transportation of Lithium-Ion Batteries with Effective Engineered Thermal Management Solutions*. Electronic Article. 2016.

[6] A. Barré, B. Deguilhem, S. Grolleau, M. Gérard, F. Suard, and D. Riu. “A review on lithium-ion battery ageing mechanisms and estimations for automotive applications”. In: *Journal of Power Sources* 241 (0) (2013), pp. 680–689.

[7] M. Vetter and L. Rohr. “13 - lithium-ion batteries for storage of renewable energies and electric grid backup”. In: *Lithium-Ion Batteries*. Ed. by G. Pistoia. Amsterdam: Elsevier, 2014, pp. 293–309. ISBN: 978-0-444-59513-3.

[8] L. Lu, X. Han, J. Li, J. Hua, and M. Ouyang. “A review on the key issues for lithium-ion battery management in electric vehicles”. In: *Journal of Power Sources* 226 (0) (2013), pp. 272–288.

[9] P. Arora, R. E. White, and M. Doyle. “Capacity fade mechanisms and side reactions in lithium-ion batteries”. In: *Journal of The Electrochemical Society* 145 (10) (1998), pp. 3647–3667.

[10] N. A. Chaturvedi, R. Klein, J. Christensen, J. Ahmed, and A. Kojic. “Algorithms for advanced battery-management systems”. In: *IEEE Control Systems* 30 (3) (2010), pp. 49–68.

[11] P. Ramadass, B. Haran, P. M. Gomadam, R. White, and B. N. Popov. “Development of first principles capacity fade model for Li-ion cells”. In: *Journal of the Electrochemical Society* 151 (2) (2004), A196–A203.

[12] X.-G. Yang, Y. Leng, G. Zhang, S. Ge, and C.-Y. Wang. “Modeling of lithium plating induced aging of lithium-ion batteries: Transition from linear to nonlinear aging”. In: *Journal of Power Sources* 360 (2017), pp. 28–40.

[13] P. Arora, M. Doyle, and R. E. White. “Mathematical modeling of the lithium deposition overcharge reaction in lithium-ion batteries using carbon-based negative electrodes”. In: *Journal of the Electrochemical Society* 146 (10) (1999), pp. 3543–3553.

[14] M. Broussely. “Aging mechanisms and calendar-life predictions in lithium-ion batteries”. In: *Advances in Lithium-Ion Batteries*. Ed. by W. A. van Schalkwijk and B. Scrosati. 1st ed. New York: Springer US, 2002. Chap. 13, pp. 393–432. ISBN: 978-0-306-47356-2.

[15] J. Vetter, P. Novák, M. R. Wagner, C. Veit, K. C. Möller, J. O. Besenhard, M. Winter, M. Wohlfahrt-Mehrens, C. Vogler, and A. Hammouche. "Ageing mechanisms in lithium-ion batteries". In: *Journal of Power Sources* 147 (1–2) (2005), pp. 269–281.

[16] M. Broussely, P. Biensan, F. Bonhomme, P. Blanchard, S. Herreyre, K. Nechev, and R. J. Staniewicz. "Main aging mechanisms in Li ion batteries". In: *Journal of Power Sources* 146 (1–2) (2005), pp. 90–96.

[17] J. Christensen and J. Newman. "Stress generation and fracture in lithium insertion materials". In: *Journal of Solid State Electrochemistry* 10 (5) (2006), pp. 293–319.

[18] Y. Shi, K. Smith, R. Zane, and D. Anderson. "Life prediction of large lithium-ion battery packs with active and passive balancing". In: *2017 American Control Conference (ACC)*. Seattle, WA, USA, 2017, pp. 4704–4709.

[19] Y.-J. He, J.-N. Shen, J.-F. Shen, and Z.-F. Ma. "State of health estimation of lithium-ion batteries: A multiscale Gaussian process regression modeling approach". In: *AIChE Journal* 61 (5) (2015), pp. 1589–1600.

[20] X. Hu, S. Li, and H. Peng. "A comparative study of equivalent circuit models for Li-ion batteries". In: *Journal of Power Sources* 198 (2012), pp. 359–367.

[21] M. Doyle, T. Fuller, and J. Newman. "Modeling of galvanostatic charge and discharge of the lithium/ polymer/insertion cell". In: *Journal of The Electrochemical Society* 140 (6) (1993), pp. 1526–1533.

[22] T. F. Fuller, M. Doyle, and J. Newman. "Simulation and optimization of the dual lithium ion insertion cell". In: *Journal of The Electrochemical Society* 141 (1) (1994), pp. 1–10.

[23] J. Newman and K. Thomas-Alyea. *Electrochemical Systems*. 3rd Edition. Hoboken, New Jersey: John Wiley Sons, Inc., 2004.

[24] P. W. C. Northrop, M. Pathak, D. Rife, S. De, S. Santhanagopalan, and V. R. Subramanian. "Efficient simulation and model reformulation of two-dimensional electrochemical thermal behavior of lithium-ion batteries". In: *Journal of The Electrochemical Society* 162 (6) (2015), A940–A951.

[25] J. Turner, S. Allu, M. Berrill, W. Elwasif, S. Kalnaus, A. Kumar, D. Lebrun-Grandie, S. Pannala, and S. Simunovic. "Safer batteries through coupled multiscale modeling". In: *Procedia Computer Science* 51 (2015), pp. 1168–1177.

[26] J. Mao, W. Tiedemann, and J. Newman. "Simulation of Li-ion cells by dualfoil model under constant-resistance load". In: *ECS Transactions* 58 (48) (2014), pp. 71–81.

[27] H. Arunachalam, S. Onori, and I. Battiato. "On veracity of macroscopic lithium-ion battery models". In: *Journal of The Electrochemical Society* 162 (10) (2015), A1940–A1951.

[28] D. Bernardi, E. Pawlikowski, and J. Newman. "A general energy balance for battery systems". In: *Journal of The Electrochemical Society* 132 (1) (1985), pp. 5–12.

[29] L. Rao and J. Newman. "Heat-generation rate and general energy balance for insertion battery systems". In: *Journal of the Electrochemical Society* 144 (8) (1997), pp. 2697–2704.

[30] K. E. Thomas-Alyea, J. Newman, and R. M. Darling. "Mathematical modeling of lithium batteries". In: *Advances in Lithium-Ion Batteries*. Ed. by W. A. van Schalkwijk and B. Scrosati. 1st ed. New York: Springer US, 2002. Chap. 12, pp. 345–392. ISBN: 978-0-306-47356-2.

[31] X. Lin, H. E. Perez, S. Mohan, J. B. Siegel, A. G. Stefanopoulou, Y. Ding, and M. P. Castanier. "A lumped-parameter electro-thermal model for cylindrical batteries". In: *Journal of Power Sources* 257 (2014), pp. 1–11.

[32] C. Zou, C. Manzie, and D. Nešic. "A framework for simplification of PDE-based lithium-ion battery models". In: *IEEE Transactions on Control Systems Technology* 24 (5) (2016), pp. 1594–1609.

[33] M. Safari, M. Morcrette, A. Teyssot, and C. Delacourt. "Multimodal physics-based aging model for life prediction of Li-ion batteries". In: *Journal of The Electrochemical Society* 156 (3) (2009), A145–A153.

[34] E. Prada, D. Di Domenico, Y. Creff, J. Bernard, V. Sauvant-Moynot, and F. Huet. "A simplified electrochemical and thermal aging model of LiFePO4-graphite Li-ion batteries: Power and capacity fade simulations". In: *Journal of The Electrochemical Society* 160 (4) (2013), A616–A628.

[35] Y. Dai, L. Cai, and R. E. White. "Capacity fade model for spinel LiMn2O4 electrode". In: *Journal of The Electrochemical Society* 160 (1) (2013), A182–A190.

[36] C. Delacourt and M. Safari. "Life simulation of a graphite/LiFePO4 cell under cycling and storage". In: *Journal of The Electrochemical Society* 159 (8) (2012), A1283–A1291.

[37] P. Ramadass, B. S. Haran, R. E. White, and B. N. Popov. "Mathematical modeling of the capacity fade of Li-ion cells". In: *Journal of Power Sources* 123 (2) (2003), pp. 230–240.

[38] J. Christensen and J. Newman. "Cyclable lithium and capacity loss in Li-ion cells". In: *Journal of The Electrochemical Society* 152 (4) (2005), A818–A829.

[39] B. S. Haran, B. N. Popov, and R. E. White. "Determination of the hydrogen diffusion coefficient in metal hydrides by impedance spectroscopy". In: *Journal of Power Sources* 75 (1) (1998), pp. 56–63.

[40] G. Ning and B. N. Popov. "Cycle life modeling of lithium-ion batteries". In: *Journal of The Electrochemical Society* 151 (10) (2004), A1584–A1591.

[41] S. Santhanagopalan, Q. Guo, P. Ramadass, and R. E. White. "Review of models for predicting the cycling performance of lithium ion batteries". In: *Journal of Power Sources* 156 (2) (2006), pp. 620–628.

[42] M. Guo, G. Sikha, and R. E. White. "Single-particle model for a lithium-ion cell: Thermal behavior". In: *Journal of The Electrochemical Society* 158 (2) (2011), A122–A132.

[43] S. Santhanagopalan and R. E. White. "Online estimation of the state of charge of a lithium ion cell". In: *Journal of Power Sources* 161 (2) (2006), pp. 1346–1355.

[44] D. Di Domenico, A. Stefanopoulou, and G. Fiengo. "Lithium-ion battery state of charge and critical surface charge estimation using an electrochemical model-based extended Kalman filter". In: *Journal of Dynamic Systems, Measurement, and Control* 132 (6) (2010), pp. 061302.1–061302.11.

[45] M. Corno, N. Bhatt, and M. Verhaegen. "An efficient control oriented modeling approach for lithium ion cells". In: *American Control Conference*. Montreal, QC, Canada, 2012, pp. 4733–4738. ISBN: 0743-1619.

[46] K. A. Smith, C. D. Rahn, and C. Y. Wang. "Control oriented 1D electrochemical model of lithium ion battery". In: *Energy Conversion and Management* 48 (9) (2007), pp. 2565–2578.

[47] V. R. Subramanian, V. D. Diwakar, and D. Tapriyal. "Efficient macro-micro scale coupled modeling of batteries". In: *Journal of The Electrochemical Society* 152 (10) (2005), A2002–A2008.

[48] J. C. Forman, S. Bashash, J. L. Stein, and H. K. Fathy. "Reduction of an electrochemistry-based Li-ion battery model via quasi-linearization and Padé approximation". In: *Journal of the Electrochemical Society* 158 (2) (2011), A93–A101.

[49] K. A. Smith, C. D. Rahn, and C. Y. Wang. "Model order reduction of 1D diffusion systems via residue grouping". In: *Journal of Dynamic Systems, Measurement, and Control* 130 (1) (2008), pp. 1–8.

[50] D. A. Noren and M. A. Hoffman. "Clarifying the Butler–Volmer equation and related approximations for calculating activation losses in solid oxide fuel cell models". In: *Journal of Power Sources* 152 (0) (2005), pp. 175–181.

[51] H. Fang, X. Zhao, Y. Wang, Z. Sahinoglu, T. Wada, S. Hara, and R. A. de Callafon. "Improved adaptive state-of-charge estimation for batteries using a multi-model approach". In: *Journal of Power Sources* 254 (2014), pp. 258–267.

[52] R. H. Milocco, J. E. Thomas, and B. E. Castro. "Generic dynamic model of rechargeable batteries". In: *Journal of Power Sources* 246 (0) (2014), pp. 609–620.

[53] J. F. Manwell and J. G. McGowan. "Lead acid battery storage model for hybrid energy systems". In: *Solar Energy* 50 (5) (1993), pp. 399–405.

[54] M. Farkhondeh and C. Delacourt. "Mathematical modeling of commercial LiFePO4 electrodes based on variable solid-state diffusivity". In: *Journal of The Electrochemical Society* 159 (2) (2012), A177–A192.

[55] M. Farkhondeh, M. Safari, M. Pritzker, M. Fowler, T. Han, J. Wang, and C. Delacourt. "Full-range simulation of a commercial LiFePO4 electrode accounting for bulk and surface effects: A comparative analysis". In: *Journal of The Electrochemical Society* 161 (3) (2014), A201–A212.

[56] A. K. Padhi, K. S. Nanjundaswamy, and J. B. Goodenough. "Phospho-olivines as positive-electrode materials for rechargeable lithium batteries". In: *Journal of The Electrochemical Society* 144 (4) (1997), pp. 1188–1194.

[57] V. Srinivasan and J. Newman. "Discharge model for the lithium iron-phosphate electrode". In: *Journal of The Electrochemical Society* 151 (10) (2004), A1517–A1529.

[58] V. Srinivasan and J. Newman. "Existence of path-dependence in the LiFePO4 electrode". In: *Electrochemical and Solid-State Letters* 9 (3) (2006), A110–A114.

[59] K. E. Thomas-Alyea. "Modeling resistive-reactant and phase-change materials in battery electrodes". In: *ECS Transactions* 16 (13) (2008), pp. 155–165.

[60] C. Wang, U. S. Kasavajjula, and P. E. Arce. "A discharge model for phase transformation electrodes: Formulation, experimental validation, and analysis". In: *The Journal of Physical Chemistry C* 111 (44) (2007), pp. 16656–16663.

[61] U. S. Kasavajjula, C. Wang, and P. E. Arce. "Discharge model for LiFePO4 accounting for the solid solution range". In: *Journal of The Electrochemical Society* 155 (11) (2008), A866–A874.

[62] S. Dargaville and T. W. Farrell. "Predicting active material utilization in LiFePO4 electrodes using a multiscale mathematical model". In: *Journal of The Electrochemical Society* 157 (7) (2010), A830–A840.

[63] W. Dreyer, J. Jamnik, C. Guhlke, R. Huth, J. Moskon, and M. Gaberscek. "The thermodynamic origin of hysteresis in insertion batteries". In: *Nat Mater* 9 (5) (2010), pp. 448–453.

[64] M. Farkhondeh, M. Pritzker, M. Fowler, M. Safari, and C. Delacourt. "Mesoscopic modeling of Li insertion in phase-separating electrode materials: Application to lithium iron phosphate". In: *Physical Chemistry Chemical Physics* 16 (41) (2014), pp. 22555–22565.

[65] P. Bai, D. A. Cogswell, and M. Z. Bazant. "Suppression of phase separation in LiFePO4 nanoparticles during battery discharge". In: *Nano Letters* 11 (11) (2011), pp. 4890–4896.

[66] D. A. Cogswell and M. Z. Bazant. "Coherency strain and the kinetics of phase separation in LiFePO4 nanoparticles". In: *ACS Nano* 6 (3) (2012), pp. 2215–2225.

[67] M. Safari and C. Delacourt. "Mathematical modeling of lithium iron phosphate electrode: Galvanostatic charge/discharge and path dependence". In: *Journal of The Electrochemical Society* 158 (2) (2011), A63–A73.

[68] M. Mastali Majdabadi, S. Farhad, M. Farkhondeh, R. A. Fraser, and M. Fowler. "Simplified electrochemical multi-particle model for LiFePO4 cathodes in lithium-ion batteries". In: *Journal of Power Sources* 275 (2015), pp. 633–643.

[69] Y. Wang, H. Fang, L. Zhou, and T. Wada. "Revisiting the state-of-charge estimation for lithium-ion batteries: A methodical investigation of the extended Kalman filter approach". In: *IEEE Control Systems* 37 (4) (2017), pp. 73–96.

[70] S. Santhanagopalan and R. E. White. "State of charge estimation using an unscented filter for high power lithium ion cells". In: *International Journal of Energy Research* 34 (2) (2010), pp. 152–163.

[71] K. A. Smith, C. D. Rahn, and C. Y. Wang. "Model-based electrochemical estimation of lithium-ion batteries". In: *IEEE International Conference on Control Applications (CCA)*. San Antonio, TX, USA, 2008, pp. 714–719.

[72] R. Ahmed, M. El Sayed, I. Arasaratnam, J. Tjong, and S. Habibi. "Reduced-order electrochemical model parameters identification and state of charge estimation for healthy and aged Li-ion batteries - Part II: Aged battery model and state of charge estimation". In: *IEEE Journal of Emerging and Selected Topics in Power Electronics* 2 (3) (2014), pp. 678–690.

[73] H. Fang, Y. Wang, Z. Sahinoglu, T. Wada, and S. Hara. "State of charge estimation for lithium-ion batteries: An adaptive approach". In: *Control Engineering Practice* 25 (2014), pp. 45–54.

[74] Y. Wang, H. Fang, Z. Sahinoglu, T. Wada, and S. Hara. "Adaptive estimation of the state of charge for lithium-ion batteries: Nonlinear geometric observer approach". In: *IEEE Transactions on Control Systems Technology* 23 (3) (2015), pp. 948–962.

[75] R. Klein, N. A. Chaturvedi, J. Christensen, J. Ahmed, R. Findeisen, and A. Kojic. "State estimation of a reduced electrochemical model of a lithium-ion battery". In: *American Control Conference*. Baltimore, Maryland, USA, 2010, pp. 6618–6623. ISBN: 0743-1619.

[76] R. Klein, N. A. Chaturvedi, J. Christensen, J. Ahmed, R. Findeisen, and A. Kojic. "Electrochemical model based observer design for a lithium-ion battery". In: *IEEE Transactions on Control Systems Technology* 21 (2) (2013), pp. 289–301.

[77] S. J. Moura, N. A. Chaturvedi, and M. Krstić. "Adaptive partial differential equation observer for battery state-of-charge/state-of-health estimation via an electrochemical model". In: *Journal of Dynamic Systems, Measurement, and Control* 136 (1) (2014), pp. 011015–1–011015–11.

[78] S. M. Rezvanizaniani, Z. Liu, Y. Chen, and J. Lee. "Review and recent advances in battery health monitoring and prognostics technologies for electric vehicle (EV) safety and mobility". In: *Journal of Power Sources* 256 (0) (2014), pp. 110–124.

[79] M. Berecibar, I. Gandiaga, I. Villarreal, N. Omar, J. Van Mierlo, and P. Van den Bossche. "Critical review of state of health estimation methods of Li-ion batteries for real applications". In: *Renewable and Sustainable Energy Reviews* 56 (2016), pp. 572–587.

[80] J. De Hoog, K. Fleurbaey, A. Nikolian, N. Omar, J.-M. Timmermans, P. Van Den Bossche, and J. Van Mierlo. "Ageing phenomena of lithium ion batteries". In: *European Electric Vehicle Congress*. Brussels, Belgium, 2014, pp. 1–13.

[81] J. Christensen and J. Newman. "Effect of anode film resistance on the charge/discharge capacity of a lithium-ion battery". In: *Journal of The Electrochemical Society* 150 (11) (2003), A1416–A1420.

[82] V. Ramadesigan, K. Chen, N. A. Burns, V. Boovaragavan, R. D. Braatz, and V. R. Subramanian. "Parameter estimation and capacity fade analysis of lithium-ion batteries using reformulated models". In: *Journal of The Electrochemical Society* 158 (9) (2011), A1048–A1054.

[83] K. Uddin, S. Perera, W. D. Widanage, L. Somerville, and J. Marco. "Characterising lithium-ion battery degradation through the identification and tracking of electrochemical battery model parameters". In: *Batteries* 2 (2) (2016), p. 13.

[84] L. Zhang, L. Wang, C. Lyu, J. Li, and J. Zheng. "Non-destructive analysis of degradation mechanisms in cycle-aged graphite/LiCoO2 batteries". In: *Energies* 7 (2014), pp. 6282–6305.

[85] S. Santhanagopalan, Q. Zhang, K. Kumaresan, and R. E. White. "Parameter estimation and life modeling of lithium-ion cells". In: *Journal of The Electrochemical Society* 155 (4) (2008), A345–A353.

[86] V. Boovaragavan, S. Harinipriya, and V. R. Subramanian. "Towards real-time (milliseconds) parameter estimation of lithium-ion batteries using reformulated physics-based models". In: *Journal of Power Sources* 183 (1) (2008), pp. 361–365.

[87] G. K. Prasad and C. D. Rahn. "Model based identification of aging parameters in lithium ion batteries". In: *Journal of Power Sources* 232 (2013), pp. 79–85.

[88] J. C. Forman, S. J. Moura, J. L. Stein, and H. K. Fathy. "Genetic identification and Fisher identifiability analysis of the Doyle–Fuller–Newman model from experimental cycling of a LiFePO4 cell". In: *Journal of Power Sources* 210 (0) (2012), pp. 263–275.

[89] S. Santhanagopalan, Q. Guo, and R. E. White. "Parameter estimation and model discrimination for a lithium-ion cell". In: *Journal of the Electrochemical Society* 154 (3) (2007), A198–A206.

[90] S. Park, D. Kato, Z. Gima, R. Klein, and S. Moura. "Optimal experimental design for parameterization of an electrochemical lithium-ion battery model". In: *Journal of The Electrochemical Society* 165 (7) (2018), A1309–A1323.

[91] A. P. Schmidt, M. Bitzer, W. Imre, and L. Guzzella. "Model-based distinction and quantification of capacity loss and rate capability fade in Li-ion batteries". In: *Journal of Power Sources* 195 (22) (2010), pp. 7634–7638.

[92] D. Zhang, S. Dey, H. E. Perez, and S. J. Moura. "Remaining useful life estimation of lithium-ion batteries based on thermal dynamics". In: *2017 American Control Conference (ACC)*. Seattle, WA, USA, 2017, pp. 4042–4047.

[93] S. Dey, B. Ayalew, and P. Pisu. "Combined estimation of state-of-charge and state-of-health of Li-ion battery cells using SMO on electrochemical model". In: *2014 13th International Workshop on Variable Structure Systems (VSS)*. Nantes, France, 2014, pp. 1–6. ISBN: 2158-3986.

[94] S. Dey and B. Ayalew. "A diagnostic scheme for detection, isolation and estimation of electrochemical faults in lithium-ion cells". In: *ASME 2015 Dynamic Systems and Control Conference*. Columbus, Ohio, USA, 2015, V001T13A001.

[95] S. Dey, B. Ayalew, and P. Pisu. "Nonlinear adaptive observer for a lithium-ion battery cell based on coupled electrochemical–thermal model". In: *Journal of Dynamic Systems, Measurement, and Control* 137 (11) (2015), pp. 111005–111005–12.

[96] L. Zheng, L. Zhang, J. Zhu, G. Wang, and J. Jiang. "Co-estimation of state-of-charge, capacity and resistance for lithium-ion batteries based on a high-fidelity electrochemical model". In: *Applied Energy* 180 (2016), pp. 424–434.

[97] S. K. Rahimian, S. Rayman, and R. E. White. "State of charge and loss of active material estimation of a lithium ion cell under low Earth orbit condition using Kalman filtering approaches". In: *Journal of The Electrochemical Society* 159 (6) (2012), A860–A872.

[98] C. Zou, A. G. Kallapur, C. Manzie, and D. Nesic. "PDE battery model simplification for SOC and SOH estimator design". In: *2015 54th IEEE Conference on Decision and Control (CDC)*. 2015, pp. 1328–1333.

[99] A. Bartlett, J. Marcicki, S. Onori, G. Rizzoni, X. G. Yang, and T. Miller. "Electrochemical model-based state of charge and capacity estimation for a composite electrode lithium-ion battery". In: *IEEE Transactions on Control Systems Technology* 24 (2) (2016), pp. 384–399.

[100] M. F. Samadi, S. M. M. Alavi, and M. Saif. "Online state and parameter estimation of the Li-ion battery in a Bayesian framework". In: *2013 American Control Conference*. Washington, DC, USA, 2013, pp. 4693–4698. ISBN: 0743-1619.

[101] W. Chen, W.-T. Chen, M. Saif, M.-F. Li, and H. Wu. "Simultaneous fault isolation and estimation of lithium-ion batteries via synthesized design of Luenberger and learning observers". In: *Control Systems Technology, IEEE Transactions on* 22 (1) (2014), pp. 290–298.

[102] A. Singh, A. Izadian, and S. Anwar. "Nonlinear model based fault detection of lithium ion battery using multiple model adaptive estimation". In: *The International Federation of Automatic Control*. Cape Town, South Africa, 2014, pp. 8546–8551.

[103] Naval Surface Warfare Center Carderock Div. Bethesda MD. *Handbook of Reliability Prediction Procedures for Mechanical Equipment*. Revision A. USA, 2011.

[104] J. Marcicki, S. Onori, and G. Rizzoni. "Nonlinear fault detection and isolation for a lithium-ion battery management system". In: *ASME 2010 Dynamic Systems and Control Conference*. Cambridge, Massachusetts, USA, 2010, pp. 607–614.

[105] Z. Liu, H. He, Q. Ahmed, and G. Rizzoni. "Structural analysis based fault detection and isolation applied for a lithium-ion battery pack". In: *IFAC-PapersOnLine* 48 (21) (2015), pp. 1465–1470.

[106] H. He, Z. Liu, and Y. Hua. "Adaptive extended Kalman filter based fault detection and isolation for a lithium-ion battery pack". In: *Energy Procedia* 75 (2015), pp. 1950–1955.

[107] S. Dey, S. Mohon, P. Pisu, and B. Ayalew. "Sensor fault detection, isolation, and estimation in lithium-ion batteries". In: *IEEE Transactions on Control Systems Technology* 24 (6) (2016), pp. 2141–2149.

[108] Z. Liu, Q. Ahmed, G. Rizzoni, and H. He. "Fault detection and isolation for lithium-ion battery system using structural analysis and sequential residual generation". In: *ASME 2014 Dynamic Systems and Control Conference*. San Antonio, TX, USA, 2014, pp. 1–10.

[109] G. Ablay. "Online Condition Monitoring of Battery Systems With a Nonlinear Estimator". In: *IEEE Transactions on Energy Conversion* 29 (1) (2014), pp. 232–239.

[110] J. A. Carcone. "Performance of lithium-ion battery systems". In: *WESCON/94. Idea/Microelectronics. Conference Record*. Anaheim, CA, USA, 1994, pp. 242–248. ISBN: 1095-791X.

[111] P. Keil and A. Jossen. "Charging protocols for lithium-ion batteries and their impact on cycle life—An experimental study with different 18650 high-power cells". In: *Journal of Energy Storage* 6 (2016), pp. 125–141.

[112] R. Klein, N. A. Chaturvedi, J. Christensen, J. Ahmed, R. Findeisen, and A. Kojic. "Optimal charging strategies in lithium-ion battery". In: *American Control Conference*. San Francisco, CA, USA, 2011, pp. 382–387. ISBN: 0743-1619.

[113] B. Suthar, V. Ramadesigan, P. W. C. Northrop, B. Gopaluni, S. Santhanagopalan, R. D. Braatz, and V. R. Subramanian. "Optimal control and state estimation of lithium-ion batteries using reformulated models". In: *American Control Conference*. Washington, DC, USA, 2013, pp. 5350–5355. ISBN: 0743-1619.

[114] M. Torchio, N. A. Wolff, D. M. Raimondo, L. Magni, U. Krewer, R. B. Gopaluni, J. A. Paulson, and R. D. Braatz. "Real-time model predictive control for the optimal charging of a lithium-ion battery". In: *2015 American Control Conference (ACC)*. Chicago, IL, USA, 2015, pp. 4536–4541. ISBN: 0743-1619.

[115] E. Garone, S. Di Cairano, and I. Kolmanovsky. "Reference and command governors for systems with constraints: A survey on theory and applications". In: *Automatica* 75 (2017), pp. 306–328.

[116] A. Bemporad. "Reference governor for constrained nonlinear systems". In: *IEEE Transactions on Automatic Control* 43 (3) (1998), pp. 415–419.

[117] K. A. Smith, C. D. Rahn, and C. Wang. "Model-based electrochemical estimation and constraint management for pulse operation of lithium ion batteries". In: *IEEE Transactions on Control Systems Technology* 18 (3) (2010), pp. 654–663.

[118] H. Perez, N. Shahmohammadhamedani, and S. Moura. "Enhanced performance of Li-ion batteries via modified reference governors and electrochemical models". In: *IEEE/ASME Transactions on Mechatronics* 20 (4) (2015), pp. 1511 –1520.

[119] R. Kalman. "A new approach to linear filtering and prediction problems". In: *ASME Transactions, Journal of Basic Engineering* 82D (1960), pp. 35–45.

[120] G. Goodwin and K. Sang Sin. *Adaptive Filtering Prediction and Control*. Englewood Cliffs, New Jersey: Prentice-Hall, Inc., 1984.

[121] D. Simon. *Optimal state estimation: Kalman, H [infinity], and nonlinear approaches*. Hoboken, N.J. : Wiley-Interscience, c2006., 2006. ISBN: 0471708585 9780471708582.

[122] R. E. Kopp and R. J. Orford. "Linear regression applied to system identification for adaptive control systems". In: *AIAA Journal* 1 (10) (1963), pp. 2300–2306.

[123] Y. Song and J. W. Grizzle. "The extended Kalman filter as a local asymptotic observer for discrete-time nonlinear systems". In: *Journal of Mathematical Systems, Estimation and Control* 5 (1) (1995), pp. 59–78.

[124] K. Reif and R. Unbehauen. "The extended Kalman filter as an exponential observer for nonlinear systems". In: *IEEE Transactions on Signal Processing* 47 (8) (1999), pp. 2324–2328.

[125] K. Reif, S. Gunther, E. Yaz, and R. Unbehauen. "Stochastic stability of the discrete-time extended Kalman filter". In: *IEEE Transactions on Automatic Control* 44 (4) (1999), pp. 714–728.

[126] E. A. Wan and R. van der Merwe. "The unscented Kalman filter". In: *Kalman Filtering and Neural Networks*. John Wiley Sons, Inc., 2002, pp. 221–280. ISBN: 9780471221548.

[127] S. J. Julier and J. K. Uhlmann. "Unscented filtering and nonlinear estimation". In: *Proceedings of the IEEE* 92 (3) (2004), pp. 401–422.

[128] P. C. Young. *Recursive estimation and time-series analysis: An introduction for the student and practitioner*. 2nd Edition. Berlin: Springer-Verlag, 2011.

[129] T. Söderström and P. Stoica. *System Identification*. Systems and Control Engineering. Englewood Cliffs: Prentice Hall, 1989.

[130] M. Blanke, M. Kinnaert, J. Lunze, and M. Staroswiecki. *Diagnosis and Fault-Tolerant Control*. 2nd Edition. Germany, 2006.

[131] P. Kapasouris, M. Athans, and G. Stein. "Design of feedback control systems for unstable plants with saturating actuators." In: *IFAC symposium on nonlinear control system design*. Pergamon Press, 1990, pp. 302–307.

[132] A. Tewari. *Modern Control Design With MATLAB and SIMULINK*. West Sussex, England: John Wiley Sons Ltd, 2002.

[133] F. Lewis, L. V. Draguna, and L. S. Vassilis. *Optimal Control*. Third Edition. Hoboken, New Jersey, 2012.

[134] I. Kolmanovsky and E. G. Gilbert. "Theory and computation of disturbance invariant sets for discrete-time linear systems". In: *Mathematical Problems in Engineering* 4 (4) (1998), pp. 317–367.

[135] E. G. Gilbert and K. T. Tan. "Linear systems with state and control constraints: The theory and application of maximal output admissible sets". In: *IEEE Transactions on Automatic Control* 36 (9) (1991), pp. 1008–1020.

[136] I. Kolmanovsky, E. Garone, and S. Di Cairano. "Reference and command governors: A tutorial on their theory and automotive applications". In: *American Control Conference (ACC), 2014*. 2014, pp. 226–241. ISBN: 0743-1619.

[137] T. Jacobsen and K. West. "Diffusion impedance in planar, cylindrical and spherical symmetry". In: *Electrochimica Acta* 40 (2) (1995), pp. 255–262.

[138] K. Smith and C.-Y. Wang. "Solid-state diffusion limitations on pulse operation of a lithium ion cell for hybrid electric vehicles". In: *Journal of Power Sources* 161 (1) (2006), pp. 628–639.

[139] C. D. Rahn and C.-Y. Wang. "Discretization methods". In: *Battery Systems Engineering*. John Wiley Sons Ltd, 2013, pp. 49–87. ISBN: 9781118517048.

[140] J. Marcicki, M. Canova, A. T. Conlisk, and G. Rizzoni. "Design and parametrization analysis of a reduced-order electrochemical model of graphite/LiFePO4 cells for SOC/SOH estimation". In: *Journal of Power Sources* 237 (2013), pp. 310–324.

[141] T. R. Tanim, C. D. Rahn, and C.-Y. Wang. "A temperature dependent, single particle, lithium ion cell model including electrolyte diffusion". In: *Journal of Dynamic Systems, Measurement, and Control* 137 (1) (2015), p. 011005.

[142] W. B. Gu and C. Y. Wang. "Thermal-electrochemical modeling of battery systems". In: *Journal of the Electrochemical Society* 147 (8) (2000), pp. 2910–2922.

[143] C. D. Rahn and C.-Y. Wang. "Governing equations". In: *Battery Systems Engineering*. John Wiley Sons Ltd, 2013, pp. 23–48. ISBN: 9781118517048.

[144] D. Simon. "Kalman filtering with state constraints: A survey of linear and nonlinear algorithms". In: *Control Theory Applications, IET* 4 (8) (2010), pp. 1303–1318.

[145] P. Young and A. Jakeman. "Refined instrumental variable methods of recursive time-series analysis Part III. Extensions". In: *International Journal of Control* 31 (4) (1980), pp. 741–764.

[146] J. Schorsch, H. Garnier, M. Gilson, and P. C. Young. "Instrumental variable methods for identifying partial differential equation models". In: *International Journal of Control* 86 (12) (2013), pp. 2325–2335.

[147] H. Garnier. "Direct continuous-time approaches to system identification. Overview and benefits for practical applications". In: *European Journal of Control* 24 (2015), pp. 50–62.

[148] M. Safari and C. Delacourt. "Modeling of a commercial graphite/LiFePO4 cell". In: *Journal of The Electrochemical Society* 158 (5) (2011), A562–A571.

[149] M. Ecker, N. Nieto, S. Käbitz, J. Schmalstieg, H. Blanke, A. Warnecke, and D. U. Sauer. "Calendar and cycle life study of Li(NiMnCo)O2-based 18650 lithium-ion batteries". In: *Journal of Power Sources* 248 (2014), pp. 839–851.

[150] C. Delacourt and M. Safari. "Analysis of lithium deinsertion/insertion in LiyFePO4 with a simple mathematical model". In: *Electrochimica Acta* 56 (14) (2011), pp. 5222–5229.

[151] J. S. Albuquerque and L. T. Biegler. "Decomposition algorithms for on-line estimation with nonlinear DAE models". In: *Computers and Chemical Engineering* 21 (3) (1997), pp. 283–299.

[152] Y. Puranik, V. A. Bavdekar, S. C. Patwardhan, and S. L. Shah. "An ensemble Kalman filter for systems governed by differential algebraic equations (DAEs)". In: *IFAC Proceedings Volumes* 45 (15) (2012), pp. 531–536.

[153] V. M. Becerra, P. D. Roberts, and G. W. Griffiths. "Applying the extended Kalman filter to systems described by nonlinear differential-algebraic equations". In: *Control Engineering Practice* 9 (3) (2001), pp. 267–281.

[154] R. Mandela, R. Rengaswamy, S. Narasimhan, and L. N. Sridhar. "Recursive state estimation techniques for nonlinear differential algebraic systems". In: *Chemical Engineering Science* 65 (16) (2010), pp. 4548–4556.

[155] R. van der Merwe. "Sigma-point Kalman filters for probabilistic inference in dynamic state-space models". Thesis. 2004.

[156] G. L. Plett. "Sigma-point Kalman filtering for battery management systems of LiPB-based HEV battery packs: Part 2: Simultaneous state and parameter estimation". In: *Journal of Power Sources* 161 (2) (2006), pp. 1369–1384.

[157] J. Newman. *FORTRAN Programs for the Simulation of Electrochemical Systems*. Web Page. 1998.

[158] A. Bemporad, A. Casavola, and E. Mosca. "Nonlinear control of constrained linear systems via predictive reference management". In: *IEEE Transactions on Automatic Control* 42 (3) (1997), pp. 340–349.

[159] I. J. Ong and J. Newman. "Double-layer capacitance in a dual lithium ion insertion cell". In: *Journal of The Electrochemical Society* 146 (12) (1999), pp. 4360–4365.

[160] M. Tang, P. Albertus, and J. Newman. "Two-dimensional modeling of lithium deposition during cell charging". In: *Journal of The Electrochemical Society* 156 (5) (2009), A390–A399.

[161] R. Hausbrand, G. Cherkashinin, H. Ehrenberg, M. Gröting, K. Albe, C. Hess, and W. Jaegermann. "Fundamental degradation mechanisms of layered oxide Li-ion battery cathode materials: Methodology, insights and novel approaches". In: *Materials Science and Engineering: B* 192 (2015), pp. 3–25.

[162] D. Tang, Y. Sun, Z. Yang, L. Ben, L. Gu, and X. Huang. "Surface structure evolution of LiMn2O4 cathode material upon charge/discharge". In: *Chemistry of Materials* 26 (11) (2014), pp. 3535–3543.

[163] D. H. Jang and S. M. Oh. "Electrolyte effects on spinel dissolution and cathodic capacity losses in 4 v Li/Li x Mn2O4 rechargeable cells". In: *Journal of The Electrochemical Society* 144 (10) (1997), pp. 3342–3348.

[164] K. Amine, J. Liu, S. Kang, I. Belharouak, Y. Hyung, D. Vissers, and G. Henriksen. "Improved lithium manganese oxide spinel/graphite Li-ion cells for high-power applications". In: *Journal of Power Sources* 129 (1) (2004), pp. 14–19.

[165] S. Ebbesen, P. Kiwitz, and L. Guzzella. "A generic particle swarm optimization Matlab function". In: *2012 American Control Conference (ACC)*. Fairmont Queen Elizabeth, Montréal, Canada, 2012, pp. 1519–1524. ISBN: 0743-1619.

[166] V. Ruiz. *Standards for the performance and durability assessment of electric vehicle batteries*. Report. European Union, 2018.

[167] V. Ruiz, A. Pfrang, A. Kriston, N. Omar, P. Van den Bossche, and L. Boon-Brett. "A review of international abuse testing standards and regulations for lithium ion batteries in electric and hybrid electric vehicles". In: *Renewable and Sustainable Energy Reviews* 81 (2018), pp. 1427–1452.

[168] N. Omar, M. Daowd, O. Hegazy, G. Mulder, J.-M. Timmermans, T. Coosemans, P. Van den Bossche, and J. Van Mierlo. "Standardization work for BEV and HEV applications: Critical appraisal of recent traction battery documents". In: *Energies* 5 (1) (2012), p. 138.

[169] Y. Firouz, S. Khaleghi, L. Pugi, L. Berzi, and E. Locorotondo. *Evaluation of international standards for lithium-ion batteries*. Report. European Commission, 2018.

[170] ISO 12405-1. *Electrically propelled road vehicles – Test specification for lithium-ion traction battery packs and systems - Part 1: High-power applications*. Standard. 2011.

[171] ISO 12405-2. *Electrically propelled road vehicles – Test specification for lithium-ion traction battery packs and systems – Part 2: High-energy applications*. Standard. 2012.

[172] ISO 12405-3. *Electrically propelled road vehicles – Test specification for lithium-ion traction battery packs and systems – Part 3: Safety performance requirements*. Standard. 2014.

[173] ISO 12405-4. *Electrically propelled road vehicles –Test specification for lithium-ion traction battery packs and systems – Part 4: Performance testing*. Standard. 2018.

[174] IEC 62660-1. *Secondary lithium-ion cells for the propulsion of electric road vehicles - Part 1: Performance testing*. Standard. 2018.

[175] IEC 62660-2. *Secondary lithium-ion cells for the propulsion of electric road vehicles - Part 2: Reliability and abuse testing*. Standard. 2018.

[176] G. Mulder, N. Omar, S. Pauwels, F. Leemans, B. Verbrugge, W. De Nijs, P. Van den Bossche, D. Six, and J. Van Mierlo. "Enhanced test methods to characterise automotive battery cells". In: *Journal of Power Sources* 196 (23) (2011), pp. 10079–10087.

[177] D. Stroe, M. Świerczyński, A. Stan, R. Teodorescu, and S. J. Andreasen. "Accelerated lifetime testing methodology for lifetime estimation of lithium-ion batteries used in augmented wind power plants". In: *IEEE Transactions on Industry Applications* 50 (6) (2014), pp. 4006–4017.

[178] J. P. Christopherson. *Battery Test Manual For Electric Vehicles*. Report. Idaho National Laboratory, 2015.